



POLITECNICO DI MILANO
DEPARTMENT OF PHYSICS
DOCTORAL PROGRAMME IN PHYSICS

HIGH-SPEED MULTIPLEX CARS IN THE ENTIRE
RAMAN-ACTIVE REGION THROUGH SUPERCONTINUUM
GENERATION IN BULK MEDIA

Doctoral Dissertation of:
Federico Vernuccio

Supervisor:
Prof. Dario Polli

Tutor:
Prof. Giulio Cerullo

The Chair of the Doctoral Program:
Prof. Marco Finazzi

2022/2023 – XXXV cycle

Acknowledgements

This PhD thesis is the result of the experimental activities carried out at Politecnico di Milano, Department of Physics, in the VIBRA laboratory, led by professor Dario Polli. The project was mainly financed by the European Union project CRIMSON under Grant Agreement No. 101016923 and from the Regione Lombardia project NEWMED under Grant Agreement No. POR FESR 2014-2020.

At the end of my PhD, I would like to express my deepest gratitude to my supervisor prof. Dario Polli for his invaluable support, patience and feedbacks in my research. I am also extremely grateful to my tutor prof. Giulio Cerullo who provided precious expertise and knowledge for the achievement of the scientific results. I would like to extend my thanks to my lab friends for their moral support, editing help and for making my time spent inside and outside the laboratory enjoyable and unforgettable. Lastly, words cannot express the importance that my family's never-ending support and love have had for the accomplishment of these results. Without them all I have done in these years would have been impossible.

Abstract

Coherent anti-Stokes Raman Scattering (CARS) microscopy is a label-free vibrational imaging technique delivering chemical maps of cells and tissues. With respect to Spontaneous Raman (SR), CARS provides several orders of magnitude higher speed by exploiting third-order nonlinear optical processes occurring between the sample and the impinging electric fields. The simplest CARS implementation employs two narrowband picosecond pulses (pump and Stokes) that are spatiotemporally superimposed at the sample plane to probe a single vibrational mode. Broadband CARS (BCARS) combines narrowband pump pulses with broadband Stokes pulses to record broad vibrational spectra, thus combining the high acquisition speed of single-frequency CARS with the chemical specificity of SR. Despite many improvements in the last decade, BCARS microscopes struggle to work in the so-called “fingerprint” spectral region ($400\text{-}1800\text{ cm}^{-1}$), because it features a weaker Raman response than the high-frequency CH-stretching region ($2800\text{-}3100\text{ cm}^{-1}$).

Here, we demonstrate a novel approach to BCARS to collect the full Raman spectrum ($400\text{-}3100\text{ cm}^{-1}$). The experimental setup starts with a 2-MHz repetition rate femtosecond fiber laser centered at 1035 nm. The system delivers high energy ($\approx 2\mu\text{J}$) pulses used for generating sub-20 fs broadband Stokes pulses (1050-1600 nm) by white-light continuum in a bulk YAG crystal, a compact and alignment-insensitive technique. Combining them with 3.7 ps narrowband pump pulses, we can generate CARS signal with high spectral resolution ($< 10\text{ cm}^{-1}$) in the entire Raman window exploiting both two-color and three-color excitation mechanisms. The reduced repetition rate unlocks two other key advantages of the system. On the one hand, it entails a longer delay ($0.5\ \mu\text{s}$) between two consecutive pulses, enabling thermal energy dissipation; on the other hand, for a given average power limited by sample degradation, higher pulse energies results in higher peak intensities, generating a stronger CARS signal thus increasing the signal-to-noise ratio and/or the acquisition speed. The system is equipped with a homemade transmission microscope to image cells and tissues at high-speed ($< 3\text{ ms}$) with a large field of view ($> 800 \times 800\ \mu\text{m}^2$). Using a novel post-processing pipeline, we deliver high-quality chemical maps, distinguishing the main chemical compounds in cancer cells and identifying cancer in liver slices of mouse models, unveiling the path for applications in histopathological settings.

Summary

This thesis reports the main achievements in the experimental Ph.D. research activity I carried out from 2019 to 2022 in the VIBRA lab of Politecnico di Milano, led by professor Dario Polli.

In these years, I contributed to the advances in BCARS microscopy by designing and constructing a BCARS microscopy system and by developing a post-processing pipeline for the analysis of the collected hyperspectral data.

Chapter 1 provides an overview of the theory behind coherent Raman scattering processes, reviewing the main BCARS implementations. Chapter 2 reports the tools needed for white-light continuum generation in bulk media, describing the nonlinear processes involved. Chapter 3 illustrates the architecture of the BCARS experimental setup and points out the advantages of the system with respect to other setups described in the literature. This chapter continues with: a full characterization of the pump and Stokes optical sources; a detailed description of the home-made microscopy unit; a description of the detection system.

Chapter 4 deals with the acquisition and post-processing methods employed for CARS spectroscopy and imaging. After a discussion about the design of the experiments, the chapter focuses on the post-processing pipeline needed for the analysis of the BCARS hyperspectral data. This part establishes a strong link between CRS applications and deep learning-based solutions. Indeed, it reports two novel convolutional neural networks used for the denoising of the CARS spectra and for the non-resonant background removal. The chapter also describes the main numerical algorithms commonly used for CARS data post-processing that I adapted from the literature. Eventually, it concludes with the main spectral unmixing methods employed in the thesis for delivering chemical maps of heterogeneous biological samples.

Chapter 5 reports the main results obtained with the BCARS experimental setup, showing BCARS spectra of solvents and chemical maps of plastic beads and biological samples, such as cells and tissues.

I believe this work constitutes a novel, compact, and robust methodology for BCARS imaging delivering high-chemically informative maps of cells and tissues in a label-free and non-destructive way. I envisage the BCARS microscopy platform will be used for biomedical applications, especially in the field of cancer research.

Contents

1	Coherent raman scattering microscopy	1
1.1	Introduction	1
1.2	Historical introduction	5
1.3	Light-matter interaction	6
1.3.1	Harmonic oscillator	6
1.3.2	Vibrational modes	7
1.3.3	Spontaneous Raman	10
1.3.4	Coherent Raman Scattering	12
1.3.5	Third order non-linear processes	15
1.3.6	Propagation equation in Four-Wave Mixing processes	16
1.4	The CARS process	18
1.4.1	Resonant and non-resonant contribution to CARS	20
1.4.2	Broadband CARS	23
1.4.3	Two-color and three-color CARS	27
1.4.4	Time-delayed CARS	32
1.4.5	Epi-detected CARS	33
1.5	The SRS process	35
1.5.1	SRS vs CARS	37
1.5.2	Broadband SRS	38
2	Supercontinuum generation in bulk media	41
2.1	Introduction	43
2.2	Self-focusing of Laser Beams	44
2.3	Self-phase Modulation of Laser Pulses	46
2.4	Nonlinear Absorption and Ionization	47
2.5	Plasma Effects	47
2.6	Chromatic dispersion	48
2.7	Self-steepening and Space-Time Focusing	49
2.8	Femtosecond filamentation	50
2.9	Conclusion	50

3	Experimental Setup and optical sources	53
3.1	Experimental setup	54
3.2	Advantages of the BCARS system	55
3.3	Characterization of the optical sources	57
3.3.1	Theory and experimental setup for SHG-FROG	57
3.3.2	Pump pulses	61
3.4	Stokes pulses	65
3.5	Microscope	69
3.6	Detection	71
4	Acquisition and post-processing of the CARS data	73
4.1	Introduction	73
4.2	Experimental design	74
4.2.1	Setup alignment	74
4.2.2	Bright-field Image	75
4.2.3	Preliminary measurements	77
4.2.4	Experiment planning	77
4.3	Data post-processing	77
4.3.1	Quality control	77
4.4	Denoising of the hyperspectral data	79
4.4.1	Denosing via Singular Value Decompositon	79
4.4.2	Denoising via machine-learning	80
4.4.3	Machine-learning fundamentals	81
4.4.4	Neural Networks fundamentals	82
4.4.5	Convolutional Neural Networks	85
4.4.6	CNN spectral denoiser	87
4.5	NRB removal	92
4.5.1	Numerical algorithms for NRB removal	93
4.5.2	NRB removal via deep learning	98
4.5.3	State-of-the-art of NRB removal via deep learning	104
4.6	Spectral unmixing	105
4.6.1	Multivariate curve resolution analysis	105
4.6.2	N-FINDR algorithm	106
4.6.3	K-means cluster analysis	106
5	Results	109
5.1	Introduction	109
5.2	Fingerprint multiplex CARS at high speed based on supercontinuum generation in bulk media and deep learning spectral denoising	110
5.2.1	Experimental setup and post-processing pipeline	110
5.2.2	BCARS spectroscopy of solvents	111
5.2.3	BCARS microscopy of plastic beads	112
5.2.4	BCARS imaging of biological tissues	114
5.2.5	Conclusion	115
5.3	Ultrabroadband CARS microscopy of biological samples with white-light continuum in bulk media	116
5.3.1	Ultrabroadband two-color CARS spectroscopy on solvents	116

5.3.2	Ultrabroadband CARS spectroscopy combining two and three-color mechanism	118
5.3.3	Ultrabroadband CARS microscopy of senescence cells	120
5.3.4	Ultrabroadband CARS microscopy of biological tissues	121
5.3.5	Conclusion	122
6	Conclusion and Outlook	123
	Glossary	129
	Bibliography	131

CHAPTER 1

Coherent raman scattering microscopy

1.1 Introduction

Optical microscopy [1] is a powerful tool for life sciences, thanks to its capability of imaging cells and tissues at the micrometer scale. Among the optical microscopy techniques, the most common ones to study biological samples are fluorescence microscopy and vibrational microscopy.

Fluorescence microscopy is well known for its superb sensitivity guaranteed by the use of fluorescence markers, which may be endogenous (e.g. fluorescent proteins) [2] or exogenous (e.g. dyes or semiconductor quantum dots) [3], that are added to cells or tissues. However, the use of external tags may lead to sample perturbation and may alter the biological functions of the investigated specimen. Moreover, photobleaching is a phenomenon that must be taken into account when dealing with fluorescent markers, since it prevents the possibility of imaging many times the same portion of the sample. Eventually, fluorescence microscopy provides little information especially when the goal is to distinguish many biomolecules in the sample. Indeed, fluorescence microscopy is impeded by the "color barrier," which limits the number of distinguishable structures to a maximum of approximately five since the employed fluorescent proteins feature broad emission bandwidths that overlap among them [4–6]. These are the reasons why many problems in life sciences call for label-free techniques that do not require the use of fluorescent markers, preventing sample perturbation and/or alteration, enabling signal stability, and distinguishing a larger number of structures in highly heterogeneous biological samples.

Vibrational microscopy [7] overcomes these hurdles by delivering chemical maps of cells and tissues in a label-free and non-invasive manner. It employs spectroscopic techniques that enable the visualization of different biomolecules analyzing their characteristic vibrational spectrum [8]. Indeed, every structure in a biological sample fea-

tures a vibrational spectrum that constitutes a signature for the identification of its main constituents, providing higher specificity than fluorescent techniques. The spectrum may be divided into three main spectral windows [9](Fig. 1.1). The first region spans from 400 to 1800 cm^{-1} and is known as the fingerprint region. It corresponds to the low energy vibrational modes of the sample and contains many sharp and congested peaks that carry information about lipids, proteins, and nucleic acids. The peaks associated with proteins are those of amino acids (such as phenylalanine at $\approx 1000 \text{ cm}^{-1}$, tyrosine, and tryptophan), those of amide-I groups of secondary protein structures (in 1500–1700 cm^{-1} region), and the stretching or deformation of carbon atoms bonded with nitrogen (C-N stretch), hydrogen (C-H rock, bend, or scissoring), or other carbon atoms (C-C stretch). The peaks of lipids are mainly the ones at 1300 cm^{-1} associated with CH_2 bonds and around the 1440-1450 cm^{-1} region correspondent to the CH and CH_2 modes. Eventually, the nucleic acids may be identified through the peaks of DNA, RNA, and nitrogenous bases. The second region of the vibrational spectrum spans from 1800 to 2700 cm^{-1} . It is known as the Raman-biological silent region of the spectrum since in general no peaks are present in this spectral window. This region is particularly exploited when using Raman-tag molecules which provide specific signals with characteristic peaks in the silent region that do not interfere with the ones of the biological constituents [10, 11]. The last region corresponds to the high-energy vibrational modes and goes from 2700 to 3100 cm^{-1} . This region displays broad peaks associated with the CH, CH_2 , and CH_3 symmetric and antisymmetric stretching through which one can discern lipids, proteins, and DNA. Moreover, this region features a signal which is stronger than the one of the fingerprint region, since the biological samples have many more oscillators with CH bonds. Beyond 3100 cm^{-1} , the spectrum of water-containing samples presents the very broad and intense Raman peak of water.

Among the vibrational techniques, vibrational absorption microscopy resonantly probes the vibrational modes of the sample using mid-infrared (MIR) light ($\lambda \approx 3\text{-}10 \mu\text{m}$) to shine it. However, vibrational microscopy is not so suitable for imaging small structures in biological specimens because of the use of very long wavelengths that prevents depth penetration due to water absorption and high spatial resolution because of the diffraction limit. Raman microscopy solves this issue, by employing visible or near-infrared (NIR) light to illuminate the sample, providing higher penetration depth and spatial resolution than its MIR counterpart. For these reasons, Raman techniques are particularly adequate to image biological samples, such as tissues and cells [13, 14]. The simplest and most employed approach for Raman techniques is known as Spontaneous Raman (SR) [15]. SR employs a quasi-monochromatic visible or NIR pump laser beam, at frequency ω_p . The vibrational information is encoded in the spontaneously emitted inelastically scattered Stokes or anti-Stokes components, at frequency $\omega_S = \omega_p - \Omega$ and $\omega_{aS} = \omega_p + \Omega$, respectively, with Ω being the vibrational resonance of the sample. These components arise in the red-shifted (for the Stokes) and blue-shifted (for the anti-Stokes) spectral region and can be easily collected using a spectrometer after properly filtering out the pump radiation. When dealing with applications in life sciences, SR techniques typically acquire the Stokes component which is more intense than the anti-Stokes one at room temperature. Indeed, the probed molecules obey a Boltzmann distribution, so that the molecules mostly remain in their lowest energy levels at thermal equilibrium, thus preventing the possibility to populate the vibra-

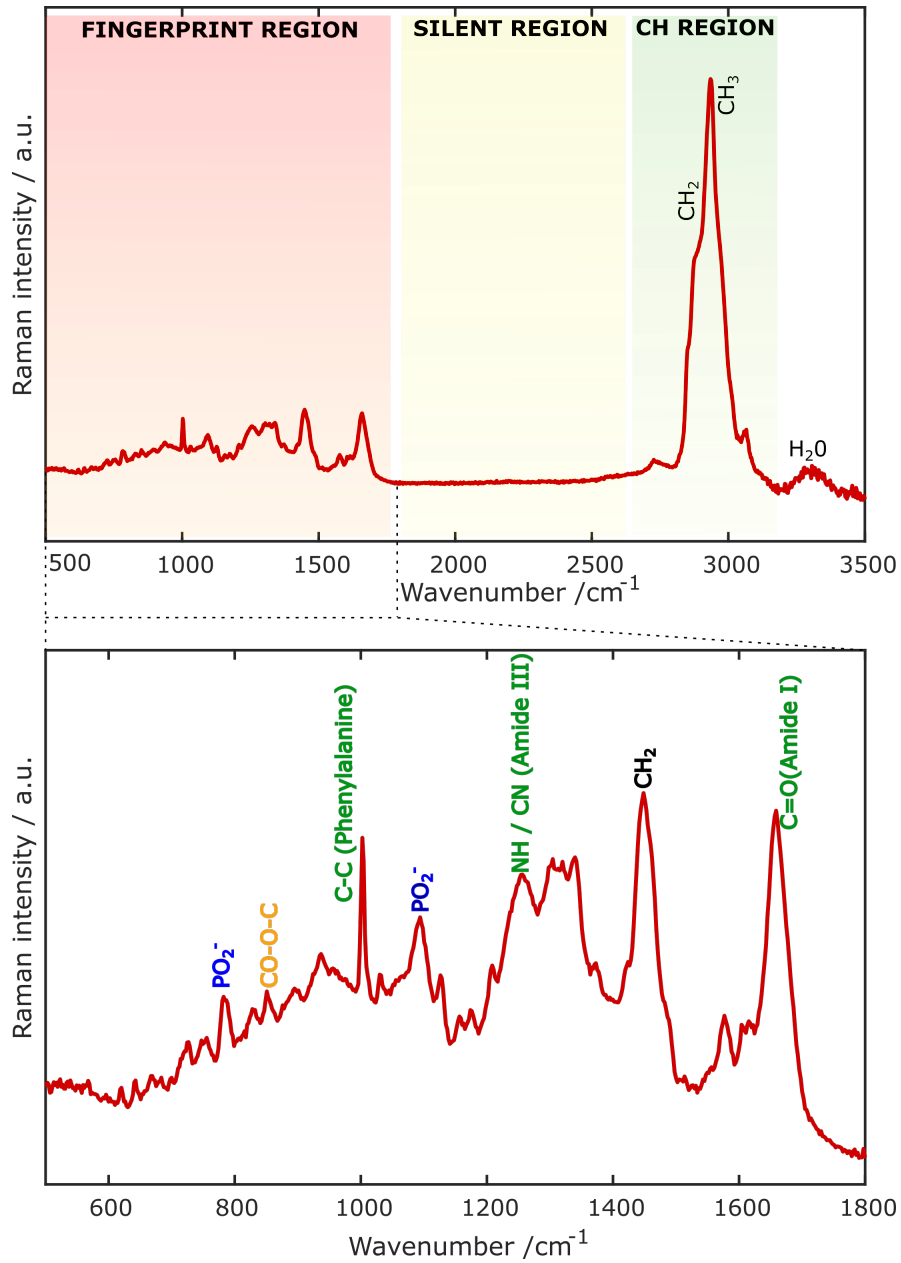


Figure 1.1: Raman spectrum of a cell in the entire Raman-active region and in the corresponding fingerprint region. The peak assignments refer to the most abundant chemical bonds in biological samples, belonging to the four major biological molecules: lipids (black), protein (green), carbohydrates (yellow), and nucleic acids (blue). Adapted from [12].

tional levels where the anti-Stokes component generates from. Thanks to its chemical specificity, SR has already been used in the biomedical field, especially for cancer diagnosis [16–21]. Despite providing high chemical information from the investigated sample, SR suffers from low scattering cross-sections, requiring long integration time (from $\approx 100\text{ms}$ to $\approx 1\text{s}$) for the acquisition of a single-pixel vibrational spectrum, thus precluding the possibility of fast imaging. Eventually, in SR the Stokes component sits on top of a background coming from the sample autofluorescence, requiring post-processing methods to subtract it.

Coherent Raman scattering (CRS) techniques [22, 23] exploit third-order nonlinear optical processes occurring between the interacting electric fields and the specimens and provide higher imaging speed than SR thanks to coherent excitation of the vibrational modes at the focal spot. In its simplest implementation, CRS employs narrow-band picosecond pulses, namely the pump at frequency ω_p and the Stokes at frequency ω_S , whose frequency shift $\Omega = \omega_p - \omega_S$ is resonant with a specific vibrational mode of the sample Ω_R . When the two trains of pulses simultaneously arrive at the sample plane, a collective molecular oscillation is induced in the focal volume. Unlike in the SR process, the molecules, in this case, vibrate coherently, and the signal originates only in the focal spot, since high power densities are required to trigger the nonlinear signal, which propagates along a phase-matched direction. Because of the non linear nature, CRS implementations provide intrinsic 3D-sectioning capabilities without the need for any confocal aperture.

We can summarize the main advantages of CRS techniques in the following list:

- CRS produces a significantly stronger signal than SR microscopy due to a coherent superposition of the vibrational responses from the excited oscillators, which enables substantially faster imaging speeds;
- Unlike fluorescence microscopy, which uses fluorophores and stainings, CRS is a non-invasive and label-free technique that prevents sample perturbation.
- It normally operates without population transfer far from the molecules electronic excited states, limiting the photobleaching of biological substances; Indeed, in comparison to the visible range, excitation in the NIR (700-1200 nm) has the benefit of having relatively low light absorption by tissues *in vivo* and reduced light scattering by turbid media, making it possible to investigate thick tissues at higher penetration depths (typically in the 0.1-1 mm range) [24]. Reduced phototoxicity and tissue damage are also other advantages of shifting the wavelength of the beams toward the infrared.
- Similar to multi-photon fluorescence microscopy [25], CRS is a nonlinear microscopy technique and the signal is only generated in the focal volume, enabling 3D imaging without the requirement for any physical confocal apertures [26];

It is evident that despite boosting the image acquisition speed (down to hundreds of nanoseconds or tens of microseconds per pixel) [27, 28], narrowband or "single frequency" CRS techniques do not offer the same wealth of information provided by SR since they only probe a single vibrational mode at a time. Broadband CRS techniques combine the high acquisition speed of narrowband CRS techniques with the high information content of SR implementations, giving access to the whole vibrational spectrum

of the scrutinized specimen. Their implementations call for broadband sources to match the vibrational coherences of the investigated sample occurring at many different frequencies. Broadband CRS is technically demanding and it is not yet established in clinics as narrowband CRS. According to the way the signal is collected, we may refer to it as hyperspectral CRS and multiplex CRS.

In hyperspectral CRS, either the pump or the Stokes is rapidly tuned to match different vibrational modes of the samples and the signal is sequentially acquired, thus reconstructing the spectrum pixel by pixel. In multiplex approaches, a narrowband beam is combined with a broadband beam to generate a signal that carries the information on a relatively large spectral region (depending on the frequency shifts covered by their combination) of the spectrum that is acquired in parallel thus providing the vibrational spectrum in a single shot.

The two most commonly employed CRS implementations are stimulated Raman scattering (SRS) [29–31] and coherent anti-Stokes Raman scattering (CARS) [32–34]. SRS measures the intensity gain of the Stokes beam (stimulated Raman gain) or the intensity loss of the pump beam (stimulated Raman loss), while CARS detects the background-free signal at the anti-Stokes frequency $\omega_a S = \omega_p + \Omega$. The details and the theoretical background for a comprehensive understanding of these two techniques will be discussed in the following sections of the chapter.

1.2 Historical introduction

In 1928, Chandrasekhara Venkata Raman, together with his student K.S. Krishnan, reported for the first time that when light passes through transparent media, the deflected light presents changes in frequency. The same effect was observed independently by Grigory Landsberg and Leonid Mandelstam, in Moscow on 21 February 1928 (one week earlier than Raman and Krishnan) [35]. This phenomenon is referred to as the inelastic scattering of an electromagnetic field and was named the Raman effect by the name of its discoverer, who received the Nobel Prize in physics in 1930 [36]. Even though the potential application for molecular spectroscopy was clear from the beginning, it was not until the invention of the first working ruby laser by Theodore Harold Maiman in 1960 that its technical implementation became possible. After that, the Raman effect became one of the most popular ways to perform molecular analysis. However, the slowness of data acquisition, due to its incoherent nature, prevents fast imaging. The first evidence of the stimulated Raman effect dates back to 1962. The effect was discovered accidentally by Eckhardt after the discovery of the laser since the process requires a laser power density of the order of 10^8W/cm^2 only achievable through stimulated emission of radiation. The first demonstration of CARS have been done in 1964 by Yajima and Takatsuji and later in 1965 by Maker and Terhune, who discovered that a four-wave-mixing process can be resonant with the vibrational modes of a sample. Since then, both SRS and CARS implementations have been widely used for spectroscopic applications. In 1982, Duncan [37] reported the first work of CARS imaging using gas lasers, while in 1999 Zumbush [34] realized CARS imaging using solid-state lasers. In the same year, Xie's group developed a novel CARS microscope characterized by a collinear geometry of two laser beams and raster scanning using near-infrared wavelengths, demonstrating the first biological applications with coher-

ent Raman [38]. The use of collinear geometry and near-infrared wavelengths greatly simplified the instrumentation and biocompatibility, triggering many applications and innovations. While CARS microscopes were invented in the early 1980s, it was only in 2007 that the first SRS microscope was developed [30]. Indeed, only after the use of modulation of the laser beams at MHz rate and phase-sensitive lock-in amplifier detection schemes, it was possible to measure SRS signals at reasonable pixel dwell times. In 2008, Xie's group reported a high-speed SRS microscope for biological imaging [29]. Nowadays, Coherent Raman scattering microscopy is a potent method for revealing the chemical mechanisms within living cells and functional materials.

1.3 Light-matter interaction

The following subsections will introduce the fundamental basics for a comprehensive understanding of the processes involved in Coherent Raman scattering. This theoretical introduction starts with the description of a simple yet effective model to study the interaction between electromagnetic waves and continues with the main concepts of spontaneous Raman and coherent Raman processes, such as CARS and SRS.

1.3.1 Harmonic oscillator

The simplest way to describe a molecule interacting with an electromagnetic field is to start by modeling the molecule as a mass attached to a spring characterized by stiffness k , as depicted in Fig. 1.2. Through this picture, it is possible to give an intuitive explanation of Raman scattering [39].

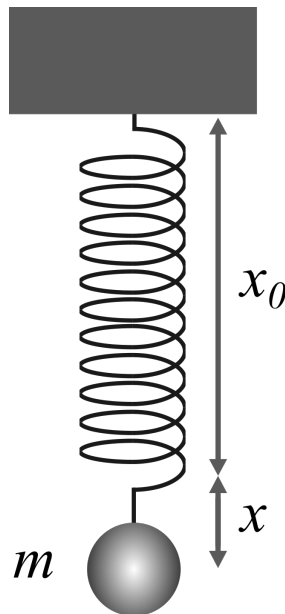


Figure 1.2: Mass-spring system. x_0 is the equilibrium position, while x is the relative displacement. Adapted from [39]

The system described is a harmonic oscillator, an ideal object whose temporal oscillation is a sine or cosine wave with constant amplitude and with a frequency that is

solely dependent on the system parameters (in this case, the mass m and the spring constant k). Consider a mass attached to a spring and set vertically, subjected to gravity. At equilibrium, we can write the equation describing its center of mass as:

$$mg - kx_0 = 0, \quad (1.1)$$

where x_0 represents the equilibrium position. Using the second dynamics law, it is possible to study the displacement x of the center of mass with respect to x_0 , which reads:

$$\frac{d^2x}{dt^2} + \omega_0^2 x = 0, \quad (1.2)$$

where we defined $\omega_0 = \frac{k}{m}$ as the system resonant frequency. Consider now a damping force experienced by the mass, directly proportional to its velocity and to a damping coefficient γ . We can add this term to eq. (1.2) and we find:

$$\frac{d^2x}{dt^2} + 2\gamma \frac{dx}{dt} + \omega_0^2 x = 0, \quad (1.3)$$

Since we would like to model the interaction with the electromagnetic field, we need to take into account a periodically oscillating excitation force. Hence we define $F(t) = F_0 \cos(\omega t)$, where F_0 represents the amplitude, while ω is the angular frequency. Introducing this driving force $F(t)$, eq.(1.3) becomes:

$$\frac{d^2x}{dt^2} + 2\gamma \frac{dx}{dt} + \omega_0^2 x = \frac{F(t)}{m}, \quad (1.4)$$

To solve this equation, it is more convenient to introduce the complex exponential notation, where $F(t) = F_0 e^{-i\omega t}$. Therefore, we can look for a solution of the form $x(\omega, t) = x(\omega) e^{-i\omega t}$, that simplifies the calculus of the temporal derivatives. Plugging these expressions in eq.(1.4) we find:

$$(-\omega^2 - 2i\gamma\omega + \omega_0^2)x(\omega)e^{-i\omega t} = \frac{F_0 e^{-i\omega t}}{m}, \quad (1.5)$$

From eq.(1.5), we can find the solution $x(\omega)$:

$$x(\omega) = \frac{F_0/m}{\omega_0^2 - \omega^2 - 2i\gamma\omega}, \quad (1.6)$$

Close to the resonance ($\omega \approx \omega_0$) and for small damping coefficient ($\gamma \ll \omega_0$), the solution of eq.(1.6) can be approximated by a complex Lorentzian function [39]:

$$x(\omega) = \frac{-F_0/(2m\omega_0)}{(\omega - \omega_0) + i\gamma}, \quad (1.7)$$

1.3.2 Vibrational modes

In the previous section, we modeled a molecule as a single mass attached to a spring. This led to eq.(1.6), which describes the movement of the mass varying the frequency of the driving force. Let us now generalize the model to describe the vibrational modes of a molecule. A vibrational mode is a periodic motion of the atoms of a molecule

Chapter 1. Coherent raman scattering microscopy

relative to each other, such that the center of mass remains still. Every vibrational mode is associated with a resonance frequency Ω_R , dictated by the atomic mass, the atomic species, the number of involved chemical bonds, the molecule geometry and symmetry, and the presence of possible hydrogen bonds. Typically, the resonance frequency of roto-vibrational modes is in the range from 1 to 4000 cm^{-1} and it can be probed by absorption spectroscopy using mid-infrared light (Fig.1.3.(b)).

A molecule with n atoms with a non-linear geometry presents $3n - 6$ vibrational modes. For example, water molecules (H_2O) has three vibrational modes (Fig.1.3.(a)). For a linear molecule, the number of vibrational modes is $3n - 5$, therefore, a diatomic molecule ($n=2$) has just one vibrational mode, which is the stretching mode. Let us now model a diatomic molecule as a system constituted by two point masses, respectively m_1 and m_2 , connected by a spring. We will assume that the equilibrium distance between the point masses is x_0 and the resonant frequency is Ω_R . We will also assume that the diatomic molecule taken into account is polar and presents an asymmetric distribution of charges, in particular, the atom m_1 will have a charge $+q$, while the atom m_2 will have a charge $-q$. The model is shown in Fig.1.3.(c).

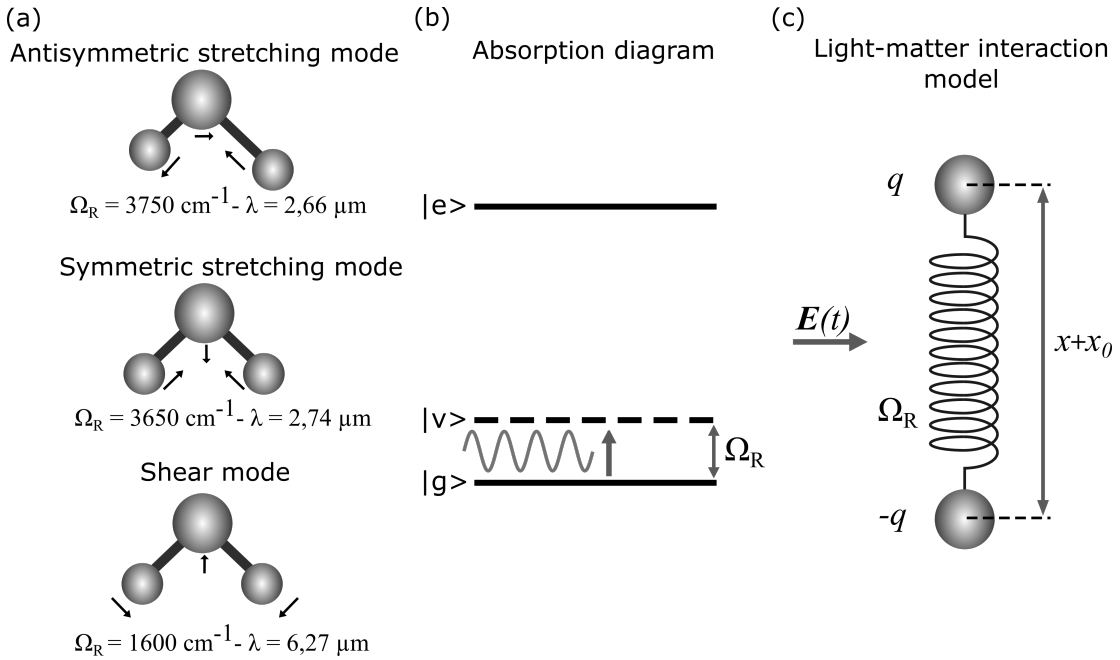


Figure 1.3: (a) Vibrational modes of H_2O . (b) Absorption diagram. (c) Model of a diatomic molecule and light-matter interaction model. Adapted from [39]

Let us consider the interaction with an electric field $\vec{E}(t)$ with angular frequency ω and linearly polarized along the molecule axis. The field will generate a Lorentz force $F_{Lorentz} = qE_0 e^{-i\omega t}$ acting on the atoms of the molecule. We can write a formula analogous to eq. (1.4):

$$\frac{d^2 x}{dt^2} + 2\gamma \frac{dx}{dt} + \Omega_R^2 x = \frac{F_{Lorentz}(t)}{\mu}, \quad (1.8)$$

where μ is the reduced mass: $\mu = m_1 m_2 / (m_1 + m_2)$, and the damping term γ represents the radiation loss of the oscillating dipole. Eq.(1.8) can be solved (as we solved eq.

(1.4)), finding the approximated solution:

$$x(\omega) = \frac{-F_{Lorentz}/(2\mu\Omega_R)}{(\omega - \Omega_R) + i\gamma}, \quad (1.9)$$

The presence of an asymmetric distribution of charges in the molecule induces a dipole moment \vec{p} , which can be expressed as $\vec{p} = q\vec{d}$, where \vec{d} is the vector displacement between the atoms, directed from the negative to the positive charge. If we consider a macroscopic medium, constituted by an ensemble of N diatomic molecules modeled as above, all subjected to the same electric field $\vec{E}(t)$, the charge displacement of every molecule will contribute to the total polarization of the medium, which can be calculated as the sum of all the single dipole moments:

$$P(\omega) = Nqx(\omega), \quad (1.10)$$

We can now define the linear electronic susceptibility as:

$$P(\omega) = \epsilon_0\chi^{(1)}(\omega)E(\omega), \quad (1.11)$$

Comparing the eq.(1.10) with eq.(1.11), and plugging in eq.(1.9), we find the expression of the linear susceptibility $\chi^{(1)}(\omega)$:

$$\chi^{(1)}(\omega) = \frac{-\frac{Nq^2}{(2\epsilon_0\mu\Omega_R)}}{(\omega - \Omega_R) + i\gamma}, \quad (1.12)$$

Expression (1.12) describes the vibrational contribution from the molecule to the susceptibility of the medium. The real part is related to the medium dispersion and it has an antisymmetric shape with respect to the resonance frequency, while the imaginary part is related to the medium absorption and is characterized by a Lorentzian shape, centered in Ω_R . The width of the Lorentzian peak of $\Im\{\chi^{(1)}\}$ is directly proportional to the damping constant γ . The real and imaginary parts are schematically depicted in Fig.1.4.

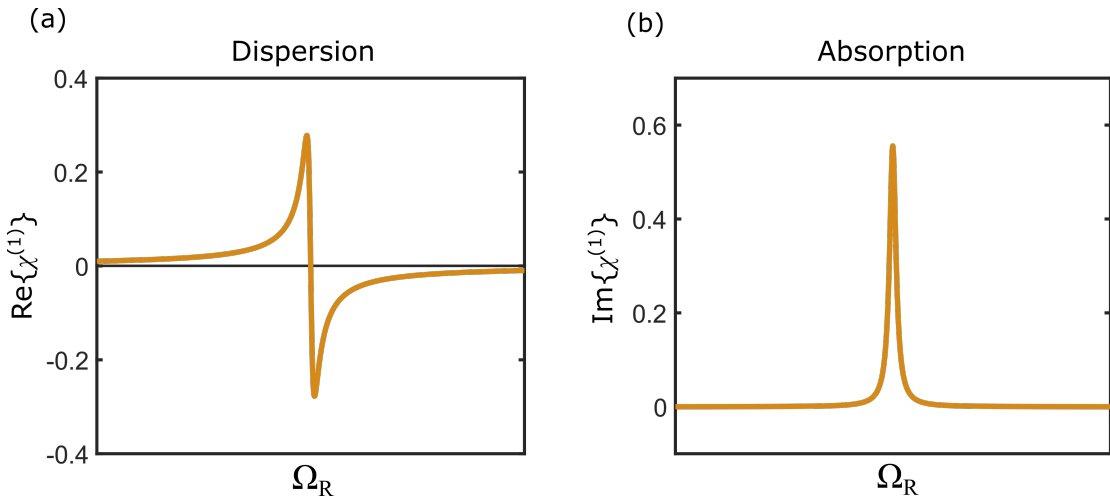


Figure 1.4: Graph of the real and imaginary parts of the linear susceptibility.

For diluted media, the refractive index is related to $\Re\{\chi^{(1)}\}$ as:

$$n(\omega) = n_0 - \frac{\Re\{\chi^{(1)}\}}{2n_0}, \quad (1.13)$$

in which n_0 is the mean refractive index of the medium. Moreover, the absorption coefficient $\alpha(\omega)$, can be calculated from $\Im\{\chi^{(1)}\}$ as:

$$\alpha(\omega) = \frac{2\pi}{\lambda_0 n_0} \Im\{\chi^{(1)}\}, \quad (1.14)$$

where $\alpha(\omega)$ is expressed in cm^{-1} and can be found in the Lambert-Beer law, describing the reduction of light intensity in a medium due to absorption of light, as:

$$I(L) = I_0 \exp(-\alpha L), \quad (1.15)$$

It is possible to exploit this feature of media in order to measure the resonance frequencies of the vibrational modes, performing spectroscopy of the analyzed medium. This technique is called IR absorption spectroscopy and allows one to identify and quantify absorption bands corresponding to different molecular species in a sample. However, IR spectroscopy suffers from low penetration depth and low spatial resolution since it requires the use of light with long wavelengths (in the MIR) to probe the vibrational modes.

1.3.3 Spontaneous Raman

To circumvent the IR absorption spectroscopy limitations mentioned in the previous section, SR can be used to reveal the vibrational modes of the samples providing higher penetration depth and spatial resolution, thanks to the use of visible or NIR quasi-monochromatic laser light. At thermodynamic equilibrium, the light-matter interaction is dominated by absorption (the light is retained by the molecules) and elastic scattering processes or Rayleigh scattering (the light deviates keeping the same frequency in a direction that is different from the incident one). Nevertheless, a smaller fraction of the incident light may be inelastically scattered, which means that it may be scattered at frequencies different from the incident one. This phenomenon is known as the "Raman effect".

In order to understand the Raman effect, let us consider again the diatomic molecule described in the previous section. Before we assumed that the molecule was polar, that is with an asymmetric charge distribution on the two atoms. In this part, we will drop this assumption. However, even though a molecule is not polar, it will have a polarizability α that depends on the intramolecular distance x . Let us assume the molecule is vibrating at the resonance frequency Ω_R . The fluctuations of the interatomic distance with respect to the equilibrium position can be described as: $x(t) = x_f \cos(\Omega_R t)$, where x_f is the amplitude fluctuation. Assuming the displacement amplitude is small, we can perform a Taylor expansion of the polarizability with respect to the equilibrium position:

$$\alpha(t) = \alpha_0 + \left(\frac{\partial \alpha}{\partial x} \right)_0 x(t), \quad (1.16)$$

The dipole moment induced by an electric field oscillating at ω_p , $E(t) = E_0 \cos(\omega_p t)$, can be calculated as:

$$\vec{p} = \epsilon_0 \alpha(t) \vec{E}(t), \quad (1.17)$$

Let us now plug the expression of the polarizability eq.(1.16) in eq.(1.17):

$$p = \epsilon_0 \left[\alpha_0 + \left(\frac{\partial \alpha}{\partial x} \right)_0 x_f \cos(\Omega_R t) \right] E_0 \cos(\omega_p t), \quad (1.18)$$

Using the Werner formula, the eq.(1.18) reads:

$$p = \epsilon_0 \alpha_0 E_0 \cos(\omega_p t) + \frac{\epsilon_0 \left(\frac{\partial \alpha}{\partial x} \right)_0 E_0 x_f}{2} \cos[(\omega_p - \Omega_R)t] + \frac{\epsilon_0 \left(\frac{\partial \alpha}{\partial x} \right)_0 E_0 x_f}{2} \cos[(\omega_p + \Omega_R)t], \quad (1.19)$$

The first term, oscillating at the same frequency as the incoming field corresponds to the Rayleigh scattering. In this case, the photons are simply scattered by the molecule without any exchange of energy. The second term is oscillating at angular frequency $\omega_S = \omega_p - \Omega_R$ and describes a red-shifted scattering known as Raman Stokes scattering. In this case, the molecule absorbs part of the energy of the light and is promoted from a ground state to a vibrationally excited state. Consequently, the outgoing photons present a lower energy with respect to the incoming ones. The third term represents the Raman anti-Stokes scattering and oscillates at $\omega_{AS} = \omega_p + \Omega_R$. In this case, the molecule goes from the excited state to the ground one, releasing energy. The outgoing photons have higher energy with respect to the incoming ones, therefore they are blue-shifted in frequency. The different types of scattering are schematically depicted in Fig. 1.5 making use of Jablonsky diagrams.

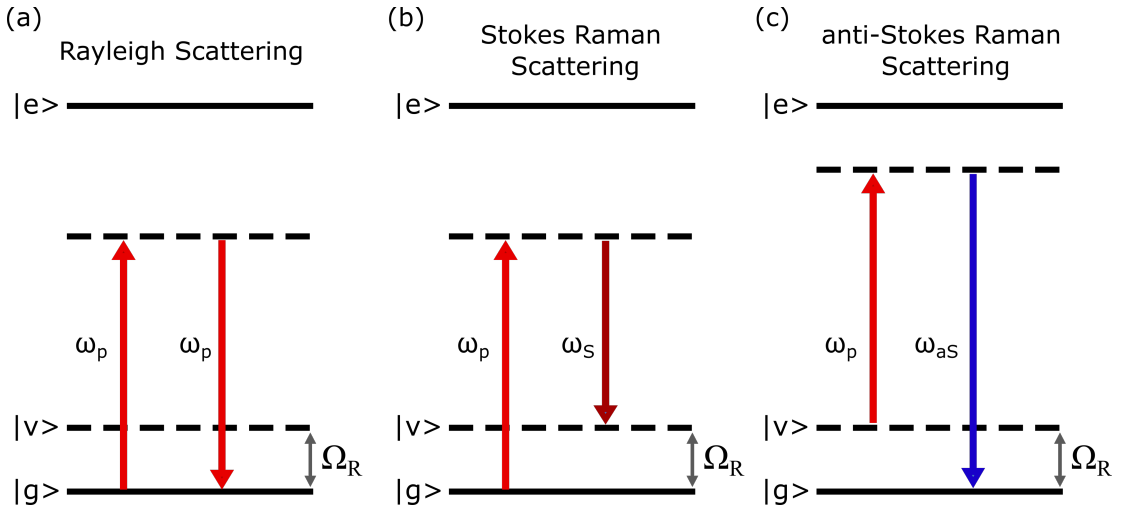


Figure 1.5: Jablonsky diagrams of (a) Rayleigh scattering, (b) Stokes Raman scattering, (c) anti-Stokes Raman scattering. The solid lines represent the fundamental or ground state $|g\rangle$, the vibrational state $|v\rangle$, and the excited state $|e\rangle$, while the dashed line is a virtual state. $|g\rangle$ and $|v\rangle$ are separated by the resonance frequency Ω_R .

However, the majority of SR spectroscopy experimental setups detect the Raman Stokes component. The main reason is why at thermal equilibrium, atomic level populations are described by the Boltzmann distribution (1.20), which gives the probability

that a system will be in the i -th state depending on the energy of the level ϵ_i and on the temperature:

$$p_i \propto e^{-\epsilon_i/kT}, \quad (1.20)$$

Therefore, the population of the excited level is lower than the one at the ground state, and they become equal at infinite temperatures. Thus, since to observe anti-Stokes scattering we need the molecule to be in the excited state, we expect a lower signal with respect to the Stokes scattering, unless the temperature is really high. From eq. (1.19), it is evident that a vibrational mode is Raman active if it satisfies the following selection rule: $(\frac{\partial\alpha}{\partial x})_0 \neq 0$. Similarly to IR absorption spectroscopy, Raman spectroscopy enables the identification of the vibrational levels of a substance by measuring the spectral distance of the Raman peaks with respect to the Rayleigh scattering peak (see Fig. 1.6).

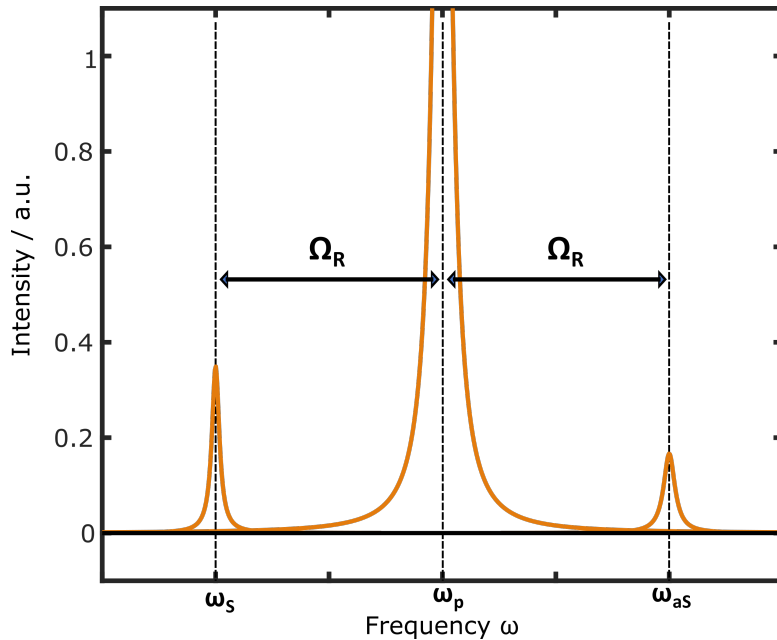


Figure 1.6: Scattered light from a molecule with a single vibrational mode at frequency Ω_R .

If a molecule presents inversion symmetry, its modes can be either Raman active and not IR active or vice-versa. In particular, symmetric modes with respect to the inversion symmetry are only Raman active, while anti-symmetric ones are only IR active. Despite SR provides several advantages with respect to MIR absorption spectroscopy, the cross-section of Raman scattering is rather poor: the order of magnitude is around 10^{-30} cm^2 (while the cross-section of single photon absorption fluorescence can reach 10^{-16} cm^2). It implies that it takes from 100 ms to 1 s for collecting a vibrational spectrum from biological samples with a sufficiently good signal-to-noise ratio, preventing the possibility of fast imaging.

1.3.4 Coherent Raman Scattering

CRS provides higher imaging speed than SR thanks to the nonlinear nature of the processes involved during the interaction of the electric fields and the sample. In this

section, we will describe the physics behind CRS processes and then we will focus on CARS and SRS processes.

Let us consider an incoming electric field, constituted by two waves, denominated pump and Stokes, respectively with frequency ω_P and ω_S :

$$E(z, t) = A_P e^{i(\omega_P t - k_P z)} + A_S e^{i(\omega_S t - k_S z)} + c.c., \quad (1.21)$$

The interference between the two fields generates a beating with frequency $\Omega = \omega_P - \omega_S$. If the beating frequency Ω matches the frequency of a vibrational mode, $\Omega_R = \Omega$, then the normal mode enters in resonance with the wave beating.

Let us consider again the diatomic molecule modeled as a harmonic oscillator, described by the eq.(1.4). Let us find the expression of the force $\vec{F}(t)$ evaluating the derivative of the energy W necessary to create a dipolar moment $\vec{p}(t) = \epsilon_0 \alpha(t) \vec{E}(t)$. The energy of a dipole in an electric field is:

$$W = \frac{1}{2} \langle \vec{p}(z, t) \cdot \vec{E}(t) \rangle = \frac{1}{2} \epsilon_0 \alpha(t) \langle E^2(z, t) \rangle, \quad (1.22)$$

using the expression (1.21) in the term $\langle E^2(z, t) \rangle$:

$$\langle E^2(z, t) \rangle = A_P A_S^* e^{i(\Omega t - Kz)} + c.c., \quad (1.23)$$

The brackets $\langle \dots \rangle$ represent the time average over one optical period.

We can now insert eq.(1.23) in eq.(1.22) and perform the derivative with respect to the intermolecular distance obtaining:

$$F(t) = \frac{dW}{dx} = \epsilon_0 \left(\frac{\partial \alpha}{\partial x} \right)_0 [A_P A_S^* e^{i(\Omega t - Kz)} + c.c.], \quad (1.24)$$

Eq. (1.24) is the expression of the driving force due to the presence of the two electric fields, namely pump and Stokes, that can be now plugged in eq.(1.4). Looking for a solution in the form:

$$x(z, t) = x(\Omega) e^{i(\Omega t - Kz)} + c.c., \quad (1.25)$$

we find that near the resonance, the molecular vibration amplitude is:

$$x(\Omega) = \frac{- \left(\frac{\epsilon_0}{2\mu\Omega_R} \right) \left(\frac{\partial \alpha}{\partial x} \right)_0 A_P A_S^*}{(\Omega - \Omega_R) + i\gamma}, \quad (1.26)$$

Therefore, if the beating frequency Ω gets close to the resonance frequency Ω_R , the vibration amplitude of the molecule $x(\Omega)$ becomes larger and induces a nonlinear polarization.

The induced nonlinear polarization can be calculated by summing up the induced dipole moments of the medium:

$$P(z, t) = N p(z, t) = N \epsilon_0 \left[\alpha_0 + \left(\frac{\partial \alpha}{\partial x} \right)_0 x(z, t) \right] E(z, t), \quad (1.27)$$

We can now distinguish two terms from eq. (1.27):

Chapter 1. Coherent raman scattering microscopy

1. the linear polarization $P^{(L)}$, directly proportional to the electric field and oscillating at the same frequency: $P^{(L)} = N\epsilon_0\alpha_0 E(z, t)$

2. The non-linear polarization $P^{(NL)}$:

$$P^{(NL)} = N\epsilon_0 \left(\frac{\partial \alpha}{\partial x} \right)_0 [x(\Omega)e^{i(\Omega t - Kz)} + c.c.] [A_P e^{i(\omega_P t - k_P z)} + A_S e^{i(\omega_S t - k_S z)} + c.c.], \quad (1.28)$$

From eq. (1.28), we find four terms radiating at different frequencies:

1. A term oscillating at frequency $\omega_{AS} = 2\omega_P - \omega_S$:

$$P(\omega_{AS}) = N\epsilon_0 \left(\frac{\partial \alpha}{\partial x} \right)_0 x(\Omega) A_P e^{-i(2k_P - k_S)z}, \quad (1.29)$$

2. A term oscillating at frequency $\omega_{CS} = 2\omega_S - \omega_P$:

$$P(\omega_{CS}) = N\epsilon_0 \left(\frac{\partial \alpha}{\partial x} \right)_0 x^*(\Omega) A_S e^{-i(2k_S - k_P)z}, \quad (1.30)$$

3. A term oscillating at frequency ω_P :

$$P(\omega_P) = N\epsilon_0 \left(\frac{\partial \alpha}{\partial x} \right)_0 x(\Omega) A_S e^{-ik_P z}, \quad (1.31)$$

4. A term oscillating at frequency ω_S :

$$P(\omega_S) = N\epsilon_0 \left(\frac{\partial \alpha}{\partial x} \right)_0 x^*(\Omega) A_P e^{-ik_S z}, \quad (1.32)$$

These terms oscillating at different frequencies act as the sources of different non-linear processes (Fig. 1.7). $P(\omega_{AS})$ gives rise to the Coherent anti-Stokes Raman scattering (CARS), $P(\omega_{CS})$ to the Coherent Stokes Raman scattering (CSRS), while $P(\omega_P)$ and $P(\omega_S)$ are the sources of Stimulated Raman scattering. CSRS is not considered when dealing with CRS techniques since ω_{CS} is in the IR where most of the detectors are noisy and with lower quantum efficiency.

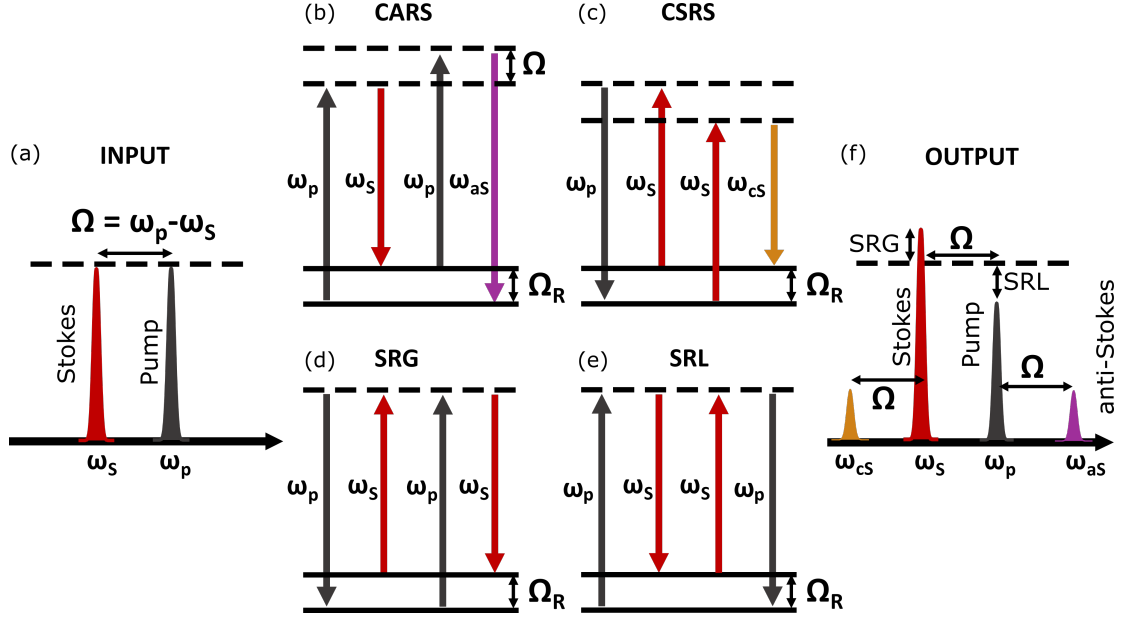


Figure 1.7: (a) Input Stokes and pump pulses in CRS processes. Jablonsky diagrams of (b) Coherent anti-Stokes Raman scattering (CARS), (c) Coherent Stokes Raman scattering (CSRS), (d) Stimulated Raman Gain (SRG), (e) Stimulated Raman Loss (SRL), (f) Output fields and generated signals (not in scale).

These expressions of the polarization suggest that CRS processes arise from the third-order nonlinear optical interaction since the interaction among three electric fields is required to give rise to the nonlinear signal. Therefore, CRS processes are four-wave mixing phenomena mediated by the third-order nonlinear susceptibility of the medium $\chi^{(3)}$.

1.3.5 Third order non-linear processes

In order to describe third-order nonlinear optical phenomena, third-order polarization should be taken into account. It can be written as:

$$P_i^{(3)}(t) = \epsilon_o \int_{-\infty}^{+\infty} dt' \int_{-\infty}^{+\infty} dt'' \int_{-\infty}^{+\infty} dt''' \chi_{ijkl}^{(3)}(t', t'', t''') E_j(t-t') E_k(t-t'-t'') E_l(t-t'-t''-t''') \quad (1.33)$$

Applying some approximations, we can simplify eq. (1.33) as:

$$P^{(3)} = \epsilon_o \chi^{(3)} E^3(t), \quad (1.34)$$

Let us now introduce an incoming electric field defined as:

$$E(t) = A_1 \cos(\omega_1 t + \phi_1) + A_2 \cos(\omega_2 t + \phi_2) + A_3 \cos(\omega_3 t + \phi_3), \quad (1.35)$$

The third order non-linear polarization could be calculated substituting (1.35) in (1.34), finding:

$$P^{(3)} = \epsilon_o \chi^{(3)} [A_1 \cos(\omega_1 t + \phi_1) + A_2 \cos(\omega_2 t + \phi_2) + A_3 \cos(\omega_3 t + \phi_3)]^3, \quad (1.36)$$

Performing the calculations, we find 22 different terms oscillating at different frequencies. These polarization terms act as new sources giving rise to radiation at the same frequency. The 22 terms can be classified in the following way:

- 3 terms at the original frequencies ω_1 , ω_2 and ω_3 , which give rise to the Optical Kerr effect,
- 3 terms at the third harmonics $3\omega_1$, $3\omega_2$ and $3\omega_3$, which is called Third Harmonic Generation (THG),
- 6 terms at $2\omega_i + \omega_j$, with $i \neq j$,
- 6 terms at $2\omega_i - \omega_j$, with $i \neq j$,
- 1 term at $\omega_1 + \omega_2 + \omega_3$,
- 3 terms at $\omega_i + \omega_j - \omega_k$, with $i \neq j \neq k$,

Therefore, a wave at a different frequency is obtained as an output. The whole process could be seen as an interaction among four waves (Fig. 1.8). For this reason, third-order phenomena are also called Four Wave Mixing (FWM) processes [40].

1.3.6 Propagation equation in Four-Wave Mixing processes

Starting from Maxwell equations and considering the propagation in nonlinear optical media, it is possible to derive, under the slowly varying envelope approximation and the plane wave approximation, the envelope propagation equation for short laser pulses in nonlinear media that, if we neglect the dispersions, reads:

$$\frac{\partial A}{\partial z} + \frac{1}{v_g(\omega_0)} \frac{\partial A}{\partial t} = -\frac{i\mu_0\omega_0 c}{2n(\omega_0)} e^{-i\Delta k z} B \quad (1.37)$$

where A e B are the envelopes of the electric field and of the nonlinear polarization ($E(z, t) = \Re\{A(z, t)e^{i(\omega_0 t - k_0 z)}\}$ and $P^{(NL)}(z, t) = \Re\{B(z, t)e^{i(\omega_0 t - k_p z)}\}$), v_g is the group velocity and Δk is the wavevector mismatch. We would like to use this equation for the FWM phenomena.

Let us define the incoming electric field in the exponential form:

$$E(t, z) = \frac{1}{2} \{ A_1(t, z)e^{i(\omega_1 t - k_1 z)} + A_2(t, z)e^{i(\omega_2 t - k_2 z)} + A_3(t, z)e^{i(\omega_3 t - k_3 z)} + A_4(t, z)e^{i(\omega_4 t - k_4 z)} + c.c. \} \quad (1.38)$$

where the expression *c.c.* stands for complex conjugate.



Figure 1.8: Conceptual scheme of the interaction between light and matter considering third order nonlinear optical processes in the FWM frame.

Let us now assume $\omega_1 + \omega_3 = \omega_2 + \omega_4$, and let us focus on the terms oscillating at the same frequencies as the incoming waves. Substituting (1.38) in (1.37) we find, after some calculations, that the third order polarization term oscillating at frequency ω_1 , namely $P_{\omega_1}^{(3)}$ reads:

$$P_{\omega_1}^{(3)}(t, z) = \frac{\epsilon_0 \chi^{(3)}}{4} 3A_2(t, z)A_4(t, z)A_3^*(t, z)e^{i[(\omega_2 - \omega_3 + \omega_4)t - (k_2 + k_4 - k_3)z]} + c.c., \quad (1.39)$$

The same reasoning could be applied to all the other terms oscillating at the original frequencies, obtaining:

$$\begin{cases} P_{\omega_1}^{(3)}(t, z) = \frac{3\epsilon_0 \chi^{(3)}}{4} A_2(t, z)A_4(t, z)A_3^*(t, z)e^{i[\omega_1 t - (k_2 + k_4 - k_3)z]} + c.c. \\ P_{\omega_2}^{(3)}(t, z) = \frac{3\epsilon_0 \chi^{(3)}}{4} A_1(t, z)A_3(t, z)A_4^*(t, z)e^{i[\omega_2 t - (k_1 + k_3 - k_4)z]} + c.c. \\ P_{\omega_3}^{(3)}(t, z) = \frac{3\epsilon_0 \chi^{(3)}}{4} A_2(t, z)A_4(t, z)A_1^*(t, z)e^{i[\omega_3 t - (k_2 + k_4 - k_1)z]} + c.c. \\ P_{\omega_4}^{(3)}(t, z) = \frac{3\epsilon_0 \chi^{(3)}}{4} A_1(t, z)A_3(t, z)A_2^*(t, z)e^{i[\omega_4 t - (k_1 + k_3 - k_2)z]} + c.c. \end{cases} \quad (1.40)$$

From (1.39), we found that the envelope of $P_{\omega_1}^{(3)}$ can be written as:

$$B(t, z) = \frac{3\epsilon_0 \chi^{(3)}}{4} A_2(t, z)A_4(t, z)A_3^*(t, z), \quad (1.41)$$

We can now plug (1.41) in (1.37) and develop the calculation for the wave at frequency ω_1 . Therefore, the propagation equation becomes:

$$\frac{\partial A_1}{\partial z} + \frac{1}{v_g(\omega_1)} \frac{\partial A_1}{\partial t} = -\frac{i\mu_0 \omega_1 c}{2n(\omega_1)} \frac{3\epsilon_0 \chi^{(3)}}{4} A_2 A_4 A_3^* e^{-i(k_2 + k_4 - k_3 - k_1)z}, \quad (1.42)$$

Let us define $k_p \equiv k_2 + k_4 - k_3$, and $\Delta k = k_1 - k_p$. We can proceed rewriting (1.42) as:

$$\frac{\partial A_1}{\partial z} + \frac{1}{v_g(\omega_1)} \frac{\partial A_1}{\partial t} = -\frac{i3\omega_1 \chi^{(3)}}{8cn(\omega_1)} A_2 A_4 A_3^* e^{i\Delta k z}, \quad (1.43)$$

where we exploited the relation $\epsilon_0 \mu_0 = \frac{1}{c^2}$. Plugging the envelope of the polarization written in (1.40) and proceeding with analogous calculation we find:

$$\begin{cases} \frac{\partial A_1}{\partial z} + \frac{1}{v_g(\omega_1)} \frac{\partial A_1}{\partial t} = -if_1 A_2 A_4 A_3^* e^{i\Delta k z} \\ \frac{\partial A_2}{\partial z} + \frac{1}{v_g(\omega_2)} \frac{\partial A_2}{\partial t} = -if_2 A_1 A_3 A_4^* e^{-i\Delta k z} \\ \frac{\partial A_3}{\partial z} + \frac{1}{v_g(\omega_3)} \frac{\partial A_3}{\partial t} = -if_3 A_2 A_4 A_1^* e^{i\Delta k z} \\ \frac{\partial A_4}{\partial z} + \frac{1}{v_g(\omega_4)} \frac{\partial A_4}{\partial t} = -if_4 A_1 A_3 A_2^* e^{-i\Delta k z}, \end{cases} \quad (1.44)$$

where we made use of f_i , defined as $f_i \equiv \frac{3\omega_i \chi^{(3)}}{8cn(\omega_i)}$. It is possible to observe that the set of equations (1.44) represents the propagation equation for four-wave mixing phenomena (neglecting dispersion for simplicity), which are characterized by the direct dependence on the term $\chi^{(3)}$, which will be analyzed in details in the following.

1.4 The CARS process

Coherent Anti-Stokes Raman scattering (CARS) can be generated by exploiting two pulses centered at different frequencies, namely the pump pulse at frequency ω_P and the Stokes pulse at frequency ω_S . When the frequency mismatch $\Omega = \omega_P - \omega_S$ matches a resonance frequency Ω_R of the scrutinized sample, all the molecules in the focal spot are resonantly excited. The vibrational mode is read by means of the interaction with a third beam, called probe beam at frequency ω_{pr} . In this configuration, the CARS signal will be emitted at the anti-Stokes frequency $\omega_{aS} = \omega_P - \omega_S + \omega_{pr}$. Typically, one chooses to work with $\omega_{pr} = \omega_P$, thus working in the degenerate CARS configuration, where $\omega_{aS} = 2\omega_P - \omega_S$.

To derive the expression of the intensity of the CARS signal, we will start from the expression of the envelope of the third-order nonlinear polarization oscillating at frequency ω_{AS} . Being a four-wave mixing process, we can write it referring to the eq. (1.41) and taking also into account the tensorial nature of the third-order susceptibility:

$$P_i^{(3)}(\vec{r}, \omega_{aS}) = \frac{3\epsilon_0}{4} \sum_{j,k,l} \chi_{ijkl}^{(3)} E_{P_j}(\vec{r}) E_{P_k}(\vec{r}) E_{S_l}^*(\vec{r}) \quad (1.45)$$

in which $i, j, k, l = \{x, y, z\}$. Since the Raman scattered light can be depolarized with respect to the incident one, we can define the Raman depolarization ratio ρ_R as:

$$\rho_R = \frac{I_R(\perp)}{I_R(\parallel)}, \quad (1.46)$$

where $I_R(\parallel)$ is the Raman intensity polarized as the pump, while $I_R(\perp)$ is perpendicular to it. The Raman depolarization ratio is a number between 0 and $\frac{3}{4}$, depending on the vibrational mode stimulated. Considering isotropic media where one-photon transitions at ω_P or ω_S are not occurring, it can be proved [39] that $\vec{P}^{(3)}(\vec{r})$ can be expressed in terms of the tensor element $\chi_{xxyy}^{(3)}$ and the Raman depolarization ratio as:

$$\vec{P}^{(3)}(\vec{r}, \rho_R; \omega_{aS}) = \frac{3\epsilon_0}{2} \chi_{xxyy}^{(3)} \left\{ \left[\vec{E}_P(\vec{r}) \cdot \vec{E}_S^*(\vec{r}) \right] \vec{E}_P(\vec{r}) + \frac{\rho_R}{1 - \rho_R} \left[E_{P_x}^2(\vec{r}) + E_{P_y}^2(\vec{r}) + E_{P_z}^2(\vec{r}) \right] \vec{E}_S^*(\vec{r}) \right\}, \quad (1.47)$$

Several considerations could be pointed out:

- if the pump and Stokes beams are linearly polarized in the same direction, the nonlinear polarization is collinear with them;
- on the other hand, if the pump and Stokes fields are linearly polarized in mutually perpendicular directions (thus, $\vec{E}_P(\vec{r}) \cdot \vec{E}_S^*(\vec{r}) = 0$), the induced polarization is aligned with the Stokes beam and the totally polarized Raman bands, characterized by $\rho_R = 0$, can not be stimulated,
- If $\rho_R = 0$, the polarization is collinear with the pump field, and maximized for $\vec{E}_P(\vec{r}) \parallel \vec{E}_S^*(\vec{r})$,

- The bigger ρ_R , the bigger the second term of eq. (1.47), resulting in a larger contribution of the anti-Stokes field along the Stokes direction.

For simplicity, in the following, we will assume that $\rho_R = 0$ and that the pump and Stokes fields are linearly polarized in the same direction. Under these assumptions and under the following conditions:

$$\omega_1 = \omega_3 = \omega_P, \quad \omega_2 = \omega_S, \quad \omega_4 = 2\omega_P - \omega_S = \omega_{aS}, \quad (1.48)$$

the induced non-linear polarization giving rise to the CARS signal reads as the expression (1.40), that is:

$$P_{\omega_{aS}}^{(3)} = \frac{3\epsilon_0\chi^{(3)}(\omega_{aS})}{4} A_P^2 A_S^* e^{i[\omega_{aS}t - (2k_P - k_S)z]} + c.c., \quad (1.49)$$

where we discarded the vectorial nature since we will consider collinear geometry in the following. We can now substitute the expression of the polarization of eq. (1.49) in the propagation equation (1.37) and move to the local time frame finding the following propagation equation:

$$\frac{dA_{aS}}{dz} = -\frac{3i\omega_{aS}}{8cn(\omega_{aS})} \chi^{(3)}(\omega_{aS}) A_P^2 A_S^* e^{-i\Delta kz}, \quad (1.50)$$

where $\Delta k = 2k_P - k_S - k_{aS}$. Let us now evaluate the CARS signal amplitude, after propagating over a distance L in a medium, integrating (1.78):

$$A_{aS}(L) = \int_0^L \frac{dA_{aS}}{dz} dz = -\frac{3i\omega_{aS}}{8cn(\omega_{aS})} \chi^{(3)}(\omega_{aS}) A_P^2 A_S^* L \operatorname{sinc}\left(\frac{\Delta k L}{2}\right) e^{i\frac{\Delta k L}{2}}, \quad (1.51)$$

where the function $\operatorname{sinc}(x) = \sin(x)/x$. From eq. (1.51), we can derive the expression of the intensity of the CARS signal, I_{aS} , knowing that $I \propto |A|^2$:

$$I_{aS}(L) \propto |\chi^{(3)}(\omega_{aS})|^2 L^2 \operatorname{sinc}^2\left(\frac{\Delta k L}{2}\right) I_P^2 I_S, \quad (1.52)$$

Eq. (1.52) represents the expression of the CARS signal coming out of a medium with length L . From this expression, we can point out that:

1. The signal scales quadratically on the pump intensity and linearly on the Stokes one. Therefore, increasing the pump intensity is more beneficial to enhance the signal.
2. The signal scales quadratically on the width of the medium L . Thus, it is hard to extract signals from thin samples.
3. In order to get a high intensity, the phase matching condition $\Delta k L \simeq 0$ should be fulfilled. This condition can be satisfied either for $\Delta k \simeq 0$ or for $L \simeq 0$. The former expression means that:

$$\Delta k = 2k_P - k_S - k_{aS} \simeq 0, \quad (1.53)$$

where the wave vectors can be written as:

$$k_P = \frac{n_P \omega_P}{c}, \quad k_S = \frac{n_S \omega_S}{c}, \quad k_{aS} = \frac{n_{aS} \omega_{aS}}{c}, \quad (1.54)$$

and $n_i = n(\omega_i)$. Due to the material dispersion, $n_P \neq n_S \neq n_{aS}$, that implies that the phase matching condition is not satisfied. However, under tight-focusing conditions, which are valid in microscopy where high numerical aperture objectives are used, Δk is approximately equal to zero. The second case in which the phase matching condition can be fulfilled is for small and thin scatterers, in which $L < \lambda_p$. This is particularly exploited in epi-detection CARS where the anti-Stokes component is collected in reflection and for which $\Delta k = 2k_p - k_S + k_{aS} = 2k_{aS} \neq 0$ so that only small scatterers can contribute to the signal generation. When phase matching condition is satisfied, since $\lim_{x \rightarrow 0} \text{sinc}(x) = 1$, we can simplify the expression of CARS intensity as:

$$I_{aS}(L) \propto |\chi^{(3)}|^2 L^2 I_p^2 I_S. \quad (1.55)$$

4. The CARS intensity also depends on $|\chi^{(3)}|^2$. We will see in the following section that $\chi^{(3)}$ is related to the concentration of scatterers. It implies that if the concentration is close to zero, dilute samples are hardly detected due to the square dependence on it. Other important considerations may be done starting from this dependence, as it will be extensively discussed in the following section.

1.4.1 Resonant and non-resonant contribution to CARS

In the previous section, the CARS process has been described analyzing the four-wave mixing propagation equation generating a signal oscillating at ω_{aS} . When dealing with the detection of the anti-Stokes component, one realizes that it is always present, even at frequency differences that are out of any vibrational resonance of the investigated specimen. To understand this phenomenon, we can consider the generation of the anti-Stokes component through the Jablonsky diagrams reported in Fig.1.9.

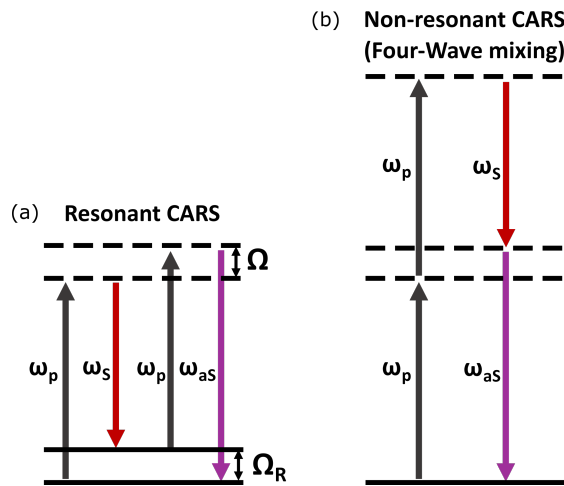


Figure 1.9: Jablonsky diagrams of (a) Resonant Coherent anti-Stokes Raman scattering (Resonant CARS), (b) Non-resonant Coherent anti-Stokes Raman scattering (Non-resonant CARS).

As we can see, starting from a pump beam and a Stokes beam, two different processes give rise to a signal at frequency $\omega_{aS} = 2\omega_p - \omega_S$. In the first case, a molecule is excited to a virtual level by the pump electric field. Then, stimulated by the Stokes field, it relaxes to a vibrational level. Subsequently, it is again excited by the pump

field, reaching a new virtual state. Eventually, it relaxes to the ground state emitting an electromagnetic wave at frequency ω_{aS} . This contribution is called Resonant CARS, and it carries information about the energy of the vibrational state, which can be calculated as $E_{|v\rangle} = \hbar\Omega_R = \hbar\omega_{AS} - \hbar\omega_P$. In the second case, after the molecule is excited by the pump field, reaching an intermediate virtual state, it interacts with the pump field again, reaching a new virtual state. Then, stimulated by the Stokes field, it relaxes to the ground state emitting two fields, namely the Stokes and the anti-Stokes component. This anti-Stokes component is called Non-Resonant CARS, since it is not related to any vibrational mode of the sample, indeed, it originates from the instantaneous electronic response of the medium.

Both contributions appear in the expression of the third-order susceptibility, which can be written as:

$$\chi_{VIB}^{(3)} = \chi_R^{(3)} + \chi_{NR}^{(3)}, \quad (1.56)$$

The resonant part $\chi_R^{(3)}$ is characterized by a real and an imaginary part and is related to the vibrational modes. While, far from electronic resonances, the non-resonant susceptibility $\chi_{NR}^{(3)}$ is real and constant.

We can derive the expression of the resonant term by comparing the eq. (1.29) of the polarization with the eq. (1.49) that reads:

$$\chi_R^{(3)} = \frac{4}{3A_P A_S^*} N \left(\frac{\partial \alpha}{\partial x} \right)_0 x(\Omega) \quad (1.57)$$

We can plug in (1.57) the expression of $x(\Omega)$ found in (1.26) obtaining:

$$\chi_R^{(3)} = \frac{a_{VIB}}{(\Omega - \Omega_R) + i\gamma}, \quad (1.58)$$

with $a_{VIB} = -\frac{2N\epsilon_0}{3\mu\Omega_R} \left(\frac{\partial \alpha}{\partial x} \right)_0^2$ a negative number which represents the oscillator strength of the molecular vibration. So far, we assumed only one vibrational mode, however, expression (1.58) can be easily generalized to a vibrational spectrum with M different modes writing the third-order susceptibility as:

$$\chi_{VIB}^{(3)} = \sum_{i=1}^M \frac{a_{VIB,i}}{(\Omega - \Omega_{R_i}) + i\gamma_i} + \chi_{NR}^{(3)} \quad (1.59)$$

where $\chi_R^{(3)} = \sum_{i=1}^M \frac{a_{VIB,i}}{(\Omega - \Omega_{R_i}) + i\gamma_i}$ represents the resonant part in (1.59). For simplicity, from now on we will consider just one vibrational mode.

Let us now consider the CARS signal intensity and its dependence on the square modulus of $\chi_{VIB}^{(3)}$:

$$I_{AS} \propto |\chi^{(3)}|^2 \propto \left| \chi_R^{(3)} + \chi_{NR}^{(3)} \right|^2 \quad (1.60a)$$

$$\propto \left| \chi_R^{(3)} \right|^2 + \left| \chi_{NR}^{(3)} \right|^2 + 2\text{Re}\{\chi_R^{(3)} \chi_{NR}^{(3)*}\} \quad (1.60b)$$

$$\propto \left| \chi_R^{(3)} \right|^2 + \left| \chi_{NR}^{(3)} \right|^2 + 2\chi_{NR}^{(3)} \text{Re}\{\chi_R^{(3)}\} \quad (1.60c)$$

where we considered that $\chi_{NR}^{(3)}$ is real. Analyzing eq. (1.60c), it is possible to observe that the CARS intensity is the sum of three different contributions:

1. A resonant contribution represented by the term $|\chi_R^{(3)}|^2$. This term carries vibrational information.
2. A non-resonant contribution represented by the term $|\chi_{NR}^{(3)}|^2$. This term is almost constant in the spectral domain if far from electronic resonances.
3. The last term, $2\chi_{NR}^{(3)}Re\{\chi_R^{(3)}\}$, is mixing the resonant and non-resonant parts giving rise to a heterodyne contribution.

Because of the interference term between the resonant and the non-resonant component, the CARS spectrum appears distorted with respect to the Spontaneous Raman spectrum. Indeed, the second and third terms of the equation give rise to the so-called non-resonant background (NRB). On the one hand, the NRB acts as a signal amplifier since the peaks sit on top of an almost flat signal (the second term); on the other hand, it distorts the typical Lorentzian peaks that assume a dispersive lineshape (due to $Re\{\chi_R^{(3)}\}$ in the third term), red-shifting the maximum of the peaks and making a minimum appear in the blue-shifted portion of the Raman peak. A representation of the different contributions to the CARS signal is reported in Fig. 1.10.

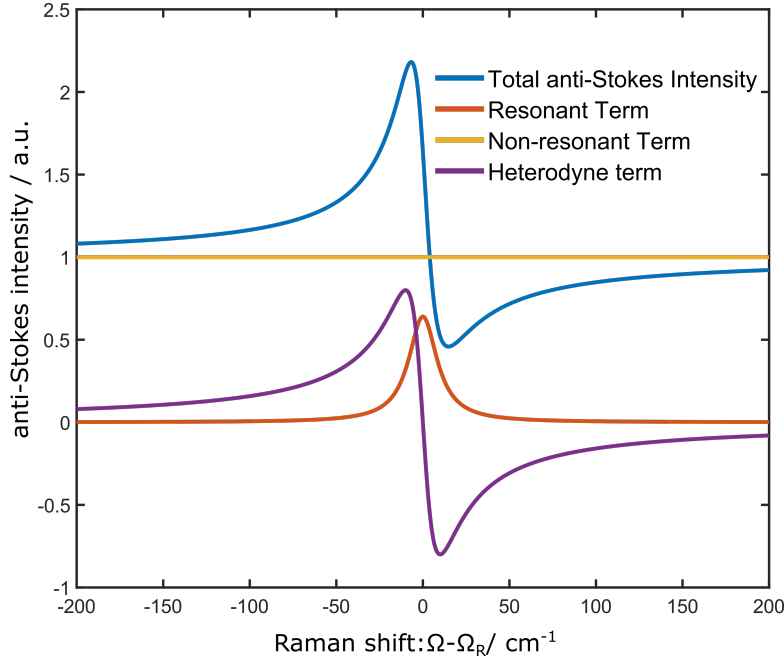


Figure 1.10: Anti-Stokes signal (blue line) in the spectral domain: the contributions from the resonant (orange line), non-resonant (yellow line), and heterodyne terms (purple line) are highlighted.

Decreasing the ratio between the resonant and the non-resonant part of the third-order susceptibility, the CARS signal is progressively more distorted but more amplified (Fig. 1.11).

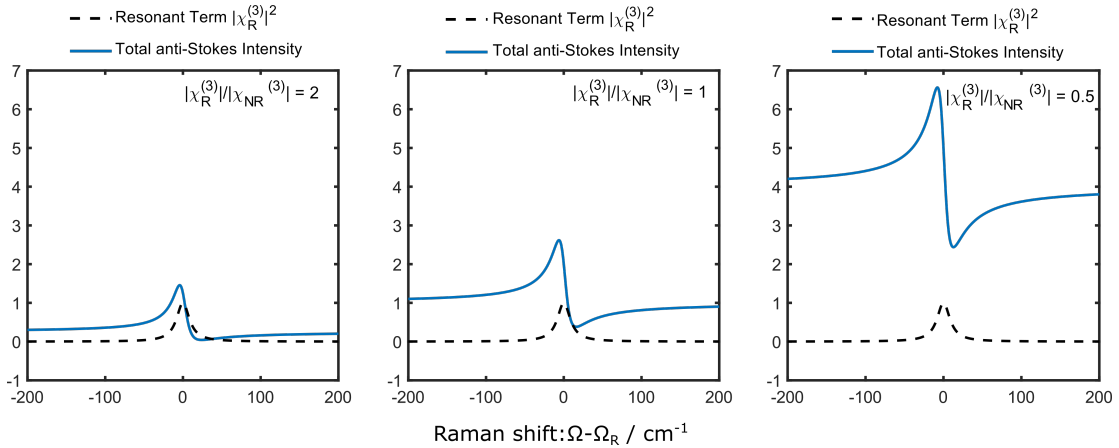


Figure 1.11: CARS signal varying the ratio between the resonant and the non-resonant contributions, respectively with (a) $\frac{|\chi_R^{(3)}|}{|\chi_{NR}^{(3)}|} = 2$, (b) $\frac{|\chi_R^{(3)}|}{|\chi_{NR}^{(3)}|} = 1$, (c) $\frac{|\chi_R^{(3)}|}{|\chi_{NR}^{(3)}|} = 0.5$.

The NRB signal shows some differences with respect to the resonant one.

1. At resonance, the NRB is dephased with respect to the resonant contribution.
2. The resonant contribution carries information on the population of a vibrational level, it will have a coherence time typically in the order of a few picoseconds. On the other hand, the NRB arises from instantaneous electronic response of the medium [41], in which only virtual levels are populated, therefore it exists only close to time zero, with the largest contribution lasting on the order of the excitation pulse duration.

Since only the resonant term carries information regarding the vibrational modes and therefore is the only meaningful part for spectroscopic applications, it is generally desired to remove the NRB from the CARS signal. Different approaches may be adopted to get rid of the NRB: one can either optically remove it via polarization CARS [42], time-resolved CARS [43, 44], and Fourier-transform CARS [32, 45] or remove it in post-processing using either numerical methods (Time-domain Kramers Kronig [46] and Maximum-Entropy-Method [47]) or deep learning based methods [48–50]. We will extensively discuss these methods in the following sections.

1.4.2 Broadband CARS

In the previous sections, we described the so-called single-frequency regime for CARS that enables the user to reach extremely high acquisition speeds, up to the video rate [27, 51]. However, the information content is strongly reduced with respect to SR, since narrowband pulses allow one to probe a single vibrational transition. Broadband CARS (BCARS) overcomes these hurdles by combining the high information content of SR spectroscopy with the high acquisition speed of CRS processes, as shown in Fig. 1.12.

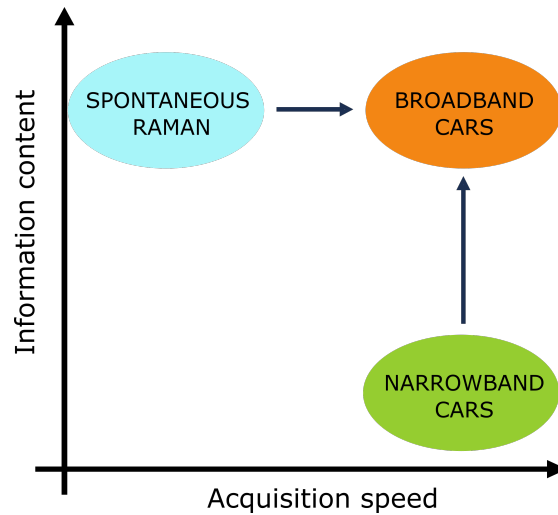


Figure 1.12: Comparison between SR and CARS techniques in terms of imaging speed and information content. Adapted from [24].

BCARS is more challenging than narrowband CARS microscopy since it requires more sophisticated technical implementations both for the handling and generation of the optical sources and for the detection of the signal. According to the way, the anti-Stokes spectrum is generated, we can distinguish two BCARS categories: hyperspectral CARS and multiplex CARS (see Fig. 1.13).

Hyperspectral CARS implementations employ two narrowband picosecond beams, the pump, and the Stokes, which are rapidly detuned to match the different Raman shifts in the sample. One usually tunes the Stokes beam to sequentially generate different anti-Stokes components. The spectrum is reconstructed by acquiring subsequent anti-Stokes signals. One method that allows us to rapidly tune the frequency shift between the pump and Stokes pulses has been pioneered by Hellerer and coworkers [52] and is known as the spectral focusing (SF) technique. The SF technique couples temporally chirped broadband femtosecond pump and Stokes pulses obtained by letting transform-limited pulses propagate into any dispersive medium so that the frequencies are distributed over time and the pulse length reaches a duration of several picoseconds. If the pump and Stokes pulses are both equally chirped, it turns out that their instantaneous frequency difference is constant, and can be varied by adjusting the delay between the two trains of pulses. In this way, a single mode at a time is probed despite using broadband pulses. The SF technique has been used for CARS microscopy and spectroscopy [52–57]. An important advancement to the technique has been introduced by Langbein et al. [58] who first realized spectral focusing using a single broadband sub-10-fs Ti:sapphire oscillator. This configuration was adopted then in many works [59–62].

On the other hand, multiplex CARS [63–75] combines a narrowband pump beam with a broadband Stokes beam generating a broadband anti-Stokes component, thus probing in parallel different Raman modes that may be acquired in the frequency domain using a spectrometer or in the time domain using a Fourier Transform approach.

Several implementations have been proposed for multiplex CARS. Some of them employ a single ultra-broadband laser providing both pump and Stokes frequencies [76, 77], while others combine narrowband pump pulses with broadband Stokes pulses

obtained by supercontinuum generation in a tapered fiber [78] or a photonic crystal fiber (PCF) [79–81]. Some methods are based on a time-domain Fourier transform approach [32,45,82–87] or use frequency combs [88–93], while others detect the CARS signal using a simple spectrometer.

We can summarize the state-of-the-art of BCARS applications by citing three main works. Hashimoto et al. [32] demonstrated broadband (spectral coverage: 200 – 1500 cm^{-1}) CARS spectroscopy at a record scan rate of 24,000 spectra/s using a time-domain Fourier-transform approach, while Camp et al. [94] reported ultra-broadband (spectral coverage: 500 – 3500 cm^{-1}) multiplex CARS microspectroscopy at 3.5-ms pixel exposure time when imaging biological tissues. More recently, Yoneyama et al. [67] proposed a multiplex CARS microscope (spectral coverage: 600 – 3600 cm^{-1}) with exposure time down to 0.8 ms, using a high-peak-power supercontinuum generated in a PCF pumped by a Q-switched microchip Nd: YVO4 laser oscillator generating sub-100-ps laser pulses at a 0.82-MHz repetition rate.

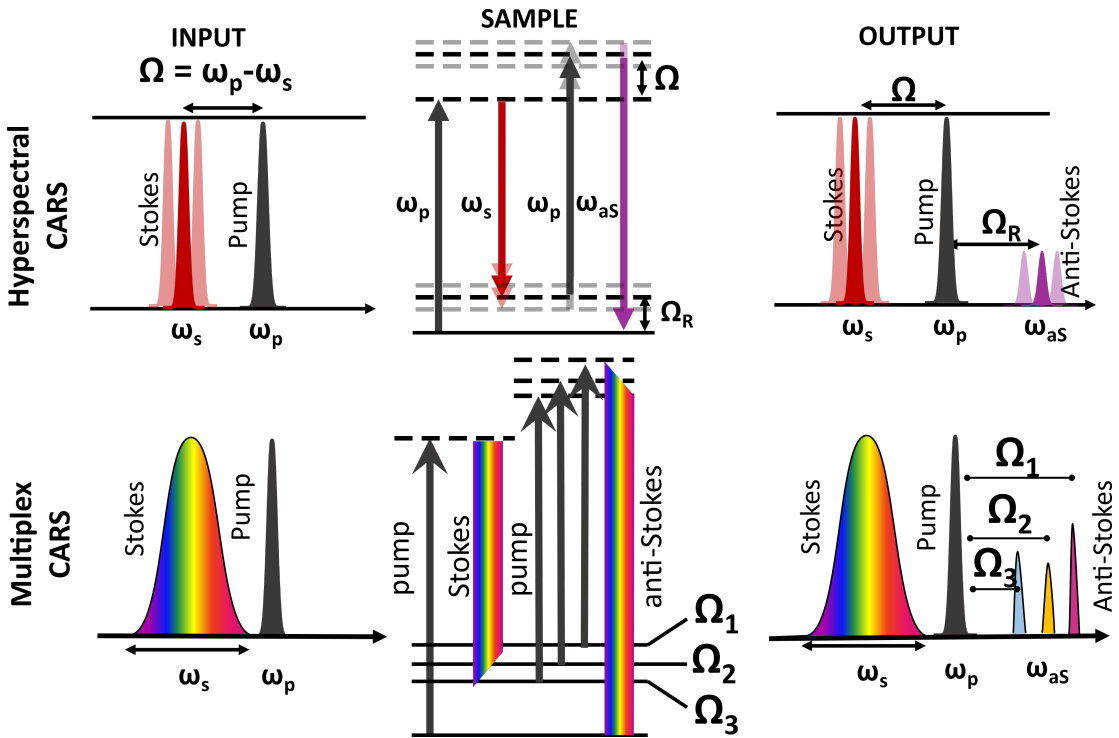


Figure 1.13: *Jablonski diagrams of the two categories of BCARS: hyperspectral CARS and Multiplex CARS.*

One of the main advantages of using BCARS rather than its narrowband counterpart is the role played by the NRB. As anticipated in the sections above, the NRB distorts and shifts the vibrational line shapes, limiting the sensitivity of the CARS apparatus. However, it can also act as a phase-coherent local oscillator, allowing heterodyne amplification of the weak resonant Raman response [95]. In a narrowband configuration, such amplification is of little help, since one acquires a single point and not the spectrum, in BCARS the NRB can be exploited to enhance the signal-to-noise ratio (SNR) of the measured spectra [94]. In this case, in order to extrapolate the pure vibrational information, the line shape distortions can be removed by exploiting numerical meth-

ods [46,47,96,97] or deep-learning approaches [48–50].

Despite many technical advancements in the detection systems, leading to higher speed and broader spectral coverage, many B-CARS systems are designed to collect Raman spectra only in the CH-stretching region [98] ($2800 - 3100 \text{ cm}^{-1}$), a spectral range that features a high density of oscillators. The spectral information in this region is rather unspecific, since it features a small number of broad Raman peaks, preventing accurate identification of different biological compounds within chemically heterogeneous biological samples. On the contrary, the low-wavenumber spectral region ($400-1800 \text{ cm}^{-1}$), also known as “fingerprint”, presents sharp and distinct peaks providing high biochemical specificity. However, the fingerprint region features weaker Raman signals requiring either longer integration times or higher average power of the pump and Stokes beams to obtain sufficiently high SNR. These requirements could damage the imaged biological samples. Moreover, the Raman peaks in the fingerprint region present a narrow linewidth and are spectrally congested, demanding a combination of high spectral resolution (down to 10 cm^{-1}) and broad spectral coverage, which are technically challenging to achieve.

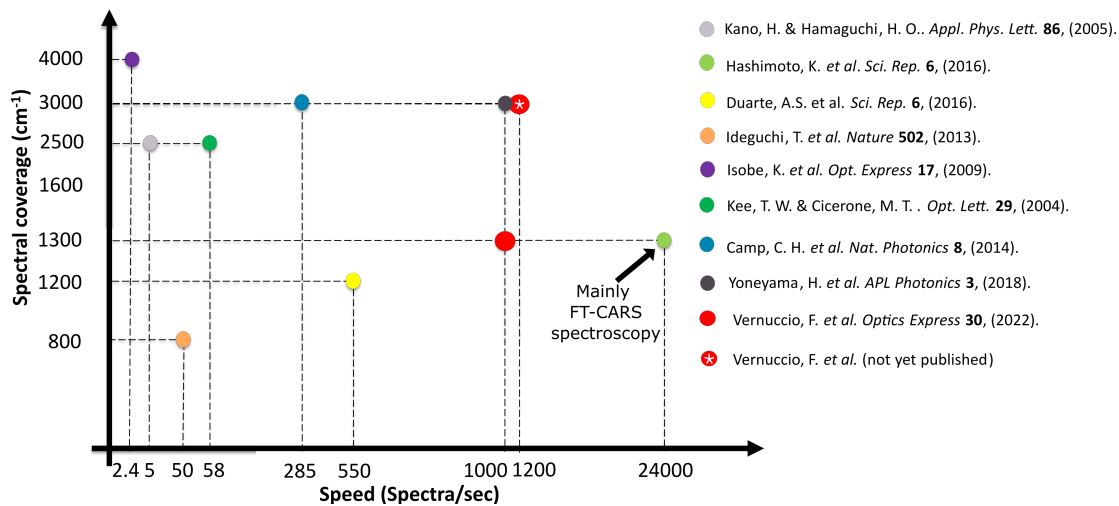


Figure 1.14: Comparison of different BCARS systems in literature in terms of speed and spectral coverage. For the comparison, we referred to the following works [32, 67, 76, 78, 83, 88, 94, 99, 100].

In the following chapters, we will describe a novel method for BCARS based on an amplified femtosecond ytterbium laser system operating at a 2-MHz repetition rate to generate pulses at 1035 nm with significantly more energy (at the μJ level) than conventional systems, typically operating at 40 or 80 MHz. This unlocks two important advantages. The first one is the possibility to produce ultra-broadband red-shifted Stokes pulses covering the entire Raman-active region ($500-3100 \text{ cm}^{-1}$) exploiting white light continuum (WLC) generation [101] in a bulk crystal rather than PCFs, as previously reported in the literature. WLC in bulk media represents a more compact, reliable, easy-to-use, and alignment-insensitive approach. It features long-term stability, comparable with that of the pump laser source itself, significant mutual correlations between the intensities of its spectral components, and low pulse-to-pulse variations [102].

The second advantage relates to the employment of a lowered repetition rate source. On the one hand, a repetition rate of 2 MHz determines a $0.5\text{-}\mu\text{s}$ temporal delay between

two consecutive pulses, giving the system more time to dissipate thermal energy and lessening photothermal damage [103]. On the other hand, for a given average power at the focus, constrained by sample degradation, more pulse energy leads to higher peak intensity, providing a stronger B-CARS signal thanks to the nonlinearity of the involved optical processes. Therefore, higher SNR and/or acquisition speed can be reached, without compromising the sample integrity.

In our setup, we use a multiplex CARS configuration. The signal is generated by overlapping narrowband pump pulses with broadband Stokes pulses, obtained through WLC generation in a 10 mm YAG crystal. The resolution of the system is provided by the narrowband pump beam, obtained by narrowing the spectral linewidth of the driving laser pulses ($< 10\text{cm}^{-1}$) via an etalon. The comparison of the performance of our experimental setup with the one in the literature mentioned above can be summarized in a graph that plots the spectral coverage in cm^{-1} versus the speed measured as spectra/sec (see Fig.1.14). This plot clearly demonstrates that our setup is at the state of the art in terms of spectral coverage enabling us to measure of full spectrum and it also features high acquisition speed, if we do not consider the work of Hashimoto et al. [32] that demonstrates very high-speed CARS spectroscopy, but not microscopy. Further details on the experimental BCARS setup will be discussed in chapter 3.

1.4.3 Two-color and three-color CARS

In section 1.4.1, we described the CARS process through the Jablonsky diagram in Fig. 1.9, where the generation of the anti-Stokes component is possible thanks two a double interaction with the pump beam and a single interaction with the Stokes beam. However, in the BCARS frame, two different excitation methods can be exploited to generate the anti-Stokes component. The interplay between these two processes depends on the order of interactions between the pump and Stokes pulses and on the properties (pulse duration and spectral bandwidth) of the employed optical sources. These two processes are the two-color and three-color mechanisms and act in parallel thus enabling us to collect signals in two different spectral regions simultaneously. To understand their differences, we may start with the expression of the CARS intensity. We previously demonstrated (in Eq. (1.52)) that the CARS intensity scales quadratically with the third-order nonlinear polarization $P^{(3)}(\omega_{aS})$, generated in the scrutinized sample as a result of the interaction of the pump \vec{E}_P and Stokes \vec{E}_S electric fields and the sample itself. Considering the nonlinear third-order susceptibility $\chi_{VIB}^{(3)}$ of the investigated specimen, the CARS intensity expression reads as follows [94]:

$$I_{CARS} \propto |P^{(3)}(\omega_{aS})|^2 \propto \left| \left\{ \chi_{VIB}^{(3)}(\omega) [E_S(\omega) \otimes E_P(\omega)] \right\} * E_P(\omega) \right|^2, \quad (1.61)$$

Where, in (1.61), \otimes and $*$ represent the cross-correlation operation and the convolution operation, respectively. This equation states that the cross-correlation term is responsible for the vibrational modes excited by the combination of pump and Stokes beams, while the convolution operation with the narrowband pump field, assumed that the cross-correlation is broad enough, defines the spectral resolution of our system. Eq. (1.61) describes the two-color CARS mechanism (in Fig. 1.15.(a)), where the narrowband pump beam interacts with the broadband Stokes beam to stimulate the vibrations

of the scrutinized samples, and then a second interaction with the narrowband pump beam probes the vibrational modes, provoking the emission of the anti-Stokes components. In this case, the modes excited derive from the inter-pulse interaction between the pump and Stokes beam, hence, they are determined by the differences in their frequencies.

Nevertheless, if the broadband Stokes beam is short enough (shorter than the vibrational oscillation period), an intra-pulse excitation mechanism occurs at the sample plane. This excitation mechanism is known as impulsive CARS or three-color mechanism (in Fig. 1.15.(b)). The vibrational coherence is directly generated by the broadband Stokes pulse, according to the so-called “impulsive stimulated Raman scattering” (ISRS) mechanism [104, 105]. The ISRS process creates a vibrational coherence in all modes with frequencies falling within the excitation Stokes bandwidth, provided that the pulse has a temporal duration close to the transform-limited value, so that all frequencies interact nearly simultaneously with the sample. After the excitation, the narrowband pump beam acts as a probe thus determining the final emission at the anti-Stokes frequencies. The three-color mechanism thus emphasizes the lower frequencies, in particular the so-called fingerprint region ($400\text{-}1800\text{ cm}^{-1}$). In the three-color mechanism, eq. (1.61) may be modified in:

$$I_{CARS} \propto \left| \left\{ \chi_{VIB}^{(3)}(\omega) [E_S(\omega) \otimes E_S(\omega)] \right\} * E_P(\omega) \right|^2 \quad (1.62)$$

The excitation profile in the three-color CARS mechanism depends on the number of permutations of each frequency shift within the Stokes bandwidth. Since the highest number of permutations corresponds to close frequencies, the three-color excitation profile vanishes by increasing the wavenumber [94]. This makes three-color CARS particularly suitable for stimulating Raman transitions at very small Raman shifts (see Fig.1.15.(b)) and in the entire fingerprint region, also exploiting the heterodyne amplification given by the NRB contribution to enhance their intrinsic weak signal.

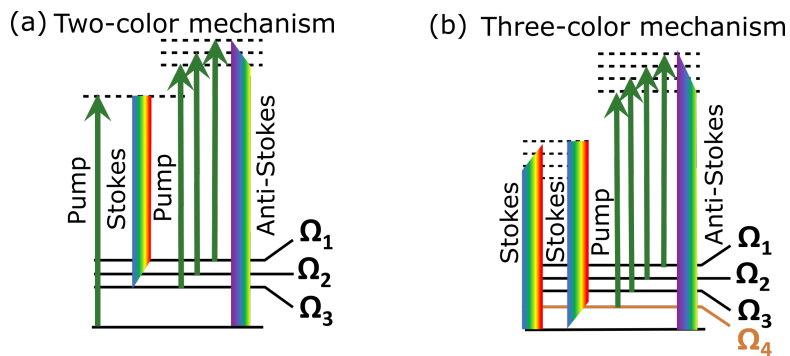


Figure 1.15: Jablonsky diagram for (a) Two-color and (b) Three-color CARS mechanisms.

We can summarize the main characteristics of the CARS signal generated by combining the two processes in the following points:

- an increase in the Stokes bandwidth, under the hypothesis of compressed pulses at the samples, determines a higher intensity and a larger bandwidth of the CARS signal generated through the three-color mechanism, but diminishes the intensity

of the signal generated by the two-color mechanism under constant average power at the sample;

- the spectral resolution of the probed vibrational modes depend only on the spectral bandwidth of the probe beam;
- the generation of the CARS signal by means of the three-color mechanism is strictly related to the pulse duration of the broadband beam. A shorter duration of the beam allows us to probe vibrational modes with higher frequency. This means that impulsive CARS is achievable only if the Stokes pulses are compressed so that its duration is shorter than the oscillation period of the vibrational modes. E.g. for the vibrational frequency at $\nu=1400 \text{ cm}^{-1}$, the last mode we can detect with the BCARS system through three-color CARS, the oscillation period T in fs is:

$$T[\text{fs}] = \frac{10^{15}}{100c\nu[\text{cm}^{-1}]} \approx 23.8\text{fs}. \quad (1.63)$$

This implies that the Stokes pulse duration should be shorter than this value, hence a sub-20 fs pulse.

- it is important to spectrally separate the contributions of the two processes to the anti-Stokes component. Indeed, the two excitation methods feature different phases, thus leading to distortion of the spectrum and signal instability.

We can better understand the role of each mechanism in the generation of the CARS signal, by assuming Gaussian pulses and looking at how the excitation profiles change, varying the parameters of each beam.

Assuming that the pump and Stokes pulses have Gaussian spectral profiles and real envelopes, which means they are temporally centered and transform-limited, we can write the cross-correlation term for the two color mechanism as:

$$E_S(\omega) \otimes E_P(\omega) = \int E_S^*(\omega') E_P(\omega + \omega') d\omega' = \frac{E_{S0} E_{P0} \sigma_P \sigma_S \sqrt{2\pi}}{\sqrt{\sigma_P^2 + \sigma_S^2}} e^{-\frac{(\omega - \omega_{P0} + \omega_{S0})^2}{2(\sigma_P^2 + \sigma_S^2)}}, \quad (1.64)$$

where E_{S0} and E_{P0} are the amplitude of the pump and Stokes beam, σ_P and σ_S are the standard deviation of the gaussian profiles related to the bandwidth of the two beams centered at ω_{P0} and ω_{S0} . In the case of the three-color process, the cross-correlation term becomes an autocorrelation term of the Stokes beam, that reads:

$$E_S(\omega) \otimes E_S(\omega) = |E_{S0}|^2 \sigma_S \sqrt{\pi} e^{-\frac{\omega^2}{4\sigma_S^2}}, \quad (1.65)$$

Eq.(1.65) shows that in the three-color mechanism the broadband Stokes pulse acts both as pump and Stokes beam. Since when we consider experimentally the pulses, we deal with their average power, rather than their amplitude, we may introduce in the previous expression the Power of each beam. For a Gaussian pulse of the form $A_0 e^{-\omega^2/2\sigma^2}$, the average power P_A can be written as $P_A \propto |A_0|^2 \sigma \sqrt{\pi}$. Introducing in eq.(1.64) and eq.(1.65) the pump, P_P , and Stokes, P_S , average powers, the two expressions become:

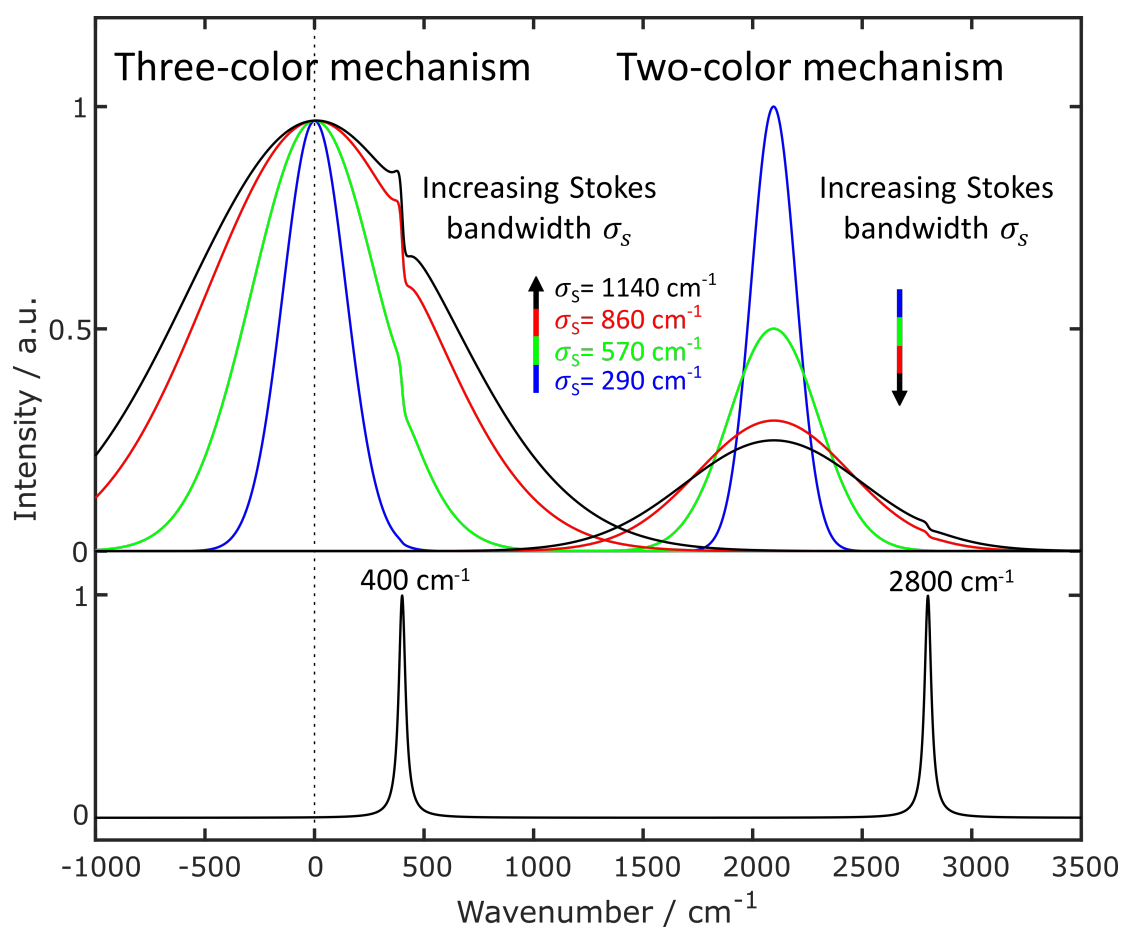


Figure 1.16: Mathematical simulation of the two excitation mechanisms for broadband CARS generation keeping fixed the average power of the pump and Stokes beam, the pump pulse bandwidth, and the nonlinear third-order susceptibility and varying the bandwidth of the broadband Stokes.

$$E_S(\omega) \otimes E_P(\omega) \propto \sqrt{P_P P_S} \frac{\sqrt{2\sigma_P \sigma_S}}{\sqrt{\sigma_P^2 + \sigma_S^2}} e^{-\frac{(\omega - \omega_{P0} + \omega_{S0})^2}{2(\sigma_P^2 + \sigma_S^2)}}, \quad (1.66)$$

$$E_S(\omega) \otimes E_S(\omega) \propto P_S e^{-\frac{\omega^2}{4\sigma_S^2}}, \quad (1.67)$$

From eq.(1.67), it is evident that the excitation profile for three-color CARS is centered at $\omega = 0$ and its maximum does not depend on the bandwidth of the Stokes beam (no dependence on σ_S), but just on its average power. The material response increases with increasing the Stokes bandwidth. In the case of two-color CARS, eq.(1.66) shows that the maximum of the signal is centered at $\omega = \omega_{P0} - \omega_{S0}$ and the material response decreases with increasing the Stokes bandwidth. Indeed in the case, where $\sigma_S \gg \sigma_P$, eq.(1.66) becomes:

$$E_S(\omega) \otimes E_P(\omega) \propto \sqrt{P_P P_S} \sqrt{\frac{2\sigma_P}{\sigma_S}} e^{-\frac{(\omega - \omega_{P0} + \omega_{S0})^2}{2(\sigma_P^2 + \sigma_S^2)}}, \quad (1.68)$$

that states that the material response scales as $\propto 1/\sqrt{\sigma_S}$.

If we want to evaluate it in the overall CARS expression, we need to consider the convolution of these two terms (the cross-correlation between pump and Stokes and the auto-correlation of the Stokes beam) with the third beam, which acts as a probe. Experimentally, the third beam is the narrowband pump beam that can be assumed as a beam with a Gaussian profile centered at ω_p . The resulting expressions for the CARS intensity in the two-color and three-color mechanisms are [94]:

$$I_{2C}(\omega) \propto \left| \frac{2\pi \chi_{VIB}^{(3)} E_{S0}^* E_{P0}^2 \sigma_P^2 \sigma_S}{\sqrt{2\sigma_P^2 + \sigma_S^2}} e^{-\frac{(\omega - 2\omega_{P0} + \omega_{S0})^2}{2(2\sigma_P^2 + \sigma_S^2)}} \right|^2 = \quad (1.69)$$

$$= \frac{4\pi^2 |\chi_{VIB}^{(3)}|^2 |E_{S0}|^2 |E_{P0}|^4 \sigma_P^4 \sigma_S^2}{2\sigma_P^2 + \sigma_S^2} e^{-\frac{(\omega - 2\omega_{P0} + \omega_{S0})^2}{(2\sigma_P^2 + \sigma_S^2)}} = \quad (1.70)$$

$$\propto \frac{4\sqrt{\pi} |\chi_{VIB}^{(3)}|^2 P_S P_P^2 \sigma_P^2 \sigma_S}{2\sigma_P^2 + \sigma_S^2} e^{-\frac{(\omega - 2\omega_{P0} + \omega_{S0})^2}{(2\sigma_P^2 + \sigma_S^2)}}, \quad (1.71)$$

$$I_{3C}(\omega) \propto \left| \frac{2\pi \chi_{VIB}^{(3)} E_{S0}^2 E_{p0} \sigma_p \sigma_S^2}{\sqrt{\sigma_p^2 + 2\sigma_S^2}} e^{-\frac{(\omega - \omega_{p0})^2}{2(\sigma_p^2 + 2\sigma_S^2)}} \right|^2 = \quad (1.72)$$

$$= \frac{4\pi^2 |\chi_{VIB}^{(3)}|^2 |E_{S0}|^4 |E_{p0}|^2 \sigma_p^2 \sigma_S^4}{\sigma_p^2 + 2\sigma_S^2} e^{-\frac{(\omega - \omega_{p0})^2}{(\sigma_p^2 + 2\sigma_S^2)}} = \quad (1.73)$$

$$\propto \frac{4\sqrt{\pi} |\chi_{VIB}^{(3)}|^2 P_S^2 P_p \sigma_p \sigma_S^2}{\sigma_p^2 + 2\sigma_S^2} e^{-\frac{(\omega - \omega_{p0})^2}{(\sigma_p^2 + 2\sigma_S^2)}}, \quad (1.74)$$

From these equations, we can say that the two-color CARS mechanism, in the case of Stokes bandwidth larger than the Pump bandwidth, scales as $1/\sigma_S$ and it is centered in $\omega = 2\omega_P - \omega_S$. On the other hand, for the three-color mechanism, the maximum signal

is centered at $\omega = \omega_p$, and in the case of a broad Stokes beam ($\sigma_S \gg \sigma_p$), the maximum intensity depends only on the average power of the input beams. Moving away from the maximum, the three-color CARS intensity scales with $e^{-(\omega - \omega_{p0})^2 / (\sigma_p^2 + 2\sigma_S^2)}$, i.e. it becomes larger increasing the bandwidth σ_S .

The dependence of the CARS signal profile with the Stokes bandwidth can be clearer with a simulation of the two processes (see Fig. 1.16). Starting from the expression of the two-color and three-color CARS mechanism in eq. (1.71) and eq. (1.74), we can consider third-order nonlinear vibrational susceptibility $\chi_{VIB}^{(3)}$ constituted by a resonant and a non-resonant term. The resonant term features two peaks with unitary amplitude centered at 400 cm^{-1} and at 2800 cm^{-1} and with FWHM equal to $\approx 36 \text{ cm}^{-1}$. The non-resonant term has been set so that the resonant to non-resonant ratio is 0.1. We considered a pump beam centered at 1034 nm with 1.1 nm FWHM and 80 mW average power and a Stokes beam centered at 1320 nm and 5 mW average Power. The FWHM of the Stokes beam has been set to four different values equal to 50, 100, 150, and 200 nm that in wavenumber correspond to $\approx 290, 570, 860, 1140 \text{ cm}^{-1}$. Inserting these numbers in the simulation, we can clearly see that for the three-color mechanism an increasing Stokes bandwidth determines a greater spectral coverage and a higher signal intensity away from the maximum. The maximum amplitude does not vary with the Stokes bandwidth but depends only on the input average powers of the two beams. On the other hand, the two-color mechanism at fixed average power (i.e. P_S and P_p are constant) features lower intensity while increasing the Stokes bandwidth, but, as for the three-color mechanism, a broader spectrum of the Stokes beam results in a broader spectral coverage.

In light of the previous discussion, we designed our BCARS experimental setup by combining both mechanisms. To cover the whole vibrational spectrum with no distortion, we carefully tuned the pulse duration of the broadband beam and its spectral coverage. We first adjusted the pulse duration at the sample plane, carefully adjusting the prism compressor stage, so to maximize the bandwidth ($400\text{-}1400 \text{ cm}^{-1}$) and the intensity of the three-color mechanism in the first portion of the spectrum. Then, we also inserted a mask after the second prism of the pulse compressor to carefully adjust the spectral bandwidth, so that the two-color mechanism starts precisely (1400 cm^{-1}) where the three-color mechanism vanishes, thus avoiding fluctuations on the spectrum due to the interference between the two processes.

All the details of the experimental design will be discussed in chapter 3.

1.4.4 Time-delayed CARS

The difference in origin between resonant and non-resonant signals in CARS suggests a straightforward method for discriminating between the two contributions. The interaction of the first two fields in vibrationally resonant CARS produces coherence in the medium. In the condensed phase, this coherence often lasts for picoseconds. Contrarily, the NRB is extremely short-lived, with the biggest contribution lasting only as long as the excitation pulse [41].

Since the non-resonant contribution survives for a time much shorter than the resonant one [106], it is possible to isolate the resonant contribution by adjusting the arrival time of the third field, which acts as a probe field. This technique is called Time-delayed CARS (TD-CARS) [43, 107–113] (Fig.1.17).

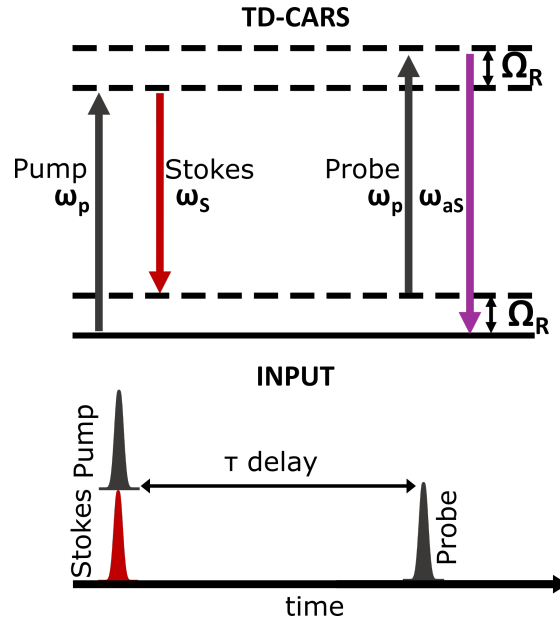


Figure 1.17: Scheme for TD-CARS. After the arrival of two synchronized beams, namely pump and Stokes beam, a third beam, the probe beam, arrives with a delay τ waiting for the decay of the NRB. If τ is sufficiently large (longer than one pulse duration) to suppress the NRB contribution, the measured anti-Stokes component will just contain the resonant contribution.

Referring to the description of the two mechanisms considering just two beams, i.e. the narrowband pump and the broadband Stokes beam, it is clear that in order to generate CARS with the two-color mechanism, there must be two interactions with the pump beam, where the first one excites the vibrational modes, while the second one probes them. Therefore, it is not possible to introduce a delay between the pump and the Stokes pulses, since no modes would be excited. On the other hand, the three-color CARS is particularly suitable for T-CARS. Indeed, in this mechanism, the Stokes beam excites the vibrational modes acting both as pump and Stokes beam, while the pump pulse acts simply as a probe. Hence, it is possible to delay the pump, suppressing the NRB contribution.

The main advantage of using T-CARS is that it is an optical solution for NRB removal. Therefore, the obtained spectra are comparable to the SR ones without the need for post-processing. However, as it has been extensively discussed in previous sections, the NRB also allows us to amplify the CARS signal. Removing it leads to lower sensitivity and a lower signal-to-noise ratio of the acquired spectra, calling for a longer integration time to acquire good-quality spectra. For these reasons, T-CARS is particularly useful for spectroscopic applications, where a longer acquisition time is still acceptable. While for microscopic applications [110], T-CARS is not the primary choice, since one looks for shorter pixel dwell time to image large field of views and not damage the biological samples.

1.4.5 Epi-detected CARS

In eq. (1.55), we found that the CARS signal scales quadratically with the thickness L of the scrutinized specimen. We derived the simple expression for the CARS intensity

assuming that the phase matching condition is accomplished, namely $\Delta\vec{k}L = 0$, in which $\Delta\vec{k} = 2\vec{k}_P - \vec{k}_S - \vec{k}_{AS}$. This approximation is generally valid in microscopy under tight focusing conditions. However, till now we implicitly considered the forward propagating signal (F-CARS). If we took into account the backward propagating signal, even under tight focusing conditions, the phase matching approximation is no more valid [114, 115].

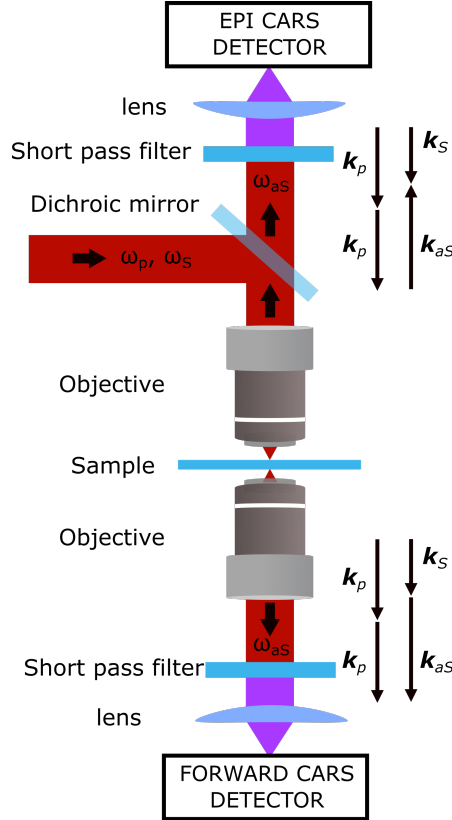


Figure 1.18: Scheme of E-CARS and F-CARS experimental set-up.

For backward propagating CARS, also called epi-detected CARS (E-CARS) [114], the intensity can be calculated as [116]:

$$I_{AS}(L) \propto |\chi^{(3)}|^2 L^2 \text{sinc}^2 \left(\frac{|\Delta\vec{k}|L}{2} \right) I_P^2 I_S, \quad (1.75)$$

In this case, the only way to get $|\Delta\vec{k}|L \simeq 0$ is through $L \simeq 0$. To understand the advantage of using E-CARS rather than F-CARS, we can consider a thin sample immersed in a solvent. Since the F-CARS signal is proportional to L^2 , the solvent signal will be stronger than the one of the thin sample, due to $L_{sample} \ll L_{solvent}$. On the other hand, the E-CARS signal of the solvent will be strongly reduced since the phase matching condition is not satisfied, while the signal coming from the thin sample will be comparable with the F-CARS signal, since $|\Delta\vec{k}|L_{sample} \simeq 0$ is valid in both directions. Therefore, epi-detected CARS enhances the signal-to-background ratio

of small scatterers, being beneficial for their identification in heterogeneous samples [116, 117].

If the dispersion of the refractive index is negligible ($n_S \simeq n_P \simeq n_{AS} \simeq n$), it is possible to provide an estimate of the critical thickness L_{crit} over which the E-CARS signal drops. Considering that the first zero of $\text{sinc}(x)$ is for $x = \pi$, the required condition to have a relevant E-CARS signal is: $|\Delta\vec{k}|L \ll \pi$. For epi-detected CARS, assuming a collinear geometry:

$$|\Delta\vec{k}| = 2k_{aS} = \frac{4n\pi}{\lambda_{aS}}, \quad (1.76)$$

Hence, applying the condition $|\Delta\vec{k}|L \ll \pi$ to (1.76), we obtain E-CARS signal if:

$$L \ll \frac{\lambda_{aS}}{4n}. \quad (1.77)$$

Therefore for biological samples, that have refractive index $n \approx 1.3$ and considering that we measure signals with $\lambda_{aS} \approx 900$ nm, $L \ll 167$ nm. It means signal mainly comes from very small scatterers of the heterogeneous biological specimens. A scheme of a microscope able to detect both F-CARS and E-CARS is depicted in 1.18.

1.5 The SRS process

The SRS process belongs to the class of coherent Raman scattering processes. While CARS probes the vibrational coherences in the Raman-active medium by means of a narrowband beam, SRS monitors directly the vibrational population states, detecting either a frequency-dependent Stokes amplification (SRG) or a frequency-dependent pump attenuation (SRL) (Fig. 1.7.(d-e)). In its simplest implementation, SRS utilizes the same excitation scheme as CARS with two narrowband input fields interacting with the Raman-active sample. Quantum mechanically, the picture of the process is the following: the interaction with the Raman active material leads to the absorption of a pump photon at frequency ω_p (that is annihilated) and the emission of a Stokes photon at frequency ω_s (that is created), while the energy difference between the two photons $\hbar(\omega_p - \omega_s)$ is absorbed by the material for energy conservation. Since energy is deposited in the material after the interaction, SRS belongs to the so-called nonlinear dissipation processes where, after the nonlinear interaction, an exchange of energy between the laser fields and the medium takes place. CARS, on the other hand, is a parametric generation process because only the fields involved in the nonlinear interaction exchange energy, while the medium, at the end of the interaction, remains in the ground state.

The mathematical expression for the amplitude of SRG and SRL can be obtained using a four-wave mixing approach. Considering the degenerate case where $\omega_1 = \omega_2 = \omega_P$ and $\omega_3 = \omega_4 = \omega_S$, the stimulated Raman gain (SRG) process can be derived from the propagation equation for the Stokes field. From eq. (1.37), inserting the expression of the envelope of the third-order nonlinear polarization oscillating at frequency ω_s , $P_{\omega_S}^{(3)} = \frac{3\epsilon_0}{4}\chi^{(3)}(\omega_S)|A_P|^2 A_S \exp(i(\omega_S t - k_S z))$, the propagation equation becomes:

$$\frac{dA_S}{dz} = -\frac{3i\omega_S}{8cn(\omega_S)}\chi^{(3)}(\omega_S)|A_P|^2 A_S e^{-i\Delta k z}, \quad (1.78)$$

Chapter 1. Coherent raman scattering microscopy

where $\Delta k = -k_p + k_s + k_p - k_s = 0$, which means that the SRS process is intrinsically phase-matched. From this equation, the amplitude of the Stokes field after propagation on a sample of length L is:

$$A_S = A_S(0)e^{-\frac{3i\omega_S}{8cn(\omega_S)}\chi^{(3)}(\omega_S)|A_P(0)|^2L} \quad (1.79)$$

By performing the first-order development, we obtain

$$A_S = A_S(0) - \frac{3i\omega_S}{8cn(\omega_S)}\chi^{(3)}(\omega_S)|A_P(0)|^2A_S(0)L \quad (1.80)$$

$$= A_S(0) + \Delta A_S \quad (1.81)$$

Since the signal ΔA_S sits on top of the original Stokes beam, to detect it one needs high-frequency modulation transfer techniques. Assuming that $|\Delta A_S| \ll A_S(0)$, the field intensity becomes:

$$I_S \propto |A_S(0) + \Delta A_S|^2 = |A_S(0)|^2 + |\Delta A_S|^2 + 2\Re\{A_S(0)^*\Delta A_S\} \quad (1.82)$$

$$\simeq |A_S(0)|^2 + \frac{3\omega_S}{4cn(\omega_S)}\Im\{\chi_R^{(3)}(\Omega)\}|A_P(0)|^2|A_S(0)|^2L \quad (1.83)$$

The first term on the right-hand side is the intensity of the Stokes beam, which we assumed remains virtually unattenuated during the nonlinear process. The second term is the interference between the incident Stokes field and the stimulated Raman field at the detector. Note that if $\chi_{VIB}^{(3)}$ is purely real, the interference term disappears, however close to resonance $\Im\{\chi_R^{(3)}\} \neq 0$ and the interference term is non-vanishing. Using modulation transfer techniques, this interference term can be electronically isolated from the other terms. Indeed, one beam is modulated at high frequency (>1 MHz, where the laser noise reaches its minimum values), and the modulation transfer on the other beam is detected using a lock-in amplifier that basically demodulates the signal acquired with a photodiode. The quantity which is physically detected in an SRG experiment is the change in intensity of the Stokes beam when the pump beam is modulated:

$$\Delta I_S = \frac{3\omega_S}{4cn(\omega_S)}\Im\{\chi_R^{(3)}(\Omega)\}I_P I_S L \quad (1.84)$$

where $I_P \propto |A_P(0)|^2$ and $I_S \propto |A_S(0)|^2$. From Eq. 1.84, we see that the plane wave model predicts that the SRG signal is proportional to the length L at the interaction volume, as well as, it has a linear dependence on the pump and on the Stokes beams (I_P and I_S). Moreover, since it is proportional to the imaginary part of the third-order nonlinear susceptibility $\chi_R^{(3)}$, the signal is directly comparable to the SR one. SRG is typically defined as:

$$SRG = \frac{\Delta I_S}{I_S(0)} = \frac{3\omega_S}{4cn(\omega_S)}\Im\{\chi_R^{(3)}(\Omega)\}I_P L \quad (1.85)$$

The analogous equation describing the forward-detected stimulated Raman loss (SRL) signal is obtained by exchanging the subscript S and P and by inverting the sign of the

imaginary part of the third-order nonlinear susceptibility. The quantity physically detected in an SRL process is the change in intensity of the pump beam when the Stokes beam is modulated:

$$SRL = \frac{\Delta I_P}{I_P(0)} = -\frac{3\omega_P}{4cn(\omega_P)} \Im\{\chi_R^{(3)}(\Omega)\} I_S L \quad (1.86)$$

For the same consideration we have done for the SRG case, the SRL signal represents a loss in intensity in the ω_P channel and it derives from destructive interference between the pump field and the induced field at ω_P .

Note that SRG signal is proportional to the pump intensity while the SRL signal is proportional to the Stokes intensity. It implies that in an SRG (SRL) experiment the pump (Stokes) intensity should be high to have a stronger signal, while the Stokes (pump) intensity should be sufficient to be revealed by the detector.

So far, we have discussed the case of forward-detected SRS signal. While the forward-propagating stimulated Raman field is always phase-matched with the incident field, in the epi-detected SRS [28] there is a non-zero wave vector phase match. Indeed it results in $|\Delta k| = 2|k_s|$ for SRG signal and $|\Delta k| = 2|k_p|$ for SRL signal. Consequently, the backward-propagation-induced phase mismatch will determine an effective coherence length L_c which is very small in water (0.3 or 0.4 μm for light beams in the NIR) and so it is only relevant in microscopy applications where a nanoscopic object is being studied whose geometry does not exceed the coherence length.

1.5.1 SRS vs CARS

SRS and CARS are two techniques that allow the user to probe the vibrational modes of the sample. They both are based on the illumination of the sample with two beams (the pump and the Stokes beam). The main difference between the two is how the information is translated in terms of the amplitude and phase of the emitted electric fields. As we have seen in previous sections, in SRS the information sits on top of the pump and Stokes fields and can be read as a loss of the pump (SRL) or a gain of the Stokes signal (SRG), while in CARS the information is encoded in the field oscillating at the anti-Stokes frequency. From an experimental point of view, it implies the use of two different approaches to extract from the measured signal the given Raman vibrational information.

The most relevant SRS advantages over CARS are:

- SRS signal scales linearly with the concentration of molecules inside the sample, thus one can retrieve also quantitative information about the target molecules, without any problem about the fact that they are present in high or low concentration. In CARS, there is a quadratic dependence on the concentration of target molecules, which means that in case of low concentration, it is difficult to distinguish the signal from the NRB.
- SRS signal is free from NRB and directly proportional to the Raman cross-section σ_{Raman} , thus one can directly compare the SRG/SRL signal with the data already known in the literature from SR. On the other hand, CARS is affected by NRB and it is difficult to perform a direct comparison of the spectra.

- Two-photon excited fluorescence overlaps the spectral region of the CARS signal, limiting its interpretation. Conversely SRS, being on top of the original beams, is not distorted by this process.
- SRS is intrinsically phase-matched, while CARS depends on phase-matching condition fulfillment that makes the applicability of deconvolution methods very hard.

Also CARS has some advantages with respect to SRS:

- CARS signal is easier to detect with respect to SRS since it is nearly a background-free process spectrally separated from the two input fields. Instead, in SRS you must detect a small variation in the number of photons on a large background (pump and Stokes) and so more sophisticated techniques are needed to detect them.
- CARS can be straightforwardly implemented in the broadband modality, enabling the detection of more chemical species at once. Indeed, in CARS a spectrometer is enough to measure the anti-Stokes component. Contrarily in SRS, the broadband modality requires a particular technological design to detect the full vibrational spectrum of the specimen based on a multi-channel lock-in technology.
- In CARS, one can exploit the presence of the NRB to amplify the weak Raman modes in the fingerprint region, whose detection in SRS is very challenging. The user can get rid of the NRB contribution either in post-processing analysis with numerical or deep-learning approaches or with optical techniques (e.g. TD-CARS or polarization CARS).

1.5.2 Broadband SRS

Also for SRS, it is possible to talk about broadband SRS techniques. We may distinguish also in this case the hyperspectral and the multiplex SRS. First SRS measures were acquired while working at single frequency using a picosecond OPO [51] The first attempts to enhance the chemical specificity through a parallel or sequential acquisition of several vibration modes were based on the tunability of the OPO themselves. However, since the OPOs have intrinsically a limited tuning speed, the acquisition of SRS images is time consuming [118] [119]. A possible solution to this problem is the so-called spectrally tailored excitation SRS [120], which is based on a tailored multiplex excitation of the vibrational modes of the investigated sample. Ozeki et al. [121] further boosted the imaging speed of hyperspectral SRS by using an approach based on a very low noise detection chain and on the possibility to scan the frequency detuning between pump and Stokes beams with a millisecond time response. In recent years a number of hyperspectral SRS setups have been developed based on the SF approach, where the scanning speed has been increased to a point to be able to interrogate each pixel at variable frequency detuning, typically within 30 – 60 μ s. [122, 123].

In multiplex SRS, a narrowband pump and a broadband Stokes are synchronized and collinearly combined and sent to the sample (into the microscope). The pump pulse, after the sample, is removed with a short-pass wavelength filter, while the broadband Stokes is sent to a multichannel detector, which can be either digital (spectrograph + CCD) or analog (diffraction grating+ photodiode array+ multichannel lock-in amplifier). Each photodiode array, like in a commercial spectrometer, records the intensity

of a different spectral portion of the incoming pulse. In order to measure this signal is, therefore, necessary that each photodiode is connected to a lock-in amplifier, hence, a multi-channel lock-in amplifier is required to perform the measurement. A similar approach for multiplex SRS has been recently developed in our laboratories [124, 125]. We realized a broadband SRS microscope equipped with a home-built multichannel lock-in amplifier capable of simultaneously measuring the SRS signal at 32 frequencies with integration time down to 44 μ s. The system has been used to measure the vibrational modes in the CH-stretching region of biological samples. In particular, it differentiates the chemical constituents of heterogeneous samples by measuring the relative concentrations of different fatty acids in cultured hepatocytes at the single lipid droplet level and identifies tumors from peritumoral tissue in a mouse model of fibrosarcoma.

An alternative approach to multiplex SRS is known as the photonic time stretch approach [126, 127]. It consists in temporally chirping the pulse to be measured, typically by a long optical fiber, to a duration of a few nanoseconds, so that it can be accurately sampled by a high-frequency analog-to-digital converter (ADC). The SRG spectra are retrieved by numeric demodulation of the collected spectra by a single photo-detector instead of a lock-in amplifier.

Another approach for broadband SRS is based on FT detection of the SRG/SRL spectrum and is referred to as *Fourier Transform-SRS* (FT-SRS) [128]. The FT approach uses a single photodetector for measuring the interferogram of the broadband Stokes beam after filtering the modulated narrowband pump beam.

A complete overview of all the multiplex implementations for SRS is out of the scope of this thesis work which is mainly focused on multiplex CARS. The reader may refer to [24].

CHAPTER 2

Supercontinuum generation in bulk media

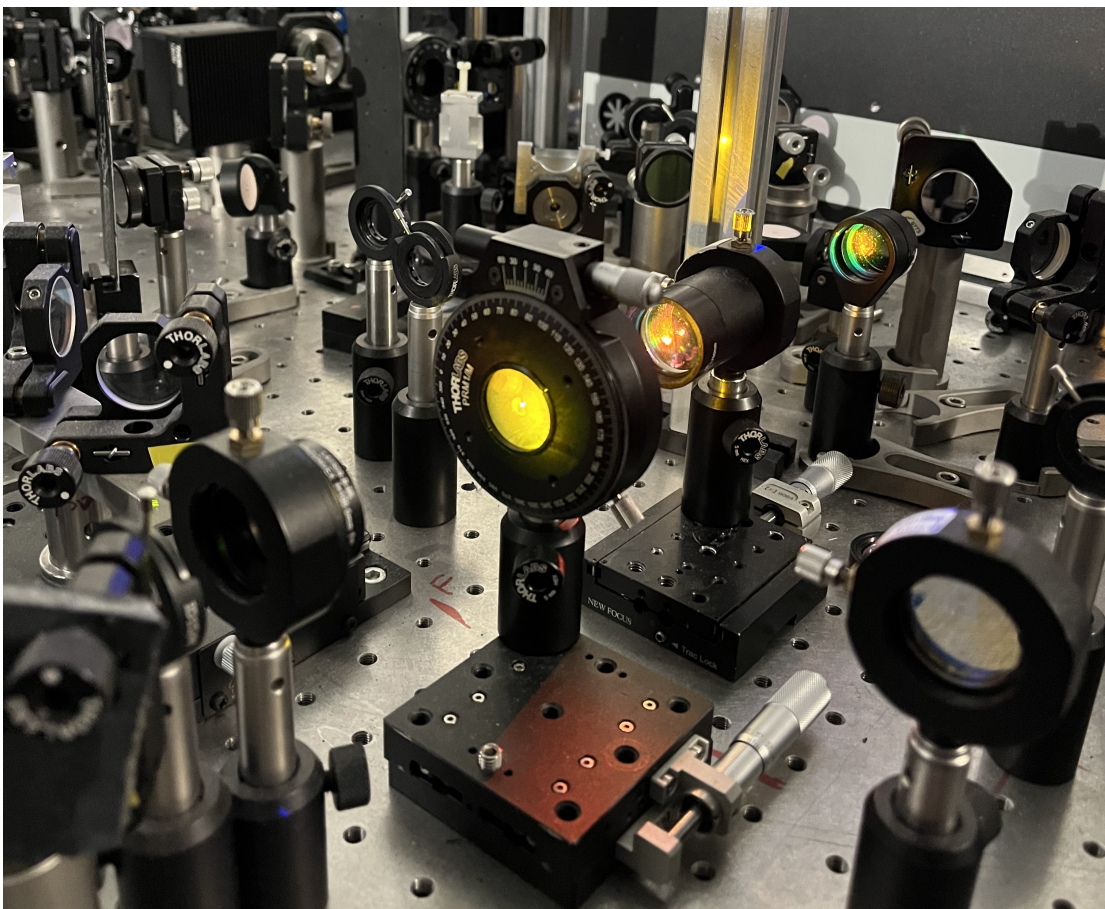


Figure 2.1: *Picture of the supercontinuum generation in a 10-mm YAG crystal from the VIBRA laboratory of Politecnico di Milano.*

This chapter deals with the theoretical description of the processes leading to white light continuum (WLC) generation that is used in the BCARS experimental setup to produce the broadband source. WLC is a complex mechanism that involves many nonlinear optical processes coming into play in a material when the impinging light intensity overcomes a threshold. Despite its theoretical complexity, it is quite simple to produce a WLC with long-term stability and a sufficiently broad spectrum thus managing to generate all the colors needed for exciting the vibrational modes in biological samples.

2.1 Introduction

WLC generation is one of the most spectacular and visually perceptible effects produced by the nonlinear propagation of intense ultrashort laser pulse in a transparent medium (Fig. 2.1).

From the practical point of view, to switch on the supercontinuum, one has to play on three main parameters: the average power of the femtosecond pulses impinging onto the crystal, the divergence of the beam at the focal spot, and the position of the crystal with respect to the focal plane. Femtosecond WLC generation constitutes a more compact, robust, efficient, low-cost, and alignment-insensitive technique rather than using Photonic crystal fiber (PCF). Moreover, it guarantees long-term stability of the broadband source, which can be even higher with respect to that of the fundamental beam that induces the process, thanks to the intrinsic nature of the filamentation process [102, 129]. It also features high spatial and temporal coherence. On the one hand, spatial coherence leads to an improvement in the quality of the spatial mode, a universal feature of the filamentation process [130]. On the other hand, the temporal coherence implies that the colors during the propagation acquire a regular chirp, thus guaranteeing the compressibility of the broadband source [131]. Eventually, the generated supercontinuum features the same polarization properties as the fundamental beam [132] and has a spectral density of the order of ≈ 10 pJ/nm [133] exhibiting mutual correlations between the intensities of the spectral components and low pulse-to-pulse fluctuations.

From a theoretical perspective, the physical process leading to the SC generation in transparent bulk media can be understood in the framework of femtosecond filamentation [102]. This process is the result of an intricate coupling between spatial and temporal effects such as diffraction, self-focusing, self-phase modulation, group velocity dispersion, multiphoton absorption, and ionization.

In the space domain, the interplay of these effects leads to the formation of a narrow light channel, termed light filament which propagates over extended distances much larger than the typical diffraction length and which leaves a narrow luminous plasma trail in its wake. In the time domain, the pulse undergoes dramatic transformations: pulse splitting or compression, pulse front steepening, and generation of optical shocks. These transformations altogether produce a broadband, spatially, and temporally coherent emission with a low angular divergence (supercontinuum), accompanied by the generation of colored conical emission.

When the filament forms in the air, the conical emission is typically longer than a meter and requires an energy of the order of several millijoules. In solids or liquids, using ultrashort laser pulses, its generation derives from nonlinear optical processes that require energies of the order of several microjoules, resulting in a conical emission

length of a few mm or cm.

2.2 Self-focusing of Laser Beams

When shining materials with a very intense pulse, their response to the electric field depends on the nonlinear terms of the dielectric polarization, which can be written as:

$$\begin{aligned}\vec{P}(z, t) &= \epsilon_0 \left[\chi^{(1)} \vec{E}(z, t) + \chi^{(2)} \vec{E}^2(z, t) + \chi^{(3)} \vec{E}^3(z, t) + \dots \right] \\ &= \vec{P}^{(1)}(z, t) + \vec{P}^{(2)}(z, t) + \vec{P}^{(3)}(z, t) + \dots\end{aligned}\quad (2.1)$$

where $\chi^{(n)}$ is the n -th order susceptibility and $\vec{P}^{(n)}$ is the n -th order contribution to the polarization.

In centrosymmetric materials (such as bulk glasses) $\chi^{(2)} = 0$, therefore the main term among the nonlinear polarization terms is the third-order one. Therefore, neglecting higher-order terms, we may write the polarization as:

$$\vec{P}(z, t) = \epsilon_0 \left(\chi^{(1)} \vec{E}(z, t) + \chi^{(3)} \vec{E}^3(z, t) \right) \quad (2.2)$$

Recalling that the third-order nonlinear polarization in a four-wave mixing process has the form of eq. (1.39), in the degenerate case, where $A_1 = A_2 = A_3 = A_4 = A$ and $\omega_1 = \omega_2 = \omega_3 = \omega_4 = \omega_0$, it reads:

$$P_{\omega_0}^{(3)}(z, t) = \frac{3\epsilon_0\chi^{(3)}}{4} |A|^2 A e^{i(\omega_0 t - k_0 z)} + c.c., \quad (2.3)$$

The expression (2.2) can be rewritten as:

$$\vec{P}_{\omega_0}(z, t) = \epsilon_0 \left[\chi^{(1)} + \frac{3\epsilon_0\chi^{(3)}}{4} |A|^2 \right] \vec{E}(z, t) = \epsilon_0 \chi \vec{E}(z, t), \quad (2.4)$$

where

$$\chi = \chi^{(1)} + \frac{3\chi^{(3)}}{4} |A|^2, \quad (2.5)$$

Since the refractive index of the medium is $n = \sqrt{1 + \chi}$, defining n_0 as the unperturbed refractive index such that $n_0^2 = 1 + \chi^{(1)}$, we find:

$$n = \sqrt{1 + \chi^{(1)} + \frac{3\chi^{(3)}}{4} |A|^2} = n_0 \sqrt{1 + \frac{3\chi^{(3)}}{4n_0^2} |A|^2}, \quad (2.6)$$

Under the assumption $\frac{3\chi^{(3)}}{4n_0^2} |A|^2 \ll 1$, implying that the nonlinear term introduces a small correction with respect to n_0 , eq. (2.6) can be approximated to:

$$n \simeq n_0 + \frac{3\chi^{(3)}}{8n_0} |A|^2, \quad (2.7)$$

Taking into account the expression of the intensity as $I(z, t) = \frac{1}{2} c \epsilon_0 n_0 |A|^2$, we find:

$$|A|^2 = \frac{2I}{c \epsilon_0 n_0}, \quad (2.8)$$

We can now plug (2.8) in (2.7) finding:

$$n \simeq n_0 + \frac{3\chi^{(3)}I}{4c\epsilon_0 n_0^2} = n_0 + n_2 I, \quad (2.9)$$

where n_2 is the nonlinear refractive index coefficient, related to $\chi^{(3)}$ by the relation:

$$n_2 = \frac{3\chi^{(3)}}{4\epsilon_0 c n_0^2} \quad (2.10)$$

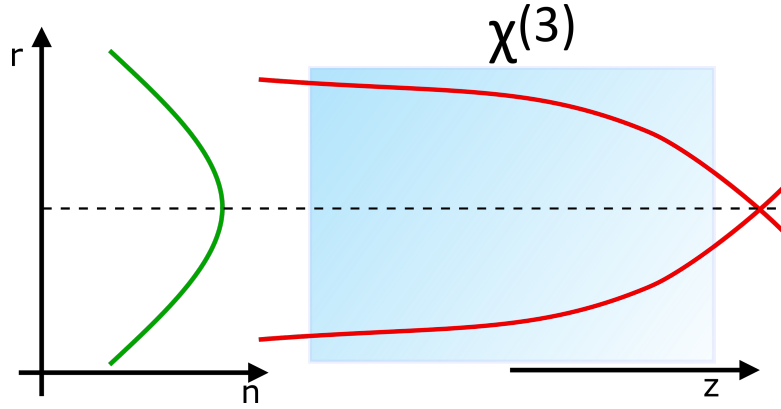


Figure 2.2: Schematic representation of Self-focusing. From the left, refractive index behavior variation in function of the radial coordinate; $\chi^{(3)}$ material with propagation along the z -axis highlighting the focusing of the beam.

The coefficient n_2 is positive for most of the dielectric media, determining that during the propagation a laser beam induces an increase of the refractive index of the medium proportional to the intensity. Hence, for a Gaussian beam with an intensity peak in the center, the beam is exposed to a higher index at the center and a lower index at the edges. Since the effect on the beam is similar to that of a lens, it is called *Kerr-induced self-focusing effect* (see Fig. 2.2). The self-focusing effect is a cumulative effect along the propagation as it makes the beam more intense in the center, enhancing the refractive index and in the absence of any saturation effect, self-focusing would end up in a catastrophic collapse at a finite propagation distance.

However, self-focusing always competes with diffraction [134]. Indeed, the intensity-dependent refractive index modifies the phase of the propagating beam but it is the action of diffraction which conveys the changes in the phase induced by nonlinearity and ultimately leads to self-focusing. In the case of a cylindrically symmetric Gaussian beam, the competition between diffraction and self-focusing is determined by the beam power. There is a critical value, called critical power P_{cr} at which diffraction and self-focusing nonlinearities are balanced. In this case, the beam shape remains fixed and the pulse is called *soliton* or *Townes mode*. The value of the critical power, derived using a model which takes into account only these two processes during the light-matter interaction, is [134]:

$$P_{cr} = \frac{3.72\lambda^2}{8\pi n_0 n_2} \quad (2.11)$$

The physical meaning of this power is that above P_{cr} , the Kerr nonlinearity overcomes diffraction and the beam shrinks upon itself and undergoes a collapsing singularity at a finite propagation distance, while below P_{cr} , diffraction overcomes self-focusing and the beam will spread.

2.3 Self-phase Modulation of Laser Pulses

Considering a time-dependent intensity profile, the refractive index varies also over time. The time dependence of the refractive index is responsible for a nonlinear change in the phase of the pulse which can be written as [102]:

$$\Phi_{nl}(t) = -\frac{\omega_o}{c} n_2 \int_0^L I(t, z) dz \quad (2.12)$$

where L is the propagation distance inside the medium. If the medium is short enough for the intensity variation along z to be negligible, the nonlinear phase becomes $\Phi_{nl}(t) = -\frac{\omega_o}{c} n_2 I(t) L$. It means that a nonlinear phase shift is accumulated during the pulse propagation. This is the reason why this effect is called *self-phase modulation*. It will result in a time-varying instantaneous frequency:

$$\omega(t) = \omega_0 + \delta\omega(t) \quad (2.13)$$

where $\delta\omega(t) = -(\omega_0 L/c) n_2 \partial I / \partial t$.

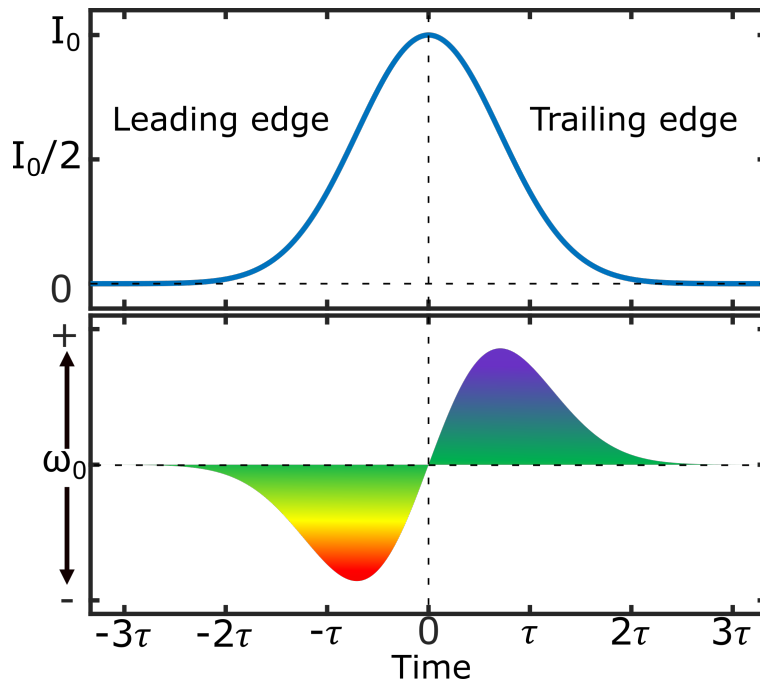


Figure 2.3: Self-phase modulation of a Gaussian pulse which produces a variation of the instantaneous frequency with time.

For a Gaussian laser pulse with intensity $I = I_0 \exp(-2t^2/\tau^2)$, where τ is related to

the pulse duration, the variation of the instantaneous frequency is:

$$\partial\omega(t) = 4\frac{\omega_0 L}{ct_p^2} n_2 I_0 t e\left(-\frac{2t^2}{\tau^2}\right) \quad (2.14)$$

The effect leads to the generation of new frequencies, leading to a negative shift of the instantaneous frequency at the leading edge of the pulse and a positive shift of the instantaneous frequency at the trailing edge of the pulse. So there will be a red-shifted spectral component at the pulse leading edge and a blue-shifted spectral component at the pulse trailing edge (see Fig. 2.3). Considering pure self-phase modulation, one notices that the same frequencies are generated at different times, so each color could give interference leading to modulation of the spectrum.

2.4 Nonlinear Absorption and Ionization

As reported in Section 2.2, as the beam self-focuses, its intensity increases and so does the nonlinear refractive index, resulting in an enhancement of the effect of self-focusing. If this process continued, it would result in a collapse of the beam. Nevertheless, this effect does not actually take place thanks to saturation processes such as multiphoton absorption and ionization, responsible for energy loss and generation of a free electron plasma, which further absorbs and defocuses the beam. The combination of self-focusing and saturation processes leads the intensity to a certain level called the *clamping intensity*. This quantity depends on the order of multiphoton absorption that is characteristic in each material and can be written as $K = 1 + \langle \frac{U_g}{\hbar\omega_0} \rangle$, where U_g is the bandgap and $\hbar\omega_0$ is the photon energy. The higher the order of multiphoton absorption, the higher the clamping intensity, thus leading to a wider spectral broadening. Hence, the broadest supercontinuum spectrum can be obtained for dielectrics with a wide bandgap [135, 136]. The typical values of clamping intensity in condensed media are of the order of a few TW/cm².

2.5 Plasma Effects

In presence of ionization of a dielectric medium, electrons are promoted from the valence band to the conduction band and this corresponds to the absorption of K photons with an energy larger than the bandgap. This process results in conduction electrons whose density transition rate varies in time proportionally to the K -th power of the laser intensity I [102]:

$$\frac{\partial\rho}{\partial t} = \frac{\beta_K}{K\hbar\omega_0} I^K \quad (2.15)$$

where β_K is the multiphoton absorption coefficient. The conduction electrons determine the variation of the refractive index of the material, according to the following relationship:

$$n = n_0 - \frac{\rho}{2n_0\rho_c} \quad (2.16)$$

where $\rho_c = \epsilon_0 m_e \omega_0^2 / e^2$ is the critical plasma density beyond which the plasma becomes opaque to an electromagnetic density at ω_0 . Considering a Gaussian beam, the plasma density is typically larger in the center of the beam compared to the tail. Therefore,

from Eq.2.16, it follows that there is a bigger reduction of the refractive index in the center of the beam. This means that the electrons in the conduction band will induce a phase curvature similar to that of a beam passing a defocusing lens. The overall effect is that the beam intensity decreases and its diameter increases leading to a so-called *plasma defocusing*.

Another effect, associated with plasma defocusing is the self-phase modulation induced by the plasma. Indeed, the nonlinear phase change is:

$$\phi_{nl}(t) = -\frac{\omega_0 L}{c} \frac{\rho(t)}{2n_0\rho_c} \quad (2.17)$$

Similar to the effect due to third-order nonlinearity, this nonlinear phase shift leads to a variation in time of the instantaneous frequency, that for a Gaussian beam is:

$$\delta\omega(t) = \frac{\omega_0 L}{c} \frac{\beta_K I_0^K}{K\hbar\omega_0 2n_0\rho_c} e^{-\frac{2Kt}{\tau^2}} \quad (2.18)$$

This effect is called *plasma-induced phase modulation* which gives rise to frequency changes that are all positive, so to a blueshift of the spectrum.

For the sake of completeness, we can provide a mathematical formula to express the clamping intensity. Combining the two expressions that determine variation in the refractive index because of self-focusing and saturation effects, we may write:

$$n_2 I_{cl} = \frac{\rho_{cl}}{2n_0\rho_c} \quad (2.19)$$

Assuming for simplicity a constant pulse with duration τ , the plasma density can be roughly written as $\rho = \beta_K (K\hbar\omega_0)^{-1} I_K t_p$, therefore the clamping intensity becomes:

$$I_{cl} = \left(\frac{2n_0 n_2 \rho_c K \hbar \omega_0}{\beta_K t_p} \right)^{\frac{1}{K-1}} \quad (2.20)$$

From Eq. 2.20, it is easy to understand that the clamping intensity depends on the material properties through the nonlinear index coefficient n_2 , on the multiphoton absorption coefficient β_K and on the number of photons absorbed K . The higher is the order of multiphoton absorption K the higher is the clamping intensity.

2.6 Chromatic dispersion

Another relevant phenomenon that comes into play when dealing with white-light generation is chromatic dispersion, which is due to the fact that waves of different frequencies travel at different velocities in a dielectric medium, resulting in the temporal spreading of the light pulse. Considering a medium with positive group delay dispersion, the fastest frequencies (low frequencies) will propagate in the leading edge of the pulse, while the slowest frequencies (high frequencies) in the trailing edge. In this case, the pulse is said to be positively chirped. Chromatic dispersion can also lead to a compression of the pulse if the pulse entering the medium is initially negatively chirped.

Chromatic dispersion is due to the dependence of the refractive index of the material n on the frequency ω . To quantify the chromatic dispersion, one can start by fitting the

2.7. Self-steepening and Space-Time Focusing

refractive index curve in the transparency region with the Sellmeier relations, which express the refractive index as a function of the wavelength:

$$n^2(\lambda) = a_0 + \sum_{j=0}^N N \frac{a_j \lambda^2}{\lambda_j^2 - \lambda^2}. \quad (2.21)$$

Chromatic dispersion can be classified as normal and anomalous dispersion. In order to distinguish them, the propagation constant of the pulse can be expressed as:

$$k(\omega) = n(\omega) \frac{\omega}{c} \quad (2.22)$$

By expanding it around the central frequency of the laser pulse ω_0 , one can write:

$$k(\omega) = k(\omega_0) + k'_0(\omega - \omega_0) + \frac{k''_0}{2}(\omega - \omega_0)^2 \quad (2.23)$$

where $k'_0 = \partial k / \partial(\omega)|_{\omega_0}$ is the inverse of the group velocity v_g and $k''_0 = \partial^2 k / \partial(\omega)^2|_{\omega_0}$ is the group velocity dispersion coefficient or GVD. For a given material, the region of normal dispersion corresponds to the positive value of GVD, where the red colors travel faster than the blue ones. Conversely, the region of anomalous dispersion corresponds to the negative value of GVD, where the blue components travel faster than the red ones. Chromatic dispersion has an important role in determining the spectrum of the supercontinuum, indeed the lower the chromatic dispersion the better the phase-matching condition for a broader range of spectral components, thus enabling the generation of light at many different colors.

2.7 Self-steepening and Space-Time Focusing

The combination of the nonlinear effects and chromatic dispersion gives rise to self-steepening. Indeed, the Kerr nonlinearity modifies not only the refractive index of the medium but also the group index, via the interplay with dispersion:

$$n^{(g)} = n_0^{(g)} + n_2^{(g)} \quad (2.24)$$

where $n_0^{(g)} = n(\omega_0) + \omega_0 dn/d\omega|_{\omega_0}$ and $n_2^{(g)}$ is proportional to n_2 and positive. As a result, the intense part of the pulse travels at a smaller velocity with respect to the low-intensity tail, resulting in a steepening of the trailing edge of the pulse.

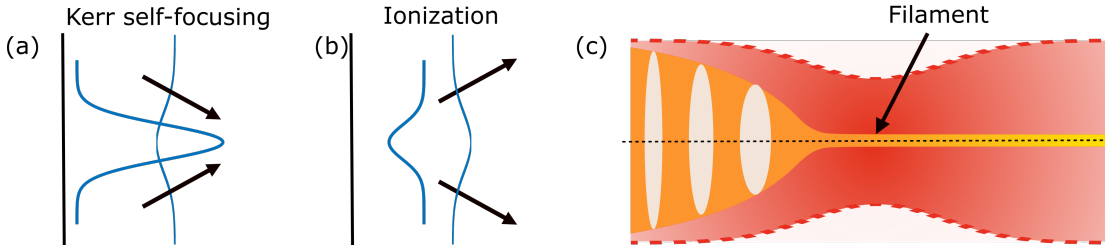


Figure 2.4: Schematic illustration of the filamentation process. (a) Self-focusing of a laser beam by optical Kerr effect. (b) Defocusing of the beam by the plasma. (c) Illustration of the collapse of the beam on itself by the Kerr effect leading to the ionization of the media with the consequent formation of a filament. Adapted from [137].

2.8 Femtosecond filamentation

Femtosecond filamentation refers to the ability of powerful femtosecond laser pulses to propagate nonlinearly over distances of several diffraction lengths in a medium with Kerr nonlinearity (see Fig. 2.4). The main process which leads to the generation of filamentation is self-focusing through which the laser beam gets narrow and intense enough to deposit its energy into a needle-shaped region along the propagation axis. Because of the strong light-matter interaction in this region, there could be the generation of an electron-hole plasma and the emission of new radiations.

One of the main proofs of femtosecond filamentation is represented by the conical emission of white light (see Fig.2.5). It is accompanied by axial supercontinuum generation. By looking at the laser beam cross-section one can observe that after the termination of the filament, it shows a white central spot surrounded by colored rings, whose wavelengths decrease from the center to the outer rings. Conical filamentation has been observed for filamentation in media of various natures and lasers of different central wavelengths.

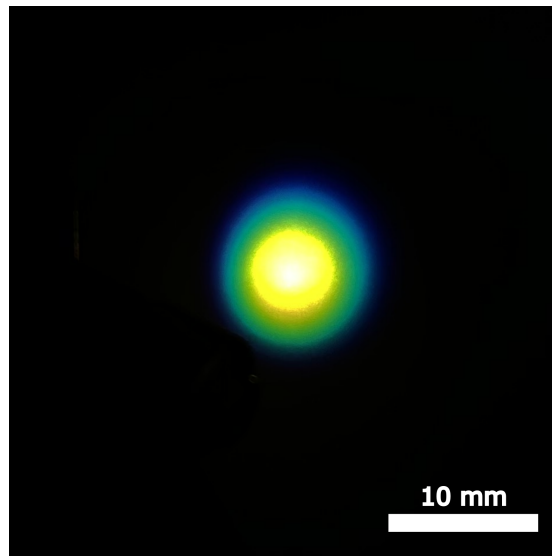


Figure 2.5: *Picture displaying the conical emission of the WLC generation in a 10-mm YAG crystal. Taken from the BCARS experimental setup described in this work.*

2.9 Conclusion

In light of the processes discussed in this chapter, supercontinuum generation [138] in bulk media is a rather complex physical phenomenon that involves many nonlinear optical processes. Indeed, the spectral broadening of a laser pulse impinging onto nonlinear crystal results from the interplay of nonlinear effects deriving from the interaction of the driving laser with a crystal. With self-focusing the beam size shrinks, leading to increased intensities. The increased intensity generates plasma, freeing electrons, which defocus the beam. When the plasma defocusing compensates for the self-focusing, a filament is created. During propagation, other nonlinear effects contribute to the broadening such as self-steepening that shortens the trailing edge of the pulse in time and

leads to a broadening towards shorter wavelengths.

CHAPTER 3

Experimental Setup and optical sources

This chapter will describe the main features of the BCARS experimental setup I designed and built during my Ph.D. The first version of the system enabled us to cover the fingerprint region of the vibrational spectrum ($500 - 1800 \text{ cm}^{-1}$) via the two-color mechanism. We employed this method to acquire the vibrational spectra of solvents, plastic spheres, and biological samples such as murine vertebrae slices. Despite the system showing very high performance in terms of acquisition speed and sensitivity, it was not possible to image plastic beads and biological samples covering also the CH-stretching region of the vibrational spectrum, because a good SNR of the spectra required high average power of the broadband Stokes beam that in most of the times led to damage of the scrutinized sample. This was one of the main reasons why I decided to find an optimal configuration of the optical sources to construct a system for imaging cells and tissues with a pixel dwell time down to 1 ms covering the full Raman spectrum ($500 - 3100 \text{ cm}^{-1}$). This configuration consists in a combination of both the excitation methods that have been widely discussed in Chapter 1 in section 1.4.3, namely the two-color and the three-color mechanism. The description of the experimental setup refers to this last configuration; however, the reader will be guided throughout the description of the next chapters to understand which configuration has been adopted for each result.

The main goal of this chapter is to provide the reader with a protocol to build a BCARS experimental setup. After describing the optical components that constitute the optical laser sources, the chapter will show a complete characterization of the pump and Stokes beam, concluding with a description of the microscope and of the employed detection system.

3.1 Experimental setup

A scheme of the BCARS system is shown in Fig. 3.1. The system starts with a commercial fiber-based ytterbium laser system (Monaco1035, Coherent) that delivers ≈ 270 fs pulses at 1035 nm wavelength with variable repetition rate and average power, which we fixed at 2 MHz and ≈ 6 W, respectively. A polarizing beam splitter divides the laser output into two branches. A half-wave plate mounted on a manual rotational stage controls the average powers of the two beams. We generate narrowband pump pulses with energy fluctuations < 1 % RMS by sending the first branch, with ≈ 2 W average power, to a high-finesse Fabry–Perot etalon (air-space etalon, SLS Optics), which allows reaching a spectral resolution of ≈ 9 cm^{-1} , that is sufficient to match the typical linewidths of vibrational Lorentzian peaks in condensed media [114]. The second replica, with ≈ 4 W average power, generates WLC in a 10 mm YAG crystal, used as broadband Stokes pulses.

For the WLC generation stage, the combination of a half-wave plate and a polarizing beam splitter cube is employed to finely tune the power impinging on the crystal. An iris is placed before the focusing lens to control the divergence of the beam driving the WLC. A 75-mm lens focuses the light onto the crystal, mounted on a single-axis translational stage, and a 75-mm achromatic doublet collimates the WLC. A long-pass filter (LP1050, Thorlabs) selects the red-shifted lobe of the WLC (1050 – 1600 nm), filtering out the fundamental beam and the blue-shifted components. An SF11 (60-cm tip-to-tip distance) prism pair compressor compensates for the chirp of the broadband beam ($\text{GDD} \approx 8000$ fs^2) introduced by its propagation through the optical path and the objectives. A homemade mask is used after the second prism of the compressor where all colors travel in parallel to finely select the bandwidth of the Stokes beam. The generated Stokes pulses feature a sub-20 fs pulse duration at the sample plane, after the illumination objective, and a bandwidth spanning 1200-1600 nm, adjustable according to the desired excitation mechanism and the application. Moreover, the source features signal stability comparable to that of the driving laser beam (< 1 % RMS).

The spatiotemporal overlap of the two pulse trains is realized by finely tuning a dichroic mirror (Di02-R1064-25x36, Semrock) and a mechanical delay line mounted in the pump path. The beams are then collinearly focused on the sample plane with a $100\times$ air objective (LCPLN100XIR, Olympus, numerical aperture (NA) = 0.85) and the transmitted B-CARS beam is collimated by an identical objective, through a homemade transmission microscope in up-right configuration. A good match between the spot size of the two beams and the dimension of the back aperture of the illumination objective is essential to avoid both losing powers before the samples and reducing the nominal NA of the employed objective, which implies a worst spatial resolution of the acquired images. While we can control the spot size of the broadband Stokes beam at the back aperture of the illumination objective by slightly tuning the position of the achromatic doublet, a telescope is needed to reduce the beam dimension of the pump beam that slightly diverges after several meters of propagation in the optical table. For these purposes, a 3:1 telescope is employed before the combiner.

The sample scanning is performed via two translational stages: PI-nano XYZ (P-545.3R8S, Physik Instrumente) and an XY motorized translation stage (U-780.DNS, Physik Instrumente), mounted one on top of the other. The former is used to finely ad-

just the position of the sample with respect to the focal spot in the X, Y, and Z directions, enabling it to move over a range of $200 \mu\text{m}$ along the three axes; the latter is used to perform the raster scanning of the sample over large areas (up to $\approx 2 \times 2 \text{cm}^2$, limited by the presence of the collection objectives that can hit the stage). The collimated beam, carrying the B-CARS signal relative to the illuminated pixel, is filtered through a short-pass filter (SP1000, Thorlabs) and focused onto the detection system with a 35 mm focusing lens (B-coated), consisting of a spectrometer with a 600 groves/mm grating (AC-TON SP2150, Princeton Instruments) and a front-illuminated CCD (BLAZE100HR, Princeton Instruments). The detection system is synchronized with the scanning stage through a custom-written Matlab interface, collecting hyperspectral images. The system enables us to scan the sample along the X-Y, X-Z, and Y-Z directions.

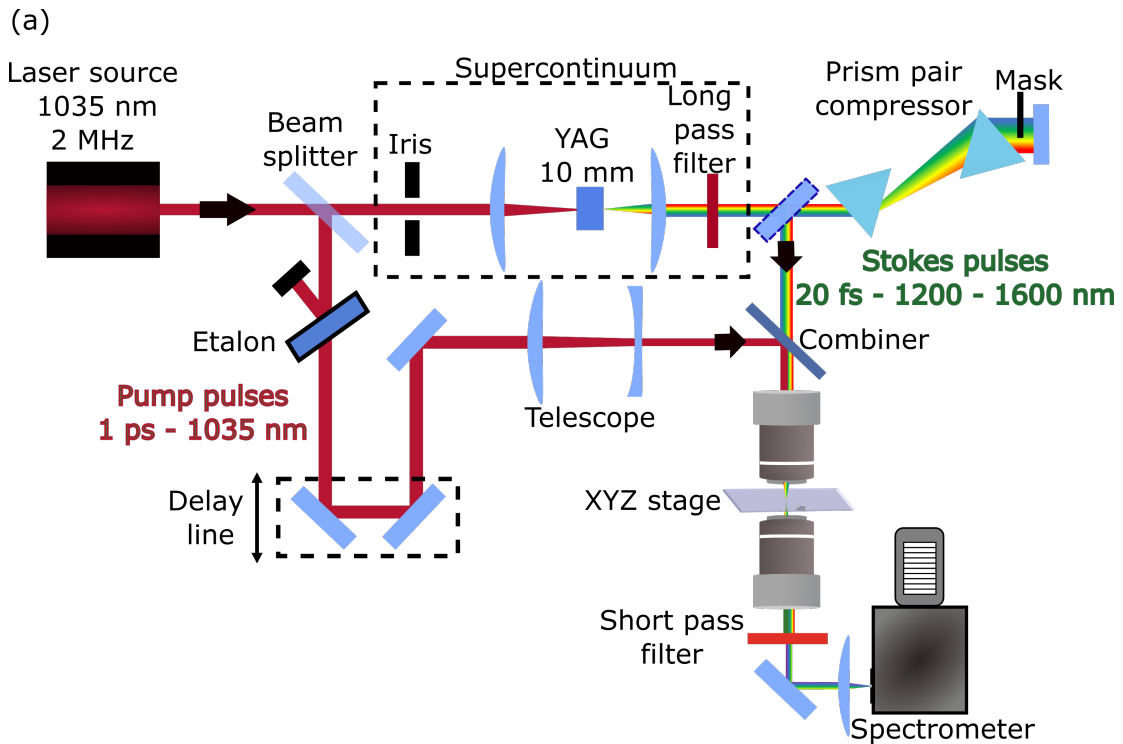


Figure 3.1: Schematic illustration of the BCARS experimental setup.

3.2 Advantages of the BCARS system

The main novelty of our BCARS microscopy system is the use of a low-repetition-rate (2 MHz) pulsed laser in the infrared. The majority of the systems based on nonlinear optical microscopy work with higher repetition rate ($\approx 40 - 80 \text{ MHz}$) fs or ps lasers [139]. Assuming a laser operating at 80 MHz and a pixel dwell time of $100 \mu\text{s}$, it implies that each pixel of the image is integrating 8000 pulses. Since nonlinear signals scale quadratically or cubically with the laser peak power, using a lower repetition rate and keeping fixed the average power and the pixel dwell time, one integrates a lower number of pulses to collect the signal from a single pixel but gain in sensitivity thanks to the higher pulse energy. In the case of the CARS signal, we know that:

$$I_{CARS} \propto |\chi_{VIB}^{(3)}|^2 I_P^2 I_S \quad (3.1)$$

Considering that the intensity of a laser pulse can be written as:

$$I = \frac{\epsilon}{\tau A} = \frac{P}{f\tau A} \quad (3.2)$$

where ϵ, τ , and A are the energy, pulse width, and focus area, respectively. The pulse energy can be also expressed in function of the average power P and repetition rate f as $\epsilon = P/f$. Hence, the CARS intensity reads as:

$$P_{CARS} = f\tau_a S A \cdot I_{CARS} \propto f\tau_a S A \cdot |\chi_{VIB}^{(3)}|^2 \left(\frac{P_P}{f\tau_P A} \right)^2 \left(\frac{P_S}{f\tau_S A} \right) \quad (3.3)$$

$$= |\chi_{VIB}^{(3)}|^2 \frac{P_P^2 P_S \tau_a S}{f^2 A^2 \tau_P^2 \tau_S} \propto \frac{1}{f^2} \quad (3.4)$$

Hence the average CARS signal scales inversely to the square of the repetition rate of the pulse laser. It demonstrates that a lower repetition rate determines a higher sensitivity of the system at a fixed pump and Stokes average power.

In light of this, the employment of a lowered repetition rate for BCARS unlocks three key advantages. The first one is the possibility to generate the broadband Stokes pulse through WLC generation in bulk crystal rather than PCF since it requires pulse energies of the order of $\approx 1\text{-}2 \mu\text{J}$, which can not be reached using a higher repetition rate laser since huge average powers would be needed. The possibility of generating WLC allows us to create a more compact, robust, simple and alignment-insensitive CARS setup that can be used for very long acquisition time without signal degradation because of the excellent long-term stability of the broadband laser source [102]. The second advantage relates to the fact that a repetition rate of 2 MHz allows a temporal delay of 0.5 μs between two consecutive pulses, leaving more time to the system for thermal energy dissipation, thus reducing photothermal damage [103]. Eventually, as we have shown above through the mathematical derivation, for a given average power at the focus, limited by sample degradation, a stronger BCARS signal can be obtained since higher pulse energy results in higher peak intensity. The higher sensitivity of our system entails higher acquisition speed and/or SNR of the acquired spectra.

Thanks to all these details, I will show in chapter 5 that our BCARS microscope delivers high-quality images at state-of-the-art acquisition speed ($< 1 \text{ ms/pixel}$), limited by the spectrometer refresh rate. Moreover, it features unprecedented specificity and sensitivity when detecting DMSO in a binary solution with water.

Another important key point of the setup is the operating range of wavelengths. Indeed, we employ optical sources in a red-shifted spectral region (1035 nm for the pump and 1050 - 1600 nm for the Stokes beam), while standard CARS setups operate with wavelengths of 800 nm for the pump and 830 - 1000 nm for the Stokes. This characteristic of the optical setup enables us to use higher laser intensities on the sample before the onset of photo-damage [140], thanks to a reduced multi-photon absorption from cell/tissue pigments and especially DNA. Nevertheless, the use of longer wavelengths for the pump and Stokes beam generate anti-Stokes components in a region of the spectrum (800 - 1000 nm) where most of the CCD sensor feature lower quantum efficiency.

However, this is not an issue, since, with respect to old CCD sensors that were front illuminated, new CCD sensors present a back-illuminated configuration guaranteeing an enhanced quantum efficiency and better performances thanks to a thick substrate of silicon. Moreover, new devices, such as the one we are employing (BLAZE HR, Princeton Instruments), are characterized by a technology that suppresses to its minimum the etaloning, which is the problematic appearance of fringes caused by constructive and destructive interference in back-illuminated sensors.

Eventually, one of the main key features of the setup is the possibility to change the parameters of the broadband Stokes beam, such as its average power, its polarization, its pulse duration, and its spectral bandwidth, thus enabling the user to use only the two-color CARS mechanism or both three-color and two-color CARS. Moreover, we can rotate the polarization and vary the average power of the pump beam. All this degree of freedom makes the system versatile depending on the application. Indeed it allows us to do polarization-sensitive measurements where an analyzer is needed for selecting the polarization of the anti-Stokes component; to investigate only the fingerprint region of the vibrational spectrum discarding the portion relative to the silent and the CH-stretching region; to perform time-delayed CARS measurements mainly used for spectroscopic applications.

3.3 Characterization of the optical sources

This section will briefly describe the sources employed for the BCARS experiments. In particular, I performed autocorrelation measurements, using a home-built second-harmonic generation frequency-resolved optical gating (SHG-FROG) setup equipped with a spectrometer (Ocean Optics USB2000-UV+VIS-ES). I will start with a brief description of the FROG setup and then present the autocorrelation measurements of the pump and Stokes pulses.

3.3.1 Theory and experimental setup for SHG-FROG

The BCARS experimental setup presented above deals with ultrashort laser pulses of the order of tens of femtoseconds or of a few picoseconds. Measurements of pulses on these time scales are an important issue since the speed required is considerably faster than that of existing photodetectors and oscilloscopes. There are several methods that allow us to resolve femtosecond pulses. Some of them are the so-called correlation measurements, which are widespread experimentally but which offer only partial information about the optical pulse. Other available techniques are the one based on frequency-resolved optical gating [141] (FROG), which are particularly robust and offer a complete characterization of a pulse, retrieving the electric field in time $E(t)$.

In a FROG experiment, one measures the spectrogram of the field $E(t)$ [142]. Such measurement requires an ultrafast gate function through which the spectrogram of the field can be reconstructed. In FROG, as in other ultrashort pulse characterization methods, the pulse is used to gate itself via a nonlinear optical interaction. Indeed, by changing the delay between the pulse-gate and the pulse itself with a motorized translational stage, it is possible to acquire for a given delay the spectrum of the gated signal [143]. If we define the electric field of the pulse as a function of time t as $E(t)$ and the one of the delayed pulses as $E(t - \tau)$ with τ the delay between the two pulses, the gated

signal is:

$$E_{gated}(t, \tau) = E(t)E(t - \tau) \quad (3.5)$$

and the correspondent spectrogram, describing the evolution of the spectral content of the gated signal as a function of the delay τ , is defined as the square modulus of the time Fourier transform of the gated function:

$$\begin{aligned} S_{FROG}(\omega, \tau) &= \left| \int_{-\infty}^{+\infty} E_{gated} e^{-i\omega t} dt \right|^2 \\ &= \left| \int_{-\infty}^{+\infty} E(t)E(t - \tau) e^{-i\omega t} dt \right|^2 \end{aligned} \quad (3.6)$$

The pulse duration can be retrieved from the intensity autocorrelation plot. Indeed, by integrating the spectrogram along the frequency domain, one obtains the intensity plot as a function of the delay τ . Once the intensity autocorrelation has been retrieved, it can be fitted with a Gaussian or with the squared of a hyperbolic secant. The pulse duration Δt_{pulse} will be related to the full width at half maximum (FWHM) of the intensity autocorrelation according to:

- for a Gaussian fit:

$$\Delta t_{pulse} = \frac{\Delta t_{AC}}{1.44} \quad (3.7)$$

- for a $sech^2(\cdot)$ fit:

$$\Delta t_{pulse} = \frac{\Delta t_{AC}}{1.55} \quad (3.8)$$

There are many ways to implement a FROG set-up, such as polarization-gating FROG [144] or Self-diffraction FROG [145], which offer reliable results but are cumbersome to implement. On the other hand, Non-collinear SHG-FROG offers the best trade-off between robustness and practical implementation. The geometry which is used in SHG-FROG is similar to the noncollinear SHG intensity autocorrelation setup, where a spectrometer is used in place of a single-pixel photodiode.

The spectrogram in Eq.3.6 is a symmetric function of τ , that is:

$$S_{FROG}(\omega, \tau) = S_{FROG}(\omega, -\tau) \quad (3.9)$$

The symmetry derives from the fact that the pulse and the gating function are identical and therefore one cannot establish whether the pulse is ahead of the gating function or the gating function is ahead of the pulse.

A further consequence of Eq.3.6 is that the fields $E(t)$ and $E(-t)$ have identical SHG-FROG traces. Moreover, measuring the traces of a transform-limited Gaussian pulse or of a linearly chirped Gaussian pulse, one can notice that there are qualitative differences between the two traces since as the chirp is increased, the trace gets wider along the axis relative to the delay τ . Nevertheless, identical traces are obtained for equal-magnitude positive and negative linear chirps. This last feature illustrates the main disadvantage of SHG-FROG: the inability to determine the sign of a chirp.

As already pointed out, FROG measurements are particularly useful to reconstruct the pulse both in terms of amplitude and phase. Indeed, if the gated signal $E_{sig}(t, \tau)$ is known, $E(t)$ can be obtained by direct integration:

$$\int E_{sig}(t, \tau) d\tau = \int E(t)g(t - \tau)d\tau \approx E(t) \quad (3.10)$$

Therefore, the problem is how to determine the signal $E_{sig}(t, \tau)$. In order to do it, it is possible to express the FROG trace in terms of $\tilde{E}_{sig}(t, \Omega)$, which is the Fourier transform of $E_{sig}(t, \tau)$ with respect to τ :

$$S_{FROG}(\omega, \tau) \approx \left| \tilde{E}_{sig}(t, \Omega) e^{-i\omega t} \right|^2 \quad (3.11)$$

where

$$\tilde{E}_{sig}(t, \Omega) = \int E_{sig}(t, \tau) e^{-j\Omega\tau} d\tau \quad (3.12)$$

Eq. 3.11 represents a phase-retrieval problem, since the main purpose is to recover $\tilde{E}_{sig}(t, \Omega)$ and hence $E_{sig}(t, \tau)$ from its two-dimensional power spectrum. While this problem does not have a unique solution in a one-dimensional frame, it turns out that in a two-dimensional one it is possible almost always to recover a unique solution.

Trebino and co-workers have published several algorithms for recovering the electric field profile from FROG data [146]. Indeed, there is no possibility of reconstructing the pulse directly, but in an indirect way using an iterative algorithm (see Fig. 3.2).

The algorithm may be divided in several steps:

- The first step consists in guessing the function $E(t)$;
- Then we multiply it for the gate function $g(t - \tau)$ thus finding $E_{sig}(t, \tau)$;
- Then we do the Fourier transform with respect to t , obtaining $\tilde{E}_{sig}(\omega, \tau)$;
- At this point, one applies the experimental data by replacing the magnitude of $\tilde{E}_{sig}(\omega, \tau)$ with the magnitude retrieved from the FROG measurement while leaving its phase unchanged, that is:

$$\tilde{E}_{sig}(\omega, \tau) \rightarrow \frac{\tilde{E}_{sig}(\omega, \tau)}{\left| \tilde{E}_{sig}(\omega, \tau) \right|} \sqrt{S_{FROG}(\omega, \tau)} \quad (3.13)$$

- Obtained the new value of $\tilde{E}'_{sig}(\omega, \tau)$, one computes its inverse Fourier transform with respect to ω to get a new $E'_{sig}(t, \tau)$
- Eventually, one integrates it with respect to τ , thus obtaining an estimate of $E(t)$ which is called $E'(t)$ that is then compared to the guessed $E(t)$. This step completes one iteration.

The algorithm continues by using the updated version of $E(t)$ until the solution converges.

One way to check for convergence is to compare the results corresponding to iteration k , that is $E^{(k)}(t)$ and $\tilde{E}^{(k)}_{sig}(\omega, \tau)$ with that of the previous iteration. Another way

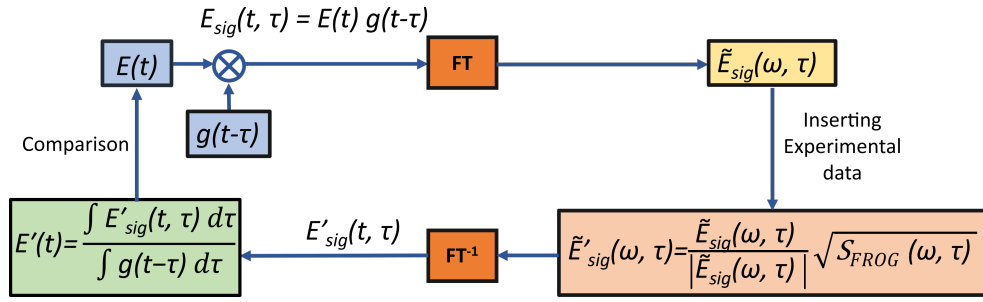


Figure 3.2: Iterative Fourier transform algorithm for retrieving the ultrashort-pulse amplitude and phase from FROG Data.

is to compute the error between the computed and experimental values. Since $E(t)$ is not known directly from the experiments, one cannot compute the error in $E^{(k)}(t)$. However, one can use $\tilde{E}_{sig}^{(k)}(\omega, \tau)$ for comparison with actual FROG data. In particular, the RMS FROG error is defined by [143]:

$$\epsilon_{FROG} = \left\{ \frac{1}{N^2} \sum_{i=1}^N \left[S_{FROG}^{(k)}(\omega_i, \tau_i) - S_{FROG}(\omega_i, \tau_i) \right]^2 \right\}^{1/2} \quad (3.14)$$

where $S_{FROG}^{(k)}(\omega, \tau) = \left| \tilde{E}_{sig}^{(k)}(\omega, \tau) \right|^2$. The algorithm should run until the FROG error cannot be made any smaller.

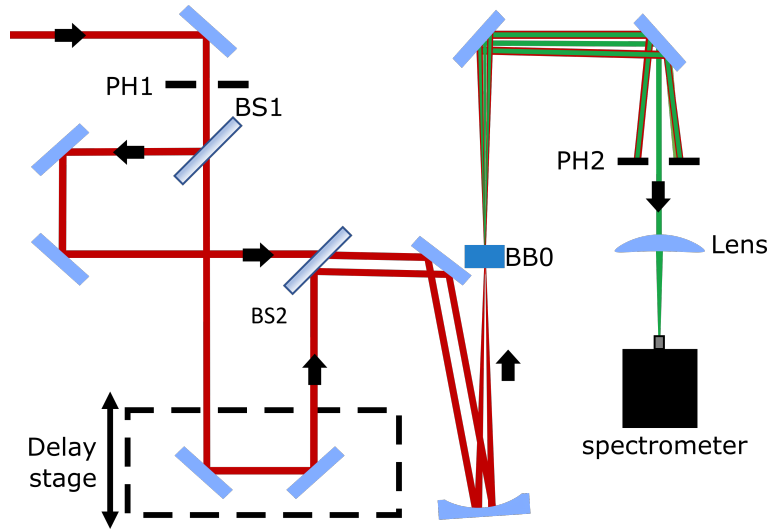


Figure 3.3: Experimental setup for SHG-FROG. PH: pinhole, BS: Beam splitter.

The experimental setup employed for the FROG data is schematically shown in Fig. 3.3. The input beam is divided into two replicas by a first beam splitter. One of the two replicas is delayed using a mechanical delay stage. Then, the beams are combined using another beam splitter. A concave mirror focalizes them onto a second SHG crystal, in our case a BBO. After the BBO, under proper phase matching conditions, the second harmonic generation beams travel on top of the original beam, while, when the two replicas overlap in time, a third beam appears in the middle of the two replicas. This

beam corresponds to the sum frequency generation (SFG) beam. A pinhole blocks the SHG and the fundamental beams, letting the SFG beam pass and travel toward a spectrometer where the beam is focused via a 50 mm plano-convex lens. By scanning the delay line, one may acquire the spectrum of the SFG beam as a function of the delay, reconstructing the spectrogram of the pulses.

3.3.2 Pump pulses

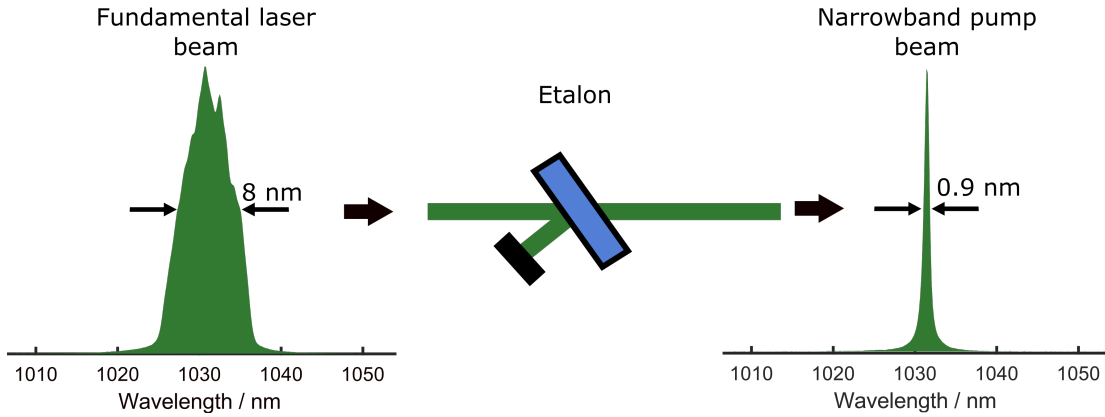


Figure 3.4: Schematic representation of the generation of the narrowband pump pulses through the etalon.

I first characterized the pump pulses of the system, measuring the spectrum and reconstructing its temporal shape using the SHG-FROG setup, by focusing the two replicas on a 1 mm BBO crystal. The fundamental laser beam at 2 MHz repetition rate has a full width at half maximum (FWHM) of 8 nm and is centered at 1033 nm (Fig. 3.5.(d)). To estimate the pulse duration and profile we performed an SHG-FROG on the fundamental laser beam. The measured spectrogram is reported in Fig. 3.5.(a). From it, we derived the intensity autocorrelation through which we estimated the pulse duration which is ≈ 270 fs (Fig. 3.5.(b)) and reconstructed the pulse temporal profile (Fig. 3.5.(c)).

The driving laser is sent to an etalon to generate narrowband laser pulses (Fig. 3.4). For this purpose, I used two different etalons in the experiments I carried out during my Ph.D. activity. In the very first configuration, I used an etalon with a free spectral range of $(\Delta\lambda)_{fsr} = 29.814$ nm and a reflectance of $R = 90\%$. Knowing these parameters, it is possible to estimate the FWHM of the narrowband output beam, that is $(\Delta\lambda)_{min}$, which can be calculated using the characteristic equations of a Fabry-Perot Cavity. Indeed, for a Fabry-Perot interferometer, one defines the *Finesse* as:

$$\mathcal{F} = \frac{(\Delta\lambda)_{fsr}}{(\Delta\lambda)_{min}} = \frac{\pi\sqrt{F}}{2}. \quad (3.15)$$

with F the *coefficient of finesse* defined as:

Pump before etalon

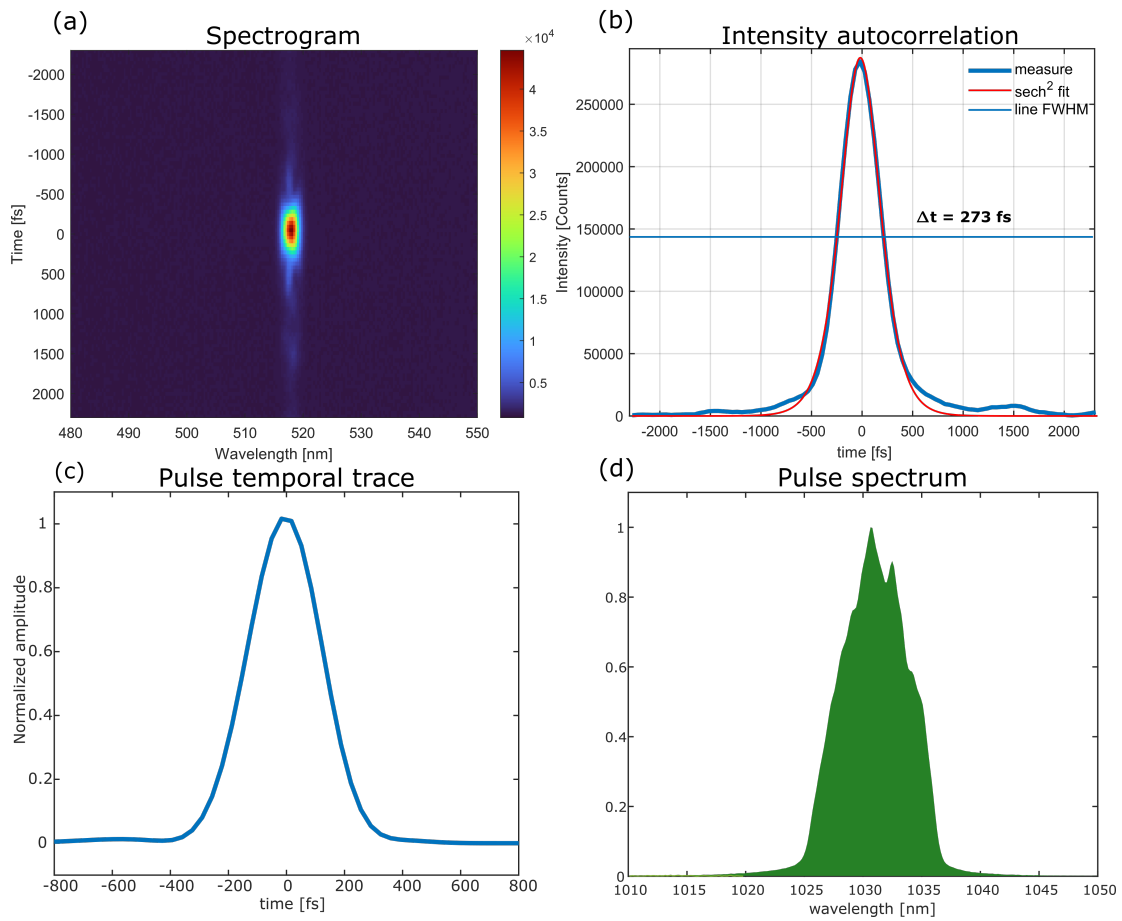


Figure 3.5: Characterization of the pump pulses before the etalon. (a) Spectrogram acquired with the SHG-FROG experimental setup employing a 1mm-BBO crystal for SFG. (b) Intensity autocorrelation reconstructed from the spectrogram in (a). (c) Pulse temporal trace obtained through the iterative algorithm. (d) Spectrum of the pump pulses measured with the same spectrometer used for CARS experiments.

3.3. Characterization of the optical sources

$$F = \frac{4R}{(1 - R)^2} \quad (3.16)$$

From these parameters, $(\Delta\lambda)_{min} \approx 1$ nm. By characterizing through an SHG-FROG the narrowband pulses using this etalon, we obtained the spectrogram in Fig. 3.6.(a) that gives us autocorrelation intensity and pump pulses temporal trace shown in panel (b) and (c). The estimated pulse duration is 1.18 ps. The spectrum of the narrowband pulses employed for CARS experiments is shown in Fig. 3.6.(d). It features a FWHM lower than 1.1 nm, guaranteeing a spectral resolution below 11 cm^{-1} , matching the typical vibrational lineshape in the active Raman region for condensed media [114].

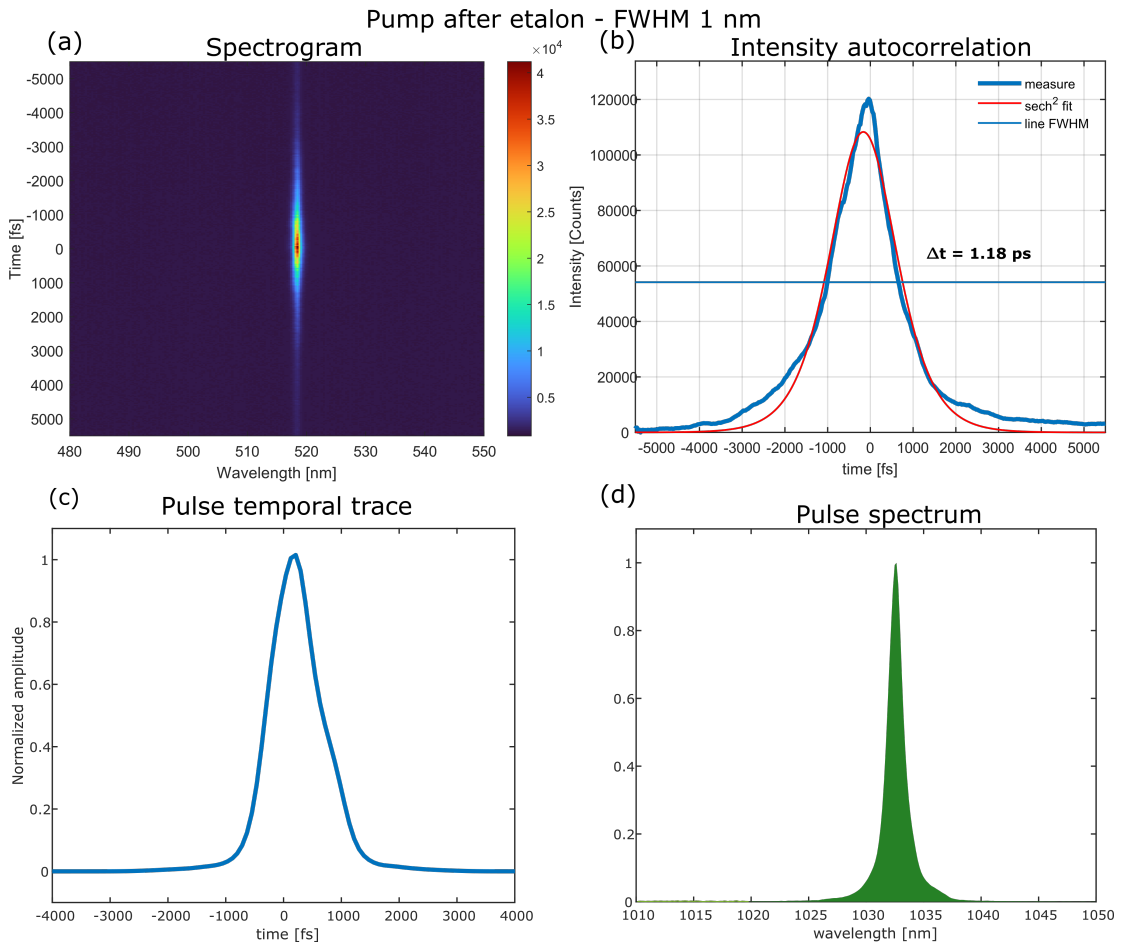


Figure 3.6: Characterization of the pump pulses after the etalon with $(\Delta\lambda)_{f_{sr}} = 29.814$ nm and $R = 90\%$. (a) Spectrogram acquired with the SHG-FROG experimental setup employing a 1mm-BBO crystal for SFG. (b) Intensity autocorrelation reconstructed from the spectrogram in (a). (c) Pulse temporal trace obtained through the iterative algorithm. (d) Spectrum of the pump pulses measured with the same spectrometer used for CARS experiments.

The second etalon we used was characterized by $(\Delta\lambda)_{f_{sr}} = 15.4$ nm and reflectance of $R = 92\%$. The calculated $(\Delta\lambda)_{min}$, in this case, is 0.4 nm, while the pulse duration measured with SHG-FROG is 3.74 ps, as reported in Fig. 3.7.(a-b). The pulse profile has been retrieved through the iterative approach for pulse reconstruction in FROG experiments (Fig. 3.7.(c)).

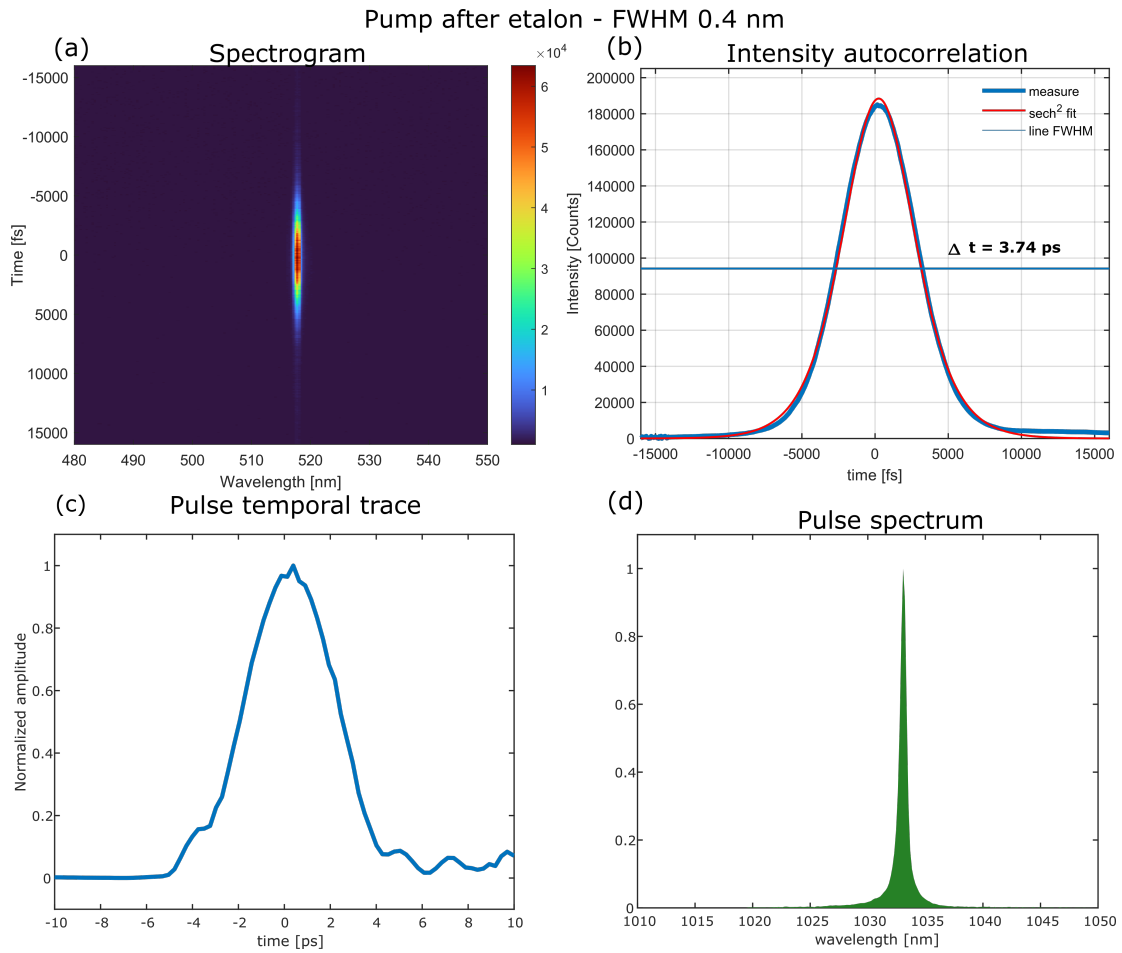


Figure 3.7: Characterization of the pump pulses after the etalon with $(\Delta\lambda)_{f_{ST}} = 15.4$ nm and $R = 92\%$. (a) Spectrogram acquired with the SHG-FROG experimental setup employing a 1mm-BBO crystal for SFG. (b) Intensity autocorrelation reconstructed from the spectrogram in (a). (c) Pulse temporal trace obtained through the iterative algorithm. (d) Spectrum of the pump pulses measured with the same spectrometer used for CARS experiments.

3.4 Stokes pulses

Broadband Stokes pulses are generated through white-light supercontinuum in bulk media. For this purpose, I employed a 10-mm YAG crystal, thus obtaining broadband spectra spanning from 1050 to 1600 nm (Fig. 3.8). I characterized the broadband Stokes pulses in 3 different cases: (i) after their generation and after an achromatic doublet with coating C and 75 mm focal length used for collimating the beam; (ii) after the prism compressor with 60 cm tip-to-tip distance of the prisms; (iii) after the prism compressor and 2.54 cm piece of glass to simulate the presence of the glass objective and estimate whether the pulses arrive at the sample plane well compressed or not.

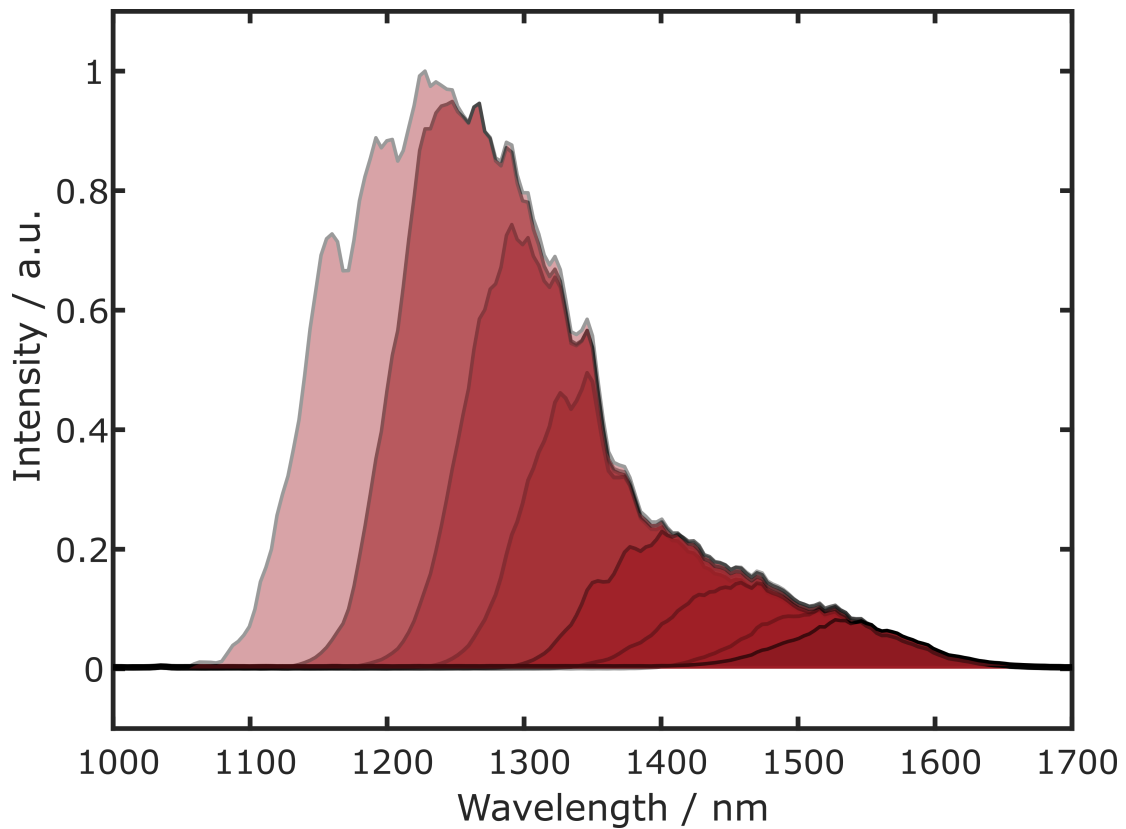


Figure 3.8: Spectra of the WLC generation in a 10 mm YAG crystal at 8 different positions of the mask inserted in the prism compressor stage.

We first estimated the pulse duration of the generated supercontinuum through the SHG-FROG experimental setup using a 300 μm -thick BBO crystal. For all the FROG measurements, we employed a thinner SHG crystal since we need a broader gain bandwidth to fully characterize the Stokes spectrum. We considered the whole supercontinuum after the collimating achromatic doublet and a long pass filter (FELH1050, Thorlabs) that removed the fundamental laser pulses. From the measured spectrogram (Fig. 3.9.(a)), we integrated along the wavelength axis to obtain the intensity autocorrelation (Fig. 3.9.(b)) and using a fitting with the squared hyperbolic secant we estimated a pulse duration of 317 fs, comparable to the duration of the pump beam. We also estimated the temporal profile as shown in Fig. 3.9.(c). In this case, we knew it was

Chapter 3. Experimental Setup and optical sources

positively chirped, so to compress this beam and avoid temporal chirp in the CARS spectra, a prism compressor was needed. The prism compressor should compensate not only for the positive dispersion introduced by propagation in free space and in the optics of the generation stage but also for the presence of the bulk glass of the illuminating microscope objective. The main aim of the compressor is to introduce a negative GDD so that it arrives compressed at the sample plane.

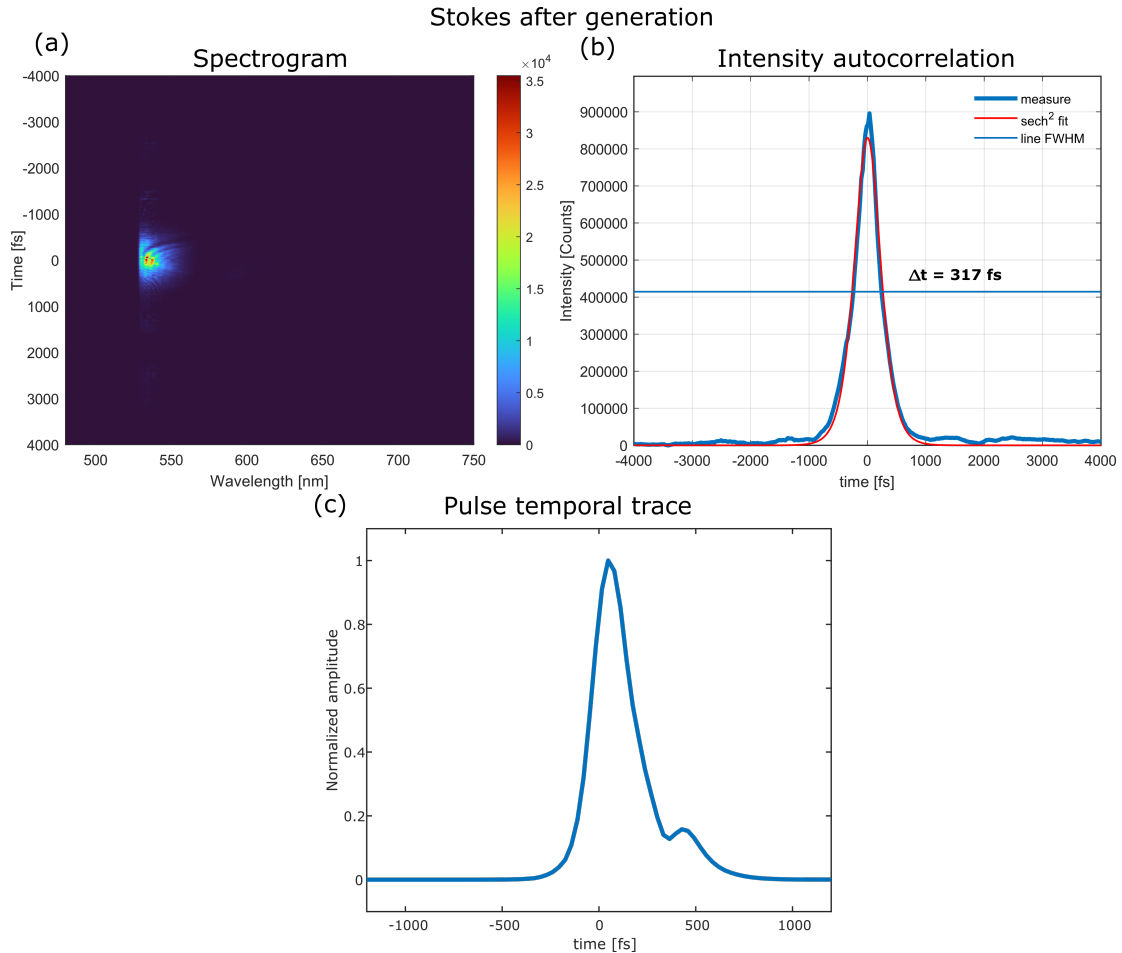


Figure 3.9: Characterization of the Stokes pulses after their generation and collimation with a 75 mm achromatic doublet. (a) Spectrogram acquired with the SHG-FROG experimental setup. The SFG was obtained by focusing the beams on a 300 μm -thick BBO crystal. A thinner crystal, with respect to the pump pulse measurements, is needed to satisfy the phase-matching condition for a broader bandwidth. (b) Intensity autocorrelation reconstructed from the spectrogram in (a). (c) Pulse temporal trace obtained through the iterative algorithm.

I estimated the group delay dispersion (GDD) of the microscope objective and of the other optics in the optical setup approximately equal to 8000 fs². This number has been obtained by recording CARS spectra at different delays between the pump and the Stokes beam and then measuring the difference in time between the arrival of the blue-shifted and red-shifted colors of the Stokes beam that generate respectively the low energy Raman modes and the high energy Raman modes. Since the pulse spectrum is particularly broad, with a bandwidth $\simeq 500$ nm, the Stokes pulses are particularly sensitive to GDD and would reach a FWHM of more than 3 ps without

compression. Therefore, I designed a 60 cm tip-to-tip prism compressor whose main

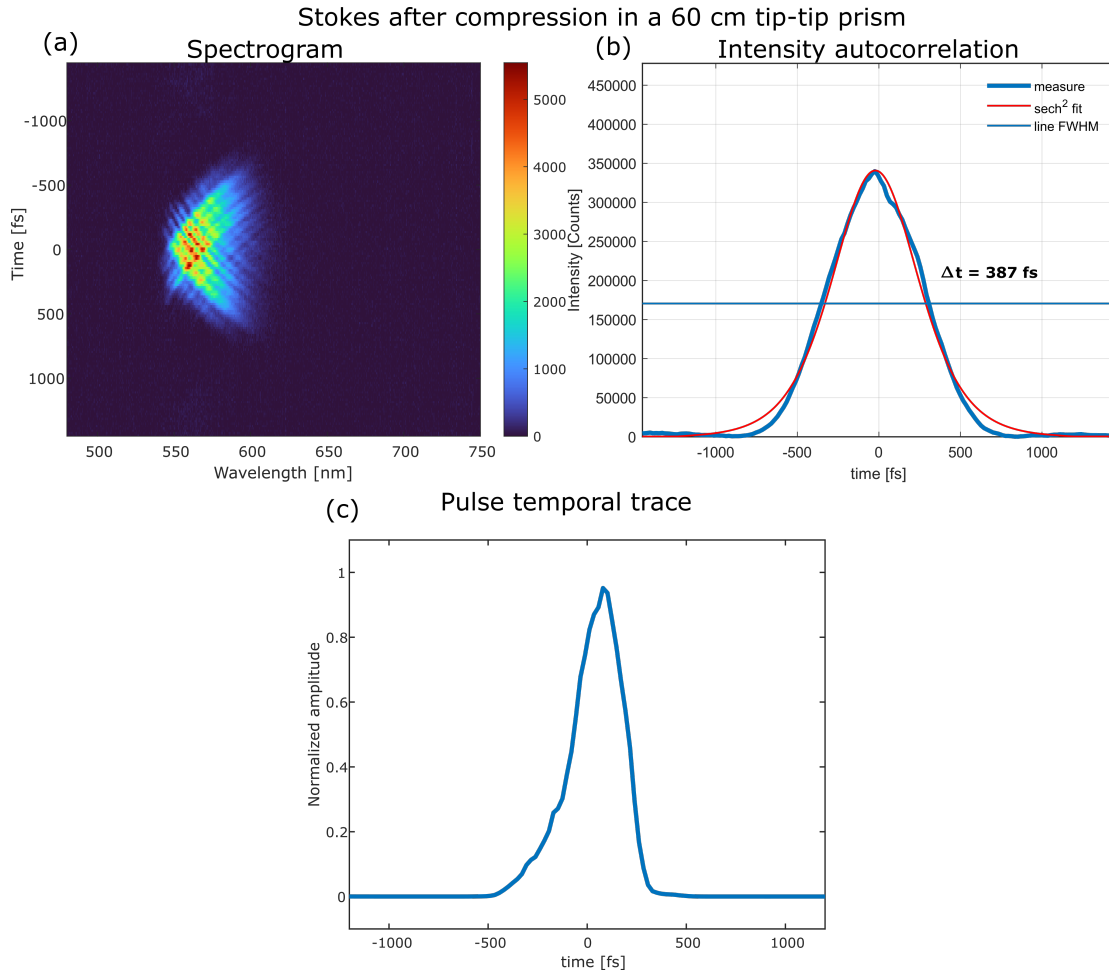


Figure 3.10: Characterization of the Stokes pulses after the compression with a 60 cm tip-to-tip prism compressor. The SFG was obtained by focusing the beams on a 300 μm -thick BBO crystal. (a) Spectrogram acquired with the SHG-FROG experimental setup. (b) Intensity autocorrelation reconstructed from the spectrogram in (a). (c) Pulse temporal trace obtained through the iterative algorithm.

aim was to compress the pulses so that after this stage they feature a negative chirp. In this way, it is possible to have very short pulses at the sample plane with $\text{GDD} \simeq 0$. Soon after this stage, we performed an SHG-FROG experiment, by acquiring the spectrogram of the broadband compressed pulses (Fig. 3.10.(a)) and retrieving the intensity autocorrelation (Fig. 3.10.(b)). By fitting this trace with a squared hyperbolic secant, we derived a pulse duration of 387 fs, confirmed also by the reconstructed temporal trace in Fig. Fig. 3.10.(c).

However, the FROG measurement does not allow us to know whether we introduced a positive or negative GDD. Therefore, in order to be sure it was negatively chirped and that the introduced negative GDD was enough to have short pulses at the sample plane for impulsive CARS generation, we inserted a 2.54-cm thick rod of glass. This piece of glass simulates the presence of the microscope objective. Indeed, it was not possible to directly measure the pulse duration at the sample plane for two main practical reasons:

(i) the beam is not collimated after the microscope objective; (ii) the microscope was too compact that was not easy to guide the beam till the SHG-FROG setup even after a very thin collimating lens.

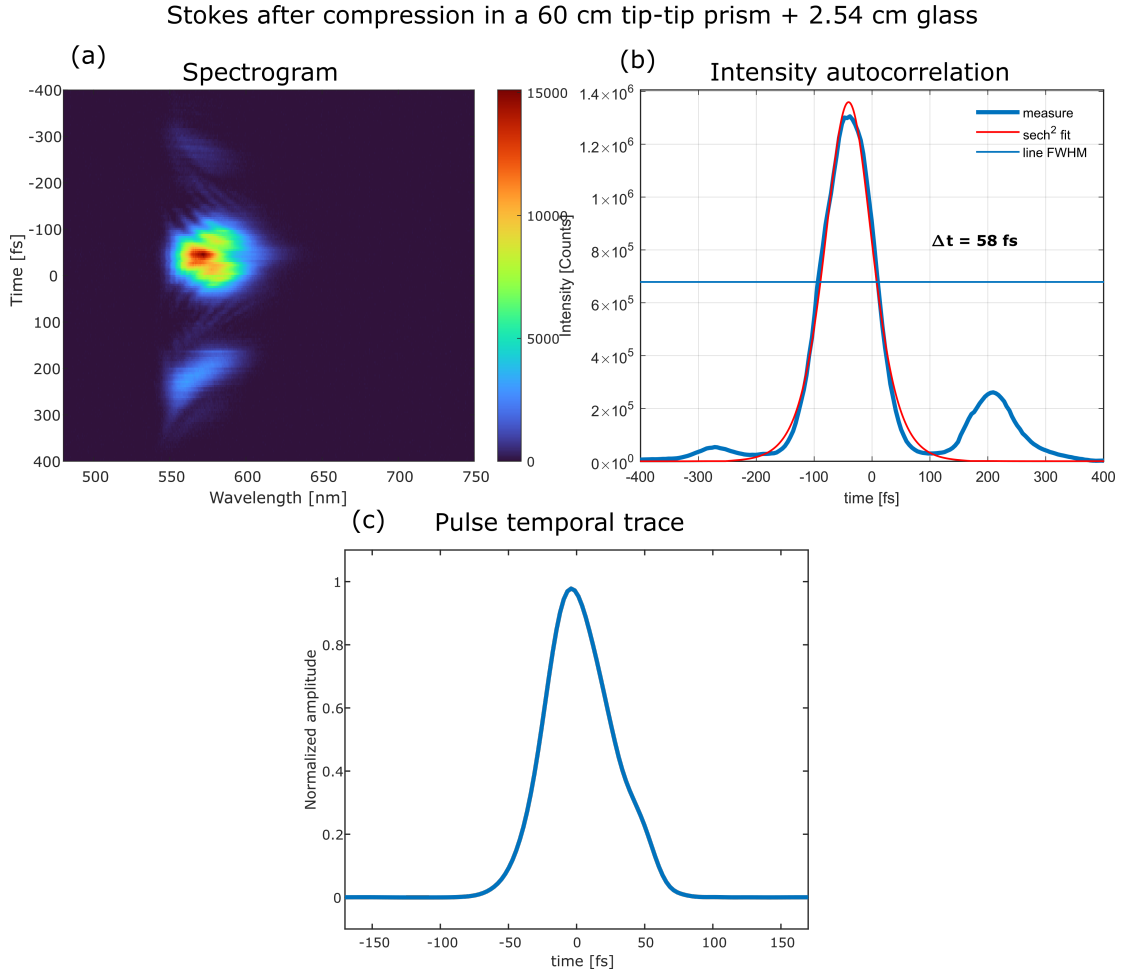


Figure 3.11: Characterization of the Stokes pulses after the compression with a 60 cm tip-to-tip prism compressor and 2.54 cm rod of glass. The SFG was obtained by focusing the beams on a 300 μm -thick BBO crystal. (a) Spectrogram acquired with the SHG-FROG experimental setup. (b) Intensity autocorrelation reconstructed from the spectrogram in (a). (c) Pulse temporal trace obtained through the iterative algorithm.

After propagating through a normally dispersive medium, the Stokes pulse results are compressed in time, with a pulse duration of 58 fs (Fig. 3.11). Thus, the hypothesis of negative GDD after the prism compressor is confirmed, and we expect a similar pulse duration at the sample plane. It can be observed that a pre-pulse and a post-pulse appear, respectively at the leading and trailing front of the pulse intensity autocorrelation, and they can be observed in the spectrogram as well for positive and negative times. The presence of these anomalies is due to the double reflection inside the piece of glass, which gives rise to a replica of the Stokes pulse, causing an unexpected SFG at positive and negative delays. Since the autocorrelation in non-collinear SHG-FROG should be symmetric with respect to the time delay, any asymmetry can be associated with experimental inaccuracies.

3.5 Microscope

After their generation, the pump and Stokes trains of pulses are combined through a dichroic mirror (Di02-R1064-25x36, Semrock) and sent to a tailor-made microscopy unit (Fig. 3.12). I designed the microscope with an upright configuration [147]. The beams travel together going from the top to the bottom. They are focused on the sample using a high NA air objective (Olympus LCPLN100XIR, NA = 0.85) mounted on an XYZ mechanical axis. The transmitted B-CARS beam is collimated by an identical objective, mounted on another XYZ mechanical stage.

The sample stage consists of two translational stages: an XYZ and an XY motorized translation stage. Their combination allows the user to move the sample, find the perfect focal plane, and perform imaging using raster scanning. I mainly use the microscopy unit working in transmission and sending to the detection unit the forward CARS signal. I also equipped the microscope with an epi-detection line inserting before the first objective a dichroic mirror (DMLP1000R). The dichroic mirror transmits the pump and Stokes beam, while it reflects the anti-Stokes components that are generated below 1000 nm. The epi-CARS signal is delivered through the detection unit using a periscope.

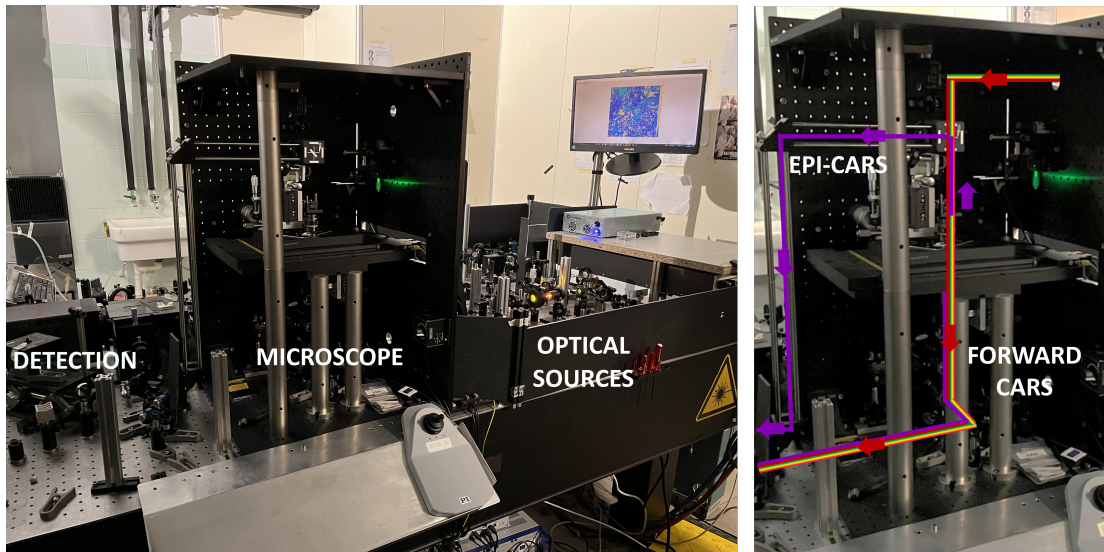


Figure 3.12: Photos of the experimental BCARS microscopy setup, highlighting the optical sources stage, the microscopy unit, and the detection part. The microscopy unit works in an up-right configuration and enables us to collect signals both in the epi and in the forward configuration.

Eventually, the microscope is equipped with a pseudo-Kohler illumination to visualize the field of view that has to be imaged with BCARS (Fig. 3.13). I refer to the illumination scheme as pseudo-Kohler rather than Kohler, since the Kohler illumination requires the insertion of an iris in the back focal plane of the condenser lens to alter the sample contrast. In my scheme, the back-focal plane of the objective is not accessible, thus preventing the use of an iris. A red LED is mounted in the bottom part of the microscope followed by a collector lens that collimates the light emitted. An iris acts as a field stop, reducing the number of rays illuminating the sample. After a mirror, a field lens focalizes the collimated light into the back focal plane of the collection

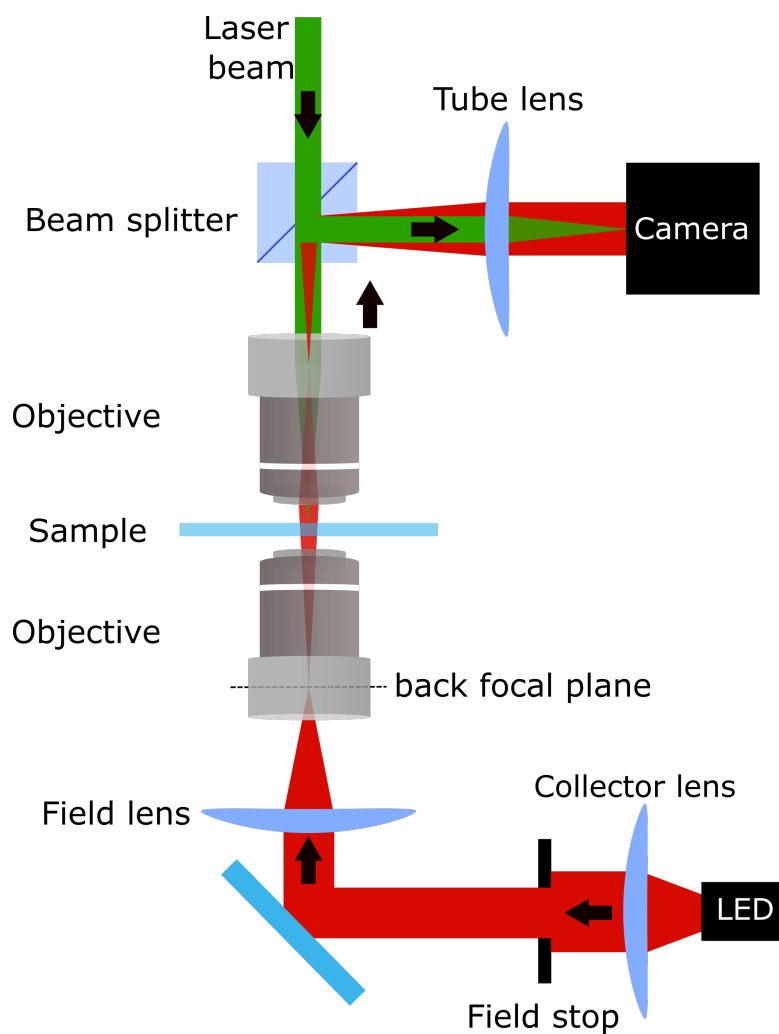


Figure 3.13: Schematic representation of the pseudo-Kohler illumination realized in the BCARS microscope. The LED light is in red, while the laser beams (pump and Stokes) are in green.

objective, thus having an illumination of the sample plane over a field of view (FOV) dependent exclusively on the magnification of the collection objective. Our objective with magnification $M = 100$ and field number $FN=22$ gives a $FOV = FN/M = 220 \mu\text{m}$.

The light is collected by the illumination objective and a beam splitter delivers it toward a CCD camera (CS165MU/M, Thorlabs) by means of a tube lens. The beam splitter is needed to also visualize the position of the laser beam (green line in Fig. 3.13) with respect to the sample.

3.6 Detection

Eventually, the setup concludes with a detection scheme that includes a short pass filter to remove the pump and Stokes pulses, and a lens to focalize the beam into the slit aperture of the spectrometer (Fig. 3.14). The lens has to be properly chosen in order to match the f-number of the spectrometer. In our case, the f-number of the monochromator (Acton SP2150p, Princeton instruments), expressed as the focal length of the lens over the diameter of the beam onto the lens ($N = F/D$), is $f/4.0$ (where $N = 4.0$). Therefore we chose a lens of 35 mm in order to properly collect the anti-Stokes light sent to the spectrometer.

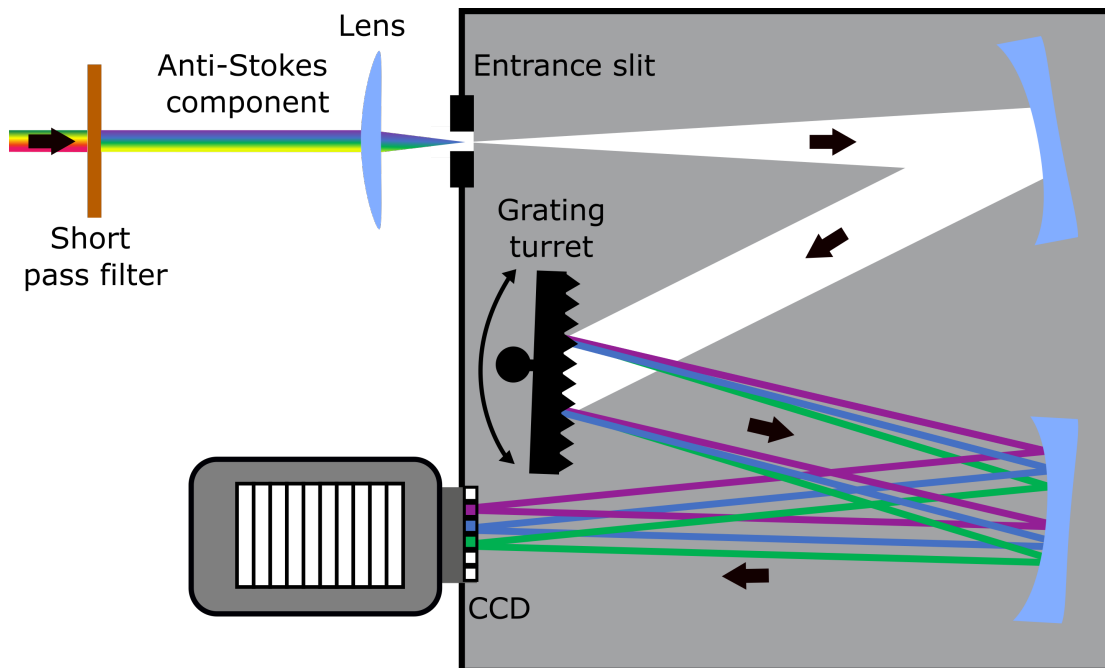


Figure 3.14: Schematic representation of the detection unit. The light is sent into a monochromator that separates the colors, while a CCD sensor with many pixels outputs the counts per pixel within a certain pixel dwell time.

The entrance slit of the monochromator has to be properly set since contributes to the spectral resolution of the acquired spectra. Indeed, the spectral resolution of a spectrometer ($\delta\lambda$) depends on four variables that are: the slit width (W_s), the spectral range of the spectrometer ($\Delta\lambda$), the pixel width (W_p), and the number of pixels in the detector. Moreover, one needs to define a constant value which is the resolution factor

Chapter 3. Experimental Setup and optical sources

(RF) that is determined by the relationship between the slit width and the pixel width. In the case were $W_s \simeq W_p$, the RF is 3. The setup is equipped with a low-noise BLAZE CCD camera (BLAZE100HR, Princeton Instrument) that features high sensitivity and high readout speeds. It has pixels whose width is $20 \times 20 \mu\text{m}^2$. We set the slit size to $20 \mu\text{m}$, while the wavelength range is $\Delta\lambda = 212 \text{ nm}$, due to the employed 600 gr/mm grating mounted onto the motorized turret of the monochromator, and the number of pixels is $n = 1340$. With these numbers, we could calculate the spectral resolution given by the system using the equation:

$$\delta\lambda = \frac{RF\Delta\lambda W_s}{nW_p} \quad (3.17)$$

This equation gives us a spectral resolution of 0.47 nm , which corresponds to 5.8 cm^{-1} .

The spectral acquisition of the detection unit is synchronized to the raster scanning motion by means of a trigger signal generated by the stage controller. I programmed a MATLAB interface (Fig. 3.15) to generate a trigger at each pixel step size, and the CCD records the spectra every time a rising edge of the trigger input signal arrives. In this way, it is possible to acquire images at very high speed, working at the minimum exposure time allowed by the CCD camera, associating each pixel to a specific spatial position without experiencing any motion artifacts or shifts in the rows of the acquired images.

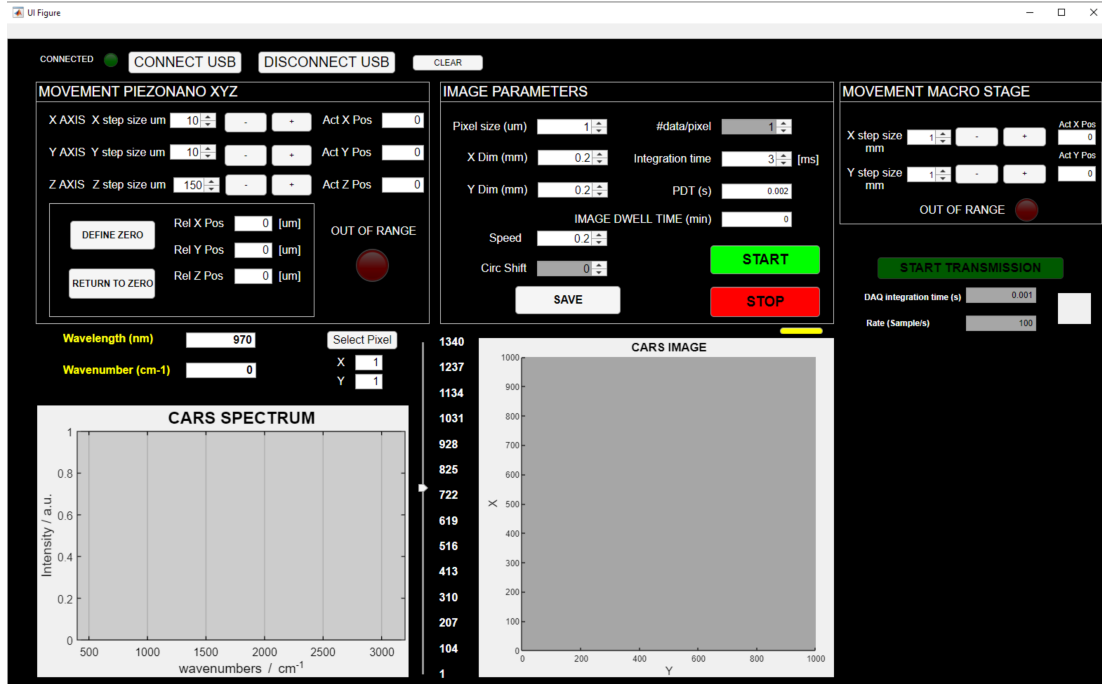


Figure 3.15: Matlab interface for the acquisition of the CARS images.

Acquisition and post-processing of the CARS data

4.1 Introduction

The BCARS system is used for spectroscopic and microscopic applications. When dealing with spectroscopic applications, one acquires a spectrum or a certain number of spectra of the same chemical analytes, while in the case of microscopic applications, the measured data are hyperspectral data, i.e., three-dimensional cubes, that have spatial and spectral information. In both cases, to recover the pure vibrational information we need to develop a post-processing pipeline made of several steps.

The analysis of the CARS data is one of the most challenging steps of CARS imaging. Indeed, the relevant chemical information one may extrapolate from the CARS data depends not only on the sample properties but also on the chosen processing steps that should take into account various parameters, such as the wavelength range of the Stokes and pump beam, their spectral distribution and the instruments that have to be correctly calibrated. Eventually, special care should be taken when analyzing the CARS data of biological samples, since spectral variations can be observed due to unavoidable biological changes, variations in sample preparation, sample degradation, or any other uncontrollable experimental factor. Besides these aspects, also the errors during the measurements and some unpredictable artifacts contribute to making the analysis of the data quite complex.

Throughout my Ph.D., I adopted different strategies for the acquisition and analysis of the CARS data. In this chapter, I will describe the experimental methods I used, the data-processing algorithms that I adapted from literature, and the algorithms that I developed or contributed to developing. All these methods have been used for the analysis of the data that will be shown in the following chapter.

The chapter will be divided into three parts:

- The first part includes the design of the experiment and the strategies adopted to decide the parameters necessary to acquire CARS spectra or images.
- The second part includes the post-processing methods applied to the experimental data and employed to obtain data comparable to the Spontaneous Raman one. The post-processing of the data may be divided into two main steps which are the noise reduction of the data and the NRB removal. For both of them, numerical algorithms and machine-learning-based models have been explored.
- The third part refers to the different approaches used after the post-processing pipeline to distinguish the different chemical constituents when imaging heterogeneous samples.

4.2 Experimental design

The first step for acquiring a good set of data is the design of the experiments [148] (see Fig. 4.1). This part is extremely important to define the set of parameters that have to be chosen for conducting the experiments. It can be divided into 4 main steps: setup alignment, bright field image for sample visualization, preliminary CARS measurements, and experimental planning.

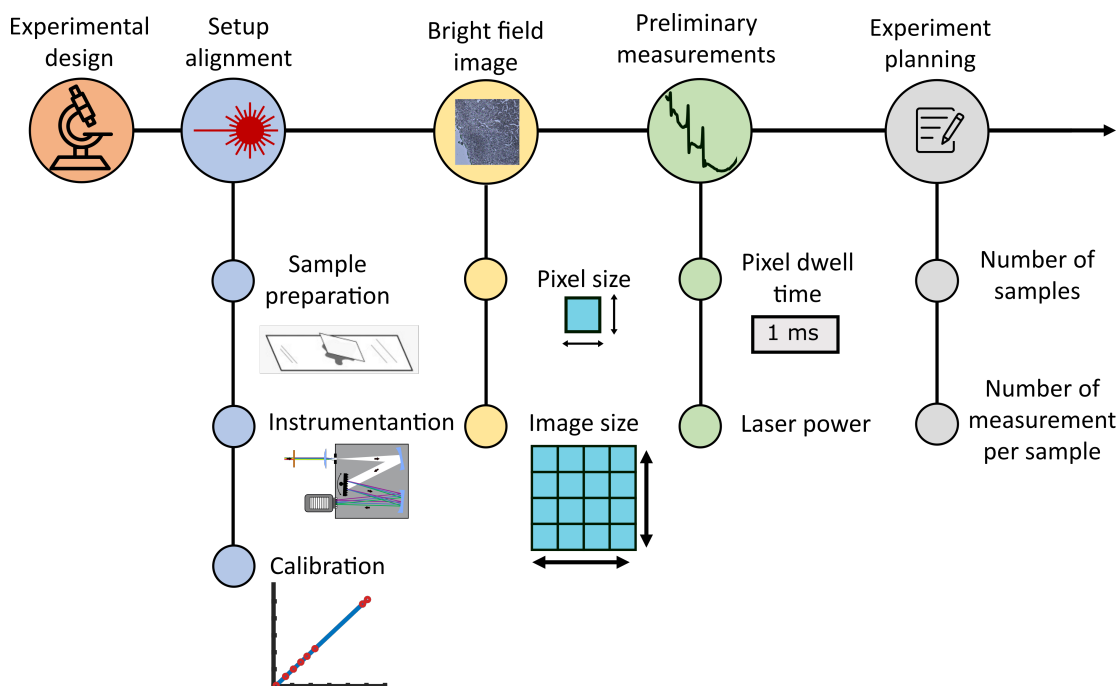


Figure 4.1: Workflow of the experimental design. It includes 4 main parts that are: setup alignment, bright field image, preliminary measurements, and experimental planning.

4.2.1 Setup alignment

The first important step in the design of the experiment consists in finding the best signal by monitoring the optical sources, their spatial and temporal overlap at the sample plane, and the alignment of the anti-Stokes component to the spectrometer. One of the

most critical steps is the stability of the broadband source. In case the WLC is not stable, the user needs to play on the three parameters of the supercontinuum stage, i.e., the impinging power, the iris aperture, and the crystal position with respect to the focal plane, monitoring the spectrum of the broadband Stokes through a NIR spectrometer (Avantes NIR256-1.7-EVO) and measuring its RMS fluctuations through a photodiode, that acquire a sequence of adjacent pulses (60000 is a good number). Usually, this procedure does not need to be done every day, since the WLC stage offers long-term stability of the source.

This first phase of the experimental design includes also sample preparation that is strictly related to the properties of the samples to be measured and the used objectives. The spectrometer used for the signal acquisition needs to be properly set through some calibration lamps for intensity and wavenumber calibration. This last step does not have to be done daily, it is enough to check it once per month. Eventually, it is highly recommended to define a calibration standard for wavenumber calibration. In particular, the standard material should be measured under the same conditions and optical geometry of the samples. For measuring biological samples or other chemical analytes, I chose toluene as the standard material because of the high number of peaks in the fingerprint and in the CH-stretching region. I daily acquire 100 toluene CARS spectra (blue curve in Fig. 4.2), 100 spectra focusing on quartz coverslip (orange curve in Figure 4.2) that we consider as NRB spectra, and 100 dark spectra with 1-ms exposure time. I average the three sets of spectral data and use them for calibrating the wavenumber axis of our system. We subtract the averaged dark spectrum from the CARS and NRB data and then compare the phase retrieved toluene spectrum (light-blue curve in Fig. 4.2), after removal of the NRB through the time-domain Kramers-Kronig algorithm [63], with the spontaneous Raman spectrum of toluene (purple curve in Fig. 4.2), acquired averaging 5 times 5-s acquisitions with a home-built Spontaneous Raman experimental setup. The wavenumber axis is calibrated by fitting a third-order polynomial function between the measured and spontaneous Raman peak positions of the main Raman peaks of toluene (for toluene I always use 8 peaks for calibration). The goodness of the calibration procedure is evaluated by computing the errors between the positions of the eight peaks of the phase retrieved and of the spontaneous Raman spectrum (see the bottom panel in Fig. 4.2).

4.2.2 Bright-field Image

After the setup alignment, including the sample preparation and the calibration procedures, the experimental design workflow includes the visualization of the investigated sample. In the case of spectroscopic application, this part can be skipped, since no imaging is necessary. However, when dealing with biological samples, such as tissues and cells, this step is crucial to establish which are the best parameters that have to be chosen for visualizing the morphological details of the sample. I use the pseudo-Kohler illumination described in the previous chapter to decide the pixel size and also image size. These parameters are often linked to each other since we are limited by the maximum number of pixels that the hypercube can have. This limit is mainly established by the post-processing steps, indeed, large hyperspectral data are more computationally demanding and require long analysis times. For these reasons, I am currently limiting the maximum size of the files to 400x400x1340 pixels, which corresponds to 214.4

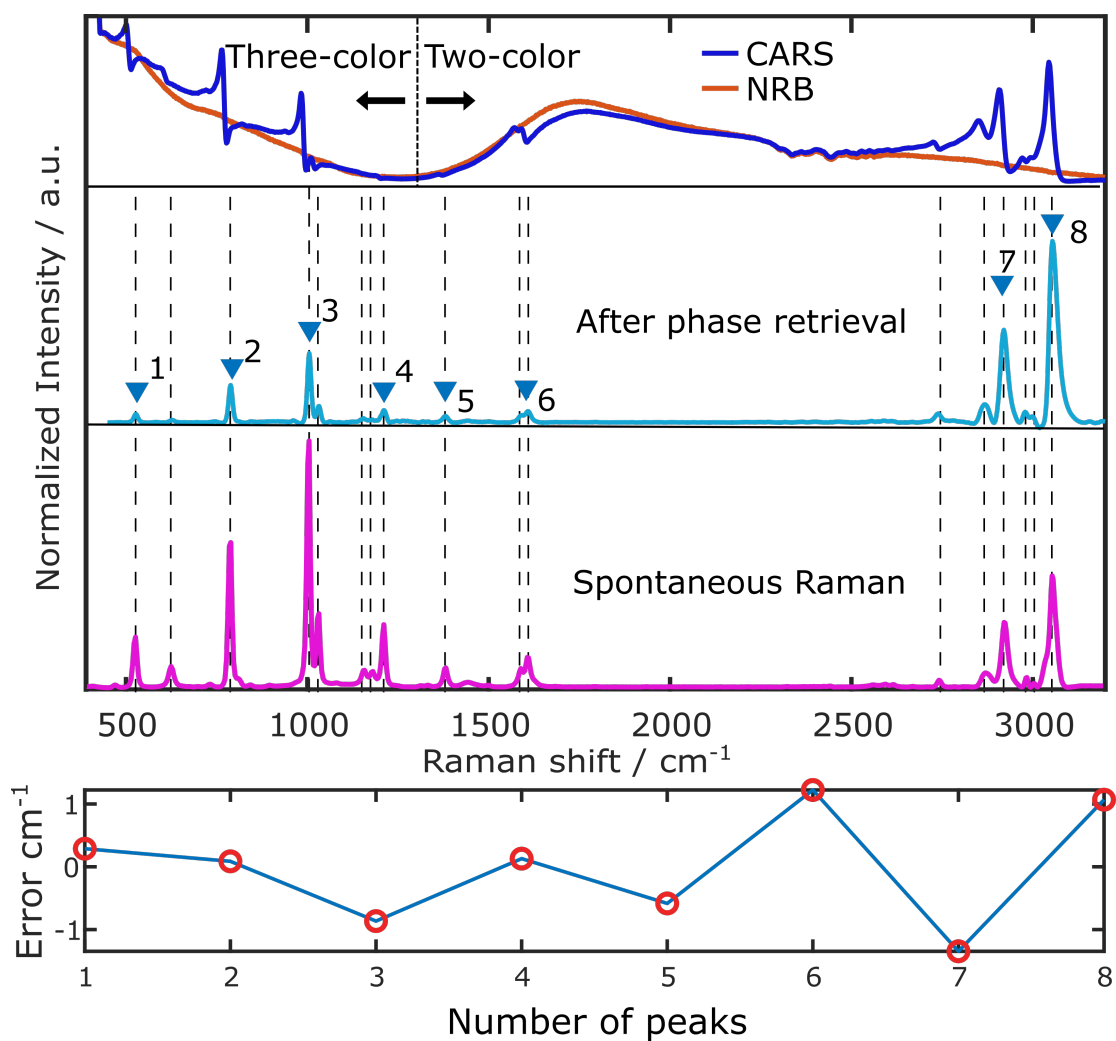


Figure 4.2: Graph showing the daily procedure I adopt for calibrating the wavenumber axis. I average 100 toluene spectra (blue curve), 100 NRB spectra measured on a quartz coverslip (orange curve), and 100 dark spectra that I subtract from the CARS and NRB spectra. The pixel exposure time is 1 ms. The phase-retrieved spectrum (light-blue curve) is obtained from the toluene CARS spectrum and the NRB one through the Kramers-Kronig algorithm. The new wavenumber axis is obtained via a third-order polynomial fitting comparing the highlighted 8 peaks of the phase retrieved spectrum with the corresponding SR peaks (purple curve). The error between the position of the peak in SR and in the calibrated phase-retrieved spectrum is computed to estimate the goodness of the calibration procedure.

Megapixels. Typical pixel sizes are 500 nm, 1 μm , 2 μm , or 4 μm enabling us a maximum field of view of 1.2 mm.

4.2.3 Preliminary measurements

Preliminary measurements are necessary during the design of the experiment to establish the type of signals one can expect from the investigated sample. These measurements allow the user to establish the pixel dwell time to have good quality spectra and also the average powers of the pump and Stokes beam at the sample plane thus avoiding sample damage. The choice of pixel dwell time and pump/Stokes powers are linked with each other. Eventually, it is highly recommended during this phase to check whether a subsequent scan of the same field of view is detrimental to the sample.

4.2.4 Experiment planning

Once all the measurement parameters have been established, the experiment planning determines the minimum number of samples required to reach a statistically meaningful conclusion and the number of measurements needed per sample.

4.3 Data post-processing

After the design of the experiment and the acquisition of the experimental data, the data present some artifacts or unwanted contributions that may derive from the instrumentation or from the sample itself. I will describe here all the steps that are needed for the removal of the artifacts and noise reduction in the acquired BCARS data, the retrieval of the pure vibrational information removing the unspecific contribution given by the NRB, and the spectral unmixing algorithm that enable us to localize different chemical species in heterogeneous samples.

The data post-processing pipeline (see Fig. 4.3) is divided into 4 main steps:

- Quality control step for deciding whether the acquired data are good, cropping the image or the spectrum, and removing artifacts;
- Denoising of the hyperspectral data that may be performed either using numerical algorithms or machine-learning models;
- Removal of the NRB implemented either using numerical algorithms or machine-learning models;
- Spectral unmixing of the hyperspectral images in which we may distinguish factorization and clusterization methods;

4.3.1 Quality control

This step aims to determine the quality of the spectra and the images acquired in the laboratory. In particular, the user should identify some anomalies and artifacts in the data such as burning effects, defocusing, device-related artifacts, or other types of data contamination (e.g. environmental light). Sometimes, part of the data can be still considered for further analysis and the images can be cleaned either by reducing the

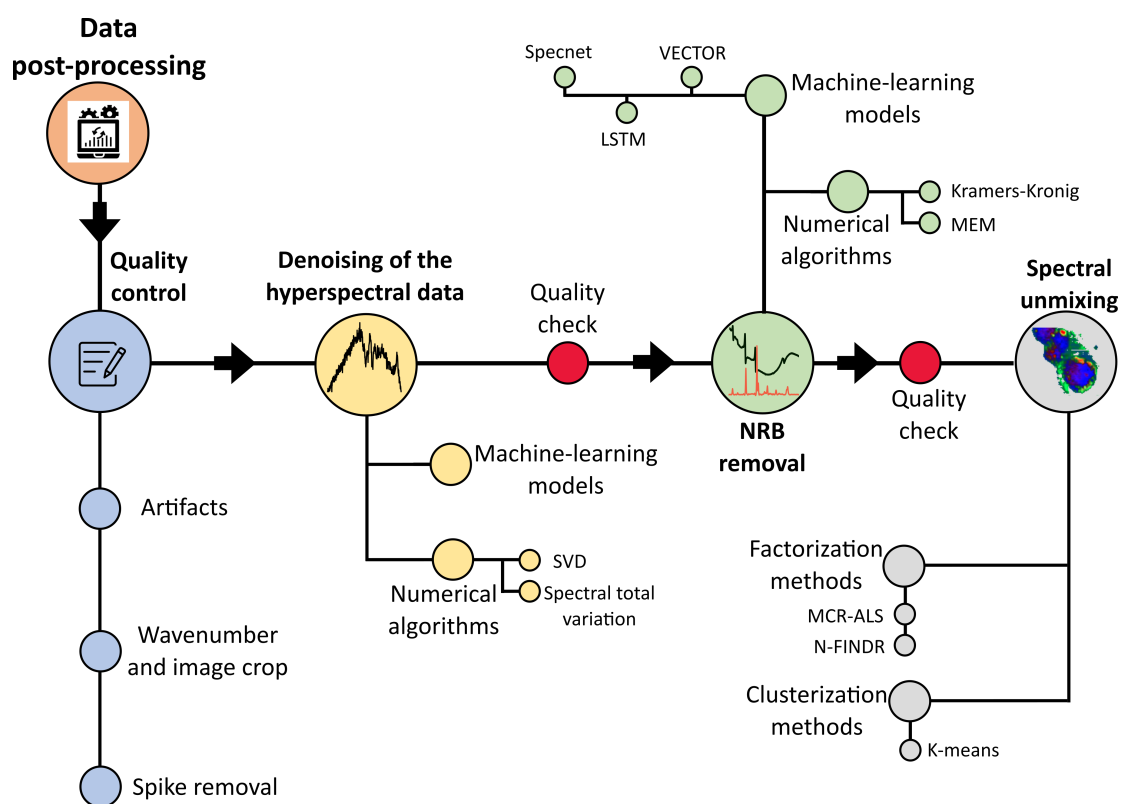


Figure 4.3: Workflow for the data post-processing. The main steps are: *Quality control; Denoising of the hyperspectral data; NRB removal; Spectral unmixing.*

image size or by removing the spectra that present evident anomalies and may alter the subsequent analysis. One important phase during quality control is spike removal. Spikes derive from electrons generated on the CCD or CMOS detector by high-energy cosmic particles. They appear randomly in the signal and are very narrow features that affect the analysis. There are different ways to detect and remove these spikes. One way is to record two spectra from the same sample in identical conditions and detect spikes by comparing the two measurements. However, acquiring two spectra for each sample is too time-consuming, especially in CARS imaging. Another possibility is to compare the spectra of two or more adjacent points in the sample, provided that their corresponding Raman features are almost the same for these two measurements. However, this approach fails if the sample is heterogeneous. Hence, a better solution is to compare each spectrum to the mean spectrum of the surrounding pixels given a spatial window size. After being detected, a spike can be removed using the median filter that replaces every point of a signal with the median of that point and a specified number of neighboring points. Accordingly, median filtering discards points that differ considerably from their surroundings.

4.4 Denoising of the hyperspectral data

After the quality check, the BCARS hyperspectral data still suffer from the presence of noise. The noise affects the measurements and needs to be removed. However, when dealing with CARS spectra the denoising task is not so straightforward, since one has to preserve the typical dispersive lineshapes while canceling the random fluctuations into the spectrum. During my Ph.D., I explored different strategies for the removal of the random noise, some of them are based on numerical algorithms such as moving-mean techniques, Fourier transform-based approaches, Savitzky-Golay filter, singular value decomposition (SVD) [60, 63], and spectral total variation (STV) [149]. Other strategies use more sophisticated models based on machine learning, a field that I studied during my Ph.D. and on which I published a review entitled: "Artificial intelligence in classical and quantum photonics" [150].

4.4.1 Denosing via Singular Value Decompositon

Among the denoising algorithms, singular value decomposition (SVD) is one of the most used for spatial and spectral denoising of the CARS hyperspectral images [60,63]. The three-dimensional BCARS dataset ($m \cdot n \cdot s$ with m the number of spatial pixels along x , n the number of spatial pixels along y , and s the number of spectral pixels) is unfolded into a two-dimensional matrix, M , whose rows represent the spectral axis with s spectral points and whose columns represent the spatial pixels ($p = m \cdot n$). The SVD algorithm factorizes this matrix into three components:

$$\mathbf{M} = \mathbf{U}\mathbf{S}\mathbf{V}^* \quad (4.1)$$

where \mathbf{U} is a two-dimensional matrix ($s \cdot s$) and contains the spectral bases (orthonormal eigenvectors), \mathbf{S} is a diagonal matrix ($s \cdot s$) containing the "singular values" (eigenvalues) ordered from the larger to the smaller, \mathbf{V} ($p \cdot s$) describes the spatial distribution of the bases in \mathbf{U} , and $*$ is the conjugate transpose. A schematic representation of the SVD decomposition is reported in 4.4.

The SVD decomposition can be considered as a decomposition of the \mathbf{M} matrix in a weighted, ordered sum of contributions, each represented by λ_i . The first singular values represent the high spatial and spectral coherent contribution, while, increasing the order i , the lower coherent parts can be found. Therefore, by setting to zero all the singular values over a certain i , we remove the singular vector with the least spatial and spectral coherence. Since the noise is characterized by complete randomness in space and by a high frequency in spectra, removing the λ_i with high i , we are effectively denoising the data [151]. After having set to zero all the λ_i , for $i > i_{filter}$, changing the matrix \mathbf{S} to $\hat{\mathbf{S}}$, the denoised matrix $\hat{\mathbf{M}}$ can be calculated as: $\hat{\mathbf{M}} = \mathbf{U}\hat{\mathbf{S}}\mathbf{V}^*$. It is worth noticing that the SVD works appropriately only in case the noise is additive and follows a gaussian distribution. However, BCARS data typically exhibits a Poisson-Gaussian noise. Therefore, before performing the SVD, we applied an Anscombe transformation [152] that acts as a variance stabilizer whitening the noise of the data. After the reconstruction of matrix \hat{M} , we apply the inverse Anscombe transformation to restore the BCARS spectra with mixed noise.

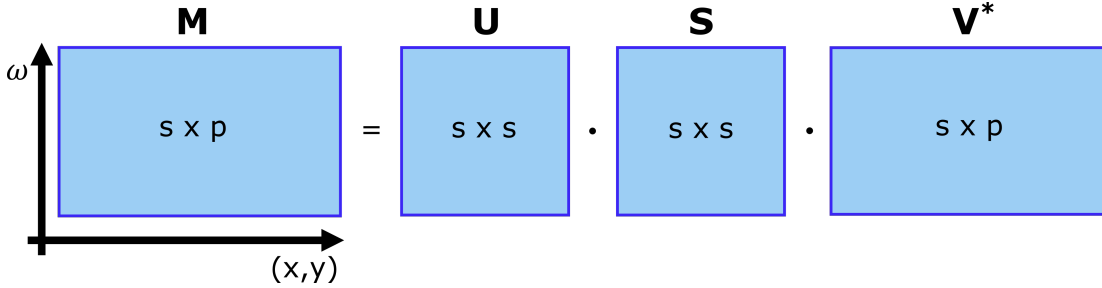


Figure 4.4: Schematic representation of SVD decomposition.

4.4.2 Denoising via machine-learning

Recently, machine-learning methods [150] have been used for denoising broadband CRS images. Machine learning (ML) is a branch of Artificial Intelligence that has had a high impact on several different scientific and engineering domains. ML is defined as the science that examines how computers can be automatically trained to solve complex tasks starting from the analysis of data. ML have become widespread thanks to the new opportunities opened by Deep Learning (DL), a methodology that exploits the advancements in computing power to solve highly complex tasks, such as computer vision, speech recognition, and self-driving cars, and that aims to approximate non-linear transfer functions, leveraging their data-driven nature. Photonics is among the most active and promising fields in science, technology, and engineering. The combination of ML-based techniques and photonics has led to groundbreaking developments in many applications and provides huge opportunities for both fields [153–156]. Indeed, on the one hand, photonics can be used to generate rich data sets for ML computational tasks, on the other hand, photonic systems are an interesting platform for AI implementations [157, 158].

A ML algorithm is able to learn information from data [159]. Depending on the kind of data available, ML tasks are divided into three macro-areas.

- Unsupervised Learning, where ML models deal with the extraction of information

from the data without any target value or label available.

- Supervised Learning, where the ML model is provided with a dataset including input-output pairs. The output data, or labels, allow the evaluation of the model performance during the training. Supervised learning can be exploited to approximate the complex or unknown function mapping the input data to the output.
- Reinforcement Learning is a specialized ML area that deals with the control of a dynamical system [160], where the model is trained to find a control law for the system so that some objective is optimized.

4.4.3 Machine-learning fundamentals

Every ML problem consists of a dataset with N entries $\mathcal{D} = (\mathbf{X}, \mathbf{y}) = \{(\mathbf{x}_i, y_i), i = 1 \dots N\}$, where \mathbf{X} is the input matrix whose rows correspond to data instances, whereas the columns are the *features* of the dataset, namely the variables or attributes of the instances. On the other hand, y_i is the corresponding ground-truth vector, representing the ideal output of the model. The features of \mathbf{X} can be numerical and/or categorical (*i.e.* input attributes encoded in the form of discrete numerical values) depending on the context, and constitute the independent variables. The goal of ML algorithms is to approximate the nonlinear transfer function $f : \mathbf{x}_i \rightarrow y_i$, acting on a set of parameters θ . For a single input-output pair, the error between the prediction and the ground truth is quantified utilizing the loss function $\mathcal{L}_i(f(\mathbf{x}_i, \theta), y_i)$. The parameters of the NN are adjusted to minimize the cost function $\mathcal{C}(f(\mathbf{X}, \theta), \mathbf{y})$ (or $\mathcal{C}(\theta)$), which is the average of the loss functions $\mathcal{L}_i(f(\mathbf{x}_i, \theta), y_i)$ over the overall training dataset. In formulae:

$$\mathcal{C}(f(\mathbf{X}, \theta), \mathbf{y}) = \frac{1}{N_{train}} \sum_{i=0}^{N_{train}} \mathcal{L}_i(f(\mathbf{x}_i, \theta), y_i) \quad (4.2)$$

with N_{train} the total amount of instances in the training set. Indeed, in ML models, the dataset is partitioned into two independent sets $\mathcal{D} = \mathcal{D}_{train} \cup \mathcal{D}_{test}$, respectively the training set and test set. The former is used to optimize the set of parameters θ , while the second is used to evaluate the performances of the model on new, unseen data. A typical training-test split is approximately 80/20%. In addition, a portion of the training set (*e.g.* 20%) is used as a validation set, meaning that it is used for an unbiased evaluation of the model during training and for fine-tuning of the model hyperparameters, which are the untrainable parameters that define the topology of the network.

When evaluating the goodness of a model one has to monitor two quantities that are the training error $E_{train} = \mathcal{C}(\mathbf{X}_{train}, \mathbf{y}_{train})$ and the test error $E_{test} = \mathcal{C}(\mathbf{X}_{test}, \mathbf{y}_{test})$. Model performances depend on many factors, such as the amount of data available (the cardinality of the training set), the number of parameters available to the model (the model complexity), and the number of optimization iterations carried out. For a reasonably good prediction, both E_{train} and E_{test} should be considered. While the minimization of E_{train} ensures that the model is learning the mapping f , the ability to perform well on new data is expressed by E_{test} . Typically E_{train} results slightly lower than E_{test} . However, if $E_{test} \gg E_{train}$ the model is *overfitting* the training set. It means that the model is utilizing its representation power to store information related to fluctuations in the training set. To mitigate overfitting one may increase the number

of data points available to train the model, or reduce the model complexity by reducing the number of parameters, or applying regularization techniques (*e.g.* L_1 , Lasso regularization, and L_2 , Ridge regularization). This crucial aspect of ML is usually referred to as *bias-variance* trade-off [161].

The goal of the model is to find a set of parameters that minimizes $\mathcal{C}(\theta)$, thus maximizing the model performance precision by leading to a minimum average error between ideal and predicted outputs. Gradient Descent is the typical procedure used to compute θ . The idea of this technique is that for every iteration we compute the cost function $\mathcal{C}(\theta)$. As an example, if the chosen loss function is the Mean Squared Error, the cost function is defined as:

$$\mathcal{C}(\theta) \equiv \text{MSE} = \frac{1}{N_{train}} \sum_{i=1}^{N_{train}} (f(\mathbf{x}_i, \theta) - y_i)^2. \quad (4.3)$$

Given the total cost for the current iteration, we can compute an update in our parameters at iteration $(t + 1)$ in the opposite direction of the gradient (∇) of $\mathcal{C}(\theta)$ with respect to the parameters at iteration t , *i.e.* in the direction of the minimum of $\mathcal{C}(\theta)$. In formulae:

$$\theta_{t+1} = \theta_t - \eta \nabla_{\theta_t} \mathcal{C}(\theta_t). \quad (4.4)$$

where η is the learning rate of the algorithm, a hyperparameter (*i.e.* a parameter that controls the learning process and is not part of weights and biases to be optimized during learning) that controls how much the parameters vary in response to the estimated error. This basic update rule has been widely investigated, and several improvements have been introduced. In particular, to avoid the computation of the gradient over the entire dataset that would be time-consuming and computationally expensive, random subsets of the dataset (mini-batches) can be used at each iteration. This reduces the computational cost and introduces stochasticity in the training, which in turn reduces overfitting. To mitigate the risk of being trapped in local minima of the cost function, some optimizers add momentum to the update rule as an exponentially weighted average over the previous values of the gradient. Among these refined optimizers, one of the most popular is the Adaptive Moment estimation optimizer (ADAM) [162]: the learning rate is adjusted based on the average first moment (the mean) and the average second moment (the uncentered variance) of the gradient of $\mathcal{C}(\theta)$.

4.4.4 Neural Networks fundamentals

DL is a ML methodology that employs deep neural networks (DNNs) to solve ML tasks. DNNs are a category of powerful function approximators. A neural network (NN) is formed of elementary units called neurons (Fig. 4.5.(a)). Each neuron receives a series of real numbers as input \mathbf{x} , computes their weighted average with a set of weights \mathbf{w} and a bias b , $z = \mathbf{x}^T \mathbf{w} + b$, and outputs a number $f(z)$ obtained applying a nonlinear function f , called the activation function. The bias term b is often incorporated in the set of weights \mathbf{w} to compact the notation, considering an extra 1 in the vector \mathbf{x} (in Fig. 4.5.(a)). The nonlinear function is the basis of the approximation power of NNs. Typical non-linear activation functions, reported in Figure 4.5.(b), are the sigmoid $\sigma(z)$, the hyperbolic tangent $\tanh(z)$, and the Rectified Linear-Unit, ReLU(z). They are

defined as:

$$\sigma(z) = \frac{1}{1 + e^{-z}}; \quad \tanh(z) = \frac{e^z - e^{-z}}{e^z + e^{-z}}; \quad \text{ReLU}(z) = \max(0, z). \quad (4.5)$$

The Universal Approximation Theorem guarantees the ability of NNs to approximate complex functions. The theorem was formulated by George Cybenko in 1989 [163, 164]. It states that a NN consisting of an input layer, a single hidden layer, and an output layer can approximate any arbitrary function between its input and output, provided that its hidden layer is adequately large. However, the size of the hidden layer grows exponentially with the complexity and nonlinearity of the function, rapidly reaching unfeasibly large levels. DNNs aim at solving this dimensional issue by stacking multiple hidden layers, exponentially increasing the approximation capabilities of each neuron of the deeper layers, hence compensating for the limited number of neurons available on each layer.

In practice, the best performances are achieved by structuring multiple layers of neurons with finite width (see Fig. 4.5.(c-d)) obtaining a deep architecture, from which the nomenclature deep neural network stems. Each neuron is linked to all the neurons of the previous and following layers in a so-called fully connected architecture. Since the information travels in one direction only, such models are often referred to as “feed-forward” neural networks.

NNs are trained in the same way described above, *i.e.* by adjusting the weights in order to minimize the cost function $\mathcal{C}(\theta)$. However, differently from other ML techniques, NNs are characterized by having a very high number of parameters; small-sized NNs have hundreds or thousands of parameters, moderately large NNs need to train a few million parameters, while the largest ones reach hundreds of millions of parameters. Despite the complex, interconnected structure of neurons and weights, the differentiability of activation functions ensures that NNs can be trained through Stochastic Gradient Descent [165]. The backpropagation algorithm [?] implements in a very efficient manner the calculation of the gradient of $\mathcal{C}(\theta)$. This algorithm leverages dynamic programming and efficient matrix multiplication, performed on Graphical Processing Units. At the heart of backpropagation is an expression for the partial derivative of the cost function with respect to any weight or bias of the network. This expression gives us detailed insights into the overall behavior of the network while changing the weights and the biases. The typical notation to refer to all the weights in the networks is w_{jk}^l . It denotes the weight from the k -th neuron in the $(l - 1)$ -th layer to the j -th neuron in the l -th layer. A similar notation is used for the biases and the activation functions. Indeed, b_j^l denotes the bias of the j -th neuron in the l -th layer, while a_j^l represents the activation of the j -th neuron in the l -th layer (see Figure 4.5.(a)). Using these notations, the activation of the j -th neuron in the l -th layer is related to the activations in the $(l - 1)$ -th layer by the equation:

$$a_j^l = f \left(\sum_k w_{jk}^l a_k^{(l-1)} + b_j^l \right) \quad (4.6)$$

where the sum is over all the k neurons of the $(l - 1)$ -th layer and f is the chosen activation function (see Eq. (4.5)). Typically, one may refer to the input of the activation function as z_j^l , that is $z_j^l = \sum_k w_{jk}^l a_k^{(l-1)} + b_j^l$.

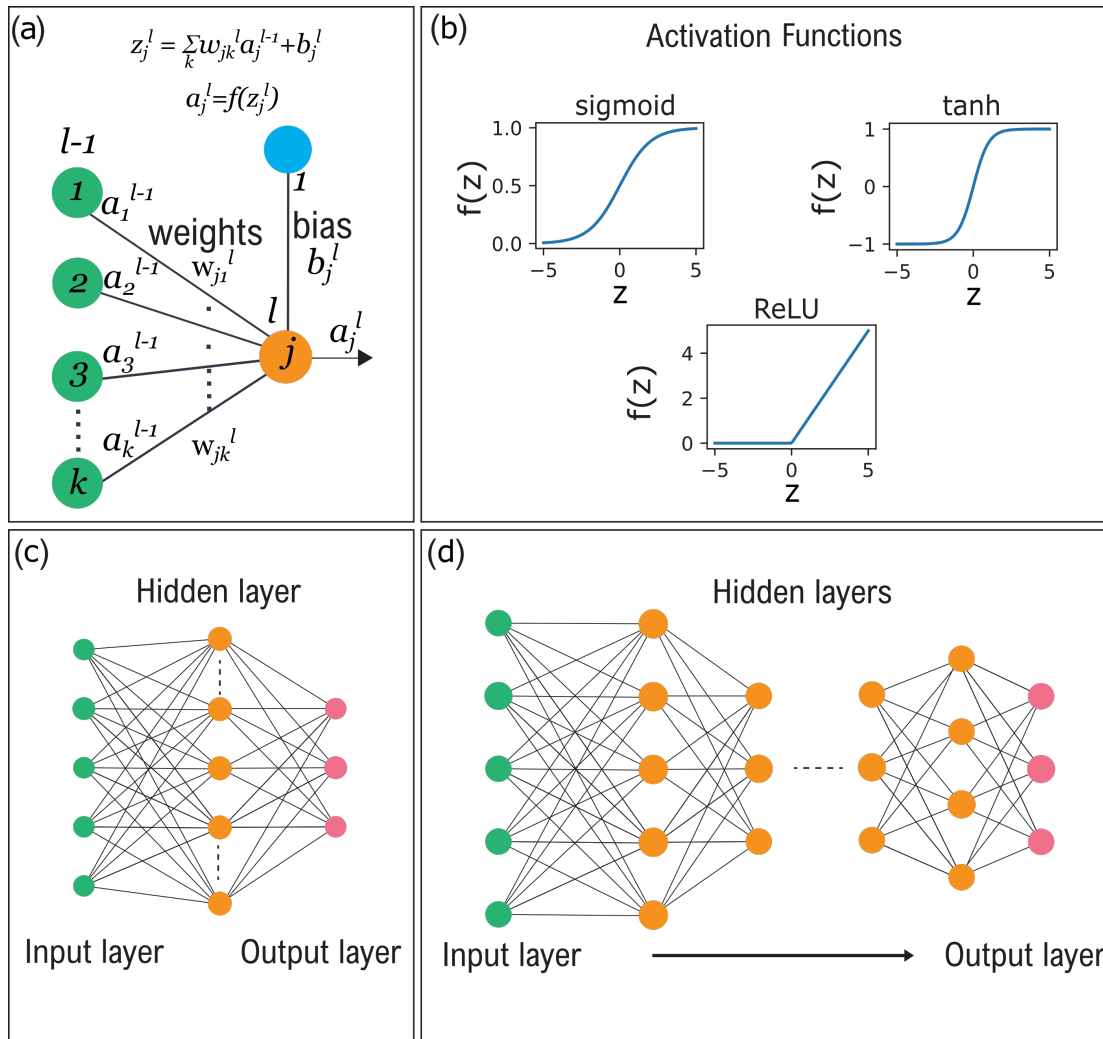


Figure 4.5: (a) Illustration of a neuron j at layer l ; (b) Plots of typical non-linear activation functions: sigmoid, tanh, ReLU; (c) Scheme of a shallow NN featuring a single hidden layer; (d) Scheme of a deep NN featuring several hidden layers. From [150]

Defining the error introduced by the j -th neuron in the l -th layer as:

$$\delta_j^l \equiv \frac{\partial \mathcal{C}}{\partial z_j^l} = \frac{\partial \mathcal{C}}{\partial a_j^l} \frac{\partial a_j^l}{\partial z_j^l} \quad (4.7)$$

the backpropagation algorithm is based on four fundamental equations. They are:

1. An equation for the error δ_j^L of the output layer L :

$$\delta_j^L = \frac{\partial \mathcal{C}}{\partial a_j^L} f'(z_j^L) \quad (4.8)$$

where $f'(z_j^L) = \left(\frac{df}{dz}\right)_{z_j^L}$ expresses how fast the activation function is changing at z_j^L .

2. An equation for the error δ_k^l of the k -th neuron in the previous layer in terms of the error δ_j^{l+1} of the j -th neuron in the next layer:

$$\delta_k^l = (w_{jk}^{l+1} \delta_j^{l+1}) f'(z_j^l) \quad (4.9)$$

3. An equation for the partial derivative of the cost function with respect to any bias in the network:

$$\frac{\partial \mathcal{C}}{\partial b_j^l} = \frac{\partial \mathcal{C}}{\partial z_j^l} \frac{\partial z_j^l}{\partial b_j^l} = \frac{\partial \mathcal{C}}{\partial z_j^l} \cdot 1 = \delta_j^l \quad (4.10)$$

4. An equation for the partial derivative of the cost function with respect to any weight in the network:

$$\frac{\partial \mathcal{C}}{\partial w_{jk}^l} = \frac{\partial \mathcal{C}}{\partial z_j^l} \frac{\partial z_j^l}{\partial w_{jk}^l} = \delta_j^l a_k^{l-1} \quad (4.11)$$

Eventually, after the input has been propagated to the network by computing activation functions $a_j^l = f(z_j^l)$, the output error is computed through Eq. (4.8). Applying the chain rule of partial derivatives from the output layer backward [?], the error is backpropagated using Eq. (4.9). Finally, Eq. (4.10) and Eq. (4.11) are used to compute the partial derivatives of the cost function with respect to any weight and bias.

4.4.5 Convolutional Neural Networks

Convolutional Neural Networks (CNNs) are one of the most popular Network architectures utilized in DL, in particular in imaging-related tasks. CNNs were first introduced in [167]. Unlike standard NNs, CNNs include the so-called convolutional layers, which may either constitute their entire end-to-end model architecture or precede standard fully-connected layers. Convolutional layers present two main features:

- Each neuron has only local connectivity with the previous layer, in the sense that its inputs come from a small set of (neighboring) neurons from the previous layer.
- In every layer, all neurons share the same weights. This set of weights takes the name of filter or “kernel”, and several different filters may be placed in the same convolutional layer to operate on the same input, as in Figure 4.6.

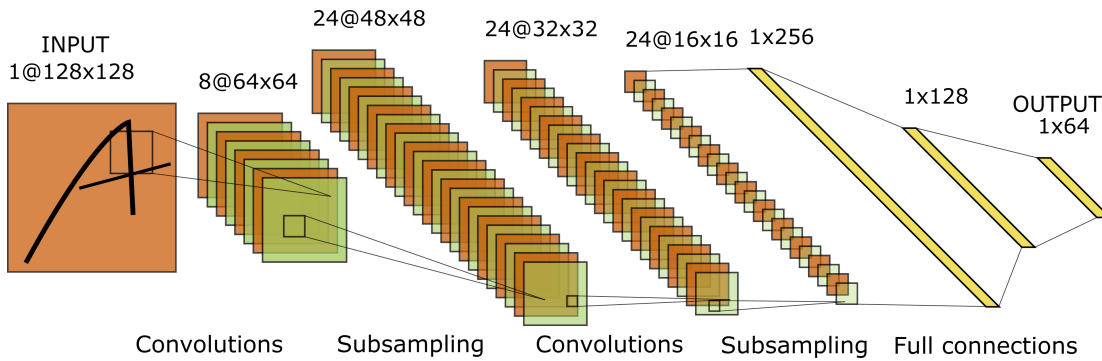


Figure 4.6: *LeNet architecture, featuring two sets of convolutional and subsampling layers, followed by two fully-connected layers and finally an output layer. As highlighted in the image, convolutional filters or kernels have local connectivity with their input, which enables feature extraction in a spatially invariant way. Adapted from [150, 166].*

The combination of these two properties, depicted in Figure 4.6, allows the characterization of CNNs in terms of the number of filters employed at each layer. One of the main advantages of CNNs is the significantly reduced number of parameters compared to standard NNs, depicted in Figure 4.5.(c-d), allowing much deeper and more complex architectures to be deployed. Besides, CNNs are also known as features extractor layers since the local connectivity of the neurons allows the network to better localize features (*e.g.*, a face) in their input, while the sharing of the weights provides spatial invariance properties to their analysis (*e.g.*, a face is recognized independently from its location in the input image). CNNs automatically extract features from data in the form of the so-called feature maps (Figure 4.6), which are the result of a kernel being cross-correlated to its input.

The most important CNNs models are U-Net and ResNet. These architectures have been used for image segmentation, with many applications in biomedical image analysis. The U-net architecture [168] consists of a contracting path and an expansive path. The contracting path has the typical structure of a convolutional network for downsampling. The expansive path consists of an upsampling to propagate context information to higher resolution layers, realized by transposed convolutional layers, and concatenation with a cropped feature map from the contracting path. As a consequence, the expansive path is more or less symmetric to the contracting path and leads to a u-shaped architecture. Hence, the U-Net architecture can be seen as a sort of encoder-decoder architecture but differs in the expansive path because of the presence of concatenations.

On the other hand, ResNet paved the way for the class of Residual Neural Networks (ResNN) [169] models. These algorithms are a technological breakthrough that effectively allowed the deployment of DNNs with over 100 layers. The constituting element of a ResNN is the residual block which is characterized by a skip connection between its input and output. The presence of these connections and their combination creates a path where the input is propagated without passing through any convolutional layer, hence preserving its informative content that is more easily provided to deeper layers. ResNNs can efficiently solve the problem of vanishing and exploding gradients. In fact, when extremely deep architectures are trained, the gradient computed by backpropagation tends to shrink to zero or become too big after several applications of

the derivative chain rule. As a result, the network parameters fail to update efficiently. The skip connections typical of ResNet allow the flow of backpropagation directly on previous layers, which proved able to solve the gradient degradation issue.

4.4.6 CNN spectral denoiser

So far, I introduced the main fundamentals of DNNs. These models have found many applications in many photonic fields and, in particular, in the field of microspectroscopy. In particular, it has proven powerful both for noise reduction and artifact removal tasks and also for accurate and efficient chemometric analysis of spectral data. The first demonstration of CRS image denoising through CNN architectures was performed by Manifold et al. [170], who employed a U-net CNN [168] architecture for SRS signals. CNNs for denoising CARS endoscopic images have been later applied by Yamato et al. [171]. Finally, Lin et al. [172] developed a spatial-spectral residual net, based on the U-net architecture, to denoise hyperspectral SRS images, training the model on images containing similar spatial features as those to be denoised. During my Ph.D. I used a CNN-based architecture to reduce the noise from the experimental CARS spectra [100] acquired with a front-illuminated CCD sensor with 1024 pixels (PIXIS100, Princeton Instruments). The training dataset consists of high-SNR BCARS spectra of six different spectroscopic grade solvents acquired with our system with a long (100 ms) exposure time. The noisy inputs are obtained by adding random noise with uniform distribution, while the outputs are obtained by computing a moving average (3 points out of 1024) of the acquired spectra, which is enough to remove the random Gaussian noise but not the dispersive features. Then, we applied data augmentation to the original dataset, reaching higher performances of the network during the training procedure.

Models, metrics and noise analysis

The CNN is inspired by the LeNet architecture and is meant to increase the SNR of the recorded spectra without incrementing the CCD exposure time. The network features 6 1D convolutional layers with rectified linear unit (ReLU) activation function, arranged as follows: (i) 32 (256,1) kernels, (ii) 64 (128,1) kernels, (iii) 96 (64,1) kernels, (iv) 128 (16,1) kernels, (v) 128 (8,1) kernels, (vi) 256 (3,1) kernels. Two average pooling layers with a (3,1) size are used to decrease the feature map dimensionality, preserving the relevant information. Eventually, 6 fully connected layers derive the prediction: (i) 64 neurons, (ii) 64 neurons, (iii) 96 neurons, (iv) 128 neurons, (v) 256 neurons, (vi) 1024 neurons. Before the last layer, a dropout layer removes 35% of the preceding neurons. The whole architecture is schematically shown in Table 4.7

For the training, we employed a batch size of 128 examples and 100 training epochs with a validation split of 20 %, which guaranteed convergence with high accuracy. The Adaptive moment estimation (Adam) optimizer was used to adapt the learning rate of the model, thus minimizing the loss function, namely the mean absolute percentage error (MAPE) between the prediction and the ground truth. Figure 4.9 shows the metrics (Loss function of the network, MAPE, Mean square error or MSE, and R2) per epoch relative to the training and validation datasets.

The hyperparameters of the network were adjusted using a balanced training dataset consisting of $6 \cdot 10^4$ high SNR experimental spectra acquired with our system at 100 ms

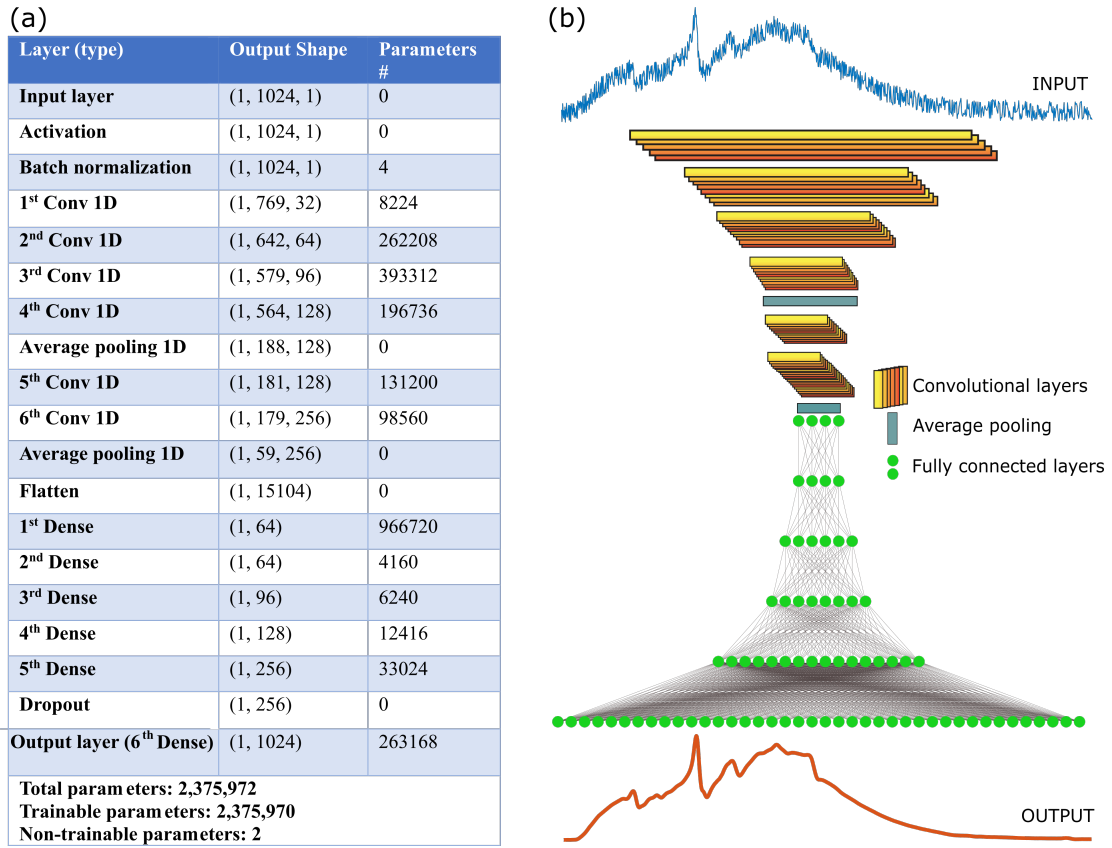


Figure 4.7: Model architecture of the CNN spectral denoiser. (a) Hyperparameters of the neural network. (b) Graphical representation of the CNN denoiser. Adapted from [100].

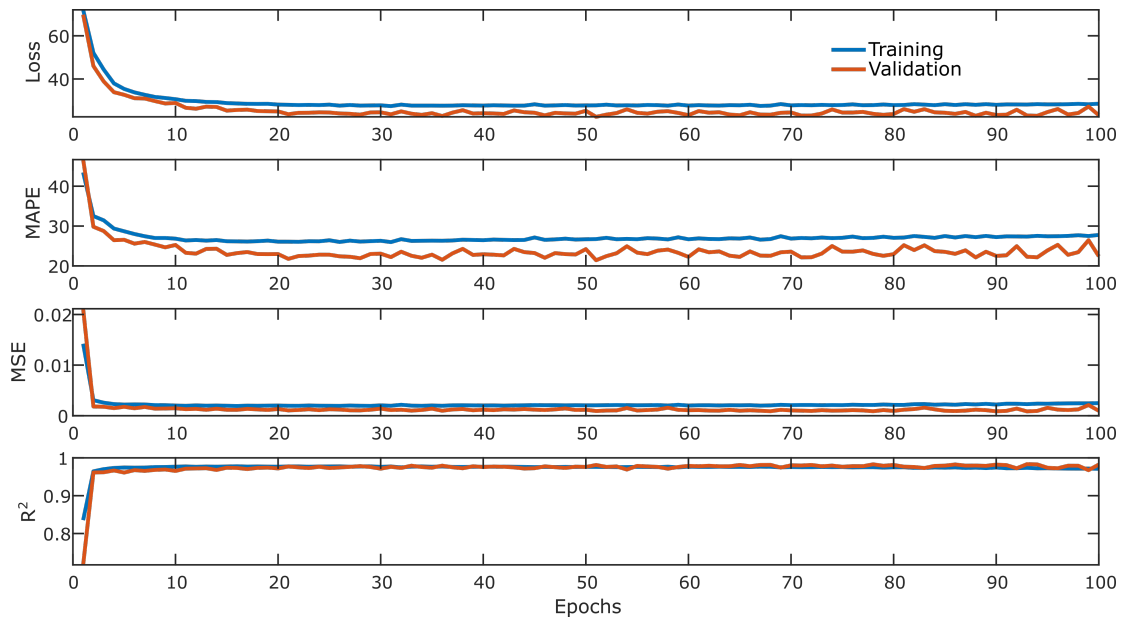


Figure 4.8: Metrics of the model for 100 epochs. From [100].

exposure time, associated with six different species (methanol, isopropanol, toluene, acetone, ethanol, dimethyl sulfoxide).

The model is able to denoise experimental spectra, still maintaining the typical dispersive lineshapes of the CARS signal and recognizing congested peaks. To quantitatively assess the robustness of the model to noise, I performed a noise analysis as reported in Fig. 4.9. We did a single training of the network with a dataset featuring uniformly distributed noise (i.e., $U(0.01,0.04)$), and tested inputs with increasing noise levels (from left to right in Fig. 4.9). In each box, we reported the noisy input spectrum (blue curve), the ground truth spectrum (black dashed lines), and the model prediction (red curve). The input is obtained by adding random noise to experimental data acquired at 100 ms. The random noise is added with uniform distribution featuring the parameters reported in the corresponding box. We used the SNR function to evaluate the performances of the model for each noise configuration. The SNR is defined as the average of the signal in the region of the peaks divided by twice the standard deviation of the spectrum in the region with no peaks. The goodness of the predicted outcome is evaluated in terms of the loss functions, namely, MAPE, MSE, and R^2 , as calculated on a minibatch of data with corresponding features. For every noisy input tested, we observed an $R^2 > 97\%$ and an $MSE < 2 \cdot 10^{-3}$. This analysis proves that even for very noisy spectral traces, the prediction is in excellent agreement with the expected ground truth.

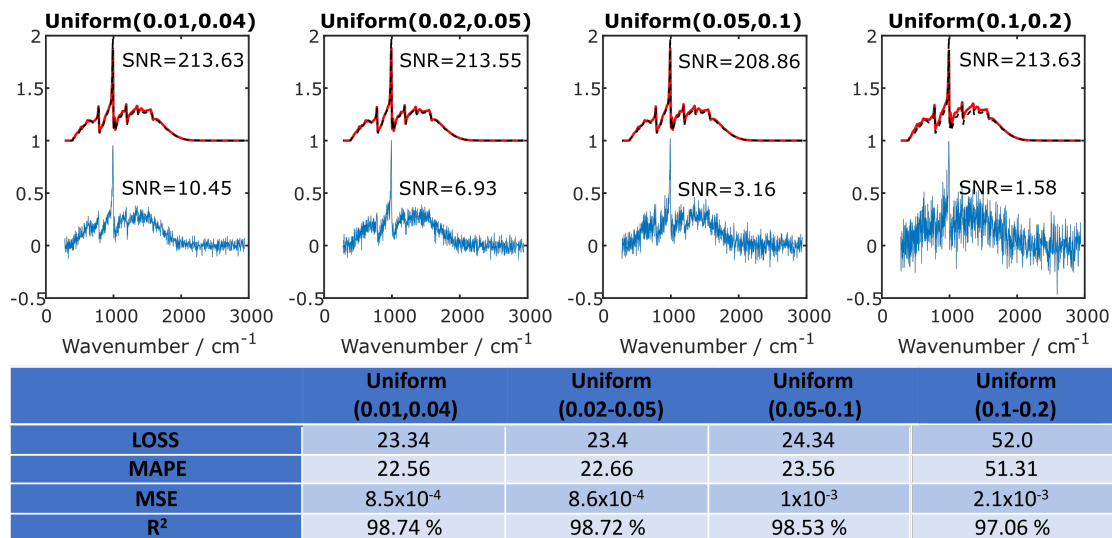


Figure 4.9: Noise analysis of the trained model on noisy test datasets of 60000 spectra. Model inputs (blue curves) feature increasing levels of randomly distributed noise from left to right. The ground truth (black dashed lines) is in excellent agreement with the model prediction (red curves) for every noise level employed in the analysis. Model performance metrics are reported in the table for each noisy case study. From [100].

Data augmentation methods

By applying spectral Data Augmentation (DA) to the original dataset, we derived $30 \cdot 10^4$ input-output pairs for an extended model training, which increased remarkably its performance on unseen test data. In fact, the DA-trained model reaches $R^2 > 98\%$ and

$MSE < 8 \cdot 10^{-4}$ on a test set of $6 \cdot 10^3$ instances. The process of DA was crucial in order to improve the accuracy of the neural network. It is performed on the input-output pairs of the original dataset. Spectra were augmented exclusively by applying intensity variations, hence, no variations in the position of the peaks along the wavelength axis were introduced. Four different methods were employed for DA (see Fig. 4.10), so that the final training dataset consists of the original dataset along with the four new ones, obtaining a 5-folds larger dataset. The first two DA methods introduce linear intensity variations, by summing to the original spectrum a line with a negative slope (DA1) or with a positive slope (DA2). Since the measured spectra are characterized by a region where there is just noise and a region where there is the CARS signal with the distorted Raman peaks, the slope is applied just to this spectral region, which we identified as the “signal region”. The line is modeled as a $y = mx$ function in the signal region, that is zero in the pixel region before the signal. The slope m is uniformly varied in order to have a variation of the last pixel of the region of the CARS signal between 8 % and 24 % of its original intensity. For the second method, the same approach is applied with the only difference that the function has a negative slope. The third and the fourth DA methods vary the spectrum intensity by summing (DA3) or subtracting (DA4) a non-symmetric triangular function to the original spectra. The function features a maximum in correspondence with the main peak of the spectrum and it is zero outside the signal region. The height of the triangular function is uniformly distributed to introduce intensity variations of the main peak of the spectrum between 2 % and 10 % for the third method or between -10 % and -2% for the fourth method.

Comparison of the CNN denoiser with numerical algorithms

The performance of the CNN denoiser has been compared with conventional algorithms (see Fig. 4.11), namely the moving mean, the Fourier-transform filtering, or the Savitzky-Golay filter. For the comparison, I used a B-CARS spectrum of toluene acquired at 100-ms exposure time. I added random noise uniformly distributed, and then I used the CNN for the denoising. The moving mean algorithm returns a spectrum where each pixel is the local mean of k -point values. The Fourier-transform approach operates a filter in the Fourier domain of the original spectrum. It zeroes all the coefficients above an arbitrary frequency, typically associated with noise, and then applies the inverse Fourier transform to obtain the denoised version of the spectrum. Finally, the Savitzky-Golay filter smooths the noisy spectrum fitting subsequent subsets of adjacent data points with a low-degree polynomial function using the method of linear least squares.

The comparison tells us that all the numerical approaches have lower prediction accuracy when compared to the denoising method via deep learning. The reason why classical mathematical methods are not suitable for this denoising task can be understood by referring to Fig. 4.11.(a). Indeed, when considering CARS spectra, it is important to preserve the typical dispersive line shape given by the interference term between the resonant vibrational response of the sample and the NRB, which results in a slow rise, a steep decay, and another slow recovery of the signal with frequency. While our neural network can recognize and maintain original spectral features (see yellow curve), moving mean, Savitzky-Golay and Fourier-transform filtering approaches introduce artifacts and/or alter peak shapes. The moving mean algorithm with high

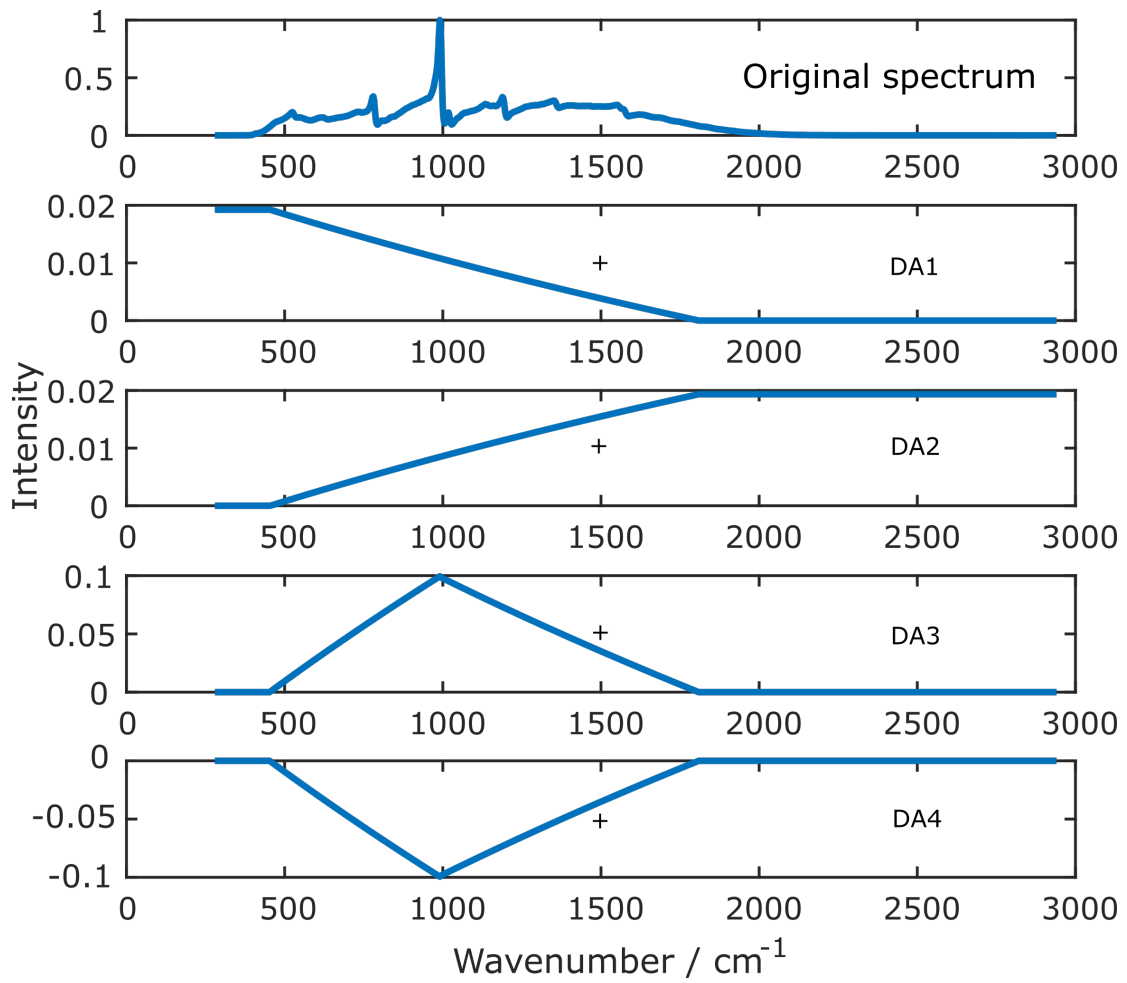


Figure 4.10: Data augmentation methods. From [100].

k-values and the Savitzky-Golay filter smooth the sharp edge of typical CARS peaks, whereas the Fourier transform cancels them by filtering out their typical high-frequency components. Eventually, we also applied the Kramers-Kronig algorithm [46] to the different spectra (in Fig. 4.11.(a)) to retrieve the imaginary part of the resonant third-order susceptibility, $\chi^{(3)}$ (4.11.(b)). These results clearly demonstrate that our neural network outperforms conventional spectral denoising methods.

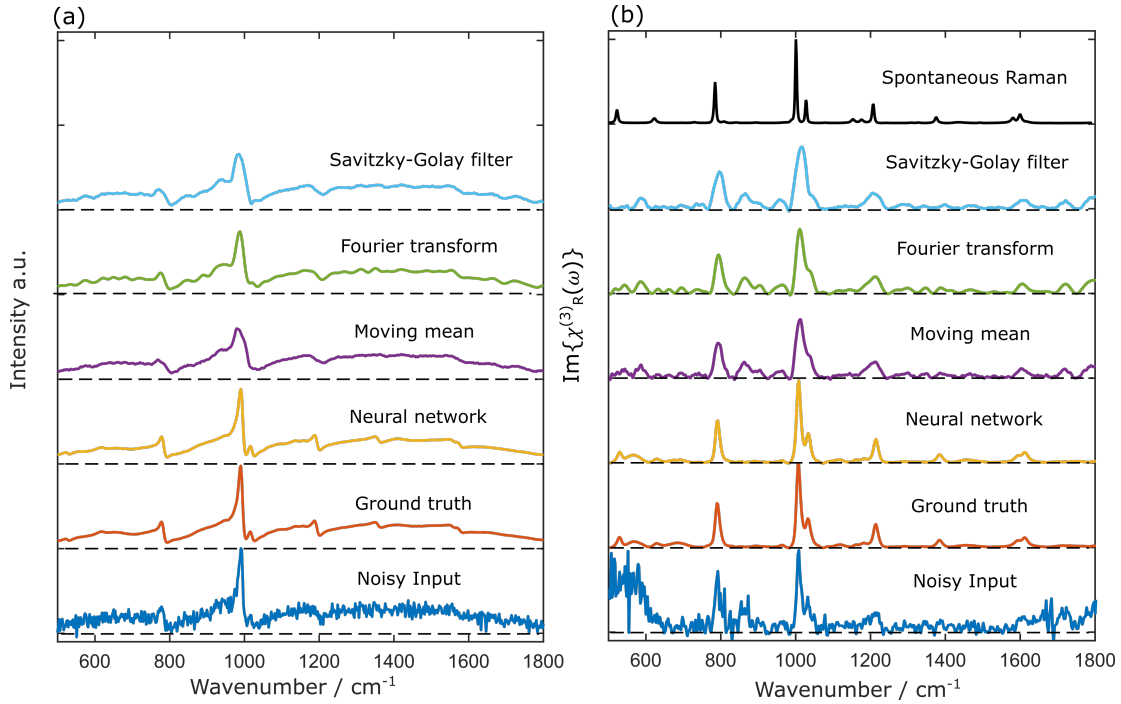


Figure 4.11: Comparison of four different denoising methods on a CARS spectrum of toluene: CNN, moving mean algorithm, Fourier-transform approach, and Savitzky-Golay filter. (a) Denoising methods on a noisy input toluene CARS spectrum (blue curve) obtained considering experimental data and adding random noise. (b) $\text{Im}\{\chi_R^{(3)}\}$ spectra retrieved through the Kramers-Kronig algorithm starting from the spectra in panel (a). A SR spectrum (black curve) of toluene acquired with 5 s exposure time is reported for comparison.

4.5 NRB removal

After the denoising of the hyperspectral data, the post-processing pipeline follows with a quality check of the data, where the user should make sure that all the peaks have been preserved and the noise reduction has properly worked. The third step of the data analysis is the removal of the NRB. As seen for the denoising of the hyperspectral data, this task can be solved using numerical algorithms or it can be read as a supervised learning task using neural networks since the function that goes from the input CARS spectrum to the output imaginary part of the resonant third-order susceptibility, $\Im\{\chi_R^{(3)}\}$, is highly nonlinear. In this section, I will describe the two methods I mainly explore during my Ph.D. for getting rid of the non-resonant background. These are the time-domain Kramers-Kronig (KK) algorithm [173] and Specnet, a CNN model we developed in our lab [48].

4.5.1 Numerical algorithms for NRB removal

Despite the existence of optical methods to suppress the NRB in CARS measurements, such as Time-resolved CARS [174] (described in 1) or Box-CARS [175], the NRB is beneficial since it acts as a heterodyne amplifier of the weak Raman signals, enabling high-sensitivity detection. Moreover, experimental implementations for its removal lead to weaker signals, hence, lower SNRs, and greater experimental complexity. Therefore, numerical methods aiming at removing the non-resonant part after acquisition have been developed. These methods are phase-retrieval methods and exploit the intrinsic heterodyne nature of the CARS signal. They may be divided into two main classes: the ones based on the maximization of entropy (Maximum Entropy method: MEM) [46] and the ones relying on phase retrieval through the time-domain Kramers-Kronig (KK) relations [63].

In section 1.4, it has been shown that the CARS intensity scales quadratically with the modulus of the third-order nonlinear vibrational susceptibility $\chi_{VIB}^{(3)}$. Recalling that $\chi_{VIB}^{(3)} = \chi_R^{(3)} + \chi_{NR}^{(3)}$, we may write:

$$I_{AS} \propto \left| \chi_R^{(3)} \right|^2 + \left| \chi_{NR}^{(3)} \right|^2 + 2\chi_{NR}^{(3)} \Re \left\{ \chi_R^{(3)} \right\}, \quad (4.12)$$

The resonant susceptibility $\chi_R^{(3)}$ is a complex number, where the real part has a dispersive shape, while the imaginary part presents a Lorentzian shape. On the other hand, the non-resonant susceptibility $\chi_{NR}^{(3)}$ is real if far from electronic resonances. If one can extrapolate the phase $\varphi(\omega)$ of $\chi^{(3)}$, it is possible to recover the spectral information embedded in $\left| \chi_R^{(3)} \right|^2$. Therefore, both MEM and KK methods aim at retrieving the phase of $\chi^{(3)}$.

Time-domain Kramers Kronig algorithm

Let us introduce the phase retrieval method based on the time-domain Kramers-Kronig (KK) relations. According to the KK connection, a function, $f(\omega)$, has an explicit, causal relationship between its real and imaginary components. As a result, if just the real (or imaginary) component is known, the imaginary (or real) component can be determined. In CARS spectroscopy, neither the real nor the imaginary part of $\chi^{(3)}$ is directly accessible. However, there is an explicit connection between the complex norm of the function and the phase if the function is square integrable [63]:

$$\ln (|f(\omega)|) = -\tilde{\mathcal{H}} \{ \phi \}, \quad (4.13)$$

$$\phi = \tilde{\mathcal{H}} \{ \ln (|f(\omega)|) \}, \quad (4.14)$$

where $\tilde{\mathcal{H}}$ is the Hilbert transform. In order to calculate it, the complex modulus of the function or its phase over an infinite frequency range should be known. However, since we can measure only a portion of the spectrum, it is possible to define a windowed version of the Hilbert transform, $\tilde{\mathcal{H}}_w$, as:

$$\tilde{\mathcal{H}}_w \{ f(x); \omega_a, \omega_b \} = \frac{\mathcal{P}}{\pi} \int_{\omega_a}^{\omega_b} \frac{f(x')}{x - x'} dx', \quad (4.15)$$

where ω_a and ω_b are the boundaries of the covered spectral range and \mathcal{P} is the Cauchy principal value.

As long as two conditions are met:

1. The Raman peaks contained within this window are not impacted by that outside of the window
2. We are far from any electronic resonances, which is valid for infrared pump and Stokes beams

the Hilbert transform is related to its windowed version in eq.(4.15) by the relation:

$$\tilde{\mathcal{H}}_w \left\{ \frac{1}{2} \ln |\chi^{(3)}|^2 \right\} \simeq \tilde{\mathcal{H}} \left\{ \frac{1}{2} \ln |\chi^{(3)}|^2 \right\} + \epsilon(\omega), \quad (4.16)$$

where $\epsilon(\omega)$ is an additive error term. Let us consider the CARS signal intensity, I_{CARS} . In section. 1.4 we wrote it in terms of the pump and Stokes intensities, however, it could also be written in terms of electric fields as we did in eq.(1.61):

$$I_{CARS}(\omega) = \left| \{ [E_S(\omega) \otimes E_P(\omega)] \chi^{(3)}(\omega) \} * E_P(\omega) \right|^2 \equiv |\tilde{C}_{st}|^2 |\tilde{\chi}^{(3)}|^2, \quad (4.17)$$

where, in eq.(4.17), \otimes and $*$ are the cross-correlation and the convolution operators respectively. Let us define the correlation between pump and probe fields as $C_{st} = [E_S(\omega) \otimes E_P(\omega)]$. it corresponds to the coherent stimulation profile. Assuming a spectrally narrow pump, we can define the effective stimulation profile \tilde{C}_{st} and the effective non-linear susceptibility as:

$$\tilde{C}_{st}(\omega) \equiv \frac{[C_{st}(\omega) * E_P(\omega)]}{\int E_P(\omega) d\omega}, \quad (4.18)$$

$$\tilde{\chi}^{(3)}(\omega) \equiv \chi^{(3)}(\omega) * E_P(\omega), \quad (4.19)$$

Therefore, performing the windowed Hilbert transform (4.15) of the logarithm of the CARS signal intensity (4.17), taking into account eq.(4.16) and applying the property in eq.(4.14), we find:

$$\phi_{CARS} = \tilde{\mathcal{H}}_w \left\{ \frac{1}{2} \ln (I_{CARS}(\omega)) \right\} \simeq \epsilon(\omega) + \tilde{\mathcal{H}}_w \left\{ \frac{1}{2} \ln |\tilde{C}_{st}(\omega)|^2 \right\} + \tilde{\mathcal{H}} \left\{ \frac{1}{2} \ln |\tilde{\chi}^{(3)}(\omega)|^2 \right\}, \quad (4.20)$$

Applying again the Hilbert transform property eq.(4.14) to eq.(4.20), we find:

$$\phi_{CARS} \simeq \epsilon(\omega) + \tilde{\mathcal{H}}_w \left\{ \frac{1}{2} \ln |\tilde{C}_{st}(\omega)|^2 \right\} + \angle \left[\chi_R^{(3)} + \chi_{NR}^{(3)} \right], \quad (4.21)$$

where the \angle operator extracts the phase. This phase term contains several contributions: the error ϵ , due to the use of the windowed version of the Hilbert transform, the contribution from the effective stimulation profile, and the contribution from both the resonant and non-resonant parts of the third-order nonlinear susceptibility. If it was possible to measure the NRB intensity $I_{NRB} = |\tilde{C}_{st}|^2 |\tilde{\chi}_{NR}^{(3)}|^2$, we could apply the windowed Hilbert transform to the ratio I_{CARS}/I_{NRB} , obtaining:

$$\begin{aligned} \phi_{CARS/NRB} &= \tilde{\mathcal{H}}_w \left\{ \frac{1}{2} \ln \left(\frac{I_{CARS}(\omega)}{I_{NRB}(\omega)} \right) \right\} \simeq \epsilon(\omega) + \tilde{\mathcal{H}}_w \left\{ \frac{1}{2} \ln \left| \tilde{C}_{st}(\omega) \right|^2 \right\} + \\ &- \left[\epsilon(\omega) + \tilde{\mathcal{H}}_w \left\{ \frac{1}{2} \ln \left| \tilde{C}_{st}(\omega) \right|^2 \right\} \right] + \angle \left[\chi_R^{(3)} + \chi_{NR}^{(3)} \right] - \angle \left[\chi_{NR}^{(3)} \right] \simeq \\ &\angle \left[\chi_R^{(3)} + \chi_{NR}^{(3)} \right], \end{aligned} \quad (4.22)$$

where in the last part of eq.(4.22) we implicitly assumed that $\chi_{NR}^{(3)}$ is real, being far from electronic resonances. Using the ratio of the CARS and NRB intensities as our signal, the complex spectrum can be written as:

$$I_{CARS/NRB} = \sqrt{\frac{I_{CARS}(\omega)}{I_{NRB}(\omega)}} \exp i\phi_{CARS/NRB} \simeq \frac{|\tilde{\chi}^{(3)}|}{|\tilde{\chi}_{NR}^{(3)}|} \exp i\angle \left[\chi_R^{(3)} + \chi_{NR}^{(3)} \right], \quad (4.23)$$

The Raman-like spectrum can be extracted as the imaginary part of $I_{CARS/NRB}$ in eq.(4.23):

$$\Im \{ I_{CARS/NRB} \} = \frac{\text{Im} \left\{ \chi_R^{(3)}(\omega) \right\}}{\left| \chi_{NR}^{(3)} \right|}, \quad (4.24)$$

where the imaginary part of the resonant third-order non-linear susceptibility carries the vibrational information. Therefore, the retrieved spectrum is directly proportional to the spontaneous Raman one, scaled by the non-resonant component.

The described method relies on a precise measurement of the non-resonant background. However, up to now, it is not possible to measure the pure contribution of the non-resonant term. To circumvent this problem, the NRB spectrum is measured from a reference material with no Raman peaks, such as glass or water. However, this leads to a multiplicative complex error which should be taken into account.

The reference measurement, I_{ref} can be linked to I_{NRB} by the multiplicative relation: $I_{ref}(\omega) = \xi(\omega)I_{NRB}(\omega)$, where $\xi(\omega)$ is assumed to be real and positive. Let us calculate the phase of the ratio I_{CARS}/I_{ref} , similarly to what we did in eq.(4.22):

$$\phi_{CARS/ref} = \tilde{\mathcal{H}}_w \left\{ \frac{1}{2} \ln \left(\frac{I_{CARS}(\omega)}{\xi(\omega)I_{NRB}(\omega)} \right) \right\} \simeq \phi_{CARS/NRB} + \underbrace{\tilde{\mathcal{H}}_w \left\{ \frac{1}{2} \ln \left(\frac{1}{\xi(\omega)} \right) \right\}}_{\phi_{err}}, \quad (4.25)$$

As we did in eq.(4.23), we can calculate the imaginary part of the spectrum obtained as the ratio $I_{CARS/ref} = I_{CARS}/I_{ref}$, where we use I_{ref} instead of I_{NRB} :

$$\text{Im} \{ I_{CARS/ref} \} = \underbrace{\sqrt{\frac{1}{\xi(\omega)}}}_{A_{err}(\omega)} \sqrt{\frac{I_{CARS}(\omega)}{I_{NRB}(\omega)}} \sin \left[\phi_{CARS/NRB} + \phi_{err} \right] \quad (4.26)$$

From eq. 4.25 and eq. 4.26, it can be seen that using a reference instead of the real NRB leads to an amplitude (A_{err}) and a phase (ϕ_{err}) error. A_{err} and ϕ_{err} are linked by the relationship:

$$\begin{aligned}\ln A_{err}(\omega) &= -\tilde{\mathcal{H}}\{\phi_{err}(\omega)\}, \\ \phi_{err}(\omega) &= \tilde{\mathcal{H}}\{\ln A_{err}(\omega)\},\end{aligned}\quad (4.27)$$

where the Hilbert transform property in eq. (4.14) has been used. However, since the Hilbert transform of a constant is equal to zero, there is an ambiguity in eq.4.27. In particular, if $\xi(\omega)$ is multiplied by a constant α , the phase error remains the same:

$$\phi_{err}(\omega) = \tilde{\mathcal{H}}\left\{\ln \frac{1}{\alpha\xi(\omega)}\right\} = \tilde{\mathcal{H}}\left\{\ln \frac{1}{\xi(\omega)}\right\}.\quad (4.28)$$

These phase and amplitude errors can be corrected with the following strategies:

1. Remove phase error via detrending $\phi_{CARS/ref}$ and correct part of the amplitude error exploiting the relationship in eq.(4.27),
2. Correct for scaling errors, related to the constant α , and for the use of the windowed version of the Hilbert transform in step 1, leading to ϵ_{err} . Then unity centering the real component of the phase-corrected spectrum [63].

Let us start with the phase correction. The phase $\phi_{CARS/ref}(\omega)$ is qualitatively similar to a Raman-like spectrum since peaks extend positively over a baseline. However, the slowly-varying phase error ϕ_{err} causes a slowly-varying deviation from the zero baselines. Therefore, isolating the erroneous baseline allows us to find ϕ_{err} . Using traditional baseline detrending methods, $\phi_{err}(\omega)$ can be extracted from $\phi_{CARS/ref}(\omega)$ and removed. Moreover, using eq. 4.27, part of the amplitude error can be corrected. The two corrections can be implemented by multiplying the retrieved spectrum $I_{CARS/ref}$ by a complex phase-correction multiplier. The phase corrected spectrum I_{pc} reads as:

$$\begin{aligned}I_{pc} &= I_{CARS/ref} \left\{ \frac{1}{\exp\left[-\tilde{\mathcal{H}}_w\{\phi_{err}(\omega)\}\right]} \exp[-i\phi_{err}(\omega)] \right\} = \\ &= \sqrt{\frac{I_{CARS}(\omega)}{I_{ref}(\omega)}} \exp i\phi_{CARS/ref} \left\{ \frac{1}{\exp\left[-\tilde{\mathcal{H}}_w\{\phi_{err}(\omega)\}\right]} \exp[-i\phi_{err}(\omega)] \right\},\end{aligned}\quad (4.29)$$

We can now proceed with the amplitude correction. In 4.28 we saw that retrieving A_{err} from ϕ_{err} leads to an ambiguity related to the scaling constant α . Furthermore, in 4.29, the windowed version of the Hilbert transform, $\tilde{\mathcal{H}}_w$, was used in place of $\tilde{\mathcal{H}}$, causing a window-effect error $\epsilon_{err}(\omega)$:

$$\tilde{\mathcal{H}}\{\phi_{err}(\omega)\} = \tilde{\mathcal{H}}_w\{\phi_{err}(\omega)\} + \epsilon_{err}(\omega),\quad (4.30)$$

Therefore we need to correct for the A_{err} ambiguity and $\epsilon(\omega)$. Both of these variables can be found by examining the real component of the phase-corrected spectrum in 4.29. Since the real component of 4.23 is unity centered, which means that

$\langle |\tilde{\chi}^{(3)}|/|\tilde{\chi}_{NR}^{(3)}| \cos \phi_{CARS/NRB} \rangle = 1$, any alteration of the mean of the real component in 4.29 is caused by the presence of the scaling constant α , thus, one could measure this mean and normalize I_{pc} by this value. Nevertheless, ϵ_{err} might give this means a frequency-dependent component. Using numerical means, though, one can find a slowly varying centerline and normalize the phase-corrected spectrum, thus removing α and ϵ_{err} in one step. Finally, a rescaled, phase-corrected, complex spectrum $I_{pc,sc}$ may be calculated as:

$$I_{pc,sc} = \frac{I_{pc}(\omega)}{\langle Re \{I_{pc}(\omega)\} \rangle (\omega)} = \frac{|\tilde{\chi}^{(3)}|}{|\tilde{\chi}_{NR}^{(3)}|} \exp [i\phi_{CARS/NRB}], \quad (4.31)$$

The KK algorithm for NRB removal demonstrates how the pure vibrational information can be extrapolated even using a reference measurement of the non-resonant background [63]. An example of the application of the algorithm is shown in Fig. 4.12.

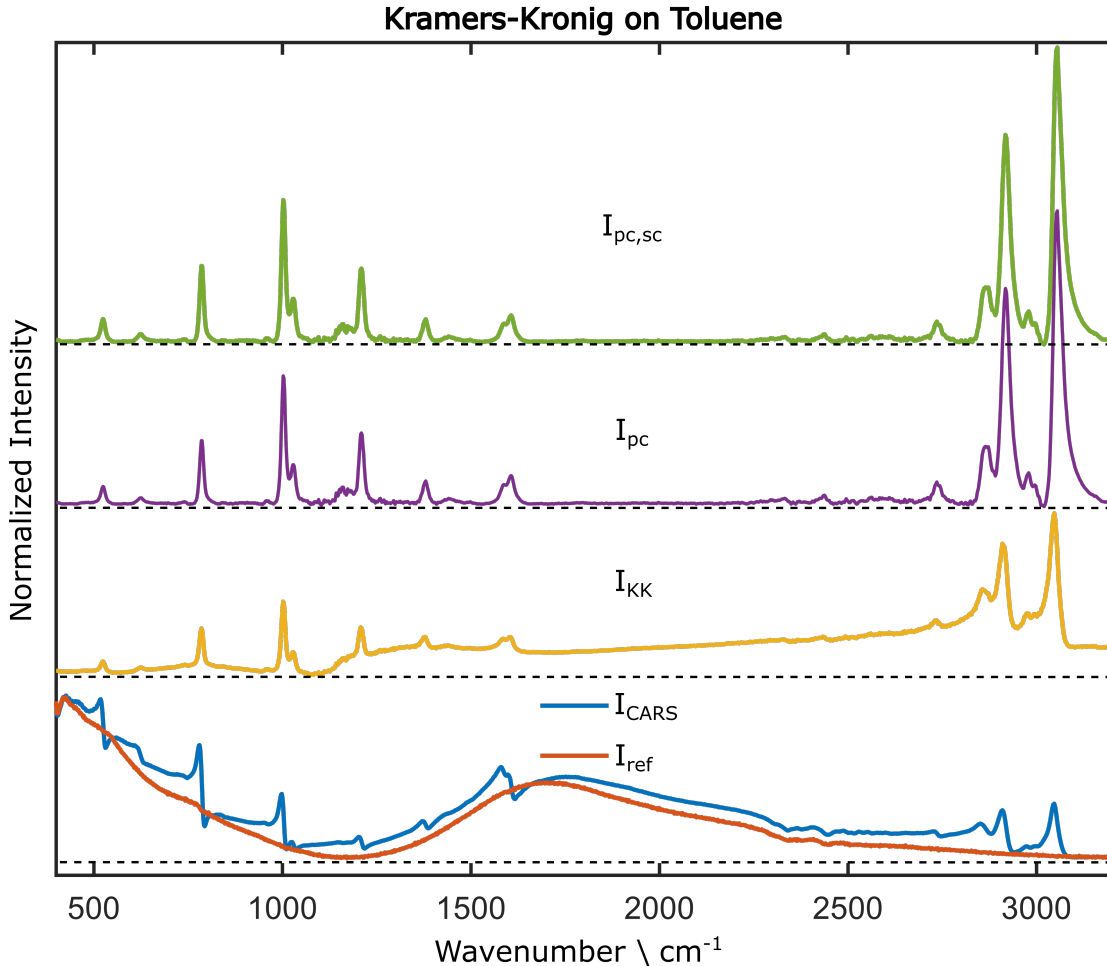


Figure 4.12: Example of the application of the KK algorithm to a spectrum of toluene. I_{CARS} : CARS spectrum of toluene (blue curve), I_{ref} reference spectrum on glass (orange curve), I_{KK} phase retrieved spectrum after the Hilbert transform (yellow curve), I_{pc} phase corrected spectrum (violet curve), $I_{pc,sc}$ phase and scale corrected spectrum (green curve).

Maximum Entropy Method

I will briefly describe the Maximum Entropy Method (MEM) which has been demonstrated to be functionally equivalent to the time-domain KK algorithm [46]. The MEM algorithm is based on the hypothesis that any inferences made from incomplete data should be consistent with maximized entropy of the associated probability distribution, given the constraints of the known information [176]. This hypothesis can be applied to compute a power spectrum $S(\nu)$ associated with discrete measured data [46, 96]. This could be applied to model the CARS lineshape as:

$$S(\nu) = \left| \frac{\beta}{1 + \sum_{k=1}^M a_k \exp(-2\pi i k \nu)} \right|^2 \equiv \left| \frac{\beta}{A_M(\nu)} \right|^2 \quad (4.32)$$

where ν is the frequency, normalized to run from 0 to 1 over the experimental range, A and β are complex coefficients, and M is the number of correlation coefficients used for reconstructing the spectrum. M can be as high as the number of spectral points (N); however, the higher order coefficients represent primarily noise, therefore typically $M \leq N/2$ is used. The coefficients a_k and β can be found solving the Toeplitz equation (4.38):

$$\begin{bmatrix} C_0 & C_1^* & \cdots & C_M^* \\ C_1 & C_0 & \cdots & C_{M-1}^* \\ \vdots & \vdots & \ddots & \vdots \\ C_M & C_{M-1} & \cdots & C_0 \end{bmatrix} \begin{bmatrix} 1 \\ a_1 \\ \vdots \\ a_M \end{bmatrix} = \begin{bmatrix} |\beta|^2 \\ 0 \\ \vdots \\ 0 \end{bmatrix} \quad (4.33)$$

where $*$ denotes the complex conjugate and C_k are the discrete Fourier transform of the CARS spectrum at a discrete set of normalized frequencies $\nu_n = n/N$, with $n = 0, 1, \dots, N$, calculated as:

$$C_k = N^{-1} \sum_{n=0}^{N-1} S(\nu_n) \exp(2\pi i k \nu_n), \quad (4.34)$$

where $S(\nu)$ is normalized by the NRB reference spectrum. Substituting the values of the coefficients a_k and β (which are found solving (4.38), taking (4.34) into account) in eq. 4.32, it is possible to find $A_M(\nu)$, from which the spectral phase ϕ_{CARS} can be retrieved as:

$$\phi_{CARS}(\nu) = \angle[A_M(\nu)], \quad (4.35)$$

This result is obtained directly from the measured spectrum, however, in (4.35), the error due to a non-real NRB contribution has not been taken into account yet. The errors introduced by the presence of a reference spectrum in place of the real NRB are assumed to contribute to a slowly varying baseline that can be subtracted in a similar way as it is done in the time-domain KK algorithm.

4.5.2 NRB removal via deep learning

The NRB removal task can also be read as a supervised machine-learning task. Indeed, the main idea is that a DNN can approximate the nonlinear and complex function that

maps the measured CARS spectrum with the imaginary part of the third-order nonlinear susceptibility. At the beginning of my Ph.D., I took part in the realization of a CNN for the removal of the NRB. This work has been published in [48].

So far I have introduced the phase reconstruction methods which are mostly used when dealing with CARS spectroscopy. However, both the KK algorithm and the MEM methods for the retrieval of the pure vibrational information and removal of the NRB contribution, require an independent measurement of a reference spectrum. Moreover, the phase-retrieved spectra rely on the choice of parameters made by the user. The main advantage of substituting these algorithms with supervised learning methods is the possibility to retrieve pure vibrational information in an unbiased way without requiring the measurement of a reference material.

Model architecture

We realized a CNN inspired by the most common Lenet architecture [167] that combines convolutional layers and fully connected layers. The formers have the main role of extrapolating the features from the CARS spectra that are the typical dispersive line-shapes deriving from the heterodyne term in the expression of the CARS signal. The latters restore the initial dimension of the inputs, generalizing the information discovered previously by the convolutional layers and correlating the feature maps derived from the input outputting the imaginary part of the third-order susceptibility. The code of the network is available online [177]. The network, called SpecNet, consists of five 1-dimensional convolutional layers with 128, 64, 16, 16, and 16 filters of dimensions 32, 16, 8, 8, and 8, respectively, followed by three fully connected layers of 32, 16, and 640 neurons (as the output is expected to have the same dimensions as the input). All layers had a ReLU (rectified Linear Unit) activation function (see Fig. 4.13.(a-b)).

Training dataset

The input data features 640 spectral points. We trained the network using a synthetic dataset. In particular, knowing that the CARS intensity scales quadratically with the modulus of $\chi_{VIB}^{(3)} = \chi_R^{(3)} + \chi_{NR}^{(3)}$, we simulated the resonant term $\chi_R^{(3)}$ as the sum of N Lorentzian functions (with N up to 15), with amplitude following a uniform distribution $\mathcal{U}(0, 1)$, width uniformly distributed as $\mathcal{U}(0.001, 0.008)$ and centered with a random frequency ν following a uniform distribution $\mathcal{U}(0, 1)$. The non-resonant contribution, mimicking the NRB in our spectra, is generated as the product of two sigmoidal functions (see Fig. 4.14.(c)), i.e. $\chi_{NR}^{(3)} = \sigma_1 \sigma_2$ with:

$$\sigma_i = \frac{1}{1 + \exp[-(\nu - c_i)s_i]} \quad (4.36)$$

where ν is the normalized frequency, $i = 1, 2$ and c, s define the center and broadness of the sigmoidal functions and are chosen so that c_1 follows a normal distribution $\mathcal{N}(0.2, 0.3)$, c_2 follows a normal distribution $\mathcal{N}(0.7, 0.3)$, and $s_{1,2}$ are opposite numbers following a normal distribution $\mathcal{N}(10, 5, 2)$. After normalizing the CARS signal, we added random noise to the CARS signal with amplitude uniformly distributed as $\mathcal{U}(0.0005, 0.003)$. The simulated CARS signal (see Fig. 4.14.(a)) has the form:

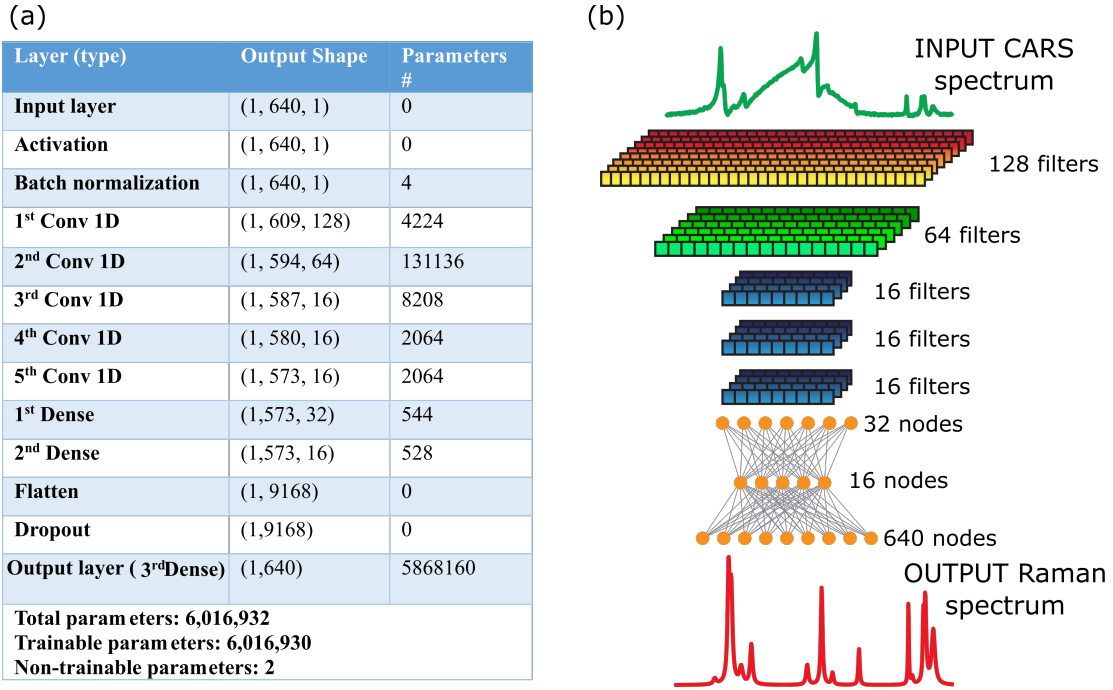


Figure 4.13: Model architecture of the SpecNet network for the NRB removal. (a) Hyperparameters of the neural network. (b) Graphical representation of the SpecNet.

$$I_{CARS} = \frac{|\chi_R^{(3)}(\nu) + \chi_{NR}^{(3)}(\nu)|}{2} + noise \quad (4.37)$$

The ground truth of the network is obtained by computing the imaginary part of $\chi_R^{(3)}(\nu)$ (see Fig. 4.14.(b)). The training dataset is constituted of 50000 instances. The loss function chosen was the mean squared error (MSE) between the true target vector y and the predicted one \hat{y} . To avoid overfitting and reduce the sensitivity of the model to noise, we utilized L^2 weight regularization [159] on the weights of the first fully connected layer with a weight of $5 \cdot 10^{-1}$. The optimization has been performed using the Adam optimizer with a batch size of 256 examples. The entire training procedure required 10 epochs. The computing time required to process a spectrum, averaged over 100 000 examples, is about 0.1 ms, which is much shorter than the current state of the art for the acquisition time of a BCARS spectrum, around 3 ms for biological tissues.

Model performances and test on experimental data

After the training, the MSE loss function of the training dataset is $6.2 \cdot 10^{-4}$ and the validation loss function is $5.64 \cdot 10^{-4}$ (see Fig. 4.15). Thanks to the capability of convolutional layers to handle spatial invariance, i.e. to recognize similar structures in different locations of the input, although the model was trained with a maximum number of peaks $N = 15$, it performs well even if the number of features is larger. Indeed, by testing the network on a sample made of more than 15 peaks, the prediction is in good agreement with the ground truth (Fig. 4.16).

Eventually, the network has shown good performances when tested on experimental data. I tested the network with experimental data acquired with the BCARS setup

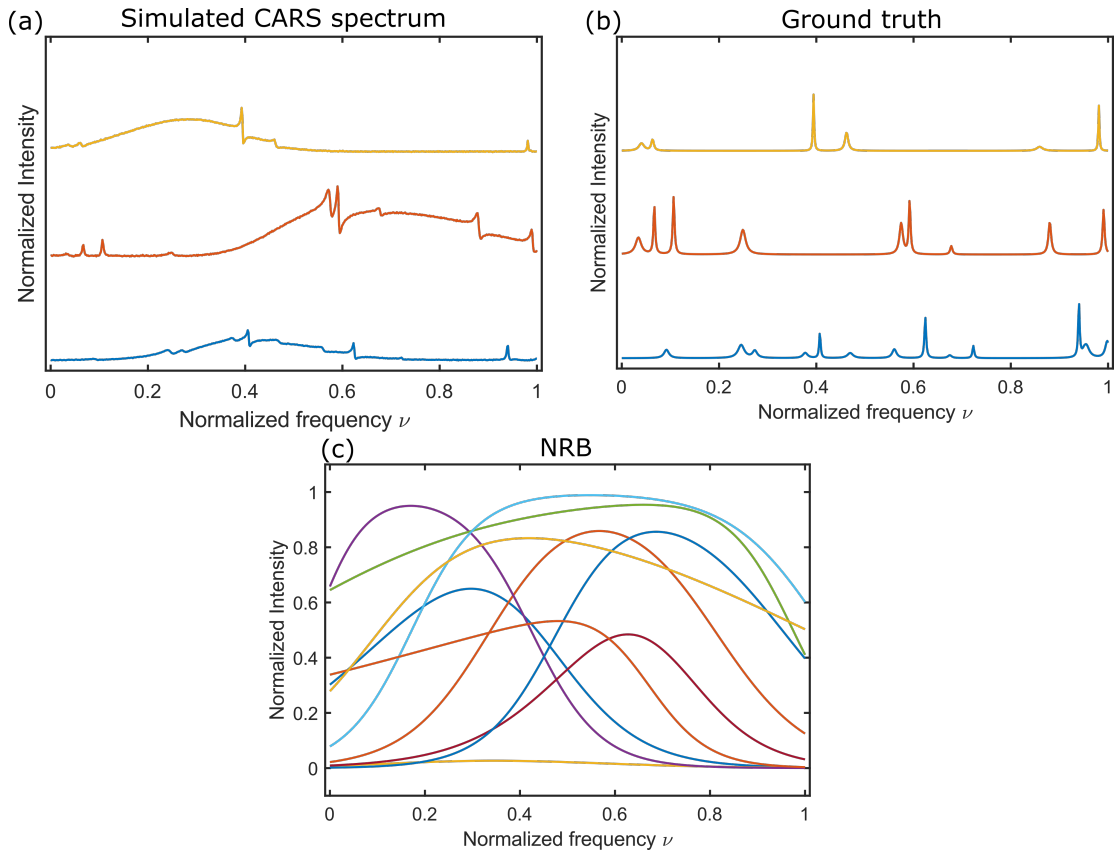


Figure 4.14: Simulated data for the SpecNet. (a) Simulated CARS spectra. (b) Ground truth relative to the simulated CARS spectra in (a). (c) Examples of the simulated nonresonant contribution deriving from the product of two sigmoidal functions.

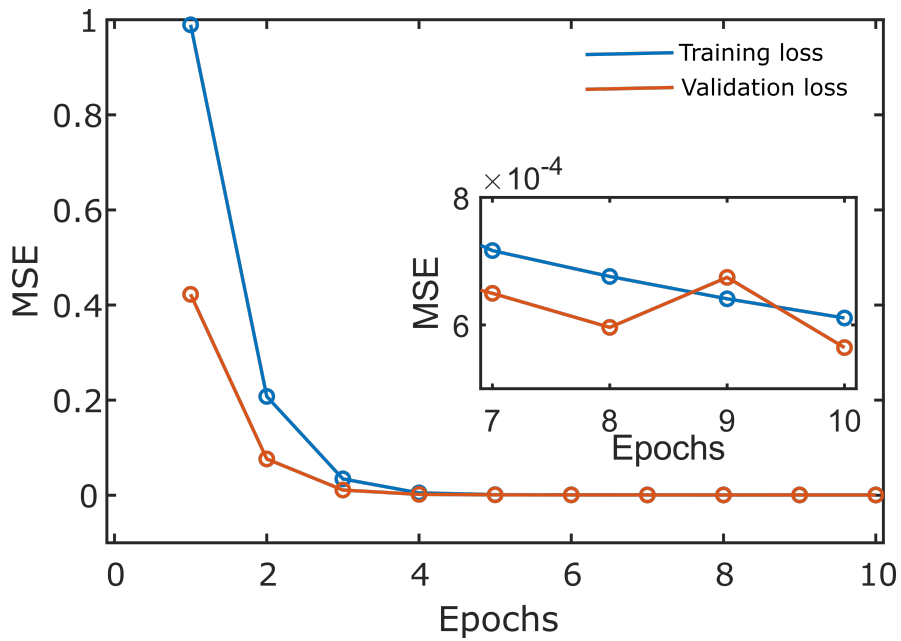


Figure 4.15: Mean square error (MSE) loss of the training and validation set after 10 epochs of training with 50000 instances.

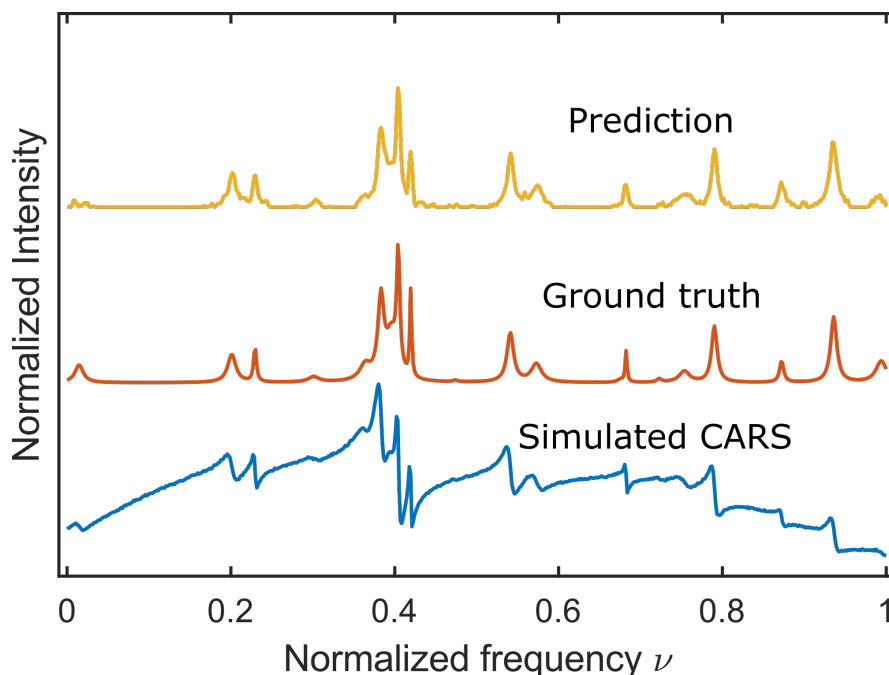


Figure 4.16: Prediction of the SpecNet on a spectrum with a higher number of spectral peaks than the typical spectra of the training dataset.

using a spectrometer equipped with a front-illuminated CCD with 1024 spectral pixels (PIXIS100, Princeton Instruments). I measured the spectra of six solvents: acetone, ethanol, methanol, isopropanol, dimethyl sulfoxide (DMSO), and toluene (see Fig. 2(a)). For these experiments, using solvents droplets deposited between two 170 μm glass coverslips (see Fig. 4.17), I set the CCD exposure time to 0.8 ms, i.e., the minimum allowed by the detector electronics, and collected single-point B-CARS spectra, spanning the whole fingerprint region from 500 to 2000 cm^{-1} . For each spectrum, I averaged 30 spectra and cropped the data selecting the whole fingerprint region to have 640 spectral points (blue curves in 4.17) and used them to feed the network after normalization. The prediction of the SpecNet (orange curves in 4.17) have been compared with the spontaneous Raman spectra obtained averaging 5 spectra acquired with 5 s integration time (grey areas in 4.17). The traces show a good agreement, indeed, all the main peaks in the fingerprint region are recognized by the network and the NRB is completely suppressed. Despite its capabilities in the recognition of the peaks, the SpecNet is still sensitive to random noise, thus making harder the recognition of small features in the fingerprint region. This last aspect calls for further improvement of the training set on which we are currently working.

Conclusion

We realized a deep-learning model called SpecNet that enables the user to remove the non-resonant background contribution from broadband CARS spectra. The model is built as a CNN with seven hidden layers. The training was performed on a simulated dataset that allows a high generalization capability to different spectral shapes of the non-resonant background. The performances of the network were assessed on real

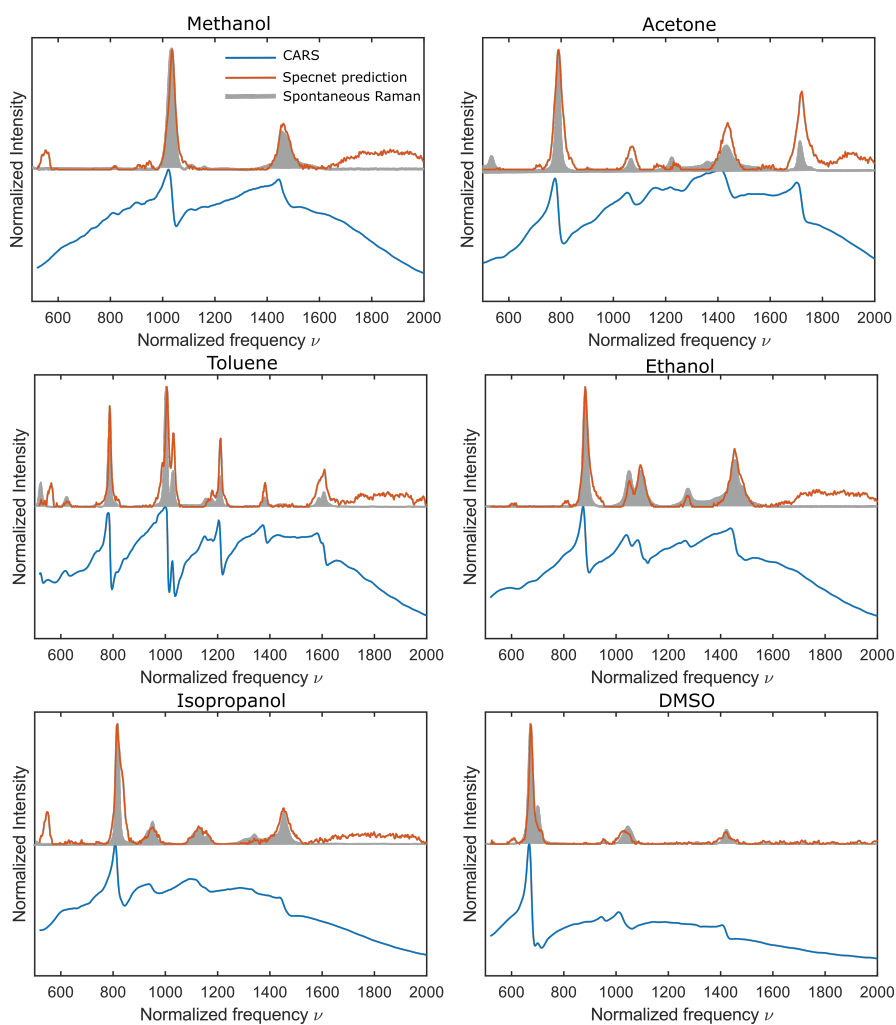


Figure 4.17: Prediction of the SpecNet on experimental data acquired on 6 different solvents acquired with the BCARS setup: methanol, acetone, toluene, ethanol, isopropanol, dimethyl sulfoxide (DMSO). Each spectrum is the average of 30 spectra acquired with 0.8 ms pixel dwell time. Spectral points: 640.

experimental data, and the model was able to correctly process them retrieving all the relevant vibrational peaks of different solvent specimens in a time of 0.1 ms, which is faster than the time required to record the spectrum. Moreover, the model does not need the independent measurement of a reference sample or any manual intervention by the operator for the processing as it is needed using numerical algorithms such as the KK algorithm or the MEM method. This could be implemented, for example, in parallel during the integration time of the next pixel so that no time is lost for the spectral processing at all, thus considerably reducing the processing time of CARS hyperspectral images.

We believe that this approach for NRB removal will speed up BCARS processing and may be implemented for online retrieval of the vibrational peaks.

4.5.3 State-of-the-art of NRB removal via deep learning

Recently, many works on NRB removal via deep learning have been published. One of them was published contemporary to ours and employs a different model and training dataset [49], while others improve the performances of the SpecNet by either changing the model architecture [50] or the training dataset [178, 179]. Houhou et al. [49] published a work in 2020, the same year as SpecNet, where the NRB removal task was tackled by a long short-term memory(LSTM) [180] topology of the network. The LSTM deals with sequential data and has the same architecture as recurrent neural networks. In 2022, Wang et al. [50] proposed a new DNN architecture called Very dEep Convolutional auTOencodeRs (VECTOR), using the same training dataset generated in out SpecNet. VECTOR is constituted by an encoder and a decoder. On the one hand, the encoder aims to compress the input to a lower dimensional latent representation without losing critical information. The decoder learns to reconstruct the input from the compressed representation. Skip connections are introduced to bypass the encoder to the decoder, thus boosting the performance of the network reaching lower MSE with respect to our SpecNet. In 2022, Junjury et al. [178] used the SpecNet and retrained the model with a new training set made of synthetic and semi-synthetic data. While the synthetic data were generated using our code, the semi-synthetic data is built starting from spontaneous Raman data, applying DA to them thus increasing the numerosity of the dataset, retrieving the real and imaginary part through the Kramers-Kronig relations and adding simulated NRB in the same way it is done for the synthetic data. The retrained model has shown potential improvement compared to the SpecNet model in terms of efficient extraction of imaginary parts across the total spectral range. Further individual peak analysis has revealed that the proposed model predicted the peak amplitudes, widths, and centers without much deviation from the true ones. The final results on the experimental CARS spectra demonstrated the potential of the approach where prediction error is 10 times less compared to the original SpecNet model. Eventually, in 2022, the same group of Junjury, led by Vartiainen, published another work [179] in which the performances of the SpecNet are boosted by fine-tuning with semi-synthetic spectra the SpecNet model trained on synthetic data.

Despite many improvements, since the publication of the SpecNet, NRB removal via deep learning is not still used for BCARS imaging. In the framework of the CRIMSON project, I am currently collaborating with other partners of the consortium in finding a generalized model that can be used with spectra acquired in different labs and can

show good prediction not only for CARS spectroscopy but also for BCARS imaging. The model combines the main features of the network published in the literature (CNN and recurrent neural networks) and will be based on a new training dataset that includes all the possible scenarios one can encounter when acquiring spectra with a BCARS system.

4.6 Spectral unmixing

After the two post-processing steps that I described above, i.e. the denoising of the hyperspectral data and the removal of the NRB, the last step consists of the unmixing of the chemical components of the heterogeneous samples. This step is intended only for microscopic applications, i.e. for CARS imaging. When doing spectroscopy other strategies, such as principal component analysis, can be used for identifying the different features of the spectra belonging to the investigated analytes. For spectral unmixing in CARS images, we can distinguish two classes of algorithms: the factorization and the clusterization methods.

The first ones have the goal of decomposing the hyperspectral dataset \mathbf{D} in a matrix of the spectra \mathbf{S} and a matrix of concentrations \mathbf{C} so that $\mathbf{D} = \mathbf{CS}^* + \epsilon$ where ϵ is the error that has to be minimized in the iterative process of the algorithms. It implies that in the factorization methods, each pixel spectrum of the image can be seen as a linear combination of the spectral basis identified by the algorithm and the coefficients of this linear combination represent the concentrations of that species in the sample. Throughout my Ph.D. experimental activity, I mainly used two factorization methods which are the multivariate curve resolution-alternating least squares (MCR-ALS) analysis and the N-FINDR algorithm.

On the other hand, the clusterization methods aim at identifying in the hyperspectral images two or more groups of pixels with similar spectral features. The spectrum associated with the cluster will be representative of all the pixels belonging to the cluster. In this case, if one pixel belongs to a group it cannot be part of the other group. So that we have as output a matrix of the representative spectra and an image where each pixel is associated with only one class. As for the clusterization methods, I mainly used the hierarchical cluster analysis and the k-means cluster analysis (KMCA).

In the following sections, I will briefly describe the main algorithms that I used for the processing of the data shown in the next chapter. These are the MCR-ALS algorithm, the N-FINDR algorithm, and the KMCA algorithm.

4.6.1 Multivariate curve resolution analysis

The MCR-ALS algorithm has been popularized by Tauler and colleagues [181–183]. For this approach, we assumed that the hyperspectral data cube \mathbf{D} , unfolded as a number of pixels times spectral points matrix, is a linear combination of the concentration \mathbf{C} and the spectral profiles \mathbf{S} of the chemical constituents of the sample, i.e., $\mathbf{D} = \mathbf{CS}^* + \epsilon$. Here, ϵ is a matrix containing the experimental error, while the superscript $*$ means the transpose of the matrix. The algorithm starts by obtaining \mathbf{C} and \mathbf{S} through a singular-value decomposition of the spectral data and these two matrices constitute the initial guesses. Assuming we want to define the guessed \mathbf{S} as the pure spectra, we could calculate $\mathbf{C} = \mathbf{DS}^*(\mathbf{S}^*\mathbf{S})^{-1}$ and $\mathbf{S}^* = (\mathbf{C}^*\mathbf{C})^{-1}\mathbf{C}^*\mathbf{D}$. These new values of \mathbf{C} and \mathbf{S} are

then optimized with an alternating least-squares (ALS) algorithm. Since CARS spectra and concentrations must be positively signed, the alternating least-squares algorithm is constrained to deliver only non-negative results. The optimized \mathbf{C} and \mathbf{S} enable us to allowed us to reconstruct a new matrix $\tilde{\mathbf{D}} = \mathbf{CS}^*$ which is compared with the initial dataset \mathbf{D} . We iterate these steps until the error ϵ is less than an arbitrary threshold value. The matrices \mathbf{C} and \mathbf{S} are respectively the chemical images of the concentrations and spectral profiles of the different species of the heterogeneous sample.

4.6.2 N-FINDR algorithm

The N-FINDR algorithm [184] is a factorization method that allows us to reduce the dimensionality of the hyperspectral data by finding the combination of spectra, called endmembers, which best represents the whole image. The algorithm is based on the maximization of a quantity which is the volume that is proportional to the determinant of a matrix \mathbf{E} that is the augmented matrix of the endmembers. Defining the i -th endmember as e_i , the augmented endmember matrix \mathbf{E} is:

$$\mathbf{E} = \begin{bmatrix} 1 & 1 & \cdots & 1 \\ e_1 & e_2 & \cdots & e_m \end{bmatrix} \quad (4.38)$$

with m the number of endmembers. The volume is defined as:

$$V(\mathbf{E}) = \frac{1}{(m-1)!} \text{abs}(|E|) \quad (4.39)$$

The algorithm begins with a random set of vectors. To find the endmembers, every pixel in the image must be evaluated as to its likelihood of being a pure or nearly pure pixel. This is done by calculating the volume with each pixel in place of each endmember. If the replacement results in an increase in volume, the pixel replaces the endmember. This procedure is repeated until there are no more replacements for endmembers. Once the endmembers are found, the spectra constitute the new basis onto which project the initial image, using a non-negatively constrained least squares algorithm. This last step finds the abundances or concentration maps of the reduced dataset.

4.6.3 K-means cluster analysis

K-means cluster analysis (KMCA) is a clusterization algorithm used for spectral unmixing. Clustering is the partitioning of the original dataset into k subsets called clusters [185, 186]. The number k of clusters is arbitrarily selected through an initial guess. The k-means algorithm starts by randomly distributing the k -clusters. Then, the algorithm assesses the distance of all spectra of the dataset to the mean cluster spectrum. Finally, it assigns each spectral trace to the cluster with the closest mean spectrum. Note that iterating the previous steps provides optimized results [186]. The main goal of the KMCA is to minimize the distances between the data within each cluster and to maximize the distances between different clusters according to some well-defined distance metric. The most employed clustering criterion is the sum of the squared Euclidean distances between each instance x_i (a pixel spectrum) and the centroid m_j (cluster center

spectrum) of the subset. This distance is known as clustering error [187]:

$$E(m_1, \dots, m_k) = \sum_{(i=1)}^N \sum_{(j=1)}^k (I(x_i \in C_j)) |x_i - m_j|^2 \quad (4.40)$$

where C_j denotes the j -th cluster and I is a function whose value is 1 when the i -th instance belongs to the cluster C_j or 0 when such instance belongs to another cluster. As mentioned above, the k -means algorithm finds locally optimal solutions with respect to this distance metric through iteration.

CHAPTER 5

Results

5.1 Introduction

In this chapter, I will present and discuss the results obtained with the BCARS system and the post-processing methods mentioned in the previous chapters. In particular, the chapter will be divided into two main sections.

The first section is entitled "Fingerprint multiplex CARS at high speed based on supercontinuum generation in bulk media and deep learning spectral denoising" and refers to all the results published in this paper [100]. For these results, the CARS spectra were obtained exploiting only the two-color mechanism and it allows us to access the fingerprint region of many samples such as solvents, polymer beads, and biological tissues, e.g. longitudinal slices of murine vertebrae. The data post-processing is based on a pipeline based of three steps: the CNN spectral denoiser, the KK algorithm for NRB removal, and spectral unmixing algorithms such as MCR-ALS and KMCA.

The second section entitled "Ultrabroadband CARS microscopy of biological samples with white light continuum in bulk media" shows the most recent results obtained with the experimental setup that combines two different excitation methods for CARS generation, the two-color, and the three-color mechanism. This configuration allows us to access the whole Raman active region of biological samples. These results are still unpublished and will be part of a manuscript that is in preparation.

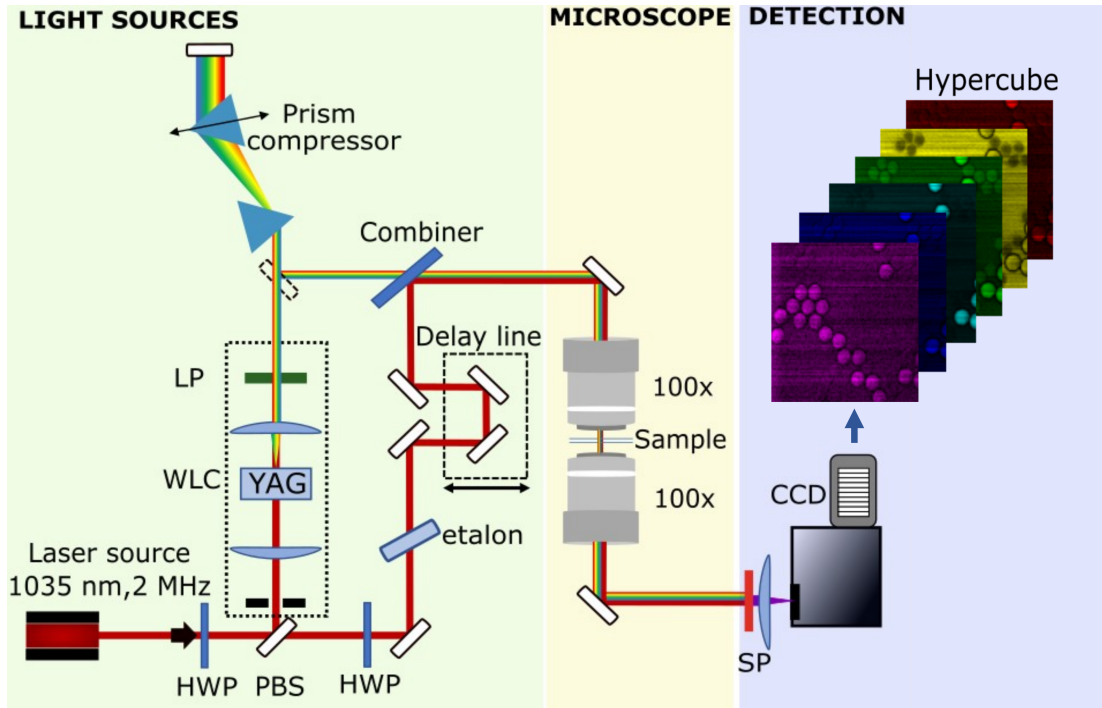


Figure 5.1: Scheme of the BCARS experimental setup. HWP: half-wave plate; PBS: polarizing beam splitter; LP: long-pass filter; SP: short-pass filter.

5.2 Fingerprint multiplex CARS at high speed based on supercontinuum generation in bulk media and deep learning spectral denoising

5.2.1 Experimental setup and post-processing pipeline

The architecture of the B-CARS microscope is shown in Fig. 5.1. The system features 1.1 ps narrowband pump pulses with energy fluctuations $<1\%$ RMS generated by spectral filtering through a high-finesse Fabry–Perot etalon, which allows reaching a spectral resolution of $\approx 11\text{cm}^{-1}$ ($\approx 1.1\text{ nm}$ FWHM bandwidth). The broadband Stokes source generated into the 10-mm YAG crystal shows very good stability with energy fluctuations $<1\%$ RMS comparable to those of the driving laser. A long-wave-pass filter selects the red-shifted lobe of the WLC (1050 – 1300 nm) that has a spectral energy density high enough to generate CARS in the entire fingerprint region even at very short pixel-dwell times. An SF-11 prism pair compresses the Stokes pulse, compensating for the dispersion introduced by the optical elements of the system. The pulse duration of the Stokes at the sample plane is comparable to the one of the pump beam since no temporal chirp is experienced when detecting the CARS spectra. The microscope is equipped with two identical 100 \times air objectives with NA=0.85. For the CARS signal acquisition, I used a spectrometer made of a monochromator (ACTON SP2150, Princeton Instruments) equipped with a front-illuminated CCD with 1024 spectral pixels (PIXIS100, Princeton Instruments). Average powers of $\approx 40\text{ mW}$ for the pump and $\approx 10\text{ mW}$ for the Stokes beam at the sample plane have been used for all the experiments.

The post-processing pipeline that I employed for the analysis of the BCARS spectra

5.2. Fingerprint multiplex CARS at high speed based on supercontinuum generation in bulk media and deep learning spectral denoising

and hyperspectral data is schematically shown in Fig. 5.2. It is divided into three main steps: (i) a spectral denoiser based on a CNN architecture to increase the SNR of the acquired CARS spectra; (ii) a numerical method to remove NRB from the spectra, based on the Kramers-Kronig relations [63], and (iii) spectral unmixing methods that are the MCR-ALS algorithm and the KMCA algorithm to discern the different chemical constituents in the heterogeneous samples.

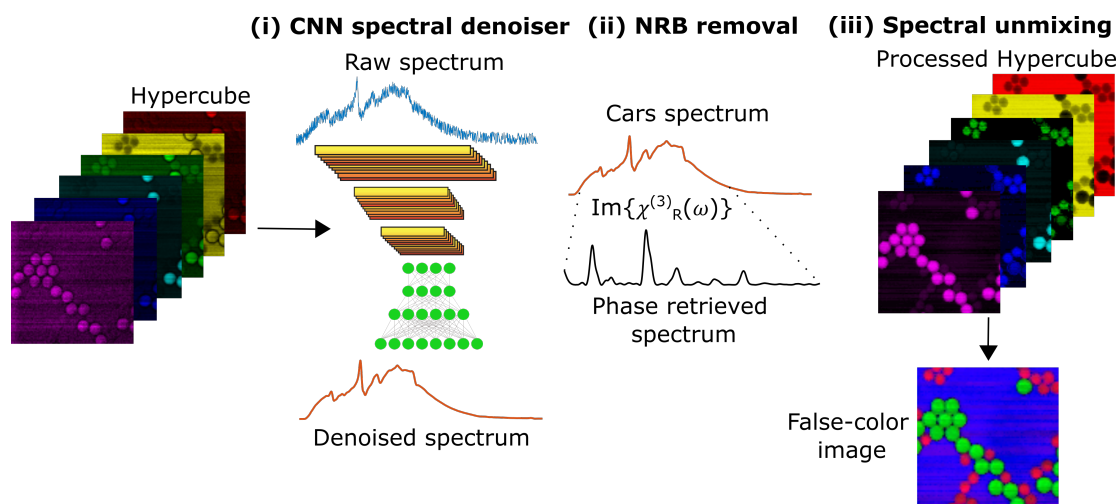


Figure 5.2: Scheme of the data processing pipeline: (i) CNN spectral denoiser, (ii) NRB removal via the KK algorithm, and (iii) Spectral unmixing methods to obtain false-color images.

5.2.2 BCARS spectroscopy of solvents

The system was first used to acquire the spectral profiles of six solvents: acetone, ethanol, methanol, isopropanol, dimethyl sulfoxide (DMSO), and toluene (see Fig. 5.3.(a)). The solvents were deposited in a sandwich configuration between two 170- μm glass coverslips (see Fig. 5.3.(b)) and I set to 0.8 ms the CCD exposure time, which is the minimum allowed by the detector electronics. The measured CARS spectra, covering the whole fingerprint region from 500 to 2000 cm^{-1} (blue curves in Fig.5.3.(a)) show the characteristic lineshapes of the CARS signal, because of the interference with the chemically unspecific NRB. A comparison of the phase retrieved spectra (red lines in Fig. 5.3.(a)), after applying the KK algorithm [46], with the SR spectra (grey areas in Fig. 5.3.(a)) shows a very good agreement both in the relative positions of the peaks and their amplitude ratios.

Then, I investigated the detection limit of the BCARS system measuring spectra of a set of binary solutions of DMSO and pure water with variable DMSO concentration, ranging from 100% to 0%. For the experiment, the exposure time was set to 10 ms, and I averaged over a hundred spectra for a total of 1-second measurement time, adopting the same sample configuration employed for solvents. Without the help of any spectral denoising method, I retrieved the pure vibrational response of the DMSO using the KK algorithm. As a reference spectrum for the KK algorithm, we used the CARS spectrum collected on the sample with pure water (0% DMSO – 100 % water). As it was expected, the response of the retrieved $\text{Im}\chi_R^{(3)}$ is linear with respect to DMSO concentration (Fig. 5.3.(c)) and the measured detection limit of the system is ≈ 14.1 mmol/L.

This limit corresponds to the value of the solvent concentration at which the main peak of DMSO in the fingerprint region at $\approx 667 \text{ cm}^{-1}$ is equal to the background signal due to noise. This result demonstrates a two-fold increase of the limit of sensitivity with respect to previously reported multiplex CARS in the fingerprint region [94].

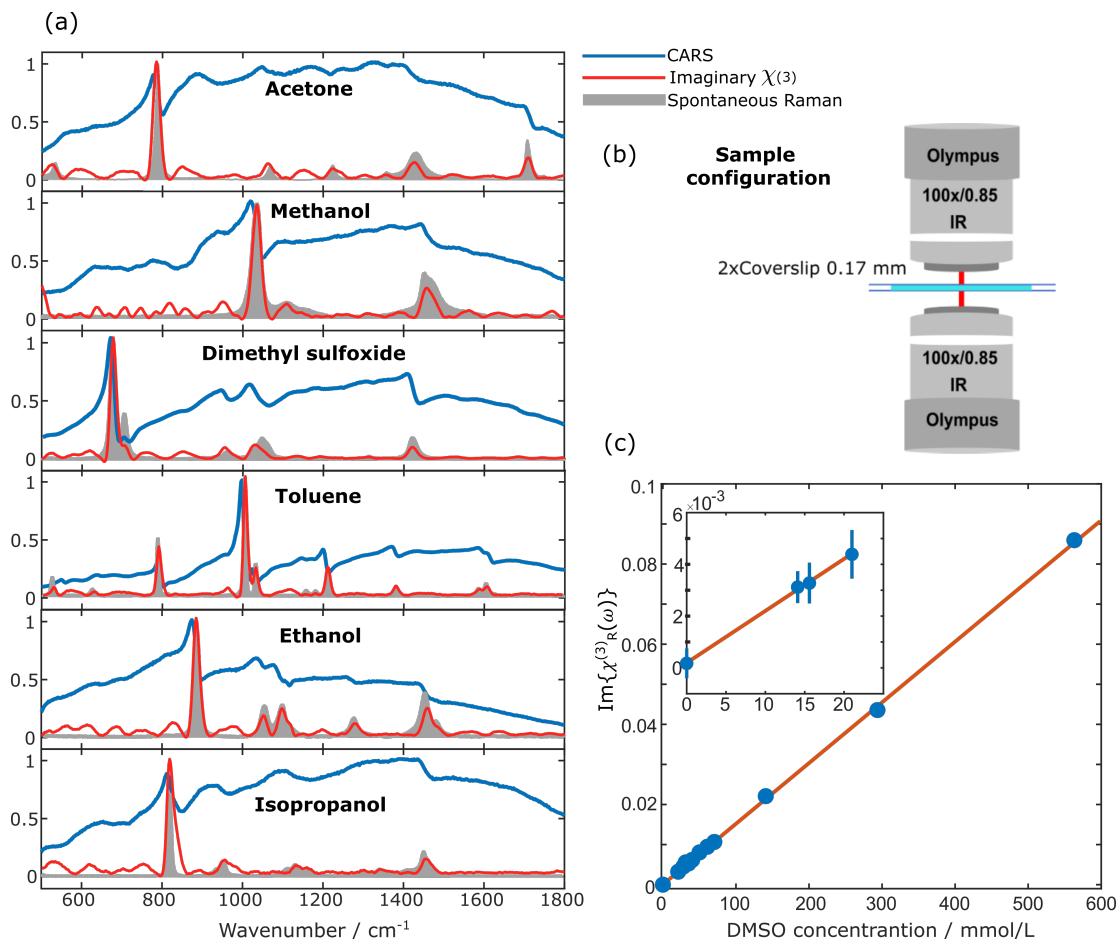


Figure 5.3: (a) BCARS raw single-point spectra (blue solid lines) acquired with 0.8-ms exposure time on six solvents (as indicated), sandwiched between two 170- μm glass coverslips. The red lines are phase-retrieved spectra after the Kramers-Kronig algorithm. SR spectra (grey areas) are also plotted for comparison. (b) Scheme of the sample configuration employed for the experiments. (c) Dilution test experiment on a binary solution of DMSO and pure water. We considered the retrieved imaginary part of the third-order resonant susceptibility of the main peak of DMSO at 667 cm^{-1} . The inset shows a zoom on the low-concentration binary solutions. Estimated sensitivity: 14.1 mmol/L of DMSO in pure water. Error bars: 1 standard deviation.

5.2.3 BCARS microscopy of plastic beads

To assess the image capabilities of the microscope, spectral hypercubes were measured. BCARS imaging is performed by raster scanning the sample in the x-y directions, without changing the z-position, and simultaneously acquiring a CARS spectrum with the CCD. Images of a sample made by mixing 10- μm polystyrene (PS) and 8- μm poly-methyl-methacrylate (PMMA) beads, immersed in DMSO were delivered (see Fig. 5.4) with 1-ms integration time (panel 5.4.(a)). The black triangles in the spectral profiles

5.2. Fingerprint multiplex CARS at high speed based on supercontinuum generation in bulk media and deep learning spectral denoising

correspond to the three main peaks relative to the three chemical species (650 cm^{-1} for DMSO, 780 cm^{-1} for PMMA, 970 cm^{-1} for PS). Note that the peaks are shifted with respect to the corresponding ones in the SR spectra (grey areas in panel 5.4.(c)) because of the distortions of the line widths introduced by NRB. Panel 5.4.(b) shows the portions of the hypercube we collected at these three specific vibrational frequencies. After the CNN-based spectral denoising and NRB removal, classification analysis was performed by applying the MCR-ALS algorithm. The number of components (i.e., the chemical species) is fixed to three. The algorithm outputs pure spectra and concentration maps (Fig. 5.4.(c)-(d)). The comparison of the reconstructed spectra with the SR ones (grey areas in panel 5.4.(c)) demonstrates the capabilities of the system of recognizing the main chemical features of heterogeneous samples in the whole fingerprint region. Indeed, in the spectra, all the peaks, even the less intense ones, can be identified. Note that in the retrieved spectrum of the $8\text{-}\mu\text{m}$ PMMA beads there is a residual peak of DMSO. This is due to a sample thickness between the two coverslips of $10\text{ }\mu\text{m}$, determined by the size of the PS beads. It implies that the DMSO solvent may be locally present in correspondence with the smaller PMMA beads.

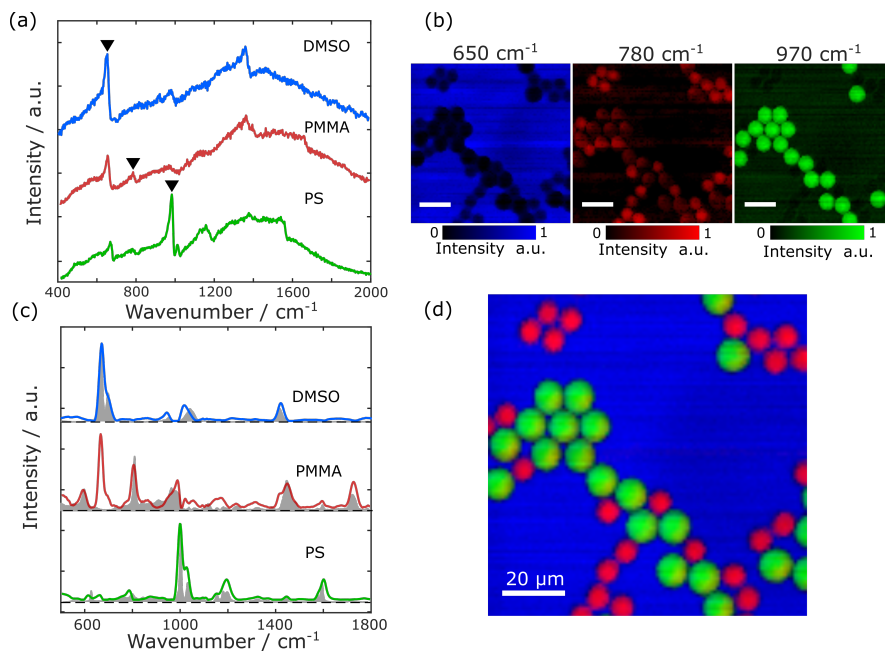


Figure 5.4: BCARS image of $10\text{-}\mu\text{m}$ PS and $8\text{-}\mu\text{m}$ PMMA beads soaked in DMSO and sandwiched between two $170\text{ }\mu\text{m}$ glass coverslips. (a) Single-pixel CARS spectra in the fingerprint region of a PS bead (green curve), DMSO (blue curve), and a PMMA bead (red curve). (b) Frames of the measured BCARS hypercube at three selected Raman shifts (black triangles in panel (a)) corresponding to three main characteristic peaks (650 cm^{-1} for DMSO, 780 cm^{-1} for PMMA, 970 cm^{-1} for PS) of the species in the fingerprint region. (c) MCR-ALS retrieved spectra of the three chemical species after the post-processing data pipeline and correspondent SR spectra (grey areas) (d) False-color image retrieved with MCR-ALS analysis, with the same color code as (c). Imaging settings: 90×90 pixels, $1\text{-}\mu\text{m}$ pixel size, 1024 spectral points, 1 ms pixel dwell time, Scale bars: $20\text{ }\mu\text{m}$, total image acquisition time: 8.1 s.

5.2.4 BCARS imaging of biological tissues

I used the BCARS microscope to map biological specimens, imaging longitudinal sections of non-decalcified methyl methacrylate (MMA)-embedded murine spine (vertebrae) [188]. The sample consists of 6- μm -thick sections including both the compact cortical part and the cancellous trabecular part of bone tissue, the latter being interspersed with bone marrow. Bone is constituted by a flexible matrix, mainly made up of type-I collagen, and by an inorganic mineral counterpart, mostly composed of calcium phosphate (hydroxyapatite), which gives rigidity to bones. The interplay of these two constituents provides tensile and compressive strength for load bearing. Conversely, bone marrow is rich in cells taking part in hematopoiesis, thus playing a crucial role in blood cell production. Consecutive tissue sections were deposited either on slides for routine histological procedures or on a polylysine-treated quartz coverslip. After removing the resin, a second 170- μm quartz coverslip was applied to obtain a sandwich configuration. I visualized the morphological details by analyzing the bright-field image of the adjacent tissue slice stained with Hematoxylin and Eosin (H&E) (Fig. 5.5.(a)). In this image, I identified a $400 \times 800\text{-}\mu\text{m}^2$ field of view (dashed area) characterized by the presence of the cells of the bone marrow, the trabecular and cortical bone, and the muscular tissue surrounding the vertebrae. The same region was imaged on the unstained slice, thus obtaining the hypercube shown in Fig. 5.5.(b-d). In this case, I selected three Raman shifts, i.e., 790 cm^{-1} for DNA, 960 cm^{-1} for hydroxyapatite and 1410 cm^{-1} for CH₂ of proteins and lipids corresponding to prominent peaks in CARS spectra (Fig. 5.5.(e)). On the denoised and processed hypercube, I applied the KMCA algorithm to identify the main chemical constituents of the sample. In this case, the KMCA is preferred to MCR-ALS since it proved to be more effective with a large-sized dataset. The concentration map and the spectra for a fixed number of clusters equal to 4 are shown in Fig. 5.5.(f-g). The images clearly show that a cluster can be associated with the region of the vertebra related to cortical and trabecular bone, another one with the bone marrow, and the last one with the muscle (see Fig. 5.5(g)). The fourth cluster accounts for empty regions of the sample. The relative spectra, i.e. the centroids of the KMCA, give us information on the chemical composition of each region of the scrutinized sample. Indeed, the centroid of the first cluster (in red) shows an intense band between 940 and 970 cm^{-1} , typically associated with phosphate bonds in hydroxyapatite (960 cm^{-1}). The small band around $1060\text{-}1080\text{ cm}^{-1}$ represents carbonate in hydroxyapatite, while the bands at $1220\text{-}1230\text{ cm}^{-1}$ correspond with amide III, proteins, the peak at $\approx 1440\text{ cm}^{-1}$ is typical of CH₂ bonds and represents both proteins and lipids (the organic matrix) and the peak at $\approx 1650\text{ cm}^{-1}$ is associated with amide I, proteins [189]. These spectral features clearly correspond to the bone, mostly characterized by mineral crystals embedded in an organic protein-rich matrix. The centroids of the second and third clusters (in green and blue respectively) are mainly characterized by vibrations around 790 cm^{-1} , typically assigned to DNA, and by strong signals in the spectral region between 1400 and 1700 cm^{-1} , mainly associated to protein and lipids. These clusters can be designated to bone marrow and to muscular tissue, marked by a high cellular fraction and protein-rich muscle fibers, respectively.

5.2. Fingerprint multiplex CARS at high speed based on supercontinuum generation in bulk media and deep learning spectral denoising

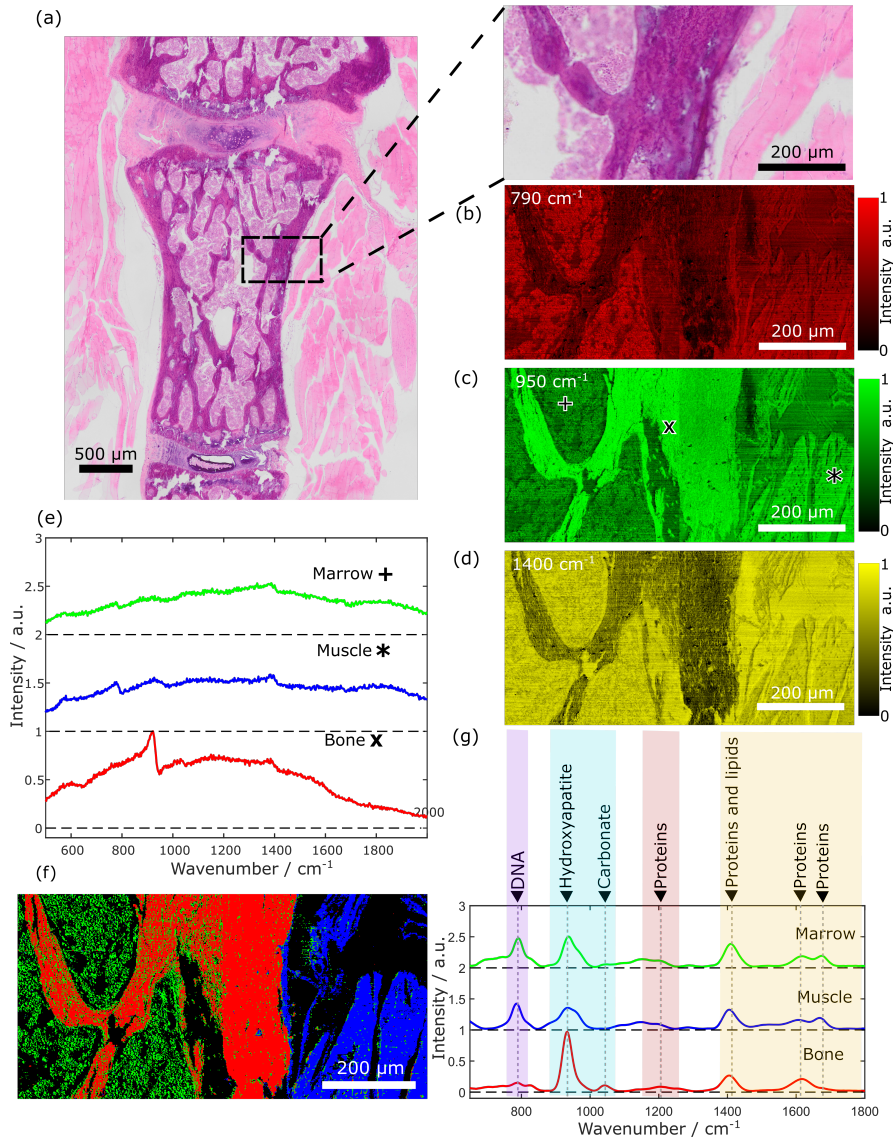


Figure 5.5: Microscopy of 6- μm thick murine spine sandwiched between two 170 μm quartz coverslips. (a) Bright-field image of a tissue slice stained with H&E. (b-d) Frames of the measured BCARS hypercube at three different Raman shifts (black triangles in panel (e)) on the unstained adjacent slice. (e) CARS spectra from the bone marrow region (green curve, +), from the muscle region (blue curve, *), and from the bone tissue (red curve, x). (f-g) Concentration map and vibrational spectra of the three clusters associated with bone marrow, muscle, and bone, obtained after denoising the data with the CNN model, NRB removal through the KK algorithm, and applying the KMCA algorithm. Imaging settings for the B-CARS dataset: 200 μm scale bar, 400 \times 800 pixels, 1- μm pixel size, 1024 spectral points, 10-ms pixel dwell time, total image acquisition time: 55 minutes.

5.2.5 Conclusion

This work demonstrates a new approach to BCARS spectroscopy and microscopy. The two key novel elements introduced are: (1) the use of a low-repetition-rate (2 MHz) pulsed laser in the infrared and (2) the advanced data-processing pipeline. The former innovation opens the possibility to make the system more simple and compact thanks

to broadband Stokes beam using WLC generation in bulk media rather than PCFs. Moreover, it enables stronger CARS signals thanks to the higher pulse energy and peak power. Eventually, it shifts the wavelength of the pump/Stokes pulses beyond $1\ \mu\text{m}$, thus limiting the multi-photon sample damage when imaging biological samples.

Thanks to these innovations, we could demonstrate extremely fast (down to 0.8-ms pixel dwell time, limited by the CCD read-out time) BCARS microscopy in the weak vibrational fingerprint region, with record-breaking sensitivity (down to 14.1 mmol/L), without compromising sample integrity.

5.3 Ultrabroadband CARS microscopy of biological samples with white-light continuum in bulk media

5.3.1 Ultrabroadband two-color CARS spectroscopy on solvents

So far, I have shown results of CARS spectra spanning the whole fingerprint region ($500\text{-}1800\ \text{cm}^{-1}$). However, as it has been discussed in chapters 2 and 3, it is possible to generate a broader WLC ($1050\text{-}1600\ \text{nm}$) playing on the incident pulse energy, on the aperture of the iris, and on the position of the 10-mm YAG crystal with respect to the focal plane. Under these conditions, the spatio-temporal superposition of the pump and Stokes beam at the focal plane allows us to generate a two-color CARS spectrum covering both the fingerprint region ($500\text{-}1800\ \text{cm}^{-1}$) and the CH-stretching region ($2700\text{-}3100\ \text{cm}^{-1}$). With this setup configuration, I measured the CARS spectrum of six different solvents (5.6). I fixed the exposure time to 0.8 ms and used higher power at the sample plane with respect to previous results, i.e., 55 mW for the pump and of 25 mW for the Stokes beam. Fig. 5.6 shows the BCARS spectra (blue curves) and relative phase retrieved spectra using the KK algorithm (red curves), where all the peaks show a good agreement with the spontaneous Raman spectrum (grey areas) acquired within 25 s (five averages with 5-s exposure time). Although these power values are sufficient to obtain a good signal for solvents, in the case of polymer beads or biological samples they are excessive and lead to sample damage.

To perform high-speed multiplex CARS imaging on biological samples covering the entire Raman active region, I modified the setup configuration. The new BCARS implementation employs a new etalon to reach 3.7 ps pump pulses thus having a higher spectral resolution, i.e. $\approx 9\ \text{cm}^{-1}$. Then, I further compress the broadband Stokes beam ($\approx 1100\text{-}1600\ \text{nm}$) reaching sub-20 fs pulses at the focal plane after the first microscope objective. The use of an ultrashort laser source with fine-tuned pulse duration and adjustable spectral range enables us to cover the first part of the vibrational spectrum (from 500 to $1400\ \text{cm}^{-1}$) through intra-pulse excitation, also called the three-color CARS mechanism, of the Stokes beam [98], using the narrowband pump beam as a probe, and the remaining part (from 1400 to $3100\ \text{cm}^{-1}$) through inter-pulse excitation, that is the two-color CARS mechanism, between the narrowband pump and the broadband Stokes beam. The combination of these two processes for broadband CARS generation allows us to obtain good quality and very broad spectra working at a moderate average power of the Stokes ($< 10\ \text{mW}$) and pump beams ($< 25\ \text{mW}$) and with $< 3\text{-ms}$ pixel exposure time when imaging soft biological tissues and cells.

5.3. Ultrabroadband CARS microscopy of biological samples with white-light continuum in bulk media

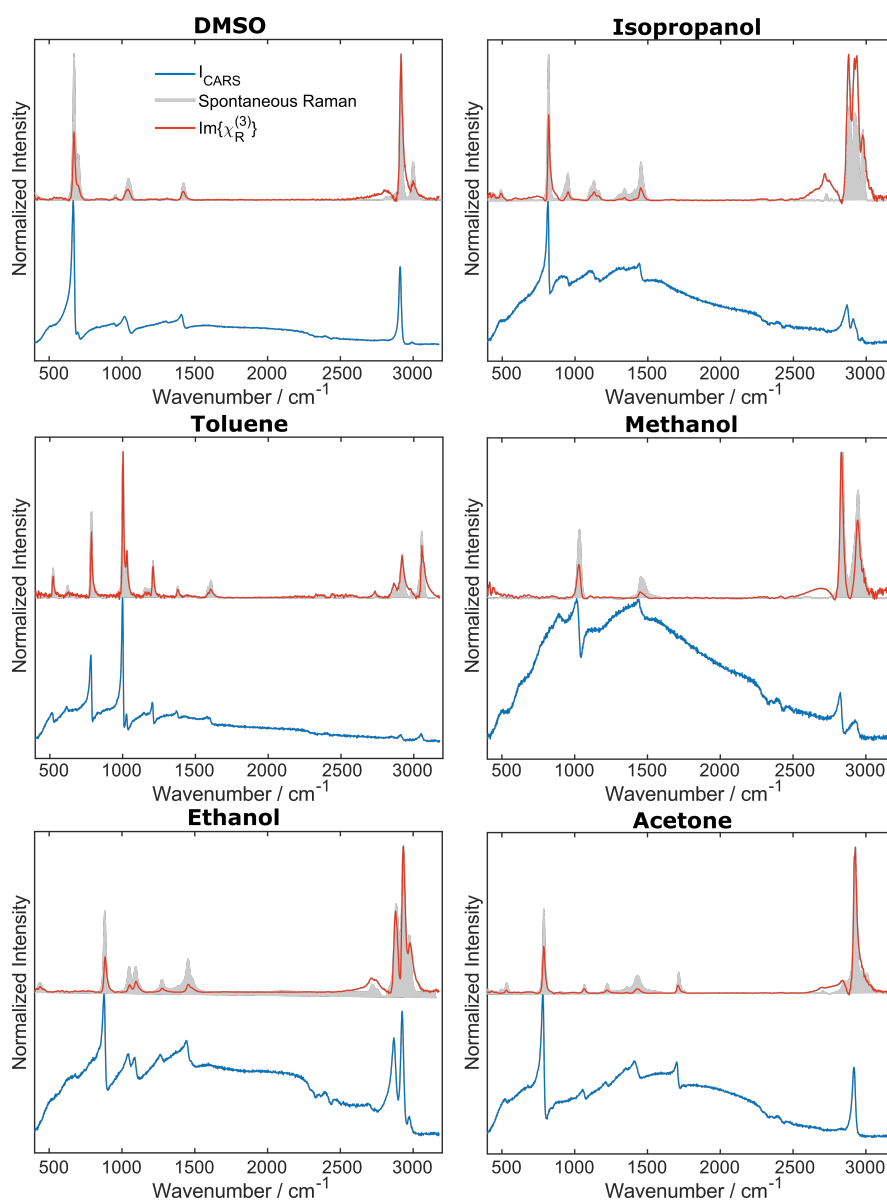


Figure 5.6: BCARS spectra of six different solvents acquired with 0.8 ms exposure time sandwiched between two 170- μm glass coverslips. The plots show the CARS intensities (blue curves), the phase retrieved spectra via the KK algorithm (red curves), and the SR spectra acquired averaging five spectra acquired with 5-s exposure time (grey areas). No denoising has been applied before the application of the KK algorithm.

5.3.2 Ultrabroadband CARS spectroscopy combining two and three-color mechanism

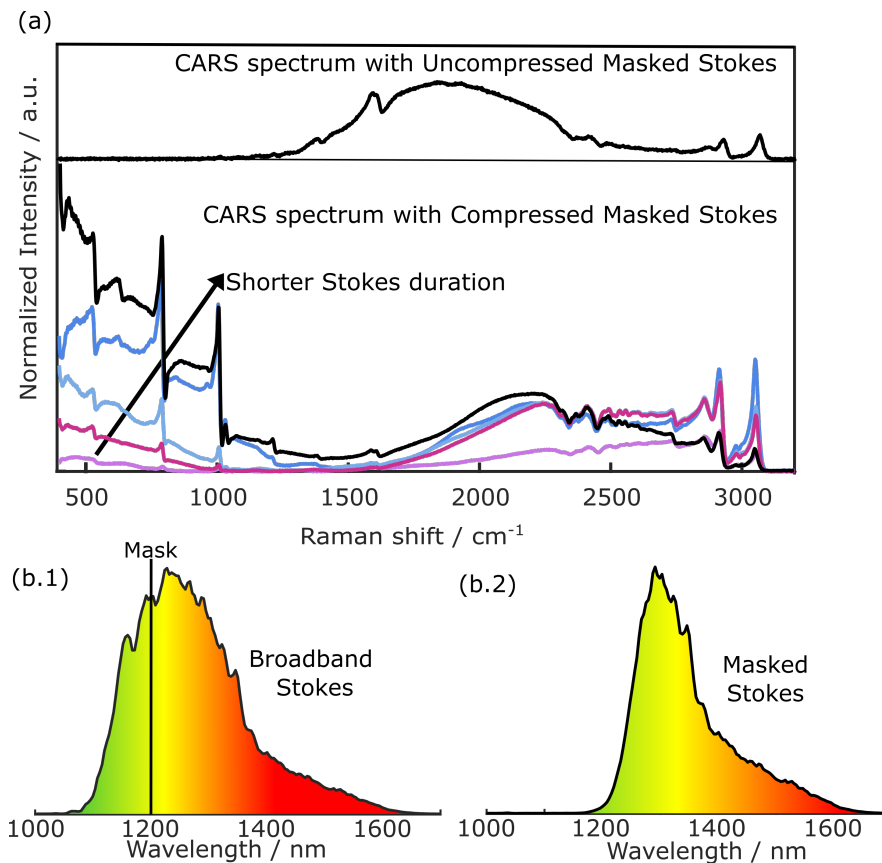


Figure 5.7: (a) CARS spectrum of toluene sandwiched between two 170 μm quartz coverslips acquired with 1-ms exposure time in two different setup configurations: masking the Stokes spectrum in (b.1) thus obtaining pulses with spectrum (b.2) without compressing it (two color CARS only); using the Stokes in (b.2) and compressing it to reach 20-fs pulses thus exciting the vibrational mode both with the three-color and the two-color mechanisms.

In the new setup configuration, the pulse duration of the broadband beam and its spectral coverage have been finely tuned. The pulse duration of the Stokes beam is adjusted by increasing the tip-to-tip distance between the two prisms of the compressor, that now is ≈ 60 cm and then it is finely tuned by changing the insertion of one of the two prisms. The bandwidth is controlled by inserting a mask in the region of the prism compressor where the colors are spatially separated.

If we just considered the situation of an uncompressed masked Stokes beam with bandwidth ≈ 1200 -1600 nm (Fig. 5.7.(b)), we can obtain spectra for toluene in the same configuration described above covering the Raman region from 1400 cm^{-1} to 3200 cm^{-1} (Fig. 5.7.(a)). By compressing the masked Stokes beam, keeping all the other parameters fixed (bandwidth and average power), we can demonstrate that at different Stokes duration, we can vary the CARS excitation profile (Fig. 5.7.(a)) in the region below 1400 cm^{-1} , while the portion above this threshold does not present substantial differences, apart from some intensity variations due to unavoidable slight misalignment of the pump and Stokes beams during the compression of the supercontin-

5.3. Ultrabroadband CARS microscopy of biological samples with white-light continuum in bulk media

uum. The optimum is achieved when the Stokes pulse duration reaches the minimum. This condition results in a spectrum that below 1400 cm^{-1} has the highest intensity and broadness. The two-color mechanism spectral coverage strictly depends on the spectral extension of the Stokes beam that reaches $\approx 1600\text{ nm}$, so considering the inter-pulse excitation between pump and Stokes beam, we could visualize Raman modes till $\approx 3400\text{ cm}^{-1}$. However, the spectrometer, for the presence of a 600 gr/mm grating, limits the accessible bandwidth to $\approx 3200\text{ cm}^{-1}$. A 300 gr/mm grating would have been good to cover a large spectral range but would have determined a lower number of spectral points in the main Raman active region of biological samples ($400 - 3100\text{ cm}^{-1}$).

The new setup configuration allows us to perform time-delayed CARS, by changing the arrival time of the narrowband pulses with respect to the broadband ones. This technique enables isolating all the modes excited only via the three-color mechanisms and optically suppressing the NRB without the need for any post-processing algorithm.

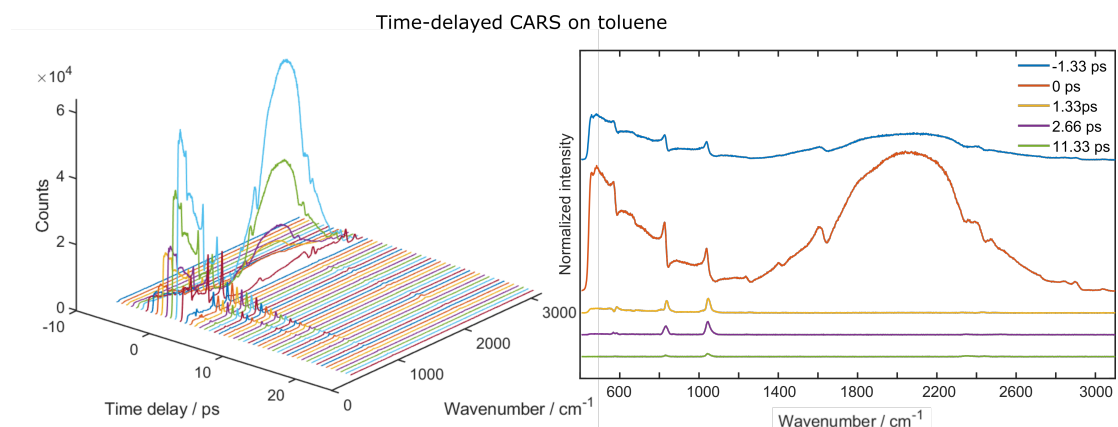


Figure 5.8: Time-delayed CARS on Toluene changing the delay between the narrowband and the broadband Stokes beam with a mechanical delay stage. Exposure time per spectrum: 0.8 ms.

Indeed, the resonant contribution in CARS is characterized by a coherence time in the order of picoseconds since vibrational levels are populated. On the other hand, the non-resonant contribution arises from electronic contributions, in which only virtual levels are populated. By changing the delay between the pump and Stokes pulses, we expect to see a reduction of the NRB after less than a hundred femtoseconds (indeed, the NRB main contribution exists for a duration comparable to the Stokes pulse duration, $\tau = 20fs$, hence it completely vanishes after $4-5\tau$). The signal generated via two-color CARS vanishes since in order to excite the modes via the two-color mechanism both pump and Stokes photons are needed simultaneously at the sample. On the other hand, in three-color CARS, increasing the delay between Stokes and pump, in which the latter acts only as a probe, it is possible to isolate the resonant contribution, which is characterized by higher coherence time. I performed time-delayed CARS spectroscopy on solvents. In particular, for the case of toluene in Fig. 5.8, we can observe how the NRB and the two-color CARS signal decrease dramatically increasing the delay. By contrast, the vibrational peaks at low wavenumbers (in the three-color CARS region) assume a Lorentzian lineshape, since there is no more heterodyne amplification given by the presence of the NRB.

5.3.3 Ultrabroadband CARS microscopy of senescence cells

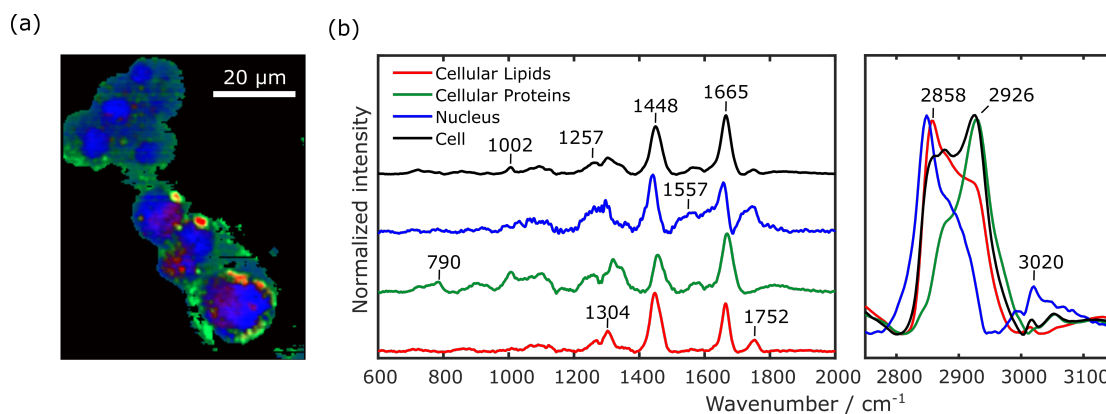


Figure 5.9: (a) BCARS image of therapy-induced senescent HepG2 cancer cells 72 hours after treatment with DFO. The false-color images highlight three different species in the cells. (b) Retrieved spectra associated with the three species in panels (a). Imaging settings: 1-ms pixel exposure time; 500-nm pixel size.

We employed the new configuration of the BCARS system to deliver chemical images on cells identifying the main subcellular components. We imaged HepG2 cancer cells with therapy induced senescence. The cells were fixed on a $22 \times 22 \text{ mm}^2$ and $170\text{-}\mu\text{m}$ thick quartz coverslip. For the measurements we adopted a sandwich configuration, using a $25 \times 50 \text{ mm}^2$ and $170\text{-}\mu\text{m}$ thick quartz coverslip on which we release a drop of PBS and then stuck the sample coverslip using enamel. The system enables us to acquire images on cells with 500-nm pixel size and 1-ms pixel dwell time. After the acquisition, we post-processed the hyperspectral data following the pipeline that includes the image denoising via SVD, the NRB removal via the time domain Kramers-Kronig algorithm, and spectral unmixing methods based on N-FINDR for distinguishing the different chemical species. The result (Fig. 5.9.(a)) shows an image of cells where the lipids (red), proteins (green), and nuclei (blue) are mapped. The spectral unmixing method employed allows us to also associate each species with its spectrum. Together with the spectra of the identified subcellular components, we report the average spectrum of the cells (black line in Fig. 5.9.(b)), obtained by averaging the spectra of the pixel of the foreground, after isolating it from the substrate (black area in Fig. 5.9.(a)) through a k-means cluster analysis. The spectra show the typical Raman peaks of cells [189]. In particular, in the fingerprint region the peak at 790 cm^{-1} is characteristic of DNA, at 1002 cm^{-1} is associated with phenylalanine, the band between $1200\text{-}1300 \text{ cm}^{-1}$ represents Amide III (proteins), the peak at 1304 cm^{-1} represents CH_2 twisting (lipids), the peak at 1448 cm^{-1} is associated with CH_2 bonds, the peak around 1557 cm^{-1} is characteristic of Amide II (proteins), the peak at 1665 cm^{-1} is typical of amide I (proteins), and the peak at 1752 cm^{-1} is typical of the $\text{C} = \text{O}$ of lipids (triglycerides). In the CH stretching region, the spectra feature broader peaks, in the red line the broad peak around 2858 cm^{-1} is related to the CH_2 symmetric stretch of lipids, in the green line the peak at 2926 cm^{-1} is related to the symmetric CH_3 stretch, due primarily to proteins, and in the blue line the peak at 3020 cm^{-1} is related to unsaturated $=\text{CH}$ stretch of lipids.

5.3. Ultrabroadband CARS microscopy of biological samples with white-light continuum in bulk media

5.3.4 Ultrabroadband CARS microscopy of biological tissues

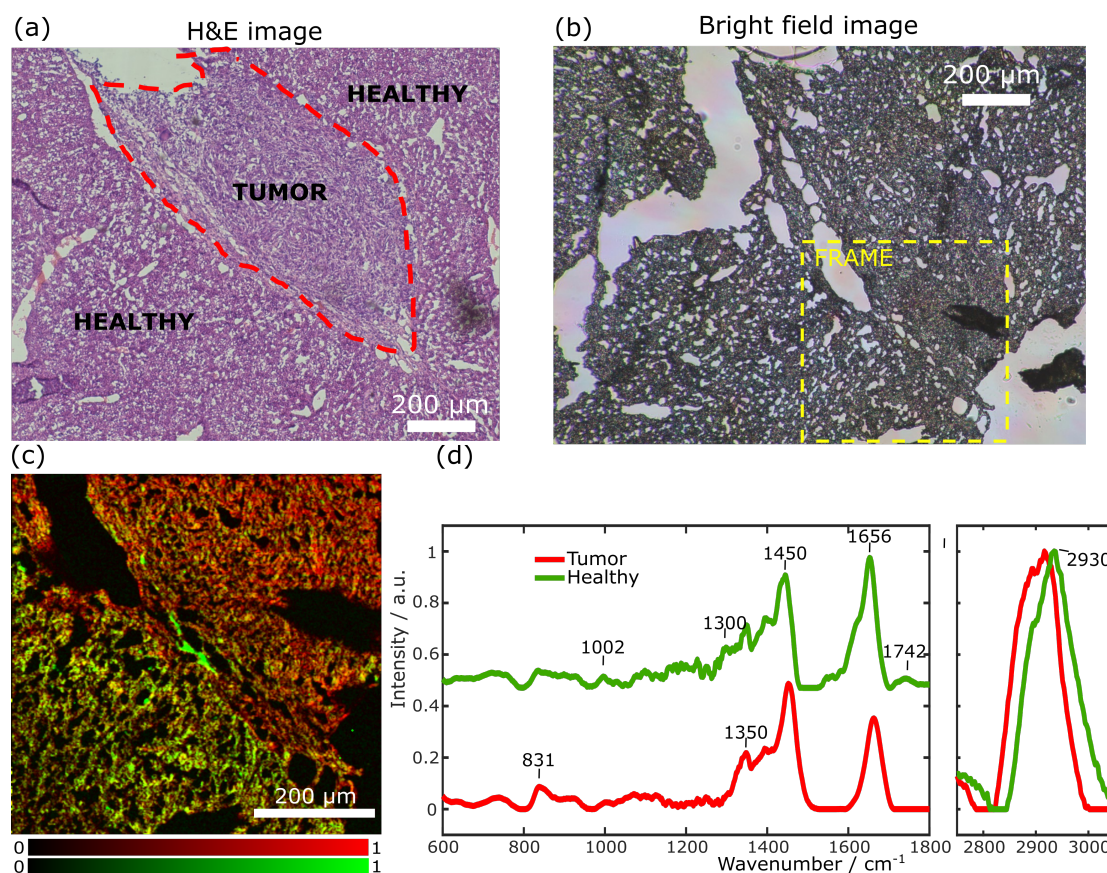


Figure 5.10: BCARS imaging on a tumoral liver slice of a mouse model. (a) Image on the H&E stained slice. (b) Bright-field image of the unstained slice used for BCARS imaging. (c) $600 \times 600 \mu\text{m}^2$ BCARS image on tumor liver obtained through N-FINDR analysis after noise and NRB removal. (d) Retrieved spectra associated to the species in panels (c). Imaging settings of panel (c): 300×300 pixels; 3-ms pixel exposure time; $2\text{-}\mu\text{m}$ pixel size.

We imaged liver slices of an orthotopic mouse model to assess the capabilities of the system in tumor recognition. This model consists of the implantation of hepatocellular carcinoma (HCC) tumor cells into the liver by direct intrahepatic injection. Tumors occur in the natural liver microenvironment and mimic the metastatic behavior of HCC. For the experiment, two adjacent $10\text{-}\mu\text{m}$ thick slices of the same liver sample were cut. The first one is treated with H&E staining and helps us localize the tumoral region (Fig. 5.10.(a)), and the other one is fixed onto a $25 \times 50 \text{ mm}^2$ $170\text{-}\mu\text{m}$ thick quartz coverslip and sandwiched with a second $170\text{-}\mu\text{m}$ thick quartz coverslip, thus constituting the unstained slice imaged with the BCARS microscope. From the bright field image (Fig. 5.10.(b)) on the unstained slices, we identify a $600 \times 600 \mu\text{m}^2$ frame for BCARS imaging with a 3-ms pixel dwell time. After denoising and NRB removal, we derived through the N-FINDR algorithm concentration maps and spectra of two different chemical constituents in the sample, the tumorous region (red) and the healthy region (green) (Fig. 5.10.(c-d)). Significant differences in the spectra are observed in correspondence with the peak at 1656 cm^{-1} associated with Amide I, more intense in the

healthy tissue (green area). The green spectrum also shows a peak around 1742 cm^{-1} , typical of lipids, that is not present in the red species. Moreover, in the CH-stretching region, the green spectrum is shifted towards higher wavenumbers with the main peak centered around 2930 cm^{-1} . This peak is characteristic of the symmetric CH_3 stretch, due primarily to protein. The spectra show other biologically relevant peaks. The broad peak centered around $810\text{--}840\text{ cm}^{-1}$ is typically associated with collagen; the peak at 1002 cm^{-1} corresponds to the presence of phenylalanine; the peak at 1300 cm^{-1} is typical of lipids, while the intense and broad peak at 1450 cm^{-1} is typical of CH_2 and CH_3 deformation. The comparison of the BCARS image and the image on the H&E slice confirms that our microscope can identify the tumoral region without the need for any staining, avoiding a time-consuming sample preparation procedure and undesired structural or chemical alteration. In addition, it provides rich chemical information on the sample composition.

5.3.5 Conclusion

I presented a new experimental approach to multiplex CARS based on a 2-MHz repetition rate amplified ytterbium fiber femtosecond laser system used to generate white light supercontinuum in bulk media. By precompressing the generated broadband Stokes pulses, we could reach at the sample plane sub-20-fs pulses that coupled with the narrowband 3.7-ps pump pulses generate a CARS signal spanning the entire Raman spectrum of biological samples. The broadband anti-Stokes signal is generated by two nonlinear processes that act in parallel, namely the three-color and the two-color mechanisms. The former derives from the intra-pulse interaction of the Stokes pulses and generates an excitation profile depending on the number of permutations of the colors inside the Stokes bandwidth. We exploited this mechanism to cover the first portion of the spectrum ($500\text{--}1400\text{ cm}^{-1}$). The latter is the result of the inter-pulse interaction between the pump and the Stokes beam and generates an excitation profile that is, under the assumption of a sufficiently narrow pump spectrum, as broad as the Stokes pulse spectrum. We employed this mechanism to cover the remaining portion of the Raman spectrum ($1400\text{--}3100\text{ cm}^{-1}$). The system thanks to the new optical design delivers highly informative chemical maps of cells and tissues with millisecond pixel dwell time. We have shown images on cancer HepG2 cells acquired with 1-ms exposure time, distinguishing lipids, proteins, and nuclei and highlighting the main peaks in each of their spectra. Eventually, we demonstrated the potentiality of the system to be used in histopathological settings, imaging a mouse liver model implanted with hepatocellular carcinoma. Comparing the results with the H&E image of an adjacent slice, we can say that our system, besides localizing the tumor and giving morphological details on the sample, provides information on the chemical composition of each region of the sample.

CHAPTER 6

Conclusion and Outlook

The last decades saw continual advances in CRS microscopy and spectroscopy techniques. CRS imaging delivers vibrational maps of the endogenous content in cells and tissues in a label-free and non-destructive way, which is particularly useful in clinical applications, such as histopathology and disease diagnosis. The main goal is to bring CRS technology to a reliable, robust, and user-friendly platform to be used in clinical settings. As it has been reviewed in Chapter 1 of this thesis, many groups are working in this respect to compact the experimental setups, increase the acquisition speed, and improve their reliability by coupling the systems with mathematical methods either based on numerical algorithms or on machine learning based models for boosting its performances.

Among the possible implementations of CRS, the most common are the ones based on SRS and CARS. The VIBRA lab in Politecnico di Milano offers a variety of systems either based on narrowband CARS and SRS or broadband CARS and SRS that have been built in the last decades. My main contribution to the lab, which constitutes the main heart of this thesis, has been the construction of an experimental setup for BCARS spectroscopy and microscopy and the development of a post-processing pipeline for the analysis of the hyperspectral data. This work describes all the steps that I followed to reach the first prototype of a BCARS microscope with white-light continuum generation in bulk media able to reveal the entire Raman active region of biological samples with unprecedented speed (<3 ms/pixel) and sensitivity (≈ 14 mmol/L).

In chapter 1, I provided an overview of the main theoretical foundations of CRS techniques, reviewing the state of the art for BCARS and its main implementations.

Chapter 2 described the main optical processes contributing to the broadening of the spectrum of a femtosecond pulse when it is focused inside a bulk crystal. Here, I also described from a practical point of view how to switch on and stabilize the WLC.

Chapter 6. Conclusion and Outlook

Chapter 3 introduced the architecture of the BCARS experimental setup with the main advantages of using this configuration rather than other solutions presented in the literature. The chapter continued with a full characterization of the optical sources and an illustration of the design of the microscope used for the acquisition of the hyper-spectral data.

Chapter 4 presented the acquisition methods and the data post-processing pipeline employed for CARS spectroscopy and imaging. In particular, I described the methods used to set the measurement parameters (e.g., pixel size, image size, pixel dwell time, and number of measurements) and then I reviewed the main algorithms used for the data denoising and artifact removal in CARS spectra. This chapter also provides an overview of machine learning and neural network fundamentals. Indeed, deep learning methods proved to be powerful tools for solving highly nonlinear problems such as the denoising of the CARS spectra or the removal of the NRB. Eventually, the chapter ended with a description of the main algorithms for spectral unmixing that I employed for delivering chemical maps of heterogeneous biological samples.

Chapter 5 reports the main results obtained with the BCARS experimental setup when using it for the spectroscopy of solvents or the microscopy of plastic beads and biological samples, such as cells and tissues. In particular, the first part of the chapter described the results obtained with a previous configuration of the system that enabled us to cover the entire fingerprint region of the vibrational spectrum using exclusively the two-color CARS mechanism. With this configuration, I demonstrated state-of-the-art speed (< 1 ms/pixel for solvents and beads) and unprecedented sensitivity for multiplex CARS spectroscopy and microscopy when detecting DMSO in water (≈ 14 mmol/L). The second part presented the main results obtained with a new configuration of the experimental setup that allows us to image cells and biological tissues acquiring spectra in the entire Raman-active region ($500 - 3200$ cm^{-1}) using moderate average power for the pump and Stokes beams at the sample. In this case, the generation of the anti-Stokes component derives from the interplay of two optical processes occurring in parallel which are the three-color and two-color CARS mechanisms. I demonstrated unprecedented speed for multiplex CARS when imaging cancer HepG2 cells (1 ms/pixel) and when imaging soft tissue such as tumor liver in mouse models (< 3 ms/pixel).

The reported results open the path toward the use of BCARS for studying cancer diseases both at the cellular and the tissue level. With respect to standard techniques which employ labels, such as fluorescence microscopy, the system enables avoiding the long preparation time of the sample and the use of markers that often alter the chemical structure or undergo photobleaching, preventing to image the same region twice. On the other hand, with respect to other label-free techniques, such as SR, it provides higher acquisition speed and does not suffer from sample autofluorescence. We envisage that the technology can be further improved in terms of acquisition speed by employing either line scanning or wide-field illumination.

Records

Publications

- F. Vernuccio*, A. Bresci*, V. Cimini, A. Giuseppi, G. Cerullo, D. Polli, , C. M. Valensise. Artificial Intelligence in Classical and Quantum Photonics. *Laser & Photonics Reviews* 2022, 16, 2100399.
- F. Vernuccio, A. Bresci, B. Talone, A. De la Cadena, C. Ceconello, R. Vanna, G. Cerullo, and D. Polli. "Fingerprint multiplex CARS at high speed based on supercontinuum generation in bulk media and deep learning spectral denoising," *Opt. Express* 30, 30135-30148 (2022) Editors' Pick.
- CM Valensise, A Giuseppi, F Vernuccio, A De la Cadena, G Cerullo, D Polli. Removing non-resonant background from CARS spectra via deep learning. *APL Photonics* 5 (6), 061305 (2020).
- A De la Cadena, F Vernuccio, B Talone, A Bresci, C Ceconello, S Das, R Vanna, G Cerullo, D Polli. Multiplex Chemical Imaging Based on Broadband Stimulated Raman Scattering Microscopy. *Jove*, 2022. DOI: 10.3791/63709
- A De la Cadena, F Vernuccio, et al. Broadband Stimulated Raman Imaging based on Multi-channel Lock-in Detection for Spectral Histopathology. *APL Photonics* 7, 076104 (2022).
- B. Talone, A. Bresci, F. Manetti, F. Vernuccio, A. De La Cadena, C. Ceconello, M. L. Schiavone, S. Mantero, C. Menale, R. Vanna, G. Cerullo, C. Sobacchi, and D. Polli. Label-free multimodal nonlinear optical microscopy reveals hallmarks of bone composition in pathophysiological conditions. *Front. Bioeng. Biotechnol.* (2022).
- K. Brzozowski, A. Bresci, F. Vernuccio, A. Pieczara, A. Adamczyk, M. Andrzejak, E. Matuszyk, D. Polli, and M. Baranska. Dye-enhanced stimulated Raman scattering (DE-SRS) microscopy. *Angewandte Chemie* (2022). Under revision.

Conferences

- F. Vernuccio, C.M. Valensise, A. Giuseppi, A. De la Cadena, G. Cerullo and D. Polli. Deep learning CARS: real-time removal of the non-resonant background. CLEO/ Europe EQEC 2021. (Oral, Speaker)
- F. Vernuccio, C.M. Valensise, A. Giuseppi, G. Cerullo and D. Polli. Deep reinforcement learning control of white-light continuum generation. CLEO/ Europe EQEC 2021. (Oral, Speaker)
- F. Vernuccio, A. Bresci, B. Talone, A. De la Cadena, C. Ceconello, R. Vanna, G. Cerullo, and D. Polli. "High-speed broadband CARS in the fingerprint region through supercontinuum generation in bulk media", SPIE, Photonic West. January 2022 (Oral, Speaker)
- F. Vernuccio, A. Bresci, B. Talone, A. De la Cadena, C. Ceconello, R. Vanna, G. Cerullo, and D. Polli "AI-assisted high-speed broadband Coherent anti-Stokes Raman scattering in the fingerprint region", Coherent Raman Microscopy and other nonlinear imaging techniques, Febbraio 2022, Jagiellonian University in Krakow. (Oral, Speaker)
- F. Vernuccio, A. Bresci, B. Talone, A. De la Cadena, C. Ceconello, R. Vanna, G. Cerullo, and D. Polli "High-speed broadband CARS in the fingerprint region through supercontinuum generation in bulk media", Focus on Microscopy April 2022 (Oral, Speaker)
- F. Vernuccio, A. Bresci, B. Talone, A. De la Cadena, C. Ceconello, R. Vanna, G. Cerullo, and D. Polli " Broadband CARS in the fingerprint region at high speed through white-light generation in bulk media", Ultrafast phenomena, Montreal, Quebec (Canada) July 2022 (Oral, Speaker).
- F. Vernuccio, C.M. Valensise, A. Giuseppi, A. De la Cadena, G. Cerullo and D. Polli. Removing Non-Resonant Background from CARS spectra via Deep Learning. ICORS 2022, Long Beach, California, August 2022 (Oral, Speaker)
- F. Vernuccio, A. Bresci, A. De la Cadena, B. Talone, C. Ceconello, F. Manetti, R. Vanna, G. Cerullo, and D. Polli High-speed broadband coherent anti-Stokes Raman scattering in the fingerprint region for biological applications. ICORS 2022, Long Beach, California, August 2022 (Oral, Speaker)
- F. Vernuccio, A. Bresci, A. De la Cadena, C. Ceconello, F. Manetti, R. Vanna, G. Cerullo, and D. Polli. High-speed broadband coherent anti-Stokes Raman scattering in the fingerprint region for biological applications. September 2022, Exeter, Contrast workshop. (Oral, Speaker)
- F. Vernuccio, C. Ceconello, A. Bresci, A. De la Cadena, F. Manetti, S. Sorrentino, R. Vanna, G. Cerullo, and D. Polli. Multiplex coherent anti-Stokes Raman scattering microscopy for biological imaging through white light continuum generation in bulk media. ECONOS 2022, Kiruna, Sweden, September 2022.(Poster)

-
- F. Vernuccio, C. Ceconello, A. Bresci, A. De la Cadena, F. Manetti, S. Sorrentino, R. Vanna, G. Cerullo, and D. Polli. Broadband SRS and CARS microscopy for biological applications. Heinrich-Heine-Universität Düsseldorf, Institut für Physikalische Chemie II. 19 January 2023. (Seminar, Speaker).
 - F. Vernuccio, A. Bresci, A. De la Cadena, C. Ceconello, F. Manetti, S. Sorrentino, R. Vanna, G. Cerullo, and D. Polli. Broadband CARS microscopy in the entire fingerprint region for biological applications. SPIE, Photonic West 2023, San Francisco. 28 January - 2 February. (Oral, Speaker).
 - F. Vernuccio, A. Bresci, A. De la Cadena, C. Ceconello, F. Manetti, S. Sorrentino, R. Vanna, G. Cerullo, and D. Polli. Broadband label-free vibrational imaging in the fingerprint region at <1 -ms pixel dwell time via deep learning. SPIE, Photonic West 2023, San Francisco. 28 January - 2 February. (Oral, Speaker).

Glossary

- BCARS** Broadband Coherent anti-Stokes Raman scattering. 23
- CARS** Coherent anti-Stokes Raman scattering. 5
- CNN** Convolutional Neural Network. 85
- CRS** Coherent Raman scattering. 4
- CSRS** Coherent Stokes Raman scattering. 14
- DA** Data Augmentation. 89
- DL** Deep Learning. 80
- DNN** Deep Neural Network. 82
- E-CARS** Epi-detection Coherent anti-Stokes Raman scattering. 34
- F-CARS** Forward Coherent anti-Stokes Raman scattering. 34
- FROG** Frequency Resolved Optical Gating. 57
- FT** Fourier Transform. 39
- FWHM** Full width at half maximum. 58, 61
- GDD** Group Delay Dispersion. 66
- ISRS** Impulsive stimulated Raman scattering. 28
- KK** Kramers-Kronig. 92, 93
- KMCA** K-means cluster analysis. 105, 106
- LSTM** Long Short-Term Memory. 104

Glossary

- MCR-ALS** Multivariate curve resolution-alternating least squares. 105
- MEM** Maximum Entropy Method. 98
- MIR** Mid-infrared. 2
- ML** Machine Learning. 80
- NA** Numerical aperture. 54
- NIR** Near-infrared. 2
- NN** Neural Network. 82
- NRB** Non-resonant background. 22
- PCF** Photonic crystal fiber. 25
- ResNN** Residual Neural Network. 86
- SF** Spectral focusing. 24
- SFG** Sum frequency generation. 61
- SHG** Sercond Harmonic generation. 57
- SR** Spontaneous Raman. 2
- SRG** Stimulated Raman Gain. 35
- SRL** Stimulated Raman Loss. 35
- SRS** Stimulated Raman scattering. 5
- STV** Spectral toal variation. 79
- SVD** Singular Value Decomposition. 79
- TD-CARS** Time-delayed Coherent anti-Stokes Raman Scattering. 32
- WLC** White Light Continuum. 26, 43

Bibliography

- [1] Michael E Dailey, Erik Manders, David R Soll, and Mark Terasaki. Confocal microscopy of living cells. In *Handbook of biological confocal microscopy*, pages 381–403. Springer, 2006.
- [2] Roger Y. Tsien. THE GREEN FLUORESCENT PROTEIN. *Annual Review of Biochemistry*, 67(1):509–544, June 1998.
- [3] M. Bruchez, M. Moronne, P. Gin, S. Weiss, and A. Alivisatos. [pdf] semiconductor nanocrystals as fluorescent biological labels.: Semantic scholar, Jan 1998.
- [4] Kevin M Dean and Amy E Palmer. Advances in fluorescence labeling strategies for dynamic cellular imaging. *Nature Chemical Biology*, 10(7):512–523, June 2014.
- [5] Lu Wei, Zhixing Chen, Lixue Shi, Rong Long, Andrew V. Anzalone, Luyuan Zhang, Fanghao Hu, Rafael Yuste, Virginia W. Cornish, and Wei Min. Super-multiplex vibrational imaging. *Nature*, 544(7651):465–470, April 2017.
- [6] Thomas Niehörster, Anna Löscherberger, Ingo Gregor, Benedikt Krämer, Hans-Jürgen Rahn, Matthias Patting, Felix Koberling, Jörg Enderlein, and Markus Sauer. Multi-target spectrally resolved fluorescence lifetime imaging microscopy. *Nature Methods*, 13(3):257–262, January 2016.
- [7] Rohit Bhargava. Infrared spectroscopic imaging: the next generation. *Appl Spectrosc*, 66(10):1091–1120, October 2012.
- [8] C. Krafft, I. W. Schie, T. Meyer, M. Schmitt, and J. Popp. Developments in spontaneous and coherent raman scattering microscopic imaging for biomedical applications. *Chemical Society Reviews*, 45(7):1819–1849, 2016.
- [9] Jiabao Xu, Tong Yu, Christos E. Zois, Ji-Xin Cheng, Yuguo Tang, Adrian L. Harris, and Wei E. Huang. Unveiling cancer metabolism through spontaneous and coherent raman spectroscopy and stable isotope probing. *Cancers*, 13(7):1718, April 2021.
- [10] S Sunder, R Mendelsohn, and HJ Bernstein. Raman studies of the ch and cd stretching regions in stearic acid and some specifically deuterated derivatives. *Chemistry and Physics of Lipids*, 17(4):456–465, 1976.
- [11] Matthew Noestheden, Qingyan Hu, Li-Lin Tay, Angela M Tonary, Albert Stolow, Roger MacKenzie, Jamshid Tanha, and John Paul Pezacki. Synthesis and characterization of cn-modified protein analogues as potential vibrational contrast agents. *Bioorganic chemistry*, 35(3):284–293, 2007.
- [12] Renzo Vanna, Alejandro De la Cadena, Benedetta Talone, Cristian Manzoni, Marco Marangoni, Dario Polli, and Giulio Cerullo. Vibrational imaging for label-free cancer diagnosis and classification. *La Rivista del Nuovo Cimento*, 45(2):107–187, Feb 2022.
- [13] Mahmoud Ghomi. *Applications of Raman spectroscopy to biology: from basic studies to disease diagnosis*, volume 5. IOS press, 2012.
- [14] GJ Puppels, FFM De Mul, Cornelis Otto, J Greve, M Robert-Nicoud, DJ Arndt-Jovin, and TM Jovin. Studying single living cells and chromosomes by confocal raman microspectroscopy. *Nature*, 347(6290):301–303, 1990.

Bibliography

- [15] George Turrell. 1 - the raman effect. In George Turrell and Jacques Corset, editors, *Raman Microscopy*, pages 1–25. Academic Press, London, 1996.
- [16] Nicholas Stone, Catherine Kendall, Jenny Smith, Paul Crow, and Hugh Barr. Raman spectroscopy for identification of epithelial cancers. *Faraday discussions*, 126:141–157, 2004.
- [17] Abigail S Haka, Karen E Shafer-Peltier, Maryann Fitzmaurice, Joseph Crowe, Ramachandra R Dasari, and Michael S Feld. Diagnosing breast cancer by using raman spectroscopy. *Proceedings of the National Academy of Sciences*, 102(35):12371–12376, 2005.
- [18] Catherine Kendall, Martin Isabelle, Florian Bazant-Hegemark, Joanne Hutchings, Linda Orr, Jaspreet Babrah, Rebecca Baker, and Nicholas Stone. Vibrational spectroscopy: a clinical tool for cancer diagnostics. *Analyst*, 134(6):1029–1045, 2009.
- [19] Matthias Kirsch, Gabriele Schackert, Reiner Salzer, and Christoph Krafft. Raman spectroscopic imaging for in vivo detection of cerebral brain metastases. *Analytical and bioanalytical chemistry*, 398(4):1707–1713, 2010.
- [20] Paola Piredda, Manuel Berning, Petra Boukamp, and Andreas Volkmer. Subcellular raman microspectroscopy imaging of nucleic acids and tryptophan for distinction of normal human skin cells and tumorigenic keratinocytes. *Anal Chem*, 87(13):6778–6785, May 2015.
- [21] U Neugebauer, T Bocklitz, J H Clement, C Krafft, and J Popp. Towards detection and identification of circulating tumour cells using raman spectroscopy. *Analyst*, 135(12):3178–3182, October 2010.
- [22] Conor L Evans, X Sunney Xie, et al. Coherent anti-stokes raman scattering microscopy: chemical imaging for biology and medicine. *Annual review of analytical chemistry*, 1(1):883, 2008.
- [23] Ji-Xin Cheng and Xiaoliang Sunney Xie. *Coherent Raman scattering microscopy*. CRC press, 2016.
- [24] Dario Polli, Vikas Kumar, Carlo M. Valensise, Marco Marangoni, and Giulio Cerullo. Broadband coherent raman scattering microscopy. *Laser & Photonics Reviews*, 12(9):1800020, 2018.
- [25] W Denk, J H Strickler, and W W Webb. Two-photon laser scanning fluorescence microscopy. *Science*, 248(4951):73–76, April 1990.
- [26] Yanping Li, Binglin Shen, Shaowei Li, Yihua Zhao, Junle Qu, and Liwei Liu. Review of stimulated raman scattering microscopy techniques and applications in the biosciences. *Advanced Biology*, 5(1):2000184, 2021.
- [27] Conor L. Evans, Eric O. Potma, Mehron Puoris’haag, Daniel Côté, Charles P. Lin, and X. Sunney Xie. Chemical imaging of tissue *in vivo* with video-rate coherent anti-stokes raman scattering microscopy. *Proceedings of the National Academy of Sciences*, 102(46):16807–16812, 2005.
- [28] Brian G Saar, Christian W Freudiger, Jay Reichman, C Michael Stanley, Gary R Holtom, and X Sunney Xie. Video-rate molecular imaging in vivo with stimulated raman scattering. *science*, 330(6009):1368–1370, 2010.
- [29] Christian W. Freudiger, Wei Min, Brian G. Saar, Sijia Lu, G. R. Holtom, Chengwei He, Jason C Tsai, Jingxuan Kang, and X. Sunney Xie. Label-free biomedical imaging with high sensitivity by stimulated raman scattering microscopy. *Science*, 322:1857 – 1861, 2008.
- [30] Evelyn Ploetz, Stefan Laimgruber, Stefan Berner, Wolfgang Zinth, and Peter Gilch. Femtosecond stimulated raman microscopy. *Applied Physics B*, 87:389–393, 2007.
- [31] P Nandakumar, A Kovalev, and A Volkmer. Vibrational imaging based on stimulated raman scattering microscopy. *New Journal of Physics*, 11(3):033026, mar 2009.
- [32] Kazuki Hashimoto, Megumi Takahashi, Takuro Ideguchi, and Keisuke Goda. Broadband coherent raman spectroscopy running at 24,000 spectra per second. *Scientific Reports*, 6(1):21036, Feb 2016.
- [33] M. D. Duncan, J. Reintjes, and T. J. Manuccia. Scanning coherent anti-stokes raman microscope. *Opt. Lett.*, 7(8):350–352, Aug 1982.
- [34] Andreas Zumbusch, Gary R Holtom, and X Sunney Xie. Three-dimensional vibrational imaging by coherent anti-stokes raman scattering. *Physical review letters*, 82(20):4142, 1999.
- [35] Eine neue erscheinung bei der lichtzerstreuung in krystallen. *Die Naturwissenschaften*, 16(28):557–558, July 1928.
- [36] Chandrasekhara Venkata Raman and Kariamanikkam Srinivasa Krishnan. A new type of secondary radiation. *Nature*, 121(3048):501–502, 1928.
- [37] M. D. Duncan, J. Reintjes, and T. J. Manuccia. Scanning coherent anti-stokes raman microscope. *Optics Letters*, 7(8):350, August 1982.

- [38] Andreas Zumbusch, Gary R. Holtom, and X. Sunney Xie. Three-dimensional vibrational imaging by coherent anti-stokes raman scattering. *Phys. Rev. Lett.*, 82:4142–4145, May 1999.
- [39] Hervé Rigneault. Chapter 1 - coherent raman scattering processes. In Ji-Xin Cheng, Wei Min, Yasuyuki Ozeki, and Dario Polli, editors, *Stimulated Raman Scattering Microscopy*, pages 3–20. Elsevier, 2022.
- [40] Robert W. Boyd. Chapter 2 - wave-equation description of nonlinear optical interactions. In Robert W. Boyd, editor, *Nonlinear Optics (Third Edition)*, pages 69–133. Academic Press, Burlington, third edition edition, 2008.
- [41] Jennifer P. Ogilvie, Meng Cui, Dmitry Pestov, Alexei V. Sokolov, and Marlan O. Scully. Time-delayed coherent raman spectroscopy. *Molecular Physics*, 106(2-4):587–594, 2008.
- [42] Ji-Xin Cheng, Lewis D. Book, and X. Sunney Xie. Polarization coherent anti-stokes raman scattering microscopy. *Optics Letters*, 26(17):1341, September 2001.
- [43] Andreas Volkmer, Lewis D Book, and X Sunney Xie. Time-resolved coherent anti-stokes raman scattering microscopy: Imaging based on raman free induction decay. *Applied Physics Letters*, 80(9):1505–1507, 2002.
- [44] Paul J. Wrzesinski, Hans U. Stauffer, Waruna D. Kulatilaka, James R. Gord, and Sukesh Roy. Time-resolved femtosecond CARS from 10 to 50 bar: collisional sensitivity. *Journal of Raman Spectroscopy*, 44(10):1344–1348, March 2013.
- [45] Miu Tamamitsu, Yusuke Sakaki, Tasuku Nakamura, G. Krishna Podagatlapalli, Takuro Ideguchi, and Keisuke Goda. Ultrafast broadband fourier-transform CARS spectroscopy at 50, 000 spectra/s enabled by a scanning fourier-domain delay line. *Vibrational Spectroscopy*, 91:163–169, July 2017.
- [46] Marcus T. Cicerone, Khaled A. Aamer, Young Jong Lee, and Erik Vartiainen. Maximum entropy and time-domain kramers-kronig phase retrieval approaches are functionally equivalent for CARS microspectroscopy. *Journal of Raman Spectroscopy*, 43(5):637–643, April 2012.
- [47] Erik M Vartiainen, Hilde A Rinia, Michiel Müller, and Mischa Bonn. Direct extraction of raman line-shapes from congested cars spectra. *Optics Express*, 14(8):3622–3630, 2006.
- [48] C. M. Valensise, A. Giuseppi, F. Vernuccio, A. De la Cadena, G. Cerullo, and D. Polli. Removing non-resonant background from CARS spectra via deep learning. *APL Photonics*, 5(6):061305, June 2020.
- [49] Rola Houhou, Parijat Barman, Micheal Schmitt, Tobias Meyer, Juergen Popp, and Thomas Bocklitz. Deep learning as phase retrieval tool for CARS spectra. *Optics Express*, 28(14):21002, July 2020.
- [50] Zhengwei Wang, Kevin O' Dwyer, Ryan Muddiman, Tomas Ward, Charles H. Camp, and Bryan M. Hennelly. VECTOR: Very deep convolutional autoencoders for non-resonant background removal in broadband coherent anti-stokes raman scattering. *Journal of Raman Spectroscopy*, 53(6):1081–1093, March 2022.
- [51] Brian G. Saar, Christian W. Freudiger, Jay Reichman, C. Michael Stanley, Gary R. Holtom, and X. Sunney Xie. Video-rate molecular imaging in vivo with stimulated raman scattering. *Science*, 330(6009):1368–1370, 2010.
- [52] Thomas Hellerer, Annika MK Enejder, and Andreas Zumbusch. Spectral focusing: High spectral resolution spectroscopy with broad-bandwidth laser pulses. *Applied Physics Letters*, 85(1):25–27, 2004.
- [53] Israel Rocha-Mendoza, Wolfgang Langbein, and Paola Borri. Coherent anti-stokes raman microspectroscopy using spectral focusing with glass dispersion. *Applied Physics Letters*, 93(20):201103, 2008.
- [54] Adrian F Pegoraro, Andrew Ridsdale, Douglas J Moffatt, Yiwei Jia, John Paul Pezacki, and Albert Stolow. Optimally chirped multimodal cars microscopy based on a single ti: sapphire oscillator. *Optics express*, 17(4):2984–2996, 2009.
- [55] Aaron D Slepko, Andrew Ridsdale, Adrian F Pegoraro, Douglas J Moffatt, and Albert Stolow. Multimodal cars microscopy of structured carbohydrate biopolymers. *Biomedical optics express*, 1(5):1347–1357, 2010.
- [56] Leila B Mostaçõ-Guidolin, Michael G Sowa, Andrew Ridsdale, Adrian F Pegoraro, Michael SD Smith, Mark D Hewko, Elicia K Kohlenberg, Bernie Schattka, Masashi Shiomi, Albert Stolow, et al. Differentiating atherosclerotic plaque burden in arterial tissues using femtosecond cars-based multimodal nonlinear optical imaging. *Biomedical optics express*, 1(1):59–73, 2010.
- [57] Marco Marangoni, Alessio Gambetta, Cristian Manzoni, Vikas Kumar, Roberta Ramponi, and Giulio Cerullo. Fiber-format CARS spectroscopy by spectral compression of femtosecond pulses from a single laser oscillator. *Optics Letters*, 34(21):3262, October 2009.
- [58] Wolfgang Langbein, Israel Rocha-Mendoza, and Paola Borri. Single source coherent anti-stokes raman microspectroscopy using spectral focusing. *Applied Physics Letters*, 95(8):081109, 2009.

Bibliography

- [59] Iestyn Pope, Wolfgang Langbein, Peter Watson, and Paola Borri. Simultaneous hyperspectral differential-cars, tpf and shg microscopy with a single 5 fs ti: Sa laser. *Optics Express*, 21(6):7096–7106, 2013.
- [60] Francesco Masia, Adam Glen, Phil Stephens, Paola Borri, and Wolfgang Langbein. Quantitative chemical imaging and unsupervised analysis using hyperspectral coherent anti-stokes raman scattering microscopy. *Analytical Chemistry*, 85(22):10820–10828, Nov 2013.
- [61] Claudia Di Napoli, Iestyn Pope, Francesco Masia, Peter Watson, Wolfgang Langbein, and Paola Borri. Hyperspectral and differential cars microscopy for quantitative chemical imaging in human adipocytes. *Biomedical optics express*, 5(5):1378–1390, 2014.
- [62] Claudia Di Napoli, Iestyn Pope, Francesco Masia, Wolfgang Langbein, Pete Watson, and Paola Borri. Quantitative spatiotemporal chemical profiling of individual lipid droplets by hyperspectral cars microscopy in living human adipose-derived stem cells. *Analytical chemistry*, 88(7):3677–3685, 2016.
- [63] Charles H. Camp, Young Jong Lee, and Marcus T. Cicerone. Quantitative, comparable coherent anti-stokes raman scattering (CARS) spectroscopy: correcting errors in phase retrieval. *Journal of Raman Spectroscopy*, 47(4):408–415, October 2015.
- [64] Esben Ravn Andresen, Henrik Nørgaard Paulsen, Victoria Birkedal, Jan Thøgersen, and Søren Rud Keiding. Broadband multiplex coherent anti-stokes raman scattering microscopy employing photonic-crystal fibers. *J. Opt. Soc. Am. B*, 22(9):1934–1938, Sep 2005.
- [65] Michiel Müller and Juleon M. Schins. Imaging the thermodynamic state of lipid membranes with multiplex cars microscopy. *The Journal of Physical Chemistry B*, 106(14):3715–3723, Apr 2002.
- [66] Hideaki Kano, Takumi Maruyama, Junko Kano, Yuki Oka, Daiki Kaneta, Tiffany Guerenne, Philippe Leproux, Vincent Couderc, and Masayuki Noguchi. Ultra-multiplex cars spectroscopic imaging with 1-millisecond pixel dwell time. *OSA Continuum*, 2(5):1693–1705, May 2019.
- [67] Hiroaki Yoneyama, Kazuhiro Sudo, Philippe Leproux, Vincent Couderc, Akihito Inoko, and Hideaki Kano. Invited article: Cars molecular fingerprinting using sub-100-ps microchip laser source with fiber amplifier. *APL Photonics*, 3(9):092408, 2018.
- [68] Ji-xin Cheng, Andreas Volkmer, Lewis D Book, and X Sunney Xie. Multiplex coherent anti-stokes raman scattering microspectroscopy and study of lipid vesicles. *The Journal of Physical Chemistry B*, 106(34):8493–8498, 2002.
- [69] Bernhard von Vacano, Lars Meyer, and Marcus Motzkus. Rapid polymer blend imaging with quantitative broadband multiplex cars microscopy. *Journal of Raman Spectroscopy: An International Journal for Original Work in all Aspects of Raman Spectroscopy, Including Higher Order Processes, and also Brillouin and Rayleigh Scattering*, 38(7):916–926, 2007.
- [70] Christoph Pohling, Tiago Backup, and Marcus Motzkus. Hyperspectral data processing for chemoselective multiplex coherent anti-stokes raman scattering microscopy of unknown samples. *Journal of biomedical optics*, 16(2):021105, 2011.
- [71] Christoph Pohling, Tiago Backup, Axel Pagenstecher, and Marcus Motzkus. Chemoselective imaging of mouse brain tissue via multiplex cars microscopy. *Biomedical optics express*, 2(8):2110–2116, 2011.
- [72] Hideaki Kano, Takumi Maruyama, Junko Kano, Yuki Oka, Daiki Kaneta, Tiffany Guerenne, Philippe Leproux, Vincent Couderc, and Masayuki Noguchi. Ultra-multiplex CARS spectroscopic imaging with 1-millisecond pixel dwell time. *OSA Continuum*, 2(5):1693, April 2019.
- [73] Tiffany Guerenne-Del Ben, Zakaniaina Rajaofara, Vincent Couderc, Vincent Sol, Hideaki Kano, Philippe Leproux, and Jean-Michel Petit. Multiplex coherent anti-stokes raman scattering highlights state of chromatin condensation in CH region. *Scientific Reports*, 9(1), September 2019.
- [74] Mutsuo Nuriya, Hiroaki Yoneyama, Kyosuke Takahashi, Philippe Leproux, Vincent Couderc, Masato Yasui, and Hideaki Kano. Characterization of intra/extracellular water states probed by ultrabroadband multiplex coherent anti-stokes raman scattering (CARS) spectroscopic imaging. *The Journal of Physical Chemistry A*, 123(17):3928–3934, April 2019.
- [75] Yuki Oka, Larina Tzu-Wei Shen, Tomoko Mori, Takumi Iwamura, Philippe Leproux, Satoshi Matsusaka, and Hideaki Kano. Label-free visualization of cellular response to molecularly targeted agents using multiplex coherent anti-stokes raman scattering and third harmonic generation microscopy. *Applied Physics Express*, 15(10):102001, September 2022.
- [76] Keisuke Isobe, Akira Suda, Masahiro Tanaka, Hiroshi Hashimoto, Fumihiko Kannari, Hiroyuki Kawano, Hideaki Mizuno, Atsushi Miyawaki, and Katsumi Midorikawa. Single-pulse coherent anti-stokes raman scattering microscopy employing an octave spanning pulse. *Opt. Express*, 17(14):11259–11266, Jul 2009.

- [77] Wolfgang Langbein, Israel Rocha-Mendoza, and Paola Borri. Single source coherent anti-stokes raman microspectroscopy using spectral focusing. *Applied Physics Letters*, 95(8):081109, 2009.
- [78] Tak W. Kee and Marcus T. Cicerone. Simple approach to one-laser, broadband coherent anti-stokes raman scattering microscopy. *Opt. Lett.*, 29(23):2701–2703, Dec 2004.
- [79] Jingjiang Xu, Baoshan Guo, Kenneth K. Y. Wong, and Kevin K. Tsia. Broadband hyperspectral coherent anti-Stokes Raman scattering microscopy for stain-free histological imaging with principal component analysis. In Ammasi Periasamy, Peter T. C. So, and Karsten König, editors, *Multiphoton Microscopy in the Biomedical Sciences XIV*, volume 8948, page 89480R. International Society for Optics and Photonics, SPIE, 2014.
- [80] Hideaki Kano and Hiro-o Hamaguchi. Ultrabroadband ($>2500\text{cm}^{-1}$) multiplex coherent anti-stokes raman scattering microspectroscopy using a supercontinuum generated from a photonic crystal fiber. *Applied Physics Letters*, 86(12):121113, 2005.
- [81] Philippe Leproux, Vincent Couderc, Annalisa De Angelis, Masanari Okuno, Hideaki Kano, and Hiro-o Hamaguchi. New opportunities offered by compact sub-nanosecond supercontinuum sources in ultra-broadband multiplex cars microspectroscopy. *Journal of Raman Spectroscopy*, 42(10):1871–1874, 2011.
- [82] Meng Cui, Manuel Joffre, Joshua Skodack, and Jennifer P. Ogilvie. Interferometric fourier transform coherent anti-stokes raman scattering. *Opt. Express*, 14(18):8448–8458, Sep 2006.
- [83] Alex Soares Duarte, Christoph Schneder mann, and Philipp Kukura. Wide-field detected fourier transform cars microscopy. *Scientific Reports*, 6(1):37516, Nov 2016.
- [84] Meng Cui, Manuel Joffre, Joshua Skodack, and Jennifer P Ogilvie. Interferometric fourier transform coherent anti-stokes raman scattering. *Optics Express*, 14(18):8448–8458, 2006.
- [85] Jennifer P Ogilvie, Emmanuel Beaufrepaire, Antioni Alexandrou, and Manuel Joffre. Fourier-transform coherent anti-stokes raman scattering microscopy. *Optics letters*, 31(4):480–482, 2006.
- [86] Kotaro Hiramatsu, Tatsuya Tajima, and Keisuke Goda. Ultrafast, dual-band coherent raman spectroscopy without ultrashort pulses. *ACS Photonics*, 9(11):3522–3528, October 2022.
- [87] Nicola Coluccelli, Edoardo Vicentini, Alessio Gambetta, Christopher R Howle, Kenneth Mcewan, Paolo Laporta, and Gianluca Galzerano. Broadband fourier-transform coherent raman spectroscopy with an ytterbium fiber laser. *Optics Express*, 26(15):18855, July 2018.
- [88] Takuro Ideguchi, Simon Holzner, Birgitta Bernhardt, Guy Guelachvili, Nathalie Picqué, and Theodor W. Hänsch. Coherent raman spectro-imaging with laser frequency combs. *Nature*, 502(7471):355–358, Oct 2013.
- [89] Fritz Keilmann, Christoph Gohle, and Ronald Holzwarth. Time-domain mid-infrared frequency-comb spectrometer. *Optics letters*, 29(13):1542–1544, 2004.
- [90] Ian Coddington, Nathan Newbury, and William Swann. Dual-comb spectroscopy. *Optica*, 3(4):414–426, 2016.
- [91] Steven T Cundiff and Jun Ye. Colloquium: Femtosecond optical frequency combs. *Reviews of Modern Physics*, 75(1):325, 2003.
- [92] Kathrin J Mohler, Bernhard J Bohn, Ming Yan, Gwénaëlle Mélen, Theodor W Hänsch, and Nathalie Picqué. Dual-comb coherent raman spectroscopy with lasers of 1-ghz pulse repetition frequency. *Optics letters*, 42(2):318–321, 2017.
- [93] Kun Chen, Tao Wu, Tao Chen, Haoyun Wei, Honglei Yang, Tian Zhou, and Yan Li. Spectral focusing dual-comb coherent anti-stokes raman spectroscopic imaging. *Optics Letters*, 42(18):3634–3637, 2017.
- [94] Charles H. Camp Jr, Young Jong Lee, John M. Heddleston, Christopher M. Hartshorn, Angela R. Hight Walker, Jeremy N. Rich, Justin D. Lathia, and Marcus T. Cicerone. High-speed coherent raman fingerprint imaging of biological tissues. *Nature Photonics*, 8(8):627–634, Aug 2014.
- [95] Michiel Müller and Andreas Zumbusch. Coherent anti-stokes raman scattering microscopy. *ChemPhysChem*, 8(15):2156–2170, October 2007.
- [96] Erik M. Vartiainen. Phase retrieval approach for coherent anti-stokes raman scattering spectrum analysis. *Journal of the Optical Society of America B*, 9(8):1209, August 1992.
- [97] Hongying Liu, Tian Lan, Xiaomei Chen, and Guoqiang Ni. Dispersion compensation based on prism compressor. In Takashige Omatu, editor, *SPIE Proceedings*. SPIE, April 2017.
- [98] Jae Yong Lee, Se-Hwa Kim, Dae Won Moon, and Eun Seong Lee. Three-color multiplex cars for fast imaging and microspectroscopy in the entire chn stretching vibrational region. *Opt. Express*, 17(25):22281–22295, Dec 2009.

Bibliography

- [99] Hideaki Kano and Hiro o Hamaguchi. Vibrationally resonant imaging of a single living cell by supercontinuum-based multiplex coherent anti-stokes raman scattering microspectroscopy. *Optics Express*, 13(4):1322, 2005.
- [100] Federico Vernuccio, Arianna Bresci, Benedetta Talone, Alejandro de la Cadena, Chiara Ceconello, Stefano Mantero, Cristina Sobacchi, Renzo Vanna, Giulio Cerullo, and Dario Polli. Fingerprint multiplex cars at high speed based on supercontinuum generation in bulk media and deep learning spectral denoising. *Opt. Express*, 30(17):30135–30148, Aug 2022.
- [101] Anne-Laure Calendron, Hüseyin Çankaya, Giovanni Cirmi, and Franz X. Kärtner. White-light generation with sub-ps pulses. *Opt. Express*, 23(11):13866–13879, Jun 2015.
- [102] Audrius Dubietis, Gintaras Tamošauskas, Rosvaldas Šuminas, Vytautas Jukna, and Arnaud Couairon. Ultrafast supercontinuum generation in bulk condensed media (invited review). 2017.
- [103] B. Talone, M. Bazzarelli, A. Schirato, F. Dello Vicario, D. Viola, E. Jacchetti, M. Bregonzio, M. T. Raimondi, G. Cerullo, and D. Polli. Phototoxicity induced in living hela cells by focused femtosecond laser pulses: a data-driven approach. *Biomed. Opt. Express*, 12(12):7886–7905, Dec 2021.
- [104] Yong-Xin Yan and Keith A Nelson. Impulsive stimulated light scattering. i. general theory. *The Journal of chemical physics*, 87(11):6240–6256, 1987.
- [105] Sanford Ruhman, Alan G Joly, and Keith A Nelson. Coherent molecular vibrational motion observed in the time domain through impulsive stimulated raman scattering. *IEEE journal of quantum electronics*, 24(2):460–469, 1988.
- [106] A Laubereau and W Kaiser. Vibrational dynamics of liquids and solids investigated by picosecond light pulses. *Reviews of Modern Physics*, 50(3):607, 1978.
- [107] Francois M Kamga and Mark G Sceats. Pulse-sequenced coherent anti-stokes raman scattering spectroscopy: a method for suppression of the nonresonant background. *Optics letters*, 5(3):126–128, 1980.
- [108] Dmitry Pestov, Gombojav O Ariunbold, Xi Wang, Robert K Murawski, Vladimir A Sautenkov, Alexei V Sokolov, and Marlan O Scully. Coherent versus incoherent raman scattering: molecular coherence excitation and measurement. *Optics letters*, 32(12):1725–1727, 2007.
- [109] Dmitry Pestov, Robert K Murawski, Gombojav O Ariunbold, Xi Wang, Miaochan Zhi, Alexei V Sokolov, Vladimir A Sautenkov, Yuri V Rostovtsev, Arthur Dogariu, Yu Huang, et al. Optimizing the laser-pulse configuration for coherent raman spectroscopy. *science*, 316(5822):265–268, 2007.
- [110] Romedi Selm, Martin Winterhalder, Andreas Zumbusch, Günther Krauss, Tobias Hanke, Alexander Sell, and Alfred Leitenstorfer. Ultrabroadband background-free coherent anti-stokes raman scattering microscopy based on a compact er: fiber laser system. *Optics letters*, 35(19):3282–3284, 2010.
- [111] Florian Adler, Alexander Sell, Florian Sotier, Rupert Huber, and Alfred Leitenstorfer. Attosecond relative timing jitter and 13 fs tunable pulses from a two-branch er: fiber laser. *Optics letters*, 32(24):3504–3506, 2007.
- [112] M Marangoni, Daniele Brida, M Quintavalle, G Cirmi, FM Pigozzo, Cristian Manzoni, F Baronio, AD Capobianco, and G Cerullo. Narrow-bandwidth picosecond pulses by spectral compression of femtosecond pulses in a second-order nonlinear crystal. *Optics express*, 15(14):8884–8891, 2007.
- [113] K Moutzouris, F Adler, F Sotier, D Träutlein, and A Leitenstorfer. Multimilliwatt ultrashort pulses continuously tunable in the visible from a compact fiber source. *Optics letters*, 31(8):1148–1150, 2006.
- [114] Ji xin Cheng, Andreas Volkmer, Lewis D. Book, and X. Sunney Xie. An epi-detected coherent anti-stokes raman scattering (e-CARS) microscope with high spectral resolution and high sensitivity. *The Journal of Physical Chemistry B*, 105(7):1277–1280, February 2001.
- [115] Erik T. Garbacik, Jeroen P. Korterik, Cees Otto, Jennifer L. Herek, and Herman L. Offerhaus. Epi-detection of vibrational phase contrast coherent anti-stokes raman scattering. *Optics Letters*, 39(20):5814, October 2014.
- [116] Andreas Volkmer, Ji-Xin Cheng, and X. Sunney Xie. Vibrational imaging with high sensitivity via epi-detected coherent anti-stokes raman scattering microscopy. *Physical Review Letters*, 87(2), June 2001.
- [117] Andreas Volkmer. Vibrational imaging and microspectroscopies based on coherent anti-stokes raman scattering microscopy. *Journal of Physics D: Applied Physics*, 38(5):R59–R81, February 2005.
- [118] Hope T Beier, Gary D Noojin, and Benjamin A Rockwell. Stimulated raman scattering using a single femtosecond oscillator with flexibility for imaging and spectral applications. *Optics express*, 19(20):18885–18892, 2011.

- [119] Esben Ravn Andresen, Pascal Berto, and Hervé Rigneault. Stimulated raman scattering microscopy by spectral focusing and fiber-generated soliton as stokes pulse. *Optics letters*, 36(13):2387–2389, 2011.
- [120] Christian W Freudiger, Wei Min, Gary R Holtom, Bingwei Xu, Marcos Dantus, and X Sunney Xie. Highly specific label-free molecular imaging with spectrally tailored excitation-stimulated raman scattering (ste-srs) microscopy. *Nature photonics*, 5(2):103–109, 2011.
- [121] Yasuyuki Ozeki, Wataru Umemura, Yoichi Otsuka, Shuya Satoh, Hiroyuki Hashimoto, Kazuhiko Sumimura, Norihiko Nishizawa, Kiichi Fukui, and Kazuyoshi Itoh. High-speed molecular spectral imaging of tissue with stimulated raman scattering. *Nature photonics*, 6(12):845–851, 2012.
- [122] Bin Liu, Hyeon Jeong Lee, Delong Zhang, Chien-Sheng Liao, Na Ji, Yuanqin Xia, and Ji-Xin Cheng. Label-free spectroscopic detection of membrane potential using stimulated raman scattering. *Applied Physics Letters*, 106(17):173704, 2015.
- [123] Dan Fu, Gary Holtom, Christian Freudiger, Xu Zhang, and Xiaoliang Sunney Xie. Hyperspectral imaging with stimulated raman scattering by chirped femtosecond lasers. *The Journal of Physical Chemistry B*, 117(16):4634–4640, 2013.
- [124] Alejandro De la Cadena, Federico Vernuccio, Andrea Ragni, Giuseppe Sciortino, Renzo Vanna, Carino Ferrante, Natalia Pediconi, Carlo Valensise, Luca Genchi, Sergey P. Laptinok, Andrea Doni, Marco Erreni, Tullio Scopigno, Carlo Liberale, Giorgio Ferrari, Marco Sampietro, Giulio Cerullo, and Dario Polli. Broadband stimulated raman imaging based on multi-channel lock-in detection for spectral histopathology. *APL Photonics*, 7(7):076104, July 2022.
- [125] Alejandro De la Cadena, Federico Vernuccio, Benedetta Talone, Arianna Bresci, Chiara Ceconello, Subir Das, Renzo Vanna, Giulio Cerullo, and Dario Polli. Multiplex chemical imaging based on broadband stimulated raman scattering microscopy. *Journal of Visualized Experiments*, (185), July 2022.
- [126] Francesco Saltarelli, Vikas Kumar, Daniele Viola, Francesco Crisafi, Fabrizio Preda, Giulio Cerullo, and Dario Polli. Broadband stimulated raman scattering spectroscopy by a photonic time stretcher. *Optics express*, 24(19):21264–21275, 2016.
- [127] Sven Dobner and Carsten Fallnich. Dispersive fourier transformation femtosecond stimulated raman scattering. *Applied Physics B*, 122(11):1–6, 2016.
- [128] Julien Réhault, Francesco Crisafi, Vikas Kumar, Gustavo Ciardi, Marco Marangoni, Giulio Cerullo, and Dario Polli. Broadband stimulated raman scattering with fourier-transform detection. *Optics express*, 23(19):25235–25246, 2015.
- [129] M. Bradler and E. Riedle. Temporal and spectral correlations in bulk continua and improved use in transient spectroscopy. *Journal of the Optical Society of America B*, 31(7):1465, June 2014.
- [130] B. Prade, M. Franco, A. Mysyrowicz, A. Couairon, H. Buersing, B. Eberle, M. Krenz, D. Seiffer, and O. Vasseur. Spatial mode cleaning by femtosecond filamentation in air. *Optics Letters*, 31(17):2601, August 2006.
- [131] D. Wegkamp, D. Brida, S. Bonora, G. Cerullo, J. Stähler, M. Wolf, and S. Wall. Phase retrieval and compression of low-power white-light pulses. *Applied Physics Letters*, 99(10):101101, September 2011.
- [132] Katsumi Midorikawa, Hiroyuki Kawano, Akira Suda, Chihiro Nagura, and Minoru Obara. Polarization properties of ultrafast white-light continuum generated in condensed media. *Applied Physics Letters*, 80(6):923–925, February 2002.
- [133] M. Bradler, P. Baum, and E. Riedle. Femtosecond continuum generation in bulk laser host materials with sub- μ j pump pulses. *Applied Physics B*, 97(3):561–574, August 2009.
- [134] P. Polynkin and M. Kolesik. Critical power for self-focusing in the case of ultrashort laser pulses. *Physical Review A*, 87(5), May 2013.
- [135] A. Brodeur and S. L. Chin. Band-gap dependence of the ultrafast white-light continuum. *Physical Review Letters*, 80(20):4406–4409, May 1998.
- [136] A. Brodeur and S. L. Chin. Ultrafast white-light continuum generation and self-focusing in transparent condensed media. *Journal of the Optical Society of America B*, 16(4):637, April 1999.
- [137] Sergey Mitryukovskiy. Coherent secondary radiation from femtosecond laser filaments. 09 2014.
- [138] Ieva Gražulevičiūtė, Milda Skeivyte, Enrika Keblyte, Justas Galinis, Gintaras Tamošauskas, and Audrius Dubietis. Supercontinuum generation in YAG and sapphire with picosecond laser pulses. *Lithuanian Journal of Physics*, 55(2), July 2015.

Bibliography

- [139] Matthew G. Clark, Gil A. Gonzalez, and Chi Zhang. Pulse-picking multimodal nonlinear optical microscopy. *Analytical Chemistry*, 94(44):15405–15414, October 2022.
- [140] Yan Fu, Haifeng Wang, Riyi Shi, and Ji-Xin Cheng. Characterization of photodamage in coherent anti-stokes raman scattering microscopy. *Optics Express*, 14(9):3942, 2006.
- [141] D.J. Kane and R. Trebino. Characterization of arbitrary femtosecond pulses using frequency-resolved optical gating. *IEEE Journal of Quantum Electronics*, 29(2):571–579, 1993.
- [142] Frank L Pedrotti and Leno S Pedrotti. *Introduction to optics*. Pearson, Upper Saddle River, NJ, 2 edition, October 1992.
- [143] Andrew Weiner. *Ultrafast optics*, volume 72. John Wiley & Sons, 2011.
- [144] Daniel J. Kane, Jeremy Weston, and Kai-Chien J. Chu. Real-time inversion of polarization gate frequency-resolved optical gating spectrograms. *Appl. Opt.*, 42(6):1140–1144, Feb 2003.
- [145] Tracy Sharp Clement, A. J. Taylor, and Daniel J. Kane. Single-shot measurement of the amplitude and phase of ultrashort laser pulses in the violet. *Opt. Lett.*, 20(1):70–72, Jan 1995.
- [146] Rick Trebino and Daniel J. Kane. Using phase retrieval to measure the intensity and phase of ultrashort pulses: frequency-resolved optical gating. *Journal of the Optical Society of America A*, 10(5):1101, May 1993.
- [147] Jeff Squier and Michiel Müller. High resolution nonlinear microscopy: A review of sources and methods for achieving optimal imaging. *Review of Scientific Instruments*, 72(7):2855–2867, July 2001.
- [148] Shuxia Guo, Jürgen Popp, and Thomas Bocklitz. Chemometric analysis in raman spectroscopy from experimental design to machine learning-based modeling. *Nature Protocols*, 16(12):5426–5459, November 2021.
- [149] Chien-Sheng Liao, Joon Hee Choi, Delong Zhang, Stanley H. Chan, and Ji-Xin Cheng. Denoising stimulated raman spectroscopic images by total variation minimization. *The Journal of Physical Chemistry C*, 119(33):19397–19403, August 2015.
- [150] Federico Vernuccio, Arianna Bresci, Valeria Cimini, Alessandro Giuseppi, Giulio Cerullo, Dario Polli, and Carlo Michele Valensise. Artificial intelligence in classical and quantum photonics. *Laser & Photonics Reviews*, 16(5):2100399, March 2022.
- [151] Charles H. Camp Jr., John S. Bender, and Young Jong Lee. Real-time and high-throughput raman signal extraction and processing in CARS hyperspectral imaging. *Optics Express*, 28(14):20422, June 2020.
- [152] M Makitalo and A Foi. Optimal inversion of the aniscombe transformation in low-count poisson image denoising. *IEEE Transactions on Image Processing*, 20(1):99–109, January 2011.
- [153] Danshi Wang and Min Zhang. Artificial intelligence in optical communications: From machine learning to deep learning. *Frontiers in Communications and Networks*, 2:656786, 2021.
- [154] Yuefeng Ji, Rentao Gu, Zeyuan Yang, Jin Li, Hui Li, and Min Zhang. Artificial intelligence-driven autonomous optical networks: 3s architecture and key technologies. *Science China Information Sciences*, 63(6):1–24, 2020.
- [155] Boris Karanov, Mathieu Chagnon, Félix Thouin, Tobias A Eriksson, Henning Bülow, Domaniç Lavery, Polina Bayvel, and Laurent Schmalen. End-to-end deep learning of optical fiber communications. *Journal of Lightwave Technology*, 36(20):4843–4855, 2018.
- [156] Darko Zibar, Molly Piels, Rasmus Jones, and Christian G Schäeffler. Machine learning techniques in optical communication. *Journal of Lightwave Technology*, 34(6):1442–1452, 2015.
- [157] Goëry Genty, Lauri Salmela, John M. Dudley, Daniel Brunner, Alexey Kokhanovskiy, Sergei Kobtsev, and Sergei K. Turitsyn. Machine learning and applications in ultrafast photonics. *Nature Photonics*, 15(2):91–101, November 2020.
- [158] Davide Piccinotti, Kevin F MacDonald, Simon A Gregory, Ian Youngs, and Nikolay I Zheludev. Artificial intelligence for photonics and photonic materials. *Reports on Progress in Physics*, 84(1):012401, December 2020.
- [159] Ian Goodfellow, Yoshua Bengio, and Aaron Courville. *Deep learning*. MIT press, 2016.
- [160] Richard S Sutton and Andrew G Barto. *Reinforcement learning: An introduction*. MIT press, 2018.
- [161] Lean Yu, Kin Keung Lai, Shouyang Wang, and Wei Huang. A bias-variance-complexity trade-off framework for complex system modeling. In *Computational Science and Its Applications - ICCSA 2006*, pages 518–527. Springer Berlin Heidelberg, 2006.

- [162] Diederik P. Kingma and Jimmy Ba. Adam: A method for stochastic optimization, 2017.
- [163] G. Cybenko. Approximation by superpositions of a sigmoidal function. *Mathematics of Control, Signals, and Systems*, 2(4):303, December 1989.
- [164] Věra Kůrková. Kolmogorov's theorem and multilayer neural networks. *Neural Networks*, 5(3):501, January 1992.
- [165] William A Gardner. Learning characteristics of stochastic-gradient-descent algorithms: A general study, analysis, and critique. *Signal processing*, 6(2):113, 1984.
- [166] Alexander LeNail. NN-SVG: Publication-ready neural network architecture schematics. *Journal of Open Source Software*, 4(33):747, January 2019.
- [167] Yann LeCun, Bernhard Boser, John S Denker, Donnie Henderson, Richard E Howard, Wayne Hubbard, and Lawrence D Jackel. Backpropagation applied to handwritten zip code recognition. *Neural computation*, 1(4):541, 1989.
- [168] Olaf Ronneberger, Philipp Fischer, and Thomas Brox. U-net: Convolutional networks for biomedical image segmentation. In *Lecture Notes in Computer Science*, pages 234–241. Springer International Publishing, 2015.
- [169] Kaiming He, Xiangyu Zhang, Shaoqing Ren, and Jian Sun. Deep residual learning for image recognition. In *2016 IEEE Conference on Computer Vision and Pattern Recognition (CVPR)*, page 770, 2016.
- [170] Bryce Manifold, Elena Thomas, Andrew T. Francis, Andrew H. Hill, and Dan Fu. Denoising of stimulated raman scattering microscopy images via deep learning. *Biomedical Optics Express*, 10(8):3860, July 2019.
- [171] Naoki Yamato, Hirohiko Niioaka, Jun Miyake, and Mamoru Hashimoto. Improvement of nerve imaging speed with coherent anti-stokes raman scattering rigid endoscope using deep-learning noise reduction. *Scientific Reports*, 10(1), September 2020.
- [172] Haonan Lin, Hyeon Jeong Lee, Nathan Tague, Jean-Baptiste Lugagne, Cheng Zong, Fengyuan Deng, Jonghyeon Shin, Lei Tian, Wilson Wong, Mary J. Dunlop, and Ji-Xin Cheng. Microsecond fingerprint stimulated raman spectroscopic imaging by ultrafast tuning and spatial-spectral learning. *Nature Communications*, 12(1), May 2021.
- [173] Yuexin Liu, Young Jong Lee, and Marcus T. Cicerone. Broadband CARS spectral phase retrieval using a time-domain kramers–kronig transform. *Optics Letters*, 34(9):1363, April 2009.
- [174] Pavel V. Kolesnichenko, Jonathan O. Tollerud, and Jeffrey A. Davis. Background-free time-resolved coherent raman spectroscopy (csrs and cars): Heterodyne detection of low-energy vibrations and identification of excited-state contributions. *APL Photonics*, 4(5):056102, 2019.
- [175] Pascal Berto, Esben Ravn Andresen, and Hervé Rigneault. Background-free stimulated raman spectroscopy and microscopy. *Phys. Rev. Lett.*, 112:053905, Feb 2014.
- [176] Edwin T Jaynes. On the rationale of maximum-entropy methods. *Proceedings of the IEEE*, 70(9):939–952, 1982.
- [177] Valensise C. Specnet. <https://github.com/Valensicv/SpecNet>, 2020.
- [178] Rajendhar Junjuri, Ali Saghi, Lasse Lensu, and Erik M. Vartiainen. Convolutional neural network-based retrieval of raman signals from CARS spectra. *Optics Continuum*, 1(6):1324, May 2022.
- [179] Ali Saghi, Rajendhar Junjuri, Lasse Lensu, and Erik M. Vartiainen. Semi-synthetic data generation to fine-tune a convolutional neural network for retrieving raman signals from CARS spectra. *Optics Continuum*, 1(11):2360, November 2022.
- [180] Sepp Hochreiter and Jürgen Schmidhuber. Long short-term memory. *Neural Computation*, 9(8):1735–1780, November 1997.
- [181] Roma Tauler. Multivariate curve resolution applied to second order data. *Chemometrics and Intelligent Laboratory Systems*, 30(1):133–146, November 1995.
- [182] Anna de Juan, Joaquim Jaumot, and Romà Tauler. Multivariate curve resolution (MCR). solving the mixture analysis problem. *Anal. Methods*, 6(14):4964–4976, 2014.
- [183] Imaiyan Chitra Ragupathy, Volker Schweikhard, and Andreas Zumbusch. Multivariate analysis of hyperspectral stimulated raman scattering microscopy images. *Journal of Raman Spectroscopy*, 52(9):1630–1642, June 2021.
- [184] Michael E. Winter. A proof of the n-FINDR algorithm for the automated detection of endmembers in a hyperspectral image. In Sylvia S. Shen and Paul E. Lewis, editors, *SPIE Proceedings*. SPIE, August 2004.

Bibliography

- [185] Ya-Juan Liu, Michelle Kyne, Cheng Wang, and Xi-Yong Yu. Data mining in raman imaging in a cellular biological system. *Computational and Structural Biotechnology Journal*, 18:2920–2930, 2020.
- [186] Miloš Miljković, Tatyana Chernenko, Melissa J. Romeo, Benjamin Bird, Christian Matthäus, and Max Diem. Label-free imaging of human cells: algorithms for image reconstruction of raman hyperspectral datasets. *The Analyst*, 135(8):2002, 2010.
- [187] Aristidis Likas, Nikos Vlassis, and Jakob J. Verbeek. The global k-means clustering algorithm. *Pattern Recognition*, 36(2):451–461, February 2003.
- [188] Ciro Menale, Lisa J Robinson, Eleonora Palagano, Rosita Rigoni, Marco Erreni, Alejandro J Almarza, Dario Strina, Stefano Mantero, Michela Lizier, Antonella Forlino, Roberta Besio, Marta Monari, Paolo Vezzoni, Barbara Cassani, Harry C Blair, Anna Villa, and Cristina Sobacchi. Absence of dipeptidyl peptidase 3 increases oxidative stress and causes bone loss. *Journal of Bone and Mineral Research*, 34(11):2133–2148, September 2019.
- [189] Abdullah Chandra Sekhar Talari, Zanyar Movasaghi, Shazza Rehman, and Ihtesham ur Rehman. Raman spectroscopy of biological tissues. *Applied Spectroscopy Reviews*, 50(1):46–111, August 2014.

List of Figures

1.1	Raman spectrum of a cell in the entire Raman-active region and in the corresponding fingerprint region. The peak assignments refer to the most abundant chemical bonds in biological samples, belonging to the four major biological molecules: lipids (black), protein (green), carbohydrates (yellow), and nucleic acids (blue). Adapted from [12].	3
1.2	Mass-spring system. x_0 is the equilibrium position, while x is the relative displacement. Adapted from [39]	6
1.3	(a) Vibrational modes of H ₂ O. (b) Absorption diagram. (c) Model of a diatomic molecule and light-matter interaction model. Adapted from [39]	8
1.4	Graph of the real and imaginary parts of the linear susceptibility.	9
1.5	Jablonsky diagrams of (a) Rayleigh scattering, (b) Stokes Raman scattering, (c) anti-Stokes Raman scattering. The solid lines represent the fundamental or ground state $ g\rangle$, the vibrational state $ v\rangle$, and the excited state $ e\rangle$, while the dashed line is a virtual state. $ g\rangle$ and $ v\rangle$ are separated by the resonance frequency Ω_R	11
1.6	Scattered light from a molecule with a single vibrational mode at frequency Ω_R	12
1.7	Coherent Raman scattering	15
1.8	Conceptual scheme of the interaction between light and matter considering third order nonlinear optical processes in the FWM frame.	16
1.9	Jablonsky diagrams of (a) Resonant Coherent anti-Stokes Raman scattering (Resonant CARS), (b) Non-resonant Coherent anti-Stokes Raman scattering (Non-resonant CARS).	20
1.10	Anti-Stokes signal (blue line) in the spectral domain: the contributions from the resonant (orange line), non-resonant (yellow line), and heterodyne terms (purple line) are highlighted.	22
1.11	CARS signal varying the ratio between the resonant and the non-resonant contributions, respectively with (a) $\frac{ x_R^{(3)} }{ x_{NR}^{(3)} } = 2$, (b) $\frac{ x_R^{(3)} }{ x_{NR}^{(3)} } = 1$, (c) $\frac{ x_R^{(3)} }{ x_{NR}^{(3)} } = 0.5$	23
1.12	Comparison between SR and CARS techniques in terms of imaging speed and information content. Adapted from [24].	24
1.13	Jablonski diagrams of the two categories of BCARS: hyperspectral CARS and Multiplex CARS.	25
1.14	Comparison of different BCARS systems in literature in terms of speed and spectral coverage. For the comparison, we referred to the following works [32, 67, 76, 78, 83, 88, 94, 99, 100].	26
1.15	Jablonsky diagram for (a) Two-color and (b) Three-color CARS mechanisms.	28
1.16	Mathematical simulation of the two excitation mechanisms for broadband CARS generation keeping fixed the average power of the pump and Stokes beam, the pump pulse bandwidth, and the nonlinear third-order susceptibility and varying the bandwidth of the broadband Stokes.	30
1.17	Scheme for TD-CARS. After the arrival of two synchronized beams, namely pump and Stokes beam, a third beam, the probe beam, arrives with a delay τ waiting for the decay of the NRB. If τ is sufficiently large (longer than one pulse duration) to suppress the NRB contribution, the measured anti-Stokes component will just contain the resonant contribution.	33
1.18	Scheme of E-CARS and F-CARS experimental set-up.	34

List of Figures

2.1	Picture of the supercontinuum generation in a 10-mm YAG crystal from the VIBRA laboratory of Politecnico di Milano.	42
2.2	Schematic representation of Self-focusing. From the left, refractive index behavior variation in function of the radial coordinate; $\chi^{(3)}$ material with propagation along the z-axis highlighting the focusing of the beam.	45
2.3	Self-phase modulation of a Gaussian pulse which produces a variation of the instantaneous frequency with time.	46
2.4	Schematic illustration of the filamentation process. (a) Self-focusing of a laser beam by optical Kerr effect. (b) Defocusing of the beam by the plasma. (c) Illustration of the collapse of the beam on itself by the Kerr effect leading to the ionization of the media with the consequent formation of a filament. Adapted from [137].	49
2.5	Picture displaying the conical emission of the WLC generation in a 10-mm YAG crystal. Taken from the BCARS experimental setup described in this work.	50
3.1	Schematic illustration of the BCARS experimental setup.	55
3.2	Iterative Fourier transform algorithm for retrieving the ultrashort-pulse amplitude and phase from FROG Data.	60
3.3	Experimental setup for SHG-FROG. PH: pinhole, BS: Beam splitter.	60
3.4	Schematic representation of the generation of the narrowband pump pulses through the etalon.	61
3.5	Characterization of the pump pulses before the etalon. (a) Spectrogram acquired with the SHG-FROG experimental setup employing a 1mm-BBO crystal for SFG. (b) Intensity autocorrelation reconstructed from the spectrogram in (a). (c) Pulse temporal trace obtained through the iterative algorithm. (d) Spectrum of the pump pulses measured with the same spectrometer used for CARS experiments.	62
3.6	Characterization of the pump pulses after the etalon with $(\Delta\lambda)_{f_{sr}} = 29,814$ nm and $R = 90\%$. (a) Spectrogram acquired with the SHG-FROG experimental setup employing a 1mm-BBO crystal for SFG. (b) Intensity autocorrelation reconstructed from the spectrogram in (a). (c) Pulse temporal trace obtained through the iterative algorithm. (d) Spectrum of the pump pulses measured with the same spectrometer used for CARS experiments.	63
3.7	Characterization of the pump pulses after the etalon with $(\Delta\lambda)_{f_{sr}} = 15.4$ nm and $R = 92\%$. (a) Spectrogram acquired with the SHG-FROG experimental setup employing a 1mm-BBO crystal for SFG. (b) Intensity autocorrelation reconstructed from the spectrogram in (a). (c) Pulse temporal trace obtained through the iterative algorithm. (d) Spectrum of the pump pulses measured with the same spectrometer used for CARS experiments.	64
3.8	Spectra of the WLC generation in a 10 mm YAG crystal at 8 different positions of the mask inserted in the prism compressor stage.	65
3.9	Characterization of the Stokes pulses after their generation and collimation with a 75 mm achromatic doublet. (a) Spectrogram acquired with the SHG-FROG experimental setup. The SFG was obtained by focusing the beams on a 300 μm -thick BBO crystal. A thinner crystal, with respect to the pump pulse measurements, is needed to satisfy the phase-matching condition for a broader bandwidth. (b) Intensity autocorrelation reconstructed from the spectrogram in (a). (c) Pulse temporal trace obtained through the iterative algorithm.	66
3.10	Characterization of the Stokes pulses after the compression with a 60 cm tip-to-tip prism compressor. The SFG was obtained by focusing the beams on a 300 μm -thick BBO crystal. (a) Spectrogram acquired with the SHG-FROG experimental setup. (b) Intensity autocorrelation reconstructed from the spectrogram in (a). (c) Pulse temporal trace obtained through the iterative algorithm.	67
3.11	Characterization of the Stokes pulses after the compression with a 60 cm tip-to-tip prism compressor and 2.54 cm rod of glass. The SFG was obtained by focusing the beams on a 300 μm -thick BBO crystal. (a) Spectrogram acquired with the SHG-FROG experimental setup. (b) Intensity autocorrelation reconstructed from the spectrogram in (a). (c) Pulse temporal trace obtained through the iterative algorithm.	68
3.12	Photos of the experimental BCARS microscopy setup, highlighting the optical sources stage, the microscopy unit, and the detection part. The microscopy unit works in an up-right configuration and enables us to collect signals both in the epi and in the forward configuration.	69
3.13	Schematic representation of the pseudo-Kohler illumination realized in the BCARS microscope. The LED light is in red, while the laser beams (pump and Stokes) are in green.	70
3.14	Schematic representation of the detection unit. The light is sent into a monochromator that separates the colors, while a CCD sensor with many pixels outputs the counts per pixel within a certain pixel dwell time.	71

3.15	Matlab interface for the acquisition of the CARS images.	72
4.1	Workflow of the experimental design. It includes 4 main parts that are: setup alignment, bright field image, preliminary measurements, and experimental planning.	74
4.2	Graph showing the daily procedure I adopt for calibrating the wavenumber axis. I average 100 toluene spectra (blue curve), 100 NRB spectra measured on a quartz coverslip (orange curve), and 100 dark spectra that I subtract from the CARS and NRB spectra. The pixel exposure time is 1 ms. The phase-retrieved spectrum (light-blue curve) is obtained from the toluene CARS spectrum and the NRB one through the Kramers-Kronig algorithm. The new wavenumber axis is obtained via a third-order polynomial fitting comparing the highlighted 8 peaks of the phase retrieved spectrum with the corresponding SR peaks (purple curve). The error between the position of the peak in SR and in the calibrated phase-retrieved spectrum is computed to estimate the goodness of the calibration procedure.	76
4.3	Workflow for the data post-processing. The main steps are: Quality control; Denoising of the hyperspectral data; NRB removal; Spectral unmixing.	78
4.4	Schematic representation of SVD decomposition.	80
4.5	(a) Illustration of a neuron j at layer l ; (b) Plots of typical non-linear activation functions: sigmoid, tanh, ReLU; (c) Scheme of a shallow NN featuring a single hidden layer; (d) Scheme of a deep NN featuring several hidden layers. From [150]	84
4.6	LeNet architecture, featuring two sets of convolutional and subsampling layers, followed by two fully-connected layers and finally an output layer. As highlighted in the image, convolutional filters or kernels have local connectivity with their input, which enables feature extraction in a spatially invariant way. Adapted from [150, 166].	86
4.7	Model architecture of the CNN spectral denoiser. (a) Hyperparameters of the neural network. (b) Graphical representation of the CNN denoiser. Adapted from [100].	88
4.8	Metrics of the model for 100 epochs. From [100].	88
4.9	Noise analysis of the trained model on noisy test datasets of 60000 spectra. Model inputs (blue curves) feature increasing levels of randomly distributed noise from left to right. The ground truth (black dashed lines) is in excellent agreement with the model prediction (red curves) for every noise level employed in the analysis. Model performance metrics are reported in the table for each noisy case study. From [100].	89
4.10	Data augmentation methods. From [100].	91
4.11	Comparison of four different denoising methods on a CARS spectrum of toluene: CNN, moving mean algorithm, Fourier-transform approach, and Savitzky-Golay filter. (a) Denoising methods on a noisy input toluene CARS spectrum (blue curve) obtained considering experimental data and adding random noise. (b) $Im\{\chi_R^{(3)}\}$ spectra retrieved through the Kramers-Kronig algorithm starting from the spectra in panel (a). A SR spectrum (black curve) of toluene acquired with 5 s exposure time is reported for comparison.	92
4.12	Example of the application of the KK algorithm to a spectrum of toluene. I_{CARS} : CARS spectrum of toluene (blue curve), I_{ref} reference spectrum on glass (orange curve), I_{KK} phase retrieved spectrum after the Hilbert transform (yellow curve), I_{pc} phase corrected spectrum (violet curve), $I_{pc,sc}$ phase and scale corrected spectrum (green curve).	97
4.13	Model architecture of the SpecNet network for the NRB removal. (a) Hyperparameters of the neural network. (b) Graphical representation of the SpecNet.	100
4.14	Simulated data for the SpecNet. (a) Simulated CARS spectra. (b) Ground truth relative to the simulated CARS spectra in (a). (c) Examples of the simulated nonresonant contribution deriving from the product of two sigmoidal functions.	101
4.15	Mean square error (MSE) loss of the training and validation set after 10 epochs of training with 50000 instances.	101
4.16	Prediction of the SpecNet on a spectrum with a higher number of spectral peaks than the typical spectra of the training dataset.	102
4.17	Prediction of the SpecNet on experimental data acquired on 6 different solvents acquired with the BCARS setup: methanol, acetone, toluene, ethanol, isopropanol, dimethyl sulfoxide (DMSO). Each spectrum is the average of 30 spectra acquired with 0.8 ms pixel dwell time. Spectral points: 640.	103
5.1	Scheme of the BCARS experimental setup. HWP: half-wave plate; PBS: polarizing beam splitter; LP: long-pass filter; SP: short-pass filter.	110

List of Figures

5.2	Scheme of the data processing pipeline: (i) CNN spectral denoiser, (ii) NRB removal via the KK algorithm, and (iii) Spectral unmixing methods to obtain false-color images.	111
5.3	(a) BCARS raw single-point spectra (blue solid lines) acquired with 0.8-ms exposure time on six solvents (as indicated), sandwiched between two 170- μm glass coverslips. The red lines are phase-retrieved spectra after the Kramers-Kronig algorithm. SR spectra (grey areas) are also plotted for comparison. (b) Scheme of the sample configuration employed for the experiments. (c) Dilution test experiment on a binary solution of DMSO and pure water. We considered the retrieved imaginary part of the third-order resonant susceptibility of the main peak of DMSO at 667 cm^{-1} . The inset shows a zoom on the low-concentration binary solutions. Estimated sensitivity: 14.1 mmol/L of DMSO in pure water. Error bars: 1 standard deviation.	112
5.4	BCARS image of 10- μm PS and 8- μm PMMA beads soaked in DMSO and sandwiched between two 170 μm glass coverslips. (a) Single-pixel CARS spectra in the fingerprint region of a PS bead (green curve), DMSO (blue curve), and a PMMA bead (red curve). (b) Frames of the measured BCARS hypercube at three selected Raman shifts (black triangles in panel (a)) corresponding to three main characteristic peaks (650 cm^{-1} for DMSO, 780 cm^{-1} for PMMA, 970 cm^{-1} for PS) of the species in the fingerprint region. (c) MCR-ALS retrieved spectra of the three chemical species after the post-processing data pipeline and correspondent SR spectra (grey areas) (d) False-color image retrieved with MCR-ALS analysis, with the same color code as (c). Imaging settings: 90×90 pixels, 1- μm pixel size, 1024 spectral points, 1 ms pixel dwell time, Scale bars: 20 μm , total image acquisition time: 8.1 s.	113
5.5	Microscopy of 6- μm thick murine spine sandwiched between two 170 μm quartz coverslips. (a) Bright-field image of a tissue slice stained with H&E. (b-d) Frames of the measured BCARS hypercube at three different Raman shifts (black triangles in panel (e)) on the unstained adjacent slice. (e) CARS spectra from the bone marrow region (green curve, +), from the muscle region (blue curve, *), and from the bone tissue (red curve, x). (f-g) Concentration map and vibrational spectra of the three clusters associated with bone marrow, muscle, and bone, obtained after denoising the data with the CNN model, NRB removal through the KK algorithm, and applying the KMCA algorithm. Imaging settings for the B-CARS dataset: 200 μm scale bar, 400×800 pixels, 1- μm pixel size, 1024 spectral points, 10-ms pixel dwell time, total image acquisition time: 55 minutes.	115
5.6	BCARS spectra of six different solvents acquired with 0.8 ms exposure time sandwiched between two 170- μm glass coverslips. The plots show the CARS intensities (blue curves), the phase-retrieved spectra via the KK algorithm (red curves), and the SR spectra acquired averaging five spectra acquired with 5-s exposure time (grey areas). No denoising has been applied before the application of the KK algorithm.	117
5.7	(a) CARS spectrum of toluene sandwiched between two 170 μm quartz coverslips acquired with 1-ms exposure time in two different setup configurations: masking the Stokes spectrum in (b.1) thus obtaining pulses with spectrum (b.2) without compressing it (two color CARS only); using the Stokes in (b.2) and compressing it to reach 20-fs pulses thus exciting the vibrational mode both with the three-color and the two-color mechanisms.	118
5.8	Time-delayed CARS on Toluene changing the delay between the narrowband and the broadband Stokes beam with a mechanical delay stage. Exposure time per spectrum: 0.8 ms.	119
5.9	(a) BCARS image of therapy-induced senescent HepG2 cancer cells 72 hours after treatment with DFO. The false-color images highlight three different species in the cells. (b) Retrieved spectra associated with the three species in panels (a). Imaging settings: 1-ms pixel exposure time; 500-nm pixel size.	120
5.10	BCARS imaging on a tumoral liver slice of a mouse model. (a) Image on the H&E stained slice. (b) Bright-field image of the unstained slice used for BCARS imaging. (c) $600\times 600\ \mu\text{m}^2$ BCARS image on tumor liver obtained through N-FINDR analysis after noise and NRB removal. (d) Retrieved spectra associated to the species in panels (c). Imaging settings of panel (c): 300×300 pixels; 3-ms pixel exposure time; 2- μm pixel size.	121